Active systems at low Reynolds numbers

Assemblies of driven filaments & swimming with flexible flagella

Cornelius Martin Weig

München 2015

Active systems at low Reynolds numbers

Assemblies of driven filaments & swimming with flexible flagella

Cornelius Martin Weig

Dissertation
an der Fakultät für Physik
der Ludwig–Maximilians–Universität
München

vorgelegt von
Cornelius Martin Weig
aus Hutthurm

München, den 2. November 2015

Erstgutachter: Prof. Erwin Frey

Zweitgutachter: Prof. Holger Stark

Tag der mündlichen Prüfung: 14. Dezember 2015

Zusammenfassung

Aktive Systeme zeigen neuartige Physik, deren Verhalten von der gewohnten Gleichgewichtsphysik in oft überraschender Weise abweicht. Ein solches Beispiel sind getriebene Teilchen, die durch Stöße ihre Laufrichtung ausrichten. Ist die Dichte solcher Teilchen hoch genug, ordnet sich plötzlich das Durcheinander der wirr umlaufenden Teilchen, und die Teilchen beginnen kollektiv in eine zufällige Richtung zu laufen. Zu diesem als Vicsek-Modell bekannten System gibt es inzwischen eine experimentelle Verwirklichung im sogenannten Motility Assay — genau genommen weiß man aber nicht wirklich, ob es sich dabei um analoge Systeme handelt oder lediglich um ähnliche Phänomenologie.

Ziel des ersten Teils dieser Arbeit war es daher, ein realistischeres Modell des Motility Assays zu entwickeln. Dazu bedienten wir uns des etablierten Modells der wurmartigen Kette um längliche Filamente darzustellen, und benutzten eine teilchen-basierte Fluid-Simulation um die hydrodynamische Wechselwirkung zwischen den Filamenten zu modellieren. Diese Filamente wurden nun mit einer konstanten Geschwindigkeit getrieben. Ein großer Vorteil dieses Modells ist, dass die hydrodynamischen Wechselwirkungen ausgeschaltet werden können, sodass der Einfluss der Hydrodynamik direkt bestimmt werden kann.
Um dieses Modell einordnen zu können, wurden als erstes einzelne Filamente und binäre Stöße zwischen Filamenten untersucht. Dabei bestätigte sich unsere Vermutung, dass die Filamente einen persistenten Zufallspfad beschreiben und bei Stößen im Mittel ausgerichtet werden. Dieser Effekt ist ausgeprägter, wenn die Filamente auch durch Hydrodynamik wechselwirken.
Sodann untersuchten wir zweidimensionale Systeme *ohne* Hydrodynamik mit bis zu 30 000 Filamenten, die aus einem zufälligen Anfangszustand starteten. Bei niedrigen Dichten bleibt dieser chaotische Zustand auch bestehen, aber sobald die Dichte einen kritischen Schwellwert übersteigt, kommt es zu einer Phasenseparation in eine geordnete Hochdichte-Region und eine ungeordnete Niedrigdichte-Region. Um diesen Phasenübergang zu charakterisieren, führten wir verschiedenste Observablen wie die gemittelte Ausrichtung, die Stärke der Dichteschwankungen, die Dichte der Gasphase und die Größenverteilung der Filamentansammlungen ein.
Analog dazu untersuchten wir dieselben Systeme *mit* Hydrodynamik, und zwar zunächst in zwei Dimensionen. Überraschenderweise ändert sich die Phänomenologie durch die hydrodynamische Wechselwirkung grundlegend. Unabhängig von der Dichte fanden wir ausschließlich weitgehend homogene und geordnete Zustände, sodass der Phasenübergang des "trockenen" Systems vollkommen ausbleibt.
Schließlich gingen wir zu einem dreidimensionalen Fluid über, während die Filamente auf zwei Dimensionen beschränkt blieben. Hier finden wir wiederum ähnlich zum trockenen System eine Aufteilung in eine Hochdichte- sowie Niedrigdichte-Region.

Im zweiten Teil untersuchten wir ebenfalls ein aktives System, allerdings völlig anderer Natur: Aktives Schwimmen durch eine zähe Flüssigkeit, wie es für Bakterien in Wasser der Fall ist. Diese können, anders als wir, nicht durch Paddeln schwimmen, sondern müssen sich regelrecht in die Flüssigkeit hineinschrauben um vom Fleck zu kommen. Bakterien wie E. Coli er-

reichen dabei eine beachtliche Effizienz, weshalb ihr Aufbau für künstliche Mikro-Schwimmer herangezogen werden kann. In einer Kollaboration mit der Gruppe von Prof. Tim Liedl haben wir versucht, diesen Schwimmmechanismus mit Hilfe von künstlichen DNA-Flagellen zu imitieren. Diese experimentelle Arbeit habe ich durch eine analytische Untersuchung der Schwimmgeschwindigkeit unterstützt.

Im Experiment werden mehrere DNA-Flagellen an einem magnetischen Kügelchen chemisch befestigt, das über ein externes Magnetfeld rotiert wird. Dabei verwickeln sich die unterschiedlich langen DNA-Flagellen zu einem einzelnen Bündel, das somit einen einzelnen Fortsatz bildet. Da dieses Bündel bei der Drehung durch die Flüssigkeit helixartig verbogen wird, bewegt sich der künstliche Schwimmer vorwärts. Ziel der analytischen Rechnung war es zunächst, die genaue Form dieses Bündels zu bestimmen. Vorarbeiten auf diesem Gebiet existieren zwar für ähnliche Fälle, nicht aber für diesen Schwimmer, da das Bündel wegen der unterschiedlich langen Flagellen eine längenabhängige Biegesteifigkeit besitzt. Aus gegebener Bündelform war es schließlich möglich, eine Vorhersage über die Schwimmgeschwindigkeit des künstlichen Schwimmers zu treffen. Trotz etlicher Näherungen und Fehlerquellen stimmen unsere Vorhersagen bis auf einen überraschend kleinen Faktor zwei mit dem Experiment überein. Unser Ansatz erlaubte es uns, die Schwimmgeschwindigkeit auf verschiedenste Parameter wie die Größe des Magnetkügelchens, die Anzahl der gebundenen DNA-Flagellen, oder deren Länge zu untersuchen. Erstaunlich hierbei ist, dass eine abnehmende Biegesteifigkeit so gut wie im gesamten untersuchten Parameterbereich die Schwimmgeschwindigkeit gegenüber einem vergleichbaren Schwimmer mit konstanter Biegesteifigkeit erhöht.

Synopsis

Active systems show novel physics with phenomena that deviate from familiar equilibrium physics in surprising ways. Such an example are driven particles which align locally. Above a certain density threshold, the chaotic movement of the particles suddenly becomes an ordered collective motion in a randomly chosen direction. This so-called Vicsek model has been realized by the actomyosin motility assay — however, it is under dispute whether model and experiment show indeed identical physics or just have a similar phenomenology.

Therefore, the goal of the first part of this work is to develop a more realistic model of the motility assay. To this end, we used the well-established worm-like chain to model the filaments of the motility assay and a particle-based fluid simulation to model the hydrodynamic interaction between the filaments. These filaments were then driven at constant speed. A big advantage of this model is its capability to selectively switch off hydrodynamic interactions, so that the effect of hydrodynamics can be determined.
In order to characterize this model, we first examined single filaments and binary collisions. Thereby, we were able to confirm our presumption that the filaments describe a persistent random walk and get, on average, aligned in collisions. This alignment was stronger if hydrodynamic interactions were enabled.
Next, we considered two-dimensional systems of up to 30 000 filaments and random initial configuration *without* hydrodynamics. At low filament densities, this mostly chaotic state prevailed, but as soon as the density exceeded a critical threshold, we found a phase separation into an ordered high-density and a disordered low-density phase. To characterize this phase transition, we looked at various observables such as the average filament direction, the strength of density fluctuations, the density of the gas phase, and the clustering behavior of the filaments.
In an analogous way, we also examined the same systems *with* hydrodynamic interactions, beginning with a two-dimensional fluid. Surprisingly, the hydrodynamic interactions fundamentally changed the observed phenomenology. Regardless of the filament density, we exclusively found mostly homogeneous and ordered states so that the phase transition of the "dry" system was completely gone.
Finally, we considered a three-dimensional fluid while keeping the filaments constrained to a plane. Such systems behaved similarly to the dry case and had the same separation into a high- and a low-density region.

In the second part of this thesis, we examined another, yet completely different active system: active swimming through a viscous fluid, as it is the case for bacteria in water. In contrast to humans, bacteria cannot swim by thrusting the surrounding water, but literally have to screw into the fluid in order to move. Bacteria such as E. coli have evolved to remarkably efficient swimmers. This is why their structure has been a blueprint for artificial microswimmers. In a collaboration with the group of Prof. Tim Liedl, we tried to imitate the bacterial swimming

mechanism using artificial DNA-flagella. I contributed to this project by an analysis of the swimming speed of these artificial swimmers.

In the experiment, multiple DNA-flagella are chemically bound to a magnetic bead, which can be rotated via an external magnetic field. Thereby, the DNA-flagella entangle to a flagellar bundle, which thus can be seen as a single appendage. Because the fluid drag deforms the bundle into a helical shape, the swimmer can move forward. The first aim of my analytical work was to determine the exact shape of this bundle. Due to a length distribution in the flagella, the flagellar bundle must have a length-dependent bending stiffness. Previous work exists for similar cases, however not for cases with varying bending stiffnesses. From a given bundle shape it is finally possible to calculate the swimming speed of our artificial swimmer. Despite several approximations and measurement errors, our theoretical predictions agree remarkably well with the measured swimming speeds. Further, our calculation made it possible to test the swimming speeds for various parameters such as the size of the magnetic bead, the number of attached DNA-flagella, or their length. Interestingly enough, a decreasing bending stiffness improved the swimming speed in virtually the full parameter space as compared to a similar swimmer with constant bending stiffness.

Contents

Part I

Motility Assay

1 Introduction to active systems

"For any non-zero temperature, there is no long-range order for continuous symmetries in two dimensions", states the Mermin-Wagner theorem [1, 2]. And yet, Vicsek et al. came up with a model that seemingly violates it [3–5] — *Something got to be wrong.*

The crucial detail we were ignoring is that the Mermin-Wagner theorem only applies to equilibrium physics, whereas the Vicsek model is by construction out of equilibrium: It is an agent-based model where particles propel at a constant speed and align their direction of movement with all neighbors in their vicinity up to some angular noise [3]. In this model, above a certain density threshold all particles start to collectively move into the same direction. This first glimpse of exciting new non-equilibrium physics has sparked intensive research in active systems [6–9]. The defining feature of an active system is that a *local* energy input constantly drives the system out of equilibrium [8].

For experiments, this local input of energy is the major challenge. Exploiting the biochemical machinery of cells has facilitated the design of experiments with active constituents on a very small scale [10–13]. For example, in the actomyosin motility assay myosin motors are attached to a surface and actively push actin filaments whereby consuming ATP [10]. At high enough actin concentrations, the actin filaments form high-densitiy clusters or moving bands where all filaments are aligned. An analogous setup to the actomyosin motility assay was later realized with dynein motors and microtubules, although with a rather different phenomenology [11, 14]. Beside organic motor proteins, also inorganic catalysts have been employed to convert chemical into mechanical energy, for example platinum covered Janus particles whose activity drives an anomalous sedimentation behavior [15, 16]. Another, completely different driving mechanism uses the spontaneous rotation of insulating spheres in a fluid due to an external electric field (Quincke rotation) which leads to collective motion at high densities [17, 18]. Maybe less sophisticated, but nevertheless quite effective are experiments where inert particles sit on a plate that is periodically shaken and thus directly transfers mechanical energy onto every single particle [19–22]. Beside these inanimate setups, there is also a large number of experiments where living bacteria act as the energy source [23–26]. Such dense suspensions of bacteria have been shown to exhibit turbulent flows even in the regime of low Reynolds numbers [25, 27].

Beside the experimental progress in active systems, theory has been quite successful in explaining some of the observed phenomenology. For example, Toner and Tu coarse-grained the Vicsek model to obtain an extended Navier-Stokes equation with further terms that are allowed by the symmetries of the model [4, 28]. This generalized hydrodynamic equation for self-propelled particles predicted large density fluctuations in the Vicsek model and the mechanism by which it overcomes the constraints of the Mermin-Wagner theorem [4, 5]. The basic principle of this mechanism is that in an ordered state where the order parameter is also a velocity, fluctuations advect the order parameter into the perpendicular direction so that spin-waves are suppressed [29]. Unfortunately, the Toner-Tu equation falls short when

it comes to the details of the Vicsek model, such as travelling density waves, or the nature of the order-disorder phase transition [30, 31]. By construction, the mean-field treatment by Toner and Tu predicts a continuous phase transition which was compatible with early simulations by Vicsek [3]. However, further work has shown that this phase transition is in fact a first order transition [30–32]. Nevertheless, phenomenological hydrodynamic equations with to-be-determined parameters have been successfully employed to further active systems, such as the cytoskeleton of cells [33], suspensions of bacteria [34, 35], and active fluids [27, 36]. Last but not least, other authors have demonstrated how microscopic collision rules can be coarse-grained into hydrodynamic equations with the added benefit that the hydrodynamic coefficients are no longer free parameters [37–39].

Beside experiment and theory, simulations have proven as a prolific playground to explore new ideas. Due to the rich phenomenology of active systems, there is now a mere zoo of models for active systems. The original model of Vicsek consisted solely of point particles with a polar alignment and showed the above-mentioned global order along with large density fluctuations [3, 40]. For an application to animal flocks, the Vicsek model was later extended by an additional potential between the particles [32, 41]. As an effective model of self-propelled polar rods, the Vicsek model was further modified by a nematic interaction among the particles [42, 43], which in particular allowed to study the differences in morphology caused by polar or nematic alignment rules [44]. Because nematic interactions are naturally mediated by stiff needles, other works replaced the point-like particles of the Vicsek model by self-propelled rods which lead to a modified swarming and clustering behavior [45–47]. Beyond the Vicsek-like types of models with related phenomenologies, other active systems have been reported to show a motility induced phase separation [48–52], jamming of propelled colloids [53, 54], or aggregation and collective swimming in squirmers [55, 56].

Now consider again the actomyosin motility assay [10]. This experiment has a density threshold above which high-density clusters or bands of actin filaments form in which all filaments point into the same direction. This phenomenology is strikingly similar to the Vicsek model, which raises the question whether experiment and model are equivalent. There are good reasons to assume that the filament interactions are in fact only short-ranged contact interactions. For example, binary collisions of filaments are almost perfectly nematic as is expected from a rod-like contact interaction [57]. Besides, in the similar system of microtubules the authors cannot find any hydrodynamic interactions prior to microtubule contact [11]. And yet, Schaller et al. explicitly show that hydrodynamic interactions between clusters of filaments do matter, which implies also long-ranged interactions [58]. As Marchetti et al. note, the connection between the actomyosin motility assay and the Vicsek model is therefore only qualitative at the moment [8].

Another shortcoming of proposed models for the motility assay is that these models treat the actin filaments either as point-like particles or as hard rods. However, actin filaments are extended semi-flexible polymers that bend easily and are therefore neither point-like nor hard rods [59–61]. The length of filaments may however play an important role in the filament interactions, because it makes interactions of multiple filaments at once much more common. The work of Suzuki et al. highlights this importance of non-binary collisions [57]. Furthermore, it was recently shown that the shape of active particles has a profound impact on the phenomenology of active systems [62]. Along that line, one has to expect that a soft semi-flexible filament behaves differently than a hard rod.

Therefore, the existing models for the actomyosin motility assay lack long-ranged hydrodynamic interactions and the flexibility of actin filaments. This work fills this gap by including hydrodynamic interactions among the filaments and modelling the filaments as semi-flexible worm-like chains.

Chapter 2 introduces our qualitative model of the motility assay, including an exhaustive list of the relevant simulation parameters in section 2.2. The numerically interested reader also finds implementation notes in section 2.3. The following chapter 3 then examines the characteristics of single polymers and polymer collisions. Systems with a large number of filaments *without* hydrodynamic interactions are treated in chapter 4, where we consider the phenomenology first (4.1) and then quantify our findings (4.2). In a broadly analogous way, chapter 5 considers systems with large numbers of filaments *with* hydrodynamic interactions. In addition to the phenomenological overview (5.1) and the quantitative analysis (5.2), section 5.3 also looks at extensions of the model. For a brief overview, the results of these chapters are summarized in sections 4.3 and 5.4, respectively. Finally, we discuss our findings in chapter 6.

2 Model definition & methods

From a theorist's point of view, the motility assay of actin filaments basically consists of two components. First, there is the solution of actin filaments in a thin aqueous film that sits between two coverslips. Second, the bottom coverslip is coated with a dense carpet of molecular motors. Additives in the solution push the actin filaments onto this functionalized surface, where the motor proteins attach to and thrust the filaments, whereby consuming dissolved ATP from the solution. Because F-actin has directionality and the used motor proteins only attach in one direction, the filaments start to move about on the lower coverslip with a speed of about $4.8\,\mu m/s$ [10].

Inspired by this experiment, we develop a model system that captures the essential ingredients of the motility assay. However, the aim is not to simulate the motility assay and try to estimate the model parameters from experimental input. Instead, we aim for a model sui generis which only behaves similar to the motility assay. Therefore we need to make simplifying assumptions about the experiment.

First, we note that the actin filaments are pushed onto the coverslip where the myosin motors keep the filaments bound. Consequently, we restrict the filament dynamics to a two-dimensional plane close to the lower boundary. Going one step further, we may even ignore the third dimension altogether and arrive at a strictly two-dimensional model. Because hydrodynamics of two dimensions is rather peculiar, we will nevertheless consider both two- and three-dimensional fluids.

In the experiment, the actin filaments have a size distribution from $2 - 10\,\mu m$ [10, 57]. To avoid spurious effects from a mixture of different actin lengths, we require all filaments to have one and the same length L in our model. Furthermore, we assume that the filaments have only one more property, the persistence length l_p which quantifies their free dynamics. Typically, the persistence length of free F-actin is about $16\,\mu m$ [59–61], although the effective persistence length when pushed on the motility assay is somewhat smaller. For our model, we therefore focus on the range of persistence length $1\,L \leq l_p \leq 10\,L$.

Next, we need to characterise the filament–motor interactions. The heavy meromyosin motor protein, which is typically used in the motility assay, exerts a force of about $1.8\,pN$ during its active thrust [10, 63]. At a typical motor spacing of $42\,nm$, the reasonable maximal force is still orders of magnitude smaller than the forces where contour length of actin starts to stretch [64]. Therefore, we can regard the filaments as inextensible. However, apart from the resulting constant speed of the filaments ($\approx 4.8\,\mu m/s$), most details of the filament–motor interactions remain unknown. In particular, there is no proper understanding of the competition for motor proteins between the filaments, which also affects filament–filament interactions. Due to our lack of knowledge, we make the very simplified assumption that filaments always move at the constant speed v_0. Furthermore, we assume that the trailing part of the filament is locked onto the path of the head, so that the filaments move like a snake

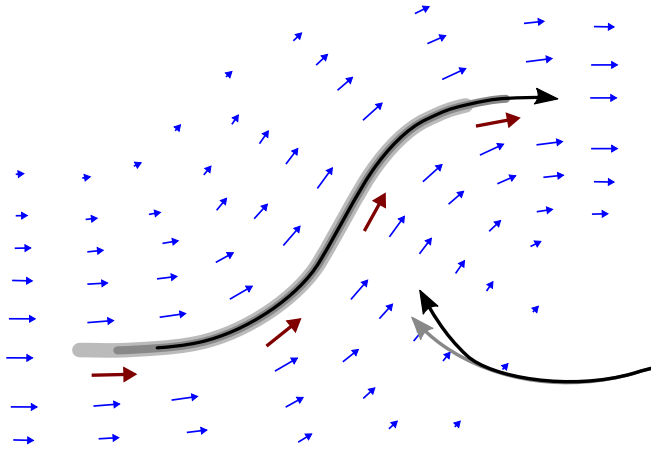

Figure 2.1 | The filaments in the motility assay move like snakes on the myosin functionalized surface. The cartoon shows a sample filament at subsequent time steps (from shaded to solid black) with the velocity of some local segments indicated by red arrows. The active motion of the filament drags the surrounding fluid along, as indicated by the blue arrows. Another filament (lower right) gets dragged along by this flow field.

(see Fig. 2.1). This is justified by the fact that at every point in time usually several motors are attached to any filament, so that transverse motions are impossible in the experiment.

Finally, the filament–filament interactions need to be specified. Because several myosin motors are attached to each actin filament at every point in time, a filament remains bound to the surface after its first contact. Consequently, the filaments all have similar distances to the functionalized surface and therefore repel sterically. In other words, if the path of one filament is blocked by another, its tip feels a repulsive force. However, a filament tip may also escape into the third dimension and reattach on the other side of an obstacle. Beside this steric interaction there is also the competition for motor proteins that may effectively cause an aligning interaction between two filaments, especially in high-density regions. Because we have no access to the microscopic details of filament interactions, we have to rely on qualitative assumptions about the interaction. Therefore, we make the crude assumption that all direct interactions amount to a potential barrier of strength $\mathcal{U}_b$ that blocks the location of one filament for other filaments. The height of this potential barrier determines whether filaments may cross each other. Note that the requirements of constant speed, snake-like movement, and strict non-crossing cannot be fulfilled in all situations. In such lockdown situations with high $\mathcal{U}_b$, it is then most natural that the filaments stop moving.

Beside the direct interaction, there is also an indirect interaction among the filaments via the viscous fluid in which the filaments are immersed. One moving filament drags the surrounding fluid along, which in turn affects other filaments (see Fig. 2.1). The relative strength of both interactions is unknown, so we take an arbitrary strength for the hydrodynamic interaction. It is one of the major aims of this work, to determine the role of hydrodynamic interactions for the patterns observed in the experiment.

The following sections of this chapter will describe in detail how we implemented this model.

2.1 Modelling the filaments

As discussed above, the filaments are fully described by their length L and their persistence length l_p. A very successful standard model for polymers of defined length and persistence length is the worm-like chain model, which is briefly summarised in the following [65–67]. For a contact interaction among filaments, we introduce an additional soft interaction with a small range.

The worm-like chain model breaks the continuous contour of the polymer into a finite number of discrete bonds, which are represented by a sequence of beads with positions $\boldsymbol{r}_1, \dots \boldsymbol{r}_m$ of mass m_b at the bond joints. A spring and bending potential between subsequent beads ensure constant bond length and correct bending angle statistics, respectively. Of course, the constant bond length cannot be perfectly achieved by a spring potential, however for our purposes it is sufficient when the filaments have almost constant length. For such purposes, it has become common practice to use a Finitely Extensible Nonlinear Elastic (FENE) spring potential, which allows for larger integration steps than for example a harmonic spring potential [68]. The FENE spring potential U_s is given by

$$U_s\big(\boldsymbol{r}_i, \boldsymbol{r}_j | R_0,\, R_{\max}\big) = \begin{cases} \frac{-1}{2}\kappa_s R_{\max}^2 \cdot \log\Big(1 - \Big(\big(r_{ij} - R_0\big)/R_{\max}\Big)^2\Big) & r_{ij} < R_{\max} \\ \infty & \text{else,} \end{cases} \tag{2.1}$$

where $r_{ij} = |\boldsymbol{r}_j - \boldsymbol{r}_i|$, R_0 is the rest length of a bond, $R_{\max}$ the maximal extensibility of a bond, and κ_s the spring constant.

In addition to the spring potential, a bending potential between subsequent bonds ensures the proper angle statistics for a given persistence length. The bending potential between two bonds is given by

$$U_\sphericalangle(\boldsymbol{u}_i,\, \boldsymbol{u}_{i+1}) = \frac{-1}{2}\kappa_b \frac{\boldsymbol{u}_i \cdot \boldsymbol{u}_{i+1}}{u_i\, u_{i+1}} \,, \tag{2.2}$$

where $\boldsymbol{u}_i = \boldsymbol{r}_{i+1} - \boldsymbol{r}_i$ is the connecting vector of two subsequent beads, u_i its length, and $\kappa_b = k_B T\, l_p / R_0$ is the bending stiffness [65, 66]. The full potential of a non-interacting single filament is therefore

$$U_{\text{free}}^{(j)}(\{\boldsymbol{r}_1, \boldsymbol{r}_2, \dots, \boldsymbol{r}_m\}) = \sum_{i=1}^{m-1} U_s\big(\boldsymbol{r}_i,\, \boldsymbol{r}_{i+1} | R_0,\, R_{\max}\big) + \sum_{i=1}^{m-2} U_\sphericalangle(\boldsymbol{u}_i,\, \boldsymbol{u}_{i+1}) \,, \tag{2.3}$$

where $\boldsymbol{r}_i$ is the position of the i$^{\text{th}}$ bead of filament j.

Finally, the filaments need to interact with other filaments in the simulation, which we model by a potential barrier as discussed above. This potential barrier is only relevant for the front end of the filament, because we want filaments to move in a snake-like fashion. Besides, after piercing an obstacle the potential energy due to the barrier does not change when moving. Consequently, the potential barrier is only applied to the tip bead $\boldsymbol{r}_1^{(j)}$ of each filament. The form of the potential is completely arbitrary, because the underlying microscopic mechanism is unknown. Therefore, we choose a simple harmonic potential with a finite range,

$$U_b^{(j)} = \frac{1}{2}\mathcal{U}_b \sum_{q=1,\, q\neq j}^{N} \sum_{i=1}^{m} \Big(\max\Big(0,\, 1 - \big|\boldsymbol{r}_i^{(q)} - \boldsymbol{r}_1^{(j)}\big|/r_c\Big)\Big)^2 \,, \tag{2.4}$$

where we have used that all filaments have the same number of beads m, $r_i^{(q)}$ is the position of the ith bead of filament q, N is the number of filaments, and $\mathcal{U}_b$ is the height of the potential barrier. The full potential of the set of N filaments is therefore

$$U = \sum_{j=1}^{N} \left(U_{\text{free}}^{(j)} + U_b^{(j)} \right) . \tag{2.5}$$

Given some valid starting configuration of the polymer with bead positions $\boldsymbol{r}_i$ and momenta $\boldsymbol{p}_i$, direct numerical integration of the equations of motion yields its time evolution.

So far, we have developed a numerical model for a collection of filaments as worm-like chains that interact via a local repulsive potential. The propulsion mechanism and the hydrodynamic interactions between the filaments are still missing. Because the propulsion mechanism is deeply interwoven with the hydrodynamic interactions, both will be treated in the following section.

2.1.1 Filaments in aqueous solution

Hydrodynamic interactions among a large number of filaments is a notoriously difficult problem, because the hydrodynamic interactions are long-ranged, so that every pair of filaments interacts. A way out is to explicitly model the fluid and define mutual interactions of the fluid on the filaments and vice versa. Thereby, the time-consuming pairwise interactions of filaments can be saved, but on the other hand one has the added complexity of dealing with the fluid. One way to efficiently model the fluid is via Multiparticle-Collision dynamics, which we briefly summarise below.

Multiparticle-Collision dynamics The Multiparticle Collision dynamics (MPC) is a particle-based simulation method that naturally incorporates thermal fluctuations and can naturally embed worm-like chains [69]. Because thermal noise is an important factor in the dynamics of actin in the motility assay, the thermal noise in the simulation is actually an advantage of the MPC method. In the MPC method, the fluid is represented by an ideal gas of particles, where every particle represents a small fluid package. Each fluid package has the same mass[1] m_f, a position $\boldsymbol{r}_i$, and a momentum $\boldsymbol{p}_i$. The goal is to update the positions and momenta of the particles in such a way that hydrodynamic behavior emerges on long time- and length-scales [69, 70].

The MPC algorithm updates momenta and positions in two steps: first, a simple streaming step where the fluid particles drift freely for a constant period of time h_{MPC}. Step two is the crucial step of the MPC algorithm and updates the momenta of the fluid particles (see Fig. 2.2). Interactions among the fluid particles therefore only happen at discrete points in time. For the MPC interaction, the simulation volume is first partitioned into cubic cells of edge length a. It is important to shift this grid of virtual cells by a random displacement $\boldsymbol{\Delta}_t^{\text{ran}}$ in every time step, otherwise the fluid is not Galilean-invariant [71]. The fluid particles are then assigned to the fluid cell c_{ijk} by their position, i.e. if

$$b \cdot a \leq r_\beta + \Delta_{t,\beta}^{\text{ran}} < (b+1) \cdot a \;\; \forall (b, \beta) \in \{(i,\, x),\, (j,\, y),\, (k,\, z)\} \; . \tag{2.6}$$

[1] There are variants of MPC with fluid particles of different mass, for our purpose this is however not necessary.

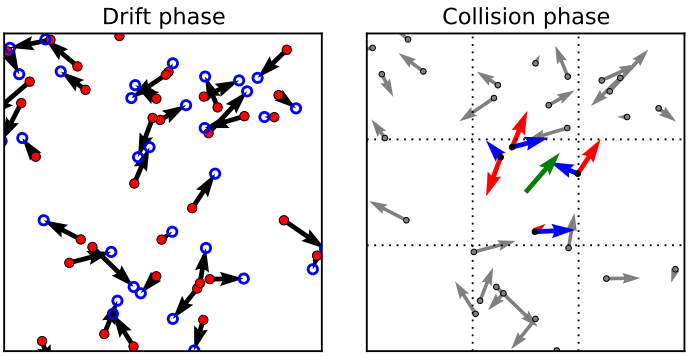

Figure 2.2 | Illustration of the two steps of the Multiparticle Collision (MPC) algorithm. **Left:** In the drift phase all fluid particles stream force-free from their current position (red dots) to their new position (blue circles) according to their velocity (black arrows). **Right:** In the Collision phase the simulation volume is subdivided into equal-sized cells (dotted lines), and each cell is processed independently of all other cells. For example, in the center cell the old momenta (red arrows) are updated with new momenta (blue arrows) while keeping the center-of-mass momentum of the cell constant (green arrow).

All fluid particles in one cell then collectively interact with each other, hence the name Multiparticle Collision Dynamics. As long as the collective interaction increases the entropy of the particles, and *locally* respects the conserved quantities, it is guaranteed that hydrodynamic behavior emerges on long time- and length-scales [69, 70]. For example, the conservation of kinetic energy leads to the diffusion of heat, the conservation momentum leads to streaming modes, and angular momentum conservation leads to circular modes.

For our purpose, not every conserved quantity is equally important. For example, the myosin motors of the motility assay constantly consume ATP and actively pull the filaments through the fluid, whereby locally releasing thermal energy into the fluid. In the experiment this energy is balanced by an exchange of thermal energy with the walls of the fluid compartment, in other words the fluid is coupled to a thermal bath. Consequently, we should relax the condition of conserving E_{kin} and instead couple each collision cell with a thermal bath of the same temperature T. Furthermore, the conservation of angular momentum within MPC is possible, but usually only necessary when the stability of circular flows is crucial [72, 73]. Because the angular momentum conservation is computationally more demanding, we neglect the $\boldsymbol{L}$-conservation in the collisions as well. As we show in Appendix A.4, this gives indeed almost identical results. To sum up, we only require the collective collision to conserve the total momentum of a cell, and thermostat the kinetic energy to a given temperature T.

Therefore, the collective collision must preserve the total fluid momentum in every cell c, $\boldsymbol{P}_c = \sum_{i \in \text{cell}} \boldsymbol{p}_i$. In the MPC approach, the momenta of all fluid particles are updated via an identical collision operator $\boldsymbol{\Omega}$ for each particle in the cell via

$$\boldsymbol{p}_i' = \frac{m_i}{M_c} \boldsymbol{P}_c + \boldsymbol{\Omega}\big[\boldsymbol{p}_i\big] \ , \tag{2.7}$$

where m_i is the mass of the i^{th} particle and $M_c = \sum_{i \in \text{cell}} m_i$ is the total mass of all particles in the cell. The momentum conservation of the collision operator $\boldsymbol{\Omega}$ then requires

$$0 \equiv \sum_{i \in \text{cell}} \boldsymbol{\Omega}\big[\boldsymbol{p}_i\big] \ .$$

In the original variant of MPC, the collision operator was simply a rotation about a randomly chosen axis, which also conserves the kinetic energy[2]. Even better suited to our problem is the Andersen thermostat variant for the collision operator, because it has an implicit thermostat [74]. Here, the collision operator $\mathbf{\Omega}$ simply generates new random momenta $\boldsymbol{p}_j^{\mathrm{ran}}$ from the equilibrium distribution of particles with mass m_f at temperature T,

$$P(p_\alpha^{\mathrm{ran}}|m_f,\,T)\,\mathrm{d}p_\alpha^{\mathrm{ran}} = \left(2\pi\, m_f k_B T\right)^{-1/2} \exp\!\left(\frac{-(p_\alpha^{\mathrm{ran}})^2}{2m_f\, k_B T}\right) \mathrm{d}p_\alpha^{\mathrm{ran}} \tag{2.8}$$
$$\langle p_\alpha^{\mathrm{ran}}, p_\beta^{\mathrm{ran}}\rangle = 2m_f\, k_B T\, \delta_{\alpha,\beta} \quad \text{with } \alpha \in \{x,y,z\}\ ,$$

for every fluid particle. To ensure the conservation of momentum, the collision operator must compensate the total momentum of the randomly chosen momenta, so that

$$\mathbf{\Omega}^{\mathrm{AT}}\left[\boldsymbol{p}_i\right] = \boldsymbol{p}_i^{\mathrm{ran}} - \frac{m_i}{M_c}\sum_{j\in\mathrm{cell}} \boldsymbol{p}_j^{\mathrm{ran}}\ . \tag{2.9}$$

Combining this collision operator with (2.7) gives the following rule for the new momenta $\boldsymbol{p}_i'$ for the Andersen variant of MPC[3]:

$$\boldsymbol{p}_i' = \frac{m_i}{M_c}\boldsymbol{P}_c + \boldsymbol{p}_i^{\mathrm{ran}} - \frac{m_i}{M_c}\sum_{j\in\mathrm{cell}} \boldsymbol{p}_j^{\mathrm{ran}} = \boldsymbol{p}_i^{\mathrm{ran}} + \frac{m_i}{M_c}\sum_{j\in\mathrm{cell}}\left(\boldsymbol{p}_j - \boldsymbol{p}_j^{\mathrm{ran}}\right) \tag{2.10}$$

Note that this formulation of the collision operator applies to fluid particles of different mass. In the following we will only use fluid particles of identical mass $m_i = m_f\ \forall 1 \le i \le N$, but for the interaction with filaments the general formulation is required.

MPC with embedded filaments One of the great advantages of a particle based fluid simulation is that there is a natural interaction mechanism with non-fluid objects that consist of particles [75, 76]. For example, the worm-like chain model for the actin filaments is based on point-like beads. These beads can be incorporated in the MPC collision by treating the filament beads as fluid particles of mass m_b, which take part in the collision phase. Thus, the filament beads and fluid particles exchange momentum via the MPC collisions. During the drift phase on the other hand, each filament evolves according to the integration of its equation of motion,

$$\dot{\boldsymbol{x}} = \boldsymbol{p}/m_b, \qquad\qquad \dot{\boldsymbol{p}} = -\frac{\partial U}{\partial \boldsymbol{x}}\ , \tag{2.11}$$

where U is given by (2.5). In other words, the momentum of a filament bead changes by two different mechanisms. First, there are h_{MPC}-periodic interactions with the MPC-fluid via (2.10), and second there are continuous interactions with other beads via the bead potential U via (2.11). For the numerical implementation, the equations of motion (2.11) have to be integrated for every filament bead using an integration step $\Delta t \le h_{MPC}$.

[2] Concretely, the Stochastic Random Direction (SRD) collision operation is $\boldsymbol{p}_i' = m_i\boldsymbol{P}_c/M_c + \mathbf{\Omega}\cdot\left(p_i - m_i\boldsymbol{P}_c/M_c\right)$, where $\mathbf{\Omega}\cdot\mathbf{\Omega}^\dagger = \mathbb{E}_d$.

[3] If the masses of the particles in a cell are not identical, the collision is almost identical, $\boldsymbol{p}_i' = \frac{m_i}{M_c}\left(\boldsymbol{P}_c - \sum_{j\in\mathrm{cell}}\boldsymbol{p}_j^{\mathrm{ran}}\right) + \boldsymbol{p}_i^{\mathrm{ran}}$, where it is implied that the random momenta also depend on the particle mass via $P(p_\alpha^{\mathrm{ran}}|m_i,\,T)$

We note that more than one filament bead may occupy the same fluid cell, leading to a direct transfer of momentum from one filament bead to another. This amounts to another source of short-ranged direct interactions among filaments. Although this spurious interaction strength is small, one has to keep in mind that it exists, so that $\mathcal{U}_b = 0$ does not imply that filaments are strictly non-interacting. Furthermore, this direct interaction of filaments implies that the width of a filaments is not precisely defined. Instead, the filament width is somewhere in the range from $[2\,r_c,\, a]$, where r_c is the cutoff radius of the contact interaction and a the width of a collision cell. It is therefore reasonable to choose r_c such that $2\,r_c \approx a$.

Propulsion mechanism of the filaments So far we have embedded the filaments in the fluid and described how the filaments interact with the fluid, so finally it is time to set the filaments in motion.

As discussed above, the aim is a propulsion model where the filaments move at a constant speed and in a snake-like fashion. We approximate this behavior by a very crude mechanism, where after every fluid interaction the bead momenta are artificially reset by the rule

$$\boldsymbol{p}_i' = \beta\, p_T\, (\boldsymbol{r}_{i-1} - \boldsymbol{r}_i)/|\boldsymbol{r}_{i-1} - \boldsymbol{r}_i| \quad \text{for } 1 < i \leq m\ . \tag{2.12}$$

Here, β is a free parameter, $p_T = \sqrt{m_b k_B T}$ is the average speed of the thermal motion of a bead[4], and m is the number of beads in this filament. This rule ensures that all but the first bead move towards the previous bead — regardless of the fluid velocity or thermal noise — and thus approximates the snake-like movement of the filament during its drift phase. Because the momenta of the tail end line up, this rule also acts as a propulsion mechanism. We stress that the head of the filament has to be excluded here, so that the leading bead actually reacts to external forces. The resulting movement speed of the filament is then in the order of $\beta p_T/m_b$, because the trailing beads collectively push the head bead. Note that the exact value of the resulting speed is not important for our model, as long as all filaments have the same speed[5].

To sum up, the filament–fluid interaction involves the following steps:

- A collective collision phase given by the MPC algorithm (2.10), where filament beads are treated as fluid beads with a different mass.
- A momentum reset by (2.12) that ensures the snake-like movement at a constant speed
- A drift phase, where the fluid particles stream uninterrupted, whereas the filaments evolve according to their equations of motion (2.11 & 2.5) with updated bead momenta as initial condition.

This model has the strength to scale linearly in the fluid volume and the number of filaments.

[4] Here it is implied that the filaments only move in two dimensions.

[5] Because the momentum of the leading bead is random, the net displacement of the whole filament depends on whether its momentum aligns with the momentum of the trailing beads. Because a net flow of fluid also aligns the leading bead with the trailing ones, this propulsion mechanism actually leads to faster filaments when aligned with the flow. Because β is usually small, this effect is however small.

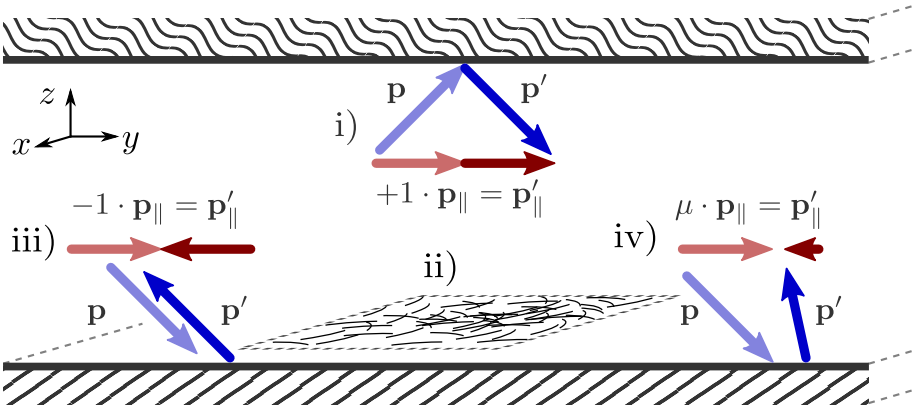

Figure 2.3 | Schematic of the 3D simulation setup with a slip boundary at the top (wavy hatched), where the momentum parallel to the boundary, $\boldsymbol{p}_\parallel$, remains unchanged by wall collisions (i). The filament motion is confined to a quasi two-dimensional surface close to the lower boundary (ii), and the fluid above this layer will be referred to as *bulk fluid*. For a strict no-slip boundary at the bottom we employ the bounce-back boundary condition, where $\boldsymbol{p}_\parallel$ flips sign in wall collisions (iii). For a more fine-grained control of the slip velocity, we also consider interpolating boundary conditions where the factor $\mu \in [-1, +1]$ gradually allows for bigger slip velocities with increasing μ (iv). Note that for very low slip velocities, we in addition use the ghost particle technique, as described in [77, 78].

2.1.2 Three-dimensional fluid

Finally, we give a short overview of the subtleties when dealing with simulations in three dimensions.

In the motility assay experiment, the extension in the x- and y-directions is about three orders of magnitude larger than the typical length of an actin filament [10]. Because such large simulation boxes are computationally infeasible, we emulate an unbounded fluid by periodic boundary conditions in the x- and y-directions. As discussed above, we assume that the filaments are confined to a quasi two-dimensional plane, while the fluid is fully three-dimensional. Because the actin filaments are pushed onto a solid wall, the plane to which the filaments are restricted to should be parallel and close to a boundary (see Fig. 2.3 ii). Although the filament beads are confined to this two-dimensional plane, the position vectors and momenta of the filament beads must be three-dimensional vectors, because the beads have to interact with fluid particles via the MPC collision operator (2.10). In order to restrict the filament dynamics to a plane, the additional potential U_w is required to keep the filaments at a given distance d_0^{wall}:

$$U_w\left(\boldsymbol{r}_i | d_0^{\text{wall}}, d_{\text{max}}^{\text{wall}}\right) = U_s\left(\boldsymbol{r}_i, \pi_z(\boldsymbol{r}_i) | d_0^{\text{wall}}, d_{\text{max}}^{\text{wall}}\right) , \tag{2.13}$$

where $\pi_z(\boldsymbol{r}) = (r_x, r_y, 0)$ is the projection onto the plane $z = 0$. We have re-used the FENE spring potential between the filament beads, because it ensures that beads are forbidden to touch the lower wall if $d_0^{\text{wall}} > d_{\text{max}}^{\text{wall}}$. Note that it is practical to give U_w the same potential strength as U_s.

In contrast to the x- and y-directions where the simulation box is periodic, the z-direction is bounded by solid walls. In the experiment, the z-height of the fluid film is about $0.1\,mm$,

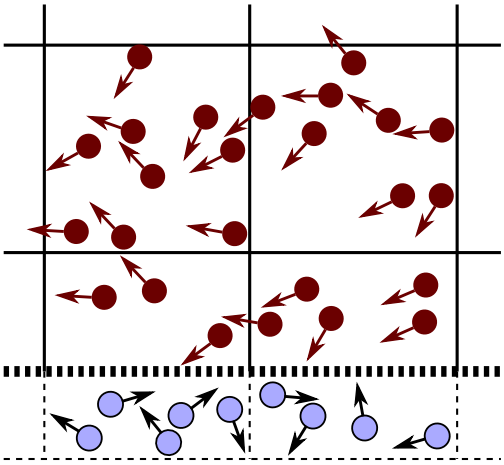

Figure 2.4 | Illustration for the ghost particle technique which increases the wall drag. A solid wall (broad broken line) cuts the fluid cells in two halves, leaving the lower fluid cells under-filled. Virtual fluid particles (blue circles) with random thermal velocities are added to the fluid cell until the mean occupation number is reached. During a collision, the real particles (red) transfer momentum onto the virtual particles with zero mean velocity, whereby the slip velocity at the wall is reduced.

so that the bulk fluid above the filaments is quite large. Because it is numerically not feasible to simulate such a large fluid volume, we may assume that the upper boundary is far away. In that case, the bulk fluid effectively feels no drag from the upper boundary, which allows to make the z-height rather small, when the upper boundary has slip boundary conditions (see Fig. 2.3 i). Such a slip-boundary is achieved by reflective boundary conditions where $p_z' = -p_z$ and $\boldsymbol{p}_\parallel' = \boldsymbol{p}_\parallel$. In that way, the fluid does not stick at the upper boundary, emulating a much larger bulk fluid.

On the other hand, the filaments are very close to the functionalized coverslip in the experiment. This coverslip is a non-moving boundary at which the fluid must also be at rest, in other words the lower z-boundary must be a no-slip boundary. The standard method to achieve such a non-slip boundary condition is the so-called bounce-back boundary condition, where the momentum of a fluid particle is flipped ($\boldsymbol{p}' = -\boldsymbol{p}$) if it hits a no-slip wall (see Fig. 2.3 iii) [77]. The bounce-back boundary condition drastically reduces the slip velocity, however for our MPC-fluid settings the slip is not completely suppressed. To further reduce the slip velocity, underful wall cells can be filled up with virtual ghost particles that have a random momentum with zero average (see Fig. 2.4). Thereby, a momentum transfer onto the wall also occurs without particles hitting the boundary, which makes the momentum transfer much more efficient [77, 78].

Finally, we will also consider a gradual increase of the slip velocity at the lower boundary. We do this by generalizing the collision condition when fluid particles hit the wall. For example, with reflective boundary conditions, the parallel momentum that is transfered onto the boundary is $\Delta\boldsymbol{p}_\parallel = \boldsymbol{p}_\parallel - \boldsymbol{p}_\parallel' = 0$, whereas for bounce-back boundary conditions it is $\Delta\boldsymbol{p}_\parallel = 2\boldsymbol{p}_\parallel$. In general, for a collision rule $p_z' = -p_z$ and $\boldsymbol{p}_\parallel' = \mu\,\boldsymbol{p}_\parallel$ the amount of momentum that is transfered onto the wall becomes $\Delta\boldsymbol{p}_\parallel = (1-\mu)\boldsymbol{p}_\parallel$ (see Fig. 2.3 iv). Because the

momentum transfer onto the wall impedes the fluid flow in the wall cell, μ can be used to tune the slip velocity at the wall from bounce-back ($\mu = -1$) to reflective ($\mu = +1$).

To sum up, this section explained the setup for simulations of the motility assay in three dimensions. In short, the filaments are confined to a two-dimensional plane close to a boundary whose slip velocity can be controlled. The opposing boundary is always a slip-boundary, which emulates the large bulk fluid between the coverslips.

2.1.3 No hydrodynamic interactions

One of the major advantages of the MPC method is the possibility to disable the hydrodynamic interactions, so that the dynamics become effectively Langevin-dynamics. Because the simulation is otherwise identical, the results of hydrodynamic versus no hydrodynamics are very well comparable.

There are a few different approaches how the hydrodynamic interactions can be suppressed. For example, instead of sorting the fluid particles into collision cells by their position (2.6), the fluid particles are assigned to random cells via random positions $\boldsymbol{r}_r$. Consequently, the collisions in the cell become non-local and therefore no hydrodynamic behavior emerges. Although this method is enlightening and elegant, it is not the most efficient, because the fluid particles need to be processed even though hydrodynamics is suppressed. However, it can be greatly simplified, by realizing that assigning thermal particles to a random cell is equivalent to adding a random momentum $\boldsymbol{p}_i^{\mathrm{ran}}$. Therefore, the total cell momentum becomes

$$\boldsymbol{P}_c = \sum_{i=1}^{n_c} \boldsymbol{p}_i^{\mathrm{ran}} + \sum_{i=1}^{n_b} \boldsymbol{p}_i^{(b)} \ , \tag{2.14}$$

where n_c is the average number of fluid particles per cell, n_b is the number of filament beads in the cell, and $\boldsymbol{p}_i^{(b)}$ the corresponding momenta. As the first term is a sum of Gaussian random numbers, the sum can be substituted by a *single* random momentum from the Gaussian distribution $P(p_\alpha^{\mathrm{ran}}|n_c \cdot m_f, T)\,\mathrm{d}p_\alpha^{\mathrm{ran}}$, where P is defined in (2.8). The collision algorithm from equation (2.10) remains otherwise unchanged[6]. Because no hydrodynamic flows are possible, the fluid particles can be removed from the simulation and only their virtual action via the noise in (2.14) is retained. Consequently, an MPC simulation without hydrodynamics can be seen as Langevin dynamics where the beads in the same collision cell receive the same random noise.

To sum up, we use an adapted worm-like chain model for the filaments which emulates the snake-like movement of actin filaments. Unless the whole simulation is two-dimensional, the filaments are locked to a thin layer near the lower z-boundary for quasi 2D dynamics. The filaments interact via a direct contact interaction given by a harmonic potential barrier of strength $\mathcal{U}_b$, so that stacking of filament intersections is suppressed. In addition, the filaments interact with a two- or three-dimensional MPC fluid that conveys indirect hydrodynamic interactions via the fluid. Last but not least, the hydrodynamic interactions can be turned off, so that the filament dynamics become Langevin-like.

[6] As mentioned above, also without hydrodynamics the filament beads within the same collision cell directly exchange momentum via (2.14) and (2.10).

2.2 Simulation parameters and unit system

Our model has a large number of simulation parameters which must be carefully adjusted for physically reasonable results. This section collects all parameters, briefly discusses related caveats, and lists the settings for the simulations in the following chapters.

Unlike the results in the following chapters, here we use a unit system that is well-suited for MPC simulations, and uses the following fundamental units:

- the cell length a
- the fluid particle mass m_f
- the mean free path of a fluid particle $\Lambda = \sqrt{k_B T/m_f} h_{MPC}/a$.

As remarked by Ihle, MPC simulations with otherwise different parameters but same Λ are equivalent [79, 80]. Consequently, $k_B T$ and h_{MPC} can be chosen freely to obtain the same Λ. For reasons of numerical efficiency, it is best to set $h_{MPC} = 1$ because this allows to save a lot of multiplications by this constant. We now give an exhaustive list of settings and parameters and briefly discuss the implications of the parameters.

$k_B T$ *Temperature*
The temperature is the most important setting in the MPC algorithm and affects the Reynolds number, the Péclet number, and the Schmidt number of the fluid [81, 82]. Because a change of temperature affects all these fluid numbers, the temperature should not be changed. Throughout this work, we used the temperature $\sqrt{k_B T} = \Lambda = 0.05$.

h_{MPC} *Time-step of the fluid collisions*
By a proper choice of the fluid temperature, the time-step can be chosen as $h_{MPC} \equiv 1$

a *Collision cell size*
We only use cubic cells and use the length a as the fundamental unit for length.

m_f *Mass of a fluid particle*
We use the mass of one fluid particle as the fundamental unit for mass.

n_c *Fluid particles per cell*
The number of fluid particles per cell affects the fluid transport coefficients, and also determines the typical ratio of flow speed to thermal noise. Here, we used $n_c = 18$, resulting in up to 10^7 fluid particles.

L_x, L_y, L_z *Size of the simulation box*
The size of the simulation box should be much larger than the filament length. Here, we used simulation boxes of $240\,a \times 240\,a$ for the two-dimensional setups and $120\,a \times 120\,a \times 10\,a$ for the three-dimensional setups. In terms of the filament length L, the dimensions of the simulation box become $80\,L \times 80\,L$ and $40\,L \times 40\,L$ for two and three dimensions, respectively.

N, $[\rho]$ *Number of filaments*
The number of filaments in the simulation corresponds to the filament density via $\rho = N/(L_x \cdot L_y)$ — also in three-dimensional setups. It is one of the free parameters that will be examined in in the range $3\,000 \le N \le 30\,000$, corresponding to a filaments density of $0.47\,n/L^2 \le \rho \le 4.69\,n/L^2$.

L, [m] *Filament length*
The filament length L corresponds to the number of filament beads m via $L = (m-1)R_0$. Because the length L defines the physical unit of length for the results in the following. Therefore it is important to always use the same filament length L. Throughout this work, we used $m = 7$, i.e. $L = 3\,a$. Note that the width of a filament can be approximated by the cutoff radius r_c or $a/2$, resulting in an aspect ratio of 1:3 to 1:3.75.

m_b *Mass of a filament bead*
The mass regulates how strongly thermal noise affects the dynamics of the filament, and in particular how strong the lateral diffusion of a filament bead is. In addition, the ratio of bead mass and fluid mass in a cell determines how effectively the fluid and filaments exchange momentum. In other words, how strong is the coupling of filaments and fluid. For an effective coupling, the total bead mass in a collision cell should be about as big as the total fluid mass in a collision cell. Here, we used $m_b = 3\,m_f$, so that $a/R_0 \cdot m_b = 1/3 \cdot n_c$.

β [v_0] *Filament driving*
This crucial parameter determines how fast the filaments move, $v_0 \approx \beta\sqrt{k_BT/m_b}$. Intuitively, it determines what fraction of the thermal kinetic energy is directed and not randomly orientated. Because the motion of a filament drags the fluid particles along, it is *extremely important* that the diffusion of fluid particles on the scale of a collision cell is stronger than this advection. In other words, it must hold that the corresponding Péclet number is smaller than one, $1 \gtrsim \mathrm{Pe} = v_T\beta\,a/D_f$ where $D_f \approx k_BT/2$ is the diffusion constant of the fluid particles [81, 82]. This gives the simple condition $\beta \lesssim \sqrt{m_b\,k_BT}/2a$. Here, we used $\beta = 0.03$, which is smaller than the upper bound $\beta \lesssim 0.043$ that is required by our parameter choice.

κ_s *Stiffness of the filament FENE bond*
This value should be much larger than $1k_BT/a$, in order to ensure that thermal fluctuations only result in bond stretching much smaller than $R_{\max}$. Here, we used $\kappa_s = 100\,k_BT/a$.

R_0 *Rest length of a filament FENE bond*
This determines, how many filament beads of the same chain are assigned to the same collision cell. To avoid "holes" along the filament, the bead spacing should be smaller than $1\,a$. Here, we follow the widely used standard setting and use $R_0 = a/2$.

$R_{\max}$ *Maximum extensibility of a filament FENE bond*
Generally, it is desirable to take $R_{\max} < R_0$. For our model it is crucial that $r_c < R_0 - R_{\max}$, because otherwise subsequent beads in a chain could be repelled via the potential barrier $\mathcal{U}_b$. If this happens, the bending stiffness of the filaments effectively increases, leading to erroneous results. Here, we used $R_{\max} = R_0/5 = 0.1\,a$.

l_p, [κ_b] *Persistence length of the filaments*
The persistence length l_p and bending stiffness κ_b are related via $\kappa_b = k_BT\,l_p$. The persistence length is one of the free parameters that will be examined in in the range $1\,L \leq l_p \leq 10\,L$ in the following.

$\mathcal{U}_b$ *Strength of the potential barrier*
The potential strength tunes the repulsion strength of the direct interaction between

filaments. It is one of the free parameters that will be examined in in the range $0\,k_BT \leq \mathcal{U}_b \leq 4k_BT$ in the following.

$\boldsymbol{r_c}$ *Width of the potential barrier*
Smaller values of r_c make the filaments rougher, therefore r_c should be chosen as large as possible. On the other hand, larger r_c also make the aspect ratio smaller, so that r_c should not be too large. An upper boundary for r_c is given by the condition $r_c < R_0 - R_{\max}$ which ensures that subsequent beads of a chain do not interact. Here, we used $r_c = 0.4\,a$.

$\boldsymbol{d_0^{\text{wall}}}$ **(only 3D)** *Average distance of a filament to the boundary*
This length sets the average distance of the 2D-plane to which the filament motion is confined and the lower z-boundary. Here, we used $d_0^{\text{wall}} = R_0 = a/2$.

$\boldsymbol{d_{\max}^{\text{wall}}}$ **(only 3D)** *Maximum extensibility of a FENE wall bond*
For our model it is crucial that $d_{\max}^{\text{wall}} < d_0^{\text{wall}}$, because otherwise filament beads can hit the boundary. Here, we used $d_{\max}^{\text{wall}} = R_0 = a/2$.

$\boldsymbol{\Delta t}$ *Integration step for the filaments*
This integration step subdivides the time between fluid collisions h_{MPC}. See section 2.3 for details about the step width. The starting value is $\Delta t = h_{MPC}/8$.

From the given parameters, one can predict the transport coefficients of the fluid [81, 82]. Given the transport coefficients, it is possible to determine the value of dimensionless fluid numbers that characterise the fluid. Among these are the Reynolds number of the filaments $\mathrm{Re} \approx 3.4$, the Schmidt number $\mathrm{Sc} \approx 57$, and the Péclet number $\mathrm{Pe} \approx 1$. The values show that the MPC fluid is a reasonable representation of an aqueous solution at small length scales.

2.3 Implementation notes

Finally, we give a few technical remarks about the numerical implementation of our model. Readers who are mainly interested in the results may skip ahead to the next chapter.

In principle all steps of the above algorithm are easily parallelizable, because every step consists of independent sub-tasks. For example, in the collision phase, every cell can be processed independently of every other cell. Similarly, in the drift phase the fluid particle displacements are independent of one another. However, the more computationally demanding integration of the equations of motion for each filament is not independent of other filaments, because $\mathcal{U}_b$ (2.4) depends on all filament positions. Because the total filament displacements over a period of h_{MPC} (one drift phase) is small, we may however assume that the potential $\mathcal{U}_b$ remains approximately constant. Therefore, every filament can be integrated via the much simpler $U_{\text{free}}^{(j)}$ (2.3), and more importantly independent of the other filaments. Figure 2.5 shows the scaling of the runtime with the number of threads n_t, which for a perfect parallelization should scale like n_t^{-1}. The data show that the scaling is close to -1 and therefore quite good.

Furthermore, figure 2.5 shows that the set of filaments requires more CPU time than the fluid (middle vs. right panel). The speed-determining step of the filament part is the integration of the equations of motion, which consequently has to be fast. To speed up the calculation,

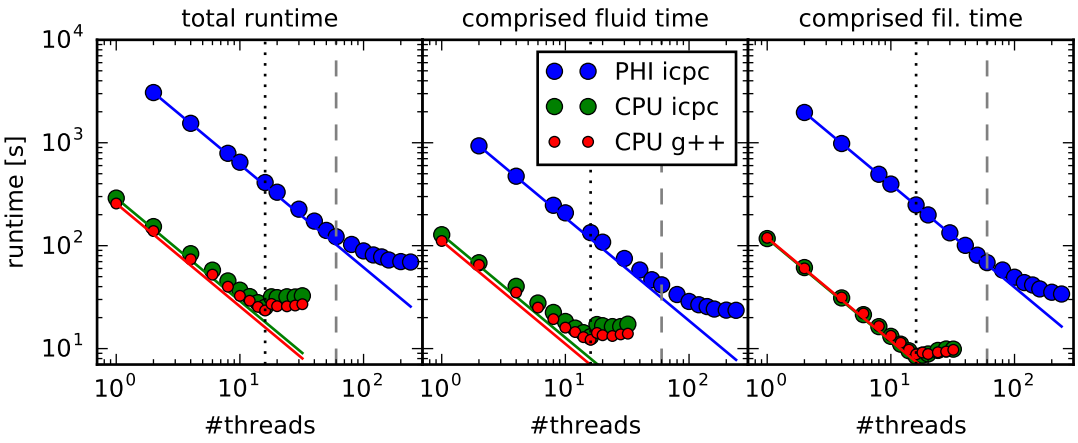

Figure 2.5 | The scaling of the total simulation runtime (left) as a function of the number of threads. The total runtime consists among others from the runtime of fluid-related parts (middle) and filament-related parts (right). The blue bullets show the runtime on the Intel phi architecture with 60 cores (vertical dashed line at 60). The other data show the runtime on a 16-core Haswell machine (vertical dotted line at 16) with the Intel compiler (green bullets) and GNU `g++` compiler (red bullets). The solid lines in the corresponding color show the optimal scaling, which is almost reached up to the number of physical cores on the respective architecture.

we optimized the force calculation as described in Appendix A.1. Furthermore, we use the Velocity-Verlet integration scheme which is simple and fast [83, 84],

$$\boldsymbol{r}(t+\Delta t) = \boldsymbol{r}(t) + \Delta t\, \boldsymbol{v}(t) + \frac{\Delta t^2}{2m}\boldsymbol{F}(t) \tag{2.15}$$

$$\boldsymbol{F}(t+\Delta t) = -\left.\frac{\partial U}{\partial \boldsymbol{r}}\right|_{\boldsymbol{r}(t+\Delta t)} \tag{2.16}$$

$$\boldsymbol{v}(t+\Delta t) = \boldsymbol{v}(t) + \frac{\Delta t}{2m}\Big(\boldsymbol{F}(t) + \boldsymbol{F}(t+\Delta t)\Big)\ . \tag{2.17}$$

The main requirement on the integration is speed, whereas accuracy only has a subordinate role because the filaments are exposed to a heat bath whose noise is much bigger than any integration error. Therefore, the integration step Δt should be chosen just below the point where the integration becomes unstable due to the non-linear effects of the FENE potential. To find out the largest tolerable Δt, we compared the Velocity-Verlet solution of a particle in a harmonic trap with its analytic solution and found that $\Delta t = h_{MPC}/8$ is accurate with only 6% relative error. Because in some rare cases the integration of the equations of motion blows up, we check that each bond length lies within $[R_0 - R_{\max},\ R_0 + R_{\max}]$ after each drift step and repeat the integration with $\Delta t/2$ if this was not the case. This is repeated up to four times ($\Delta t/16$), until an error is reported. There were only two cases where the integration could not be recovered in this way, such that a previous snapshot had to be loaded.

Last but not least, the other speed-determining operation is the generation of random numbers. Our implementation uses a handcrafted version of the Mersenne Twister that is tuned for the `SSE2` instruction set [85–87]. Furthermore, these random numbers need to be transformed into Gaussian random numbers, for which we employ the ziggurat algorithm which is the fastest known method for this task [88]. Finally, we periodically do a locality sorting

of the fluid particles along a space-filling Peano-Hilbert curve, so that physically neighboring particles are also in the same memory region [89]. Because the memory access to the fluid particles is the bottleneck of the MPC algorithm, this speeds up the MPC part by a factor of ≈ 2. The graphical figures in this work were done with `inkscape` and all figures were created with the `matplotlib` plotting library [90, 91].

3 Filament motion and binary collisions

3.1 Characterization of the filament motion

In order to get an understanding for the behavior of our model for propelled filaments, we looked at the properties of the trajectory of a single filament.

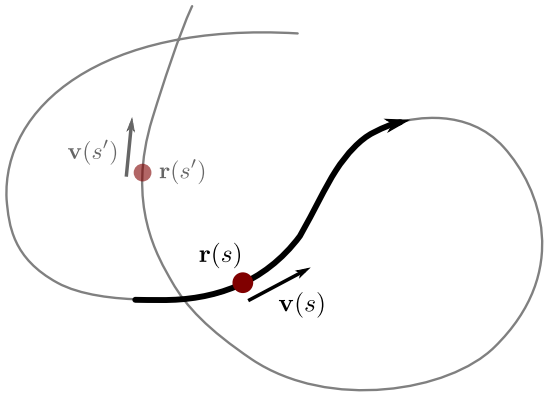

Figure 3.1 | An exemplary path of a single filament. In order to determine the properties of the random walk of the filament, we tracked one bead (red) in the tail of the filament and recorded its position $\boldsymbol{r}(t)$ and velocity $\boldsymbol{v}(t)$. This bead follows the path of the head bead as if on tracks. An inner bead has the advantage that it picks up less noise so that its velocity correlation is cleaner.

Due to the construction of the propulsion mechanism only the head bead may wiggle freely, whereas the tail beads can only move towards the next bead. As long as the angle distribution of the head bead remains unaffected by the driving mechanism, it seems plausible that the path described by a *driven* filament is a persistent random walk whose persistence length L_p is determined by the persistence length of a *free* filament l_p. If the path of the driven filaments is indeed a persistent random walk, the tangent correlation along the trajectory is given by

$$\langle \boldsymbol{n}(s') \cdot \boldsymbol{n}(s) \rangle = \exp\big(|s' - s|/L_p\big) \ . \tag{3.1}$$

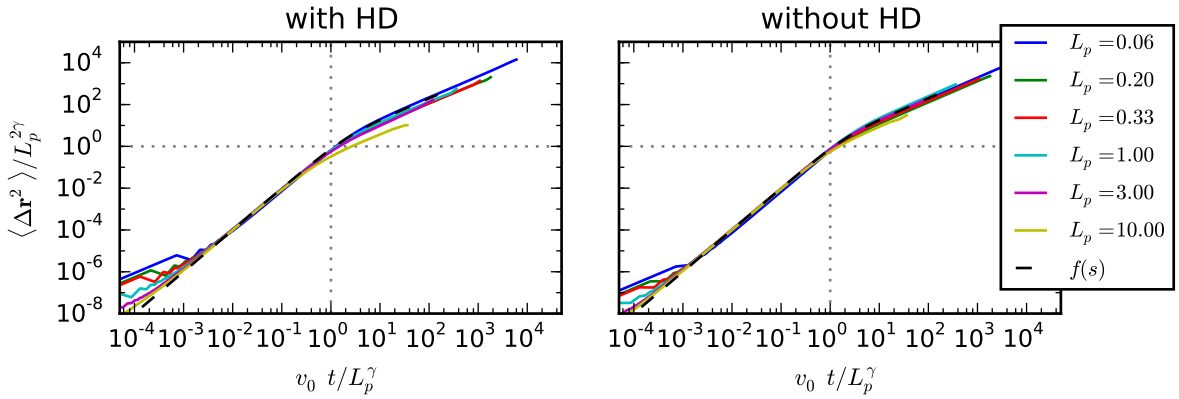

Figure 3.2 | The mean-squared displacement of an isolated filament in a two-dimensional setup as a function of time and rescaled according to the scaling assumption (3.2) with $L_p = l_p^\gamma$. The panels show data with 2D hydrodynamics (left) and purely Brownian dynamics (right). Apart from very late times, the errors are smaller than the line width. The collapse of the data onto the master curve $f(x) = 2\left(x + (\mathrm{e}^{-x} - 1)\right)$ (dashed black line) supports the assumption that isolated filaments perform a persistent random walk with persistence length $L_p \approx l_p$.

From the tangent correlation, it is possible to calculate the expected mean-squared displacement

$$\begin{aligned}
\Big\langle \big(\boldsymbol{r}(t+t') - \boldsymbol{r}(t')\big)^2 \Big\rangle_{t'} &\equiv \int_{t'} \mathrm{d}t' \left(\int_{t'}^{t'+t} v_0 \boldsymbol{n}(v_0\,\tau)\,\mathrm{d}\tau \right)^2 \\
&= v_0^2 \int_{t'} \mathrm{d}t' \int_0^t \mathrm{d}\tau' \int_0^t \mathrm{d}\tau\ \boldsymbol{n}(v_0\,(t'+\tau)) \cdot \boldsymbol{n}(v_0\,(t'+\tau')) \\
&\overset{!}{=} v_0^2 \int_0^t \mathrm{d}\tau' \int_0^t \mathrm{d}\tau\ \exp\!\big(-v_0|\tau-\tau'|/L_p\big) \\
&= \ldots = 2\,L_p^2 \left(\frac{v_0\,t}{L_p} + \big(\exp(-v_0\,t/L_p) - 1\big) \right) ,
\end{aligned} \tag{3.2}$$

where we used that the filaments move at a constant speed v_0 and the time average in the second line can be approximated by (3.1). Note that the filament speed v_0 is not a free parameter but given by $v_0 \approx \beta \sqrt{k_B T / m_b}$ (see 2.2). As a consequence, we conjecture that the recorded mean-squared displacement from our simulation collapses onto a single master curve when rescaled by

$$\Big\langle \big(\boldsymbol{r}(t+t') - \boldsymbol{r}(t')\big)^2 \Big\rangle_{t'} = L_p^2 f(v_0\,t/L_p) \ , \tag{3.3}$$

and the scaling function can be approximated by $f(x) = 2\big(x + (\mathrm{e}^{-x} - 1)\big)$. Figure 3.2 shows the rescaled mean-squared displacement for different persistence lengths of the filaments. The data were acquired from a moving average of the corresponding interval along the path realization and the corresponding error was estimated by the fluctuation of independent realizations. The fact that the curves for different persistence lengths l_p collapse very well onto a single master curve, validates our conjecture that the random walk of a single filament is indeed a persistent random walk. Although not shown, we find a better collapse for the case with

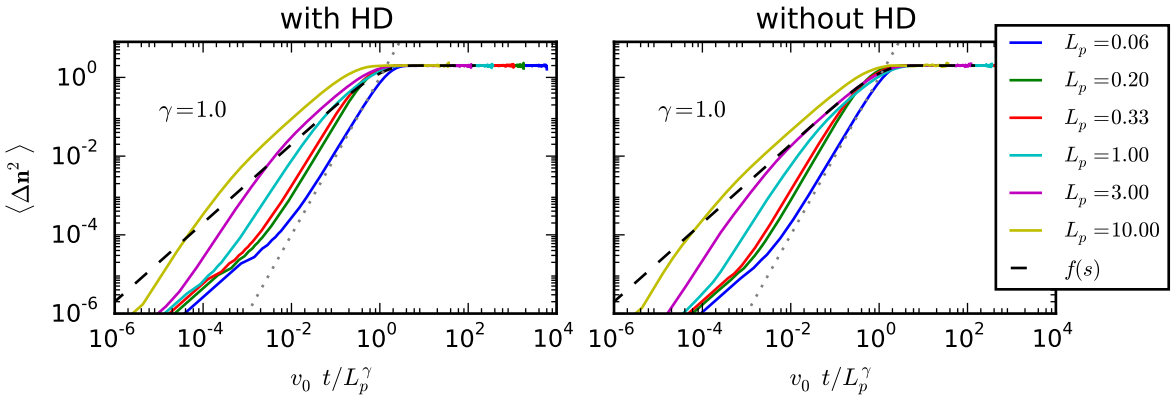

Figure 3.3 | The measured tangent diffusion for an isolated filament in a two-dimensional setup as function of time and rescaled according to the scaling assumption (3.4). The panels show data with 2D hydrodynamics (left) and purely Brownian dynamics (right). Apart from very late times, the errors are smaller than the line width. For small times, the data deviate considerably from the expected scaling $f(x) = 2\,(1 - \mathrm{e}^{-x})$ (dashed black line). There are tree different scaling regimes (see footnote 1): a diffusive regime at very small time-scales (only for $l_p \ll L$), a quadratic regime at intermediate times, and another diffusive regime (only for $l_p \gg L$). For times $t \gtrsim L_p/v_0$ the data transition into a plateau as is expected. The data are in good agreement with the tangent diffusion of a snake-like movement.

hydrodynamics with $L_p = l_p^\gamma$ and $\gamma \approx 0.85$, meaning a less persistent random walk. As the focus of this work is on the phenomena of many filaments, it is however absolutely sufficient to assume $L_p \approx l_p$ for both cases.

To sum up, Fig. 3.2 confirms that the propelled filament walks in a directed fashion over a period of $\hat{t} \approx l_p/v_0$ which causes a quadratic growth of the mean-squared displacement. For later times, the filament starts to lose its direction and begins to move isotropically, giving rise to the diffusive behavior with linear scaling.

To confirm this picture, we also looked at the diffusion of the tangent vector $\boldsymbol{n}(s)$ along the contour of the path, $\big\langle \big(\boldsymbol{n}(t+t') - \boldsymbol{n}(t')\big)^2 \big\rangle_{t'}$. With equation (3.1) the tangent diffusion can be given analytically,

$$\Big\langle \big(\boldsymbol{n}(t+t') - \boldsymbol{n}(t')\big)^2 \Big\rangle_{t'} = 2 - 2\big\langle \boldsymbol{n}(t+t') \cdot \boldsymbol{n}(t') \big\rangle_{t'} \stackrel{!}{=} 2\Big(1 - \exp\big(-v_0|t|/L_p\big)\Big)\ . \tag{3.4}$$

So when time is rescaled to $\hat{t} = v_0\,t/L_p$, the data should collapse onto a single master curve $f(x) = 2\big(-\exp(-x)\big)$. Figure 3.3 shows the tangent diffusion for the same data set as in Fig. 3.2, where again $L_p = l_p^\gamma$ with $\gamma = 1$. In agreement with Fig. 3.2 the tangent diffusion saturates at about $\hat{t} = 1$, confirming the isotropic and erratic movement for times greater than this time-scale. On the other hand on short time-scales, the measured curves deviate substantially from the predicted behavior. Instead of the one purely diffusive scaling regime as expected from (3.4), we find two diffusive and one quadratic scaling regime[1]. The first diffusive regime is only observed for filaments with weak bending rigidity and shows up at small times. It is caused by an unwanted spurious angular relaxation which happens during the drift phase of the filament. The snake-like movement of a filament can only be imposed

[1]Note that most data show only two of the three scaling regimes.

at full drift phase intervals h_{MPC}, but for filaments the drift phase is again subdivided into chunks $\Delta t \leq h_{MPC}/8$ (see 2.2). Consequently, during intervals of h_{MPC} the filaments may evolve freely, leading to this diffusive regime at small time-scales. Due to the rescaling of time in Fig. 3.3, the time-scale h_{MPC} shifts for different L_p. After this first diffusive regime, we find a quadratic regime telling that the tangent changes deterministically on that time-scale. Remembering that the filament follows its contour like on a track, it is evident that the tangent changes deterministically when tracing out a bend in the contour. Beyond the point where the tangent retraces a bend of the filament, the tangent diffusion is determined by the tangent correlation along the path, giving rise to the second diffusive regime. Finally, at the time $\hat{t} \approx 1$ the tangent becomes uncorrelated with its initial orientation leading to the plateau at late times. Note that for $L_p < L$ this means that the second diffusive regime must be absent.

Concerning the scaling parameter γ, we find that the scaling parameter of $\gamma \approx 1$ for pure Brownian motion and $\gamma < 1$ for 2D hydrodynamics does not contradict our results from above. However, because the data necessarily deviate from the predicted curve at small times as discussed above a single master curve remains to be found. Therefore, these data cannot be used to estimate γ.

In summary, we find that the path of a single filament can be well described by a persistent random walk whose persistence length is approximately given by the persistence length of a free filament. This also shows that the relation for the filament speed $v_0 \approx \beta \sqrt{k_B T/m_b}$ holds reasonably well which was not evident from our propulsion mechanism (see 2.1.1). This picture applies very well to the case of pure Brownian motion and reasonably well to the case with a two-dimensional fluid. For the latter case, the persistence length L_p seems to be shifted towards smaller persistence lengths $L_p \approx l_p^{0.85}$, a difference that is irrelevant in what follows. Note that isolated actin filaments in the actomyosin motility assay also perform a persistent random walk so that our model reproduces the dynamics of a free filament [10].

3.2 Binary collisions of filaments

For an understanding of the behavior of multiple filaments, it is essential to characterize binary collisions of the propelled filaments. In the following, we therefore examine binary collisions of the filaments and determine the characteristics of the collisions.

To that end, we prepared the filaments to collide in a controlled manner, such that every collision has a defined incoming angle Θ_{in} and a defined offset b (see Fig. 3.4). For simulations with 2D hydrodynamics, it is important to move the filaments in from afar, so that the fluid flow around the filaments is correctly established. In order to have well-defined initial conditions, we disabled the internal dynamics of the filaments until right before two filaments came into direct contact. This direct contact arises from the interaction potential of the tip with other beads (2.4) (here repeated),

$$U_b^{(j)} = \frac{1}{2}\mathcal{U}_b \sum_{q=1,\, q\neq j}^{N} \sum_{i=1}^{m} \Big(\max\Big(0,\, 1 - \big|\boldsymbol{r}_i^{(q)} - \boldsymbol{r}_1^{(j)}\big|/r_c\Big)\Big)^2$$

for distances of tip and some other bead below the cutoff threshold r_c. We expect that the outcome will depend on the height of the potential barrier, $\mathcal{U}_b$, and other filament properties such as its persistence length l_p. Other important filament properties such as its total length L, travel speed v_0, cutoff radius r_c, or bond length were not examined. For example, filament length L and cutoff radius r_c determine the aspect ratio and roughness of the filaments, so that the collision outcome should depend on both parameters. However, rescaling L requires to rescale all other dimensional quantities that involve a length unit such as v_0, the size of the simulation box, and the filament density. This quickly becomes impractical, because larger simulations are not feasible. Therefore, to have comparable results we only used our standard settings with $L = 3\,a$, $v_0 = 0.03\sqrt{k_B T/m_b}$, and $r_c = 0.4\,a$ where a is the width of a collision cell.

Figure 3.5 shows exemplary traces of the measured angle between to filaments

$$\Theta\big(t|\Theta_{in},\, b,\, \mathcal{U}_b\big) \equiv \cos^{-1}\big(\boldsymbol{n}_1(t) \cdot \boldsymbol{n}_2(t)\big) \tag{3.5}$$

for exemplary filament parameters and various incoming angles Θ_{in}. Every measurement was repeated at least 2×10^3 times, because thermal noise has considerable impact on the outcome

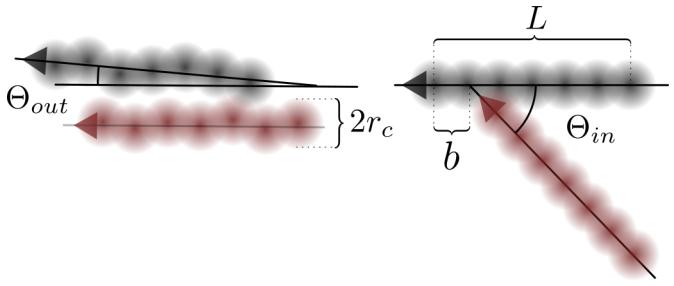

Figure 3.4 | Schematic setup for the binary collision of two filaments. The filaments start at a distance of $2\,L$ from the collision site and move in with their internal dynamics disabled. Just before direct contact, the internal dynamics are enabled and the angle between the two filaments is recorded until the filaments have travelled a distance of $3\,L$.

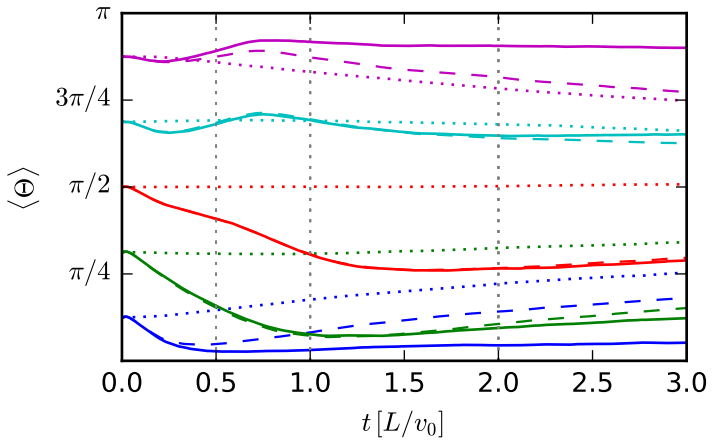

Figure 3.5 | Measured angle between two filaments as a function of time for various initial angles Θ_{in} (colors). The ensemble mean of the measured angle $\langle\Theta\rangle$ is shown as dashed lines, and the reference model Θ^0 of pure angular diffusion as dotted lines. The solid lines show the angular change that is caused by the contact interaction, $\langle\Theta\rangle - \left(\Theta_{in} - \Theta^0\right)$ (3.6). The filament parameters are $l_p = 2\,L$, $\mathcal{U}_b = 2\,k_BT$, and the impact parameter is $b = 0$. Every curve is the average of at least 2×10^3 realisations. Errors are up to three times the line width and omitted for clarity.

of a single collision event and only the mean is shown. At a closer look, it becomes evident that especially at late times, the measured change of the angle $\langle\Theta\rangle$ must have a considerable contribution from angular diffusion, because the filaments can no longer be in contact. In order to correct for this spurious angle change due to angular diffusion, a reference model without interaction is required. Unfortunately, we could not find an analytic expression for the angle between two non-interacting filaments over time. Therefore we performed reference simulations with strictly non-interacting filaments and measured the angle between the filaments as a function of time, $\Theta^0\big(t|\Theta_{in}\big)$ (see Figs. 3.5 and 3.6). In contrast to $\Theta\big(t|\Theta_{in},\, b,\, \mathcal{U}_b\big)$, Θ^0 does not depend on $\mathcal{U}_b$ or b, because the filaments are non-interacting. This quantity now serves as a calibration that allows to isolate the angular change that is attributable to the interaction between two filaments. Two observations from Fig. 3.6 are evident: due to angular diffusion the filaments lose their initially well-defined relative orientation over time. Because uncorrelated direction vectors on average have a zero scalar product and the arc-cosine of zero is $\pi/2$, the relative angle between the filaments approaches $\pi/2$. Furthermore, this relaxation towards the equilibrium angle is faster the more flexible the filament is.

With this zero model for the angular diffusion of non-interacting filaments, the effect of the interaction onto the angular change can be estimated by

$$\Theta_{out}\big(t|\Theta_{in},\, b,\, \mathcal{U}_b\big) = \Theta\big(t|\Theta_{in},\, b,\, \mathcal{U}_b\big) - \Big(\Theta_{in} - \Theta^0\big(t|\Theta_{in}\big)\Big)\ . \tag{3.6}$$

Figure 3.5 shows this procedure for a few exemplary filament parameters and various incoming angles Θ_{in}.

This dataset is too verbose to be of much use, therefore a more condensed picture is required. In particular, the full time evolution of $\Theta_{out}\big(t|\Theta_{in},\, b,\, \mathcal{U}_b\big)$ contains a lot of redundant information, because the angular change at *specific* points in time is usually sufficient. There are natural choices for characteristic points in time, if one imagines non-interacting filaments.

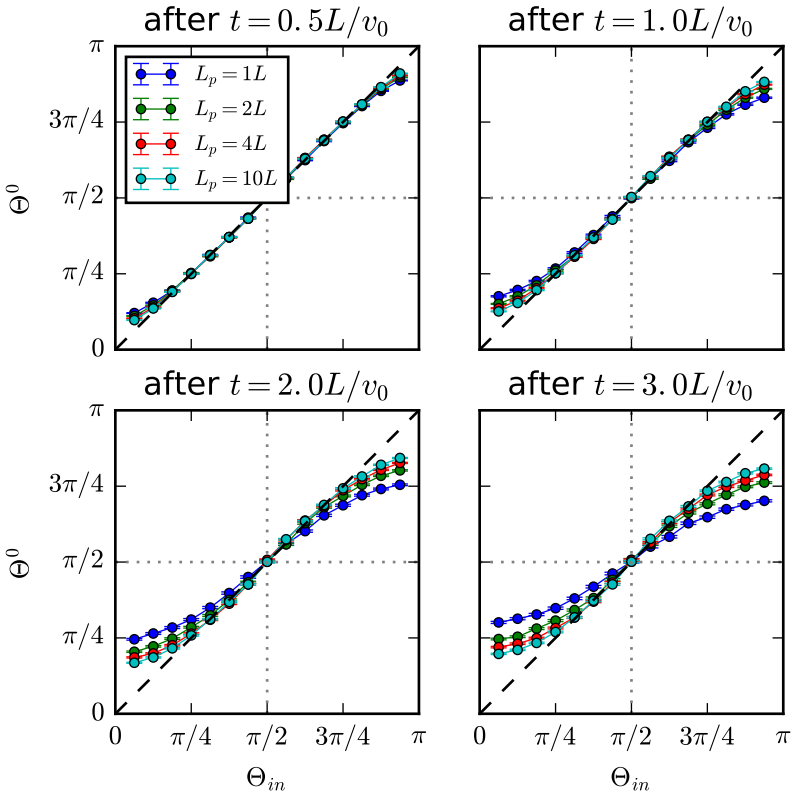

Figure 3.6 | The average angle between two *non-interacting* filaments, $\Theta^0\big(t|\Theta_{in}\big)$, as a function of the input angle for four different points in time. As the filaments are strictly non-interacting, the angular change between the filaments is solely due to angular diffusion. The angular change from this measurement serves as reference to isolate the influence of filament interactions.

First, for a head-on collisions with $\Theta_{in} = \pi$, the filaments fully overlap at a time $t \approx \frac{L}{2\,v_0}$, so we can expect that around this time the filaments are in full contact for large Θ_{in}. Looking at Fig. 3.5 confirms that the initial collision phase is over by that time. Second, for very small collision angles $\Theta_{in} \approx 0$, the filaments fully overlap at a time $t \approx \frac{L}{v_0}$, and comparing with Fig. 3.5 shows that for $\Theta_{in} < \pi/2$ Θ_{out} ceases to decrease around that time. Finally, to also have a point in time where the collision should be over, we also look at time $t = \frac{2L}{v_0}$.

In summary, this section has introduced a setup for controlled collisions of filaments. This setup allows to measure the average angles between filaments during a collision, and via a reference model that accounts for angular diffusion the angular change can be attributed to the interaction of filaments.

3.2.1 Binary filament collisions without hydrodynamics

First, we consider the dependency on the impact parameter b and the repell strength $\mathcal{U}_b$ for "dry" simulations without hydrodynamics.

When $\mathcal{U}_b = 0$, Fig. 3.7 shows a marginal effect on the angle for any impact parameter b. This seemingly unsurprising result is actually an important consistency check, because even

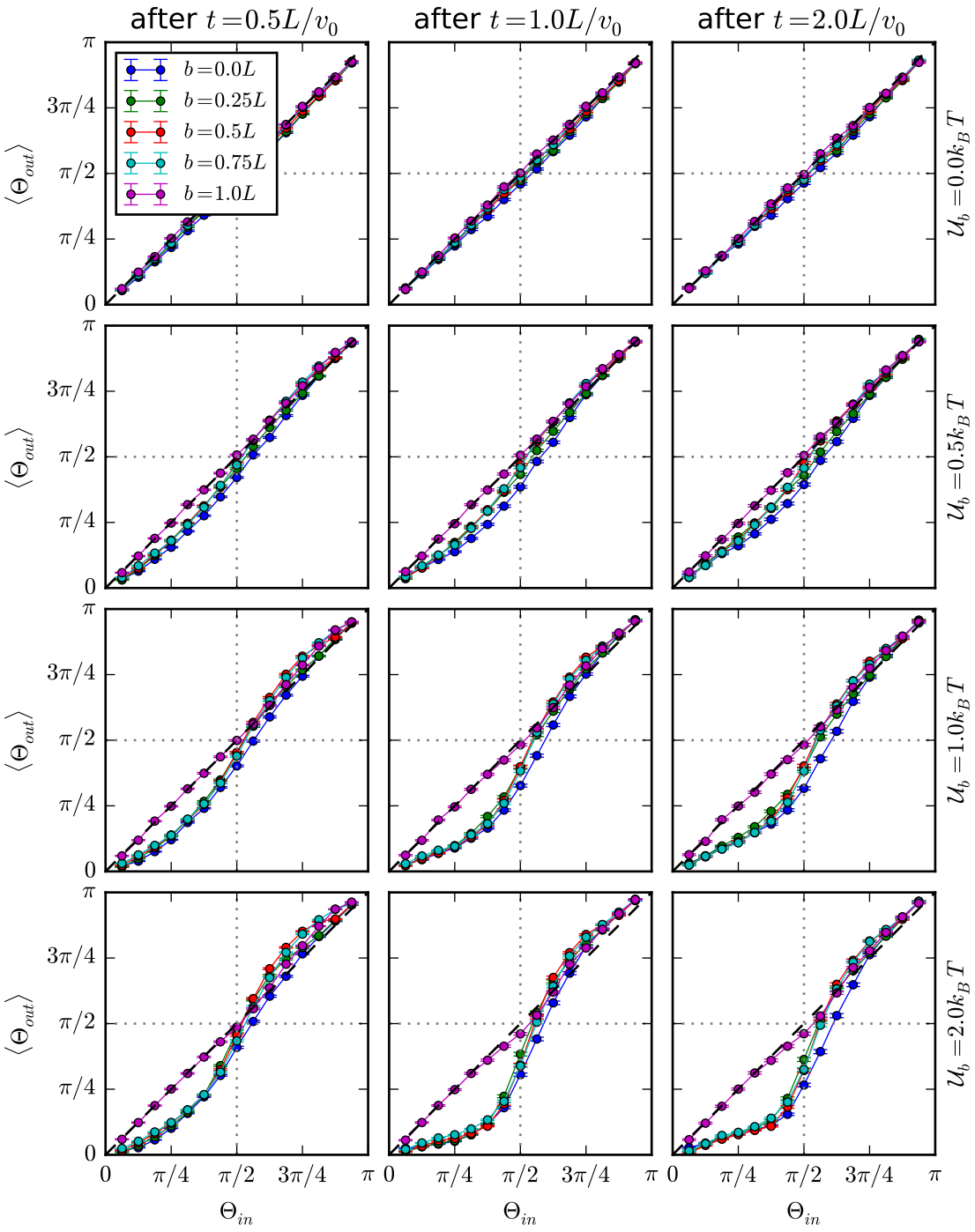

Figure 3.7 | The average angle as defined in (3.6) between to colliding filaments with persistence length $l_p = 2\,L$ for different times (columns) and repulsion potential $\mathcal{U}_b$ (rows). The graphs show nearly identical angles for different impact parameters b except for spot-on collisions ($b = 0$) and misses ($b = L$). For $\mathcal{U}_b = 0\,k_BT$ the interaction is only very weak. On the other hand for $\mathcal{U}_b > 0$, the interaction is in general aligning and gets an increasing nematic component for higher $\mathcal{U}_b$. Although not shown, the results for $\mathcal{U}_b = 4\,k_BT$ are nearly identical to $\mathcal{U}_b = 2\,k_BT$. Standard errors are indicated by horizontal lines and are smaller than the symbol size.

for vanishing $\mathcal{U}_b$, there is a spurious interaction between the filaments. It is caused by a momentum exchange that occurs when beads of different filaments share the same collision cell. This spurious interaction could be removed for Brownian dynamics, but for runs with hydrodynamics it is inevitable. In order to make our results with and without hydrodynamics maximally comparable, we decided to keep this spurious interaction. Because the angular change for $\mathcal{U}_b = 0$ is smaller than angular diffusion, this interaction is usually irrelevant. Only at extremely large densities, this spurious interaction will play a role, as will be shown below (see 4.2).

For non-zero interaction strength $\mathcal{U}_b$, we find an aligning effect of the filament collision which becomes stronger for higher $\mathcal{U}_b$. Over the entire range of parameters, the impact parameter b has only a minor influence on the collision. As Fig. 3.7 shows, the impact parameters $b = \frac{1}{4}L$, $b = \frac{1}{2}L$, and $b = \frac{3}{4}L$ seem to be almost equivalent. This indifference is readily explained with our filament model, so consider again the situation of Fig. 3.4. Because the collided-on beads in the tail of the black filament cannot respond to external forces due to the condition to move towards the next bead in the chain, the black head — and therefore the whole filament — is not affected by the collision along its tail. On the other hand, the collision outcome of the red filament is only determined by the interaction of its head with a few beads along the tail of the black filament. The position of these black beads along the tail is irrelevant for the red filament, as long as they form the same angle. This explains why the outgoing angle is nearly indifferent to the impact parameter in the range $0 < b < L$.

This leaves the two special cases $b = 0$ where the heads collide spot-on and $b = L$ where they narrowly miss. As expected, for $b = L$ the filaments pass by almost without noticing each other, and only for very strong $\mathcal{U}_b$ a marginal effect is found. So indeed, the filaments pass by without affecting each other. For $b = 0$ on the other hand, the effect is very similar to $0 < b < L$ although it is even stronger aligning so that the slight nematic character for $\Theta_{in} > \pi/2$ is almost completely lost.

For interaction strengths $\mathcal{U}_b > 1\,k_BT$, the collision becomes aligning for small angles, and slightly anti-aligning for $\Theta_{in} \gtrsim \frac{\pi}{2}$. This nematic character agrees well with our picture of the filaments behaving like rods which slide along their contour when in contact. However, if the potential barrier is not high enough, the sliding only happens if $|\Theta_{in} - \pi/2|$ is small, otherwise the filaments can cross each other, resulting in only a small net change of Θ_{out}. As a consequence, the interaction becomes more pronounced for increasing $\mathcal{U}_b$ and approaches a limiting behavior which is already reached for $\mathcal{U}_b \approx 2\,k_BT$. The results for $\mathcal{U}_b = 4\,k_BT$ are not shown, because they hardly differ from the results with $\mathcal{U}_b = 2\,k_BT$.

The picture of sliding rods is however not perfect, because the interaction would then have to be point-symmetric around the point $(\pi/2, \pi/2)$ which it apparently is not. The reason for this discrepancy is that filaments are represented by spherical beads, whose surface is best defined as the equi-potential surface of the repulsion potential (2.4),

$$S_F(e) \equiv \left\{ x | e = \mathcal{U}_b \sum_{i=1}^{N_q} \max\left(0,\, \left(r_c - \left|\boldsymbol{r}_i - x\right|\right)^2\right) \right\} . \tag{3.7}$$

Typically, a colliding filament "sees" the potential $S_F(1\,k_BT)$, so it is clear that this surface is quite rough. This roughness drags the filament head of a colliding filament along if Θ_{in} is small enough, leading to a much more polar character of the collision than one would expect

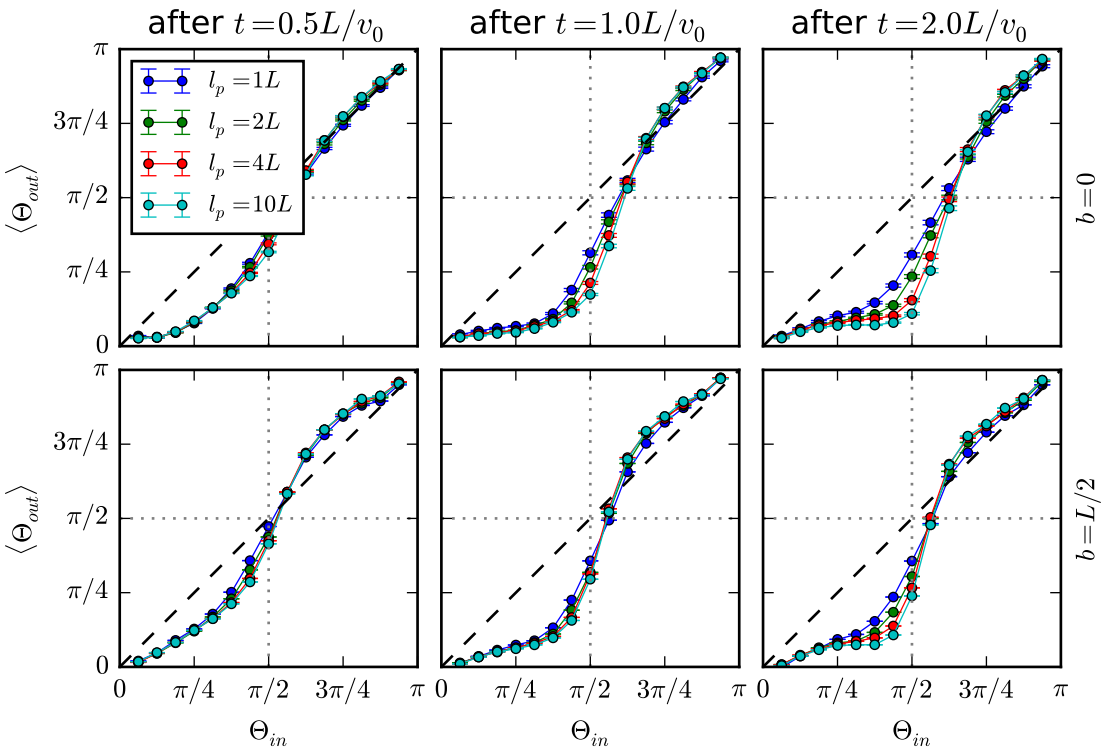

Figure 3.8 | The angular change of two colliding filaments at $\mathcal{U}_b = 2\,k_BT$ for different filament stiffnesses l_p at different times (columns) and for impact parameter $b = 0$ (top panels) and $b = L/2$ (bottom panels). For both $b = 0$ and $b = L/2$, the overall character of the collision shows only a small dependence on the filament stiffness. The main difference shows up at $\pi/4 < \Theta_{in} < 2\pi/3$ and is due to a more persistent preservation of the outgoing angle for stiff filaments.

from the picture of a contact interaction of rods. An extension of the collision rule to a more nematic interaction is possible but left for future investigation.

Finally, consider the influence of the filament stiffness l_p on the collision characteristics. Figure 3.8 shows only a small dependence of the collision on the stiffness of the filaments in the range from $l_p = 1\,L$ to $l_p = 10\,L$ irrespective of the collision parameter b. However, it is instructive to also consider the differences in the time evolution of Θ_{out} for the ranges of small $\Theta_{in} < \pi/2$ and $\Theta_{in} > \pi/2$. Consider the time-evolution of Θ_{out} for the collision parameter $b = L/2$. For initial angles $\Theta_{in} < \pi/2$, Fig. 3.8 shows nearly identical Θ_{out} up to $t = \frac{L}{v_0}$ where the alignment is close to maximal. Only at the last displayed point in time, $t = \frac{2L}{v_0}$, the angles for different l_p start to deviate from each other and the alignment passes away. Because angular diffusion destroys alignment as soon as aligning forces become ineffective, this observation allows to estimate the duration of a collision. In this case of small incoming angles, it follows that the collision takes about $t \approx \frac{L}{v_0}$. On the other hand for large collision angles Θ_{out} up $t = \frac{L}{v_0}$, the anti-alignment is already maximal at $t \approx \frac{L}{2\,v_0}$ and already starts to relax to the equilibrium value at $t \approx \frac{L}{v_0}$. Hence, a collision event for large collision angles is about twice as fast as for small collision angles. The geometry of aligning and anti-aligning collision gives a good explanation for this observation: if a collision event is aligning, the filaments run side-by-side after they have travelled a full length L. On the other hand if a

collision event is anti-aligning, the filaments are side-by-side after they have travelled only $L/2$, because the filaments run in opposite directions. Although not shown here, qualitativley analogous results hold for intermediate $\mathcal{U}_b$.

In summary, we have found that the bending stiffness l_p only has a small impact on the collision characteristics. Similarly, the outcome of a collision event is nearly identical of a wide range of impact parameters b, unless b is very small in which case the collision becomes more polar, or so large that the filaments miss. The major influence determining the collision outcome has the height of the potential barrier $\mathcal{U}_b$. For $\mathcal{U}_b = 0\,k_BT$, we found only a marginal interaction of the filaments, and as soon as the potential was non-zero the interaction became effective. Beyond $\mathcal{U}_b > 2\,k_BT$ the interaction becomes insensitive to increasing $\mathcal{U}_b$, because filaments cannot cross anymore.

3.2.2 Binary filament collisions with hydrodynamics

With the understanding of the dry collision, it is now possible to clarify the role of hydrodynamic interactions in the collision process of two filaments. Analogously to the data of dry runs, all data are diffusion compensated according to (3.6), re-using the reference model from Fig. 3.6. Although this reference was acquired from a dry run, it corresponds to an identical environment for the filaments except for the hydrodynamic interaction, hence it has exactly the desired properties. In analogy to Fig. 3.7, Fig. 3.9 shows the average observed angle Θ_{out} at different times and collision parameters. Comparing this with Fig. 3.7, we observe a similar signature as for dry runs. In addition, this signature is superimposed with an aligning interaction from a hydrodynamic interaction of the filaments. This hydrodynamic component acts aligning along the whole length of the filament, so that even for large angles, where the dry case was anti-aligning, the interaction becomes aligning in the long run. Beside the added hydrodynamic alignment, very similar observations hold as for the dry case, however with subtle differences. For example, with hydrodynamics there is a slight dependence on the impact parameter in the range $0 < b < L$, if $\mathcal{U}_b$ is small. This small effect comes from a dependence of the strength of the hydrodynamic flow field on the position along the filament, so that the net force on a colliding filament becomes dependent on where along the filament the collision happens. However, this effect can only come into play, if the contact interaction allows the filaments to cross which apparently is only the case for $\mathcal{U}_b < 1\,k_BT$.

The other eye-catching difference to the dry interaction is interaction that occurs for $b = L$, where the filaments had simply passed by in the pure Brownian case. Although this effect is virtually the same for all $\mathcal{U}_b$, it is best visible for $\mathcal{U}_b = 2\,k_BT$, because there its graph is not overlayed with other curves. It shows, how the alignment is most efficient around $\Theta_{in} \approx \pi/2$ which is readily explained by the larger fluid drag perpendicular than along the orientation of a rod. Furthermore, it highlights that with hydrodynamics, the interaction of two filaments becomes non-local and has a long range. Admittedly, the two-dimensional hydrodynamics of our setup exaggerate the strength and range of the hydrodynamic interaction. However, even in three-dimensional environments the aligning effect of hydrodynamics plays an important role and acts on length-scales much larger than direct contact.

Analogously to the dry case, Fig. 3.10 shows the collision angle for different filaments stiffnesses l_p. A comparison to Fig. 3.8 shows again a very similar signature of the collision, with the expected added polarity due to the aligning hydrodynamic drag. In contrast to the

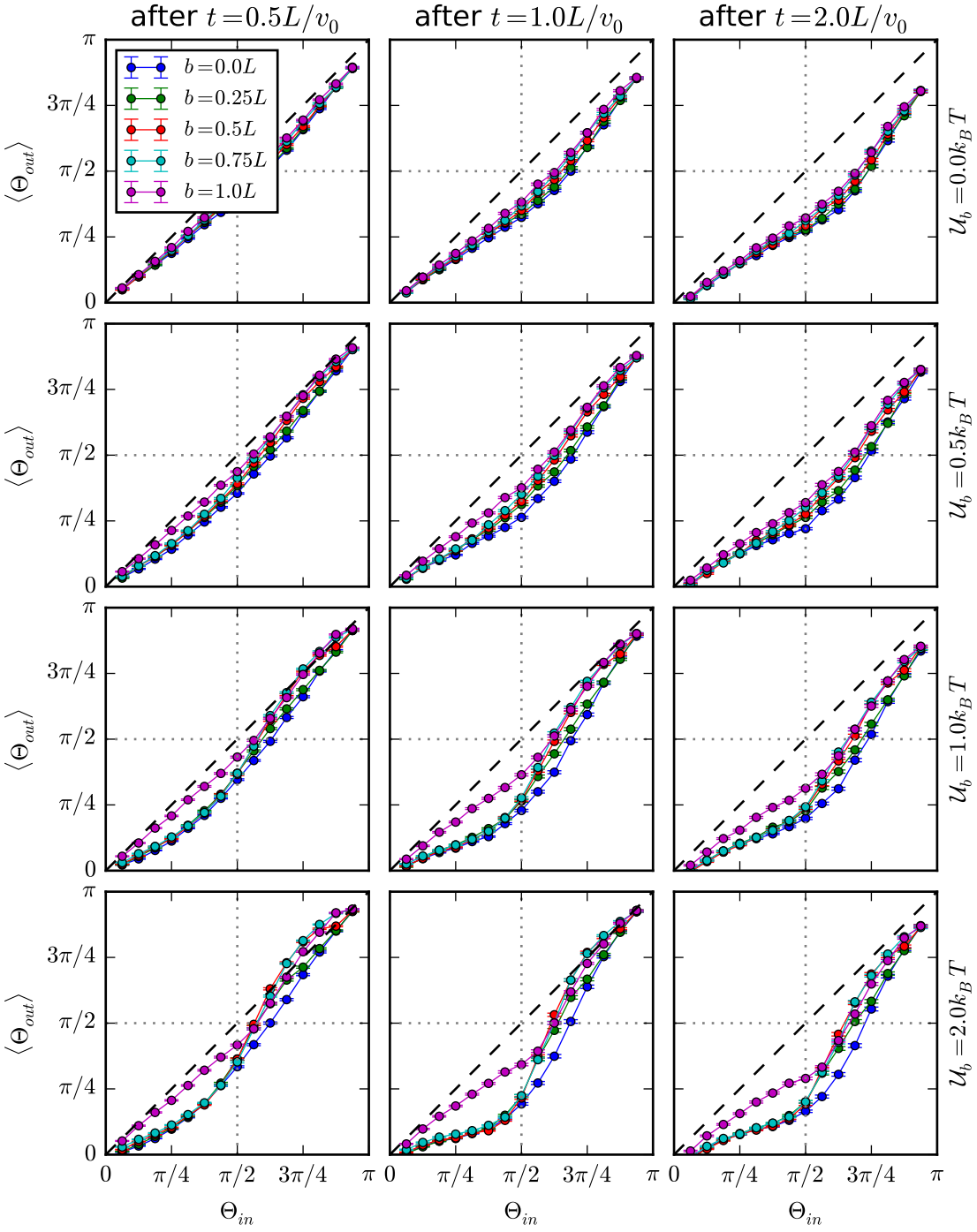

Figure 3.9 | The average angle as defined in (3.6) between to colliding filaments with persistence length $l_p = 2\,L$ for different times (columns) and repulsion potential $\mathcal{U}_b$ (rows). The data show nearly identical angles for different impact parameters b except for spot-on collisions ($b = 0$) and misses ($b = L$). In general, the interactions show a similar signature as the dry collisions, but with an additional aligning component from the hydrodynamic interaction especially at later times. Although not shown, the results for $\mathcal{U}_b = 4\,k_B T$ are nearly identical to $\mathcal{U}_b = 2\,k_B T$. Standard errors are indicated by horizontal lines and are smaller than the symbol size.

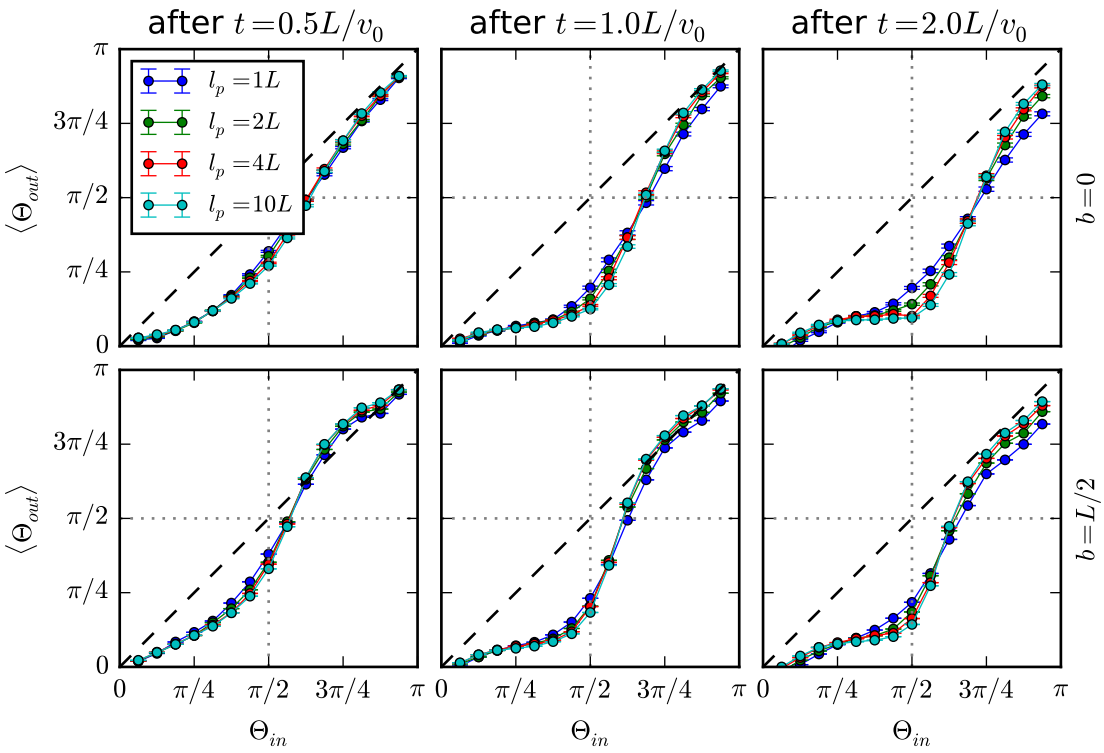

Figure 3.10 | The angular change of two colliding filaments at $\mathcal{U}_b = 2\,k_BT$ for different filament stiffnesses l_p at different times (columns) and for impact parameter $b = 0$ (top panels) and $b = L/2$ (bottom panels). Compared to the dry case Fig. 3.8, the collsision shows a stronger alignment and also a small stiffness dependence at larger Θ_{in}.

dry case, however, we find a dependence of $\langle\Theta_{out}\rangle$ on the filament stiffness for high incoming angles. This difference comes about from the fact that the hydrodynamic acts as a soft force that competes against the bending stiffness of the filaments. In contrast to the contact interaction which is so strong that it dominates any bending forces, the hydrodynamic drag is a real competition against the bending stiffness of a filament. Because of that, easily bendable filaments align quicker with the flow field of another filament than stiff filament, leading to the observed dependence of the collsision angle.

By now, it has become clear that the major effect of the hydrodynamic interaction is a stronger alignment. For a better comparison of the collision characteristics with and without hydrodynamics, we introduce a polarization index

$$\begin{aligned}\mathcal{S}_\rho(t) &= \frac{2}{\pi}\int_0^\pi \mathrm{d}\Theta_{in}\,\rho(\Theta_{in})\,\Delta\Theta_{out}(\Theta_{in}) \\ &= \frac{2}{\pi}\int_0^\pi \mathrm{d}\Theta_{in}\,\rho(\Theta_{in})\Big(\Theta_{out}\big(t|\Theta_{in},\,b,\,\mathcal{U}_b\big) - \Theta_{in}\Big)\,,\end{aligned} \tag{3.8}$$

which characterizes the polarity of the interaction. The idea is to average the angular change over the distribution of collision angles and normalize it to the interval $[-1, +1]$. In the following, we make the assumption that all incoming angles are equally likely, so that the distribution becomes flat, $\rho(\Theta_{in}) = \frac{1}{\pi}$. Consequently, a perfectly anti-aligning interaction with $\Theta_{out}(\Theta_{in}) = \pi$ would have an index $\mathcal{S} = 1$, whereas a perfectly aligning interaction with

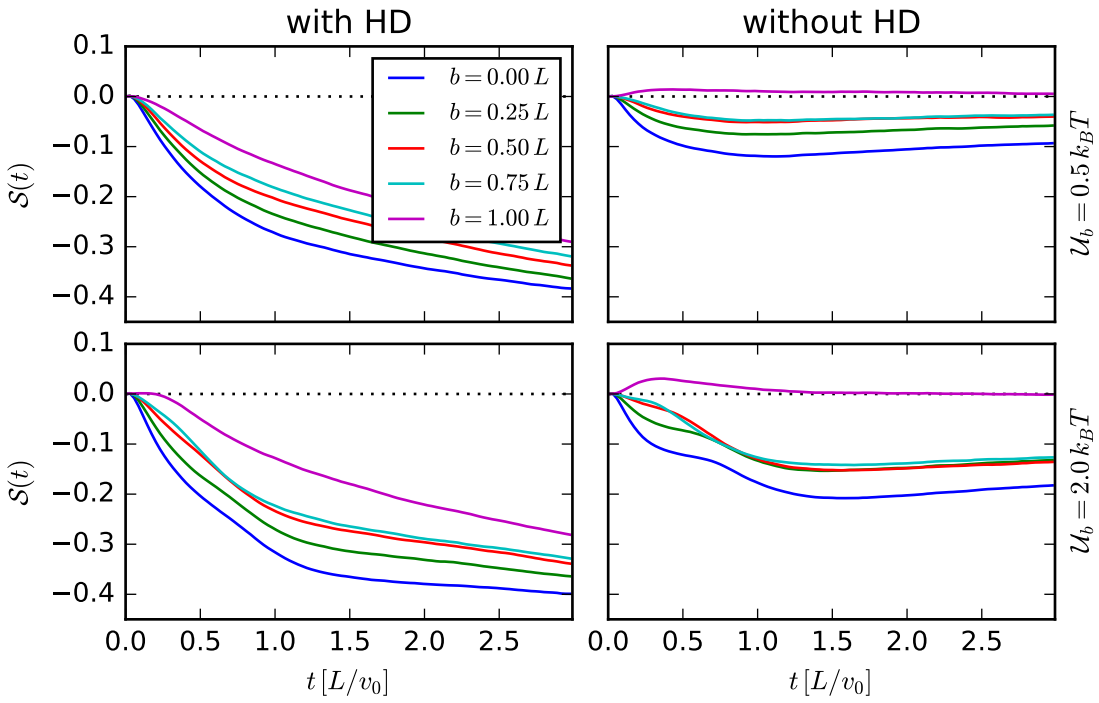

Figure 3.11 | Polarization index as defined in (3.8) shown for intermediate (top) and strong (bottom) repulsion $\mathcal{U}_b$. For otherwise identical parameters, the collision with hydrodynamics (left column) is much more aligning and the hydrodynamic interaction continues to align the filaments for much longer than in dry simulation. On the other hand for interactions without hydrodynamics, $\mathcal{S}$ quickly reaches an extremal value and relaxes to the equilibrium value thereafter.

$\Theta_{out}(\Theta_{in}) = 0$ would have an index if $\mathcal{S} = -1$. On the other hand, if the interaction does not change the polarization in the mean, $\mathcal{S}$ becomes zero. In other words, $\mathcal{S}$ is a measure if an initially homogeneous distribution of filament angles becomes more polar or anti-polar by interactions between the filaments.

Figure 3.11 shows a palpable difference in the polarization index between collisions with and without hydrodynamics. In the dry case, the $\mathcal{S}$ decreases for higher $\mathcal{U}_b$, while there is virtually no dependence in b with the exception of $b = 0$. This is in complete accordance to our above analysis of the collision charactersistics. In addition, the polarization index shows a small anti-alignment at small times for $b = L$ which has elapsed our attention so far. An explanation for this transient effect is that $b = L$ corresponds to a very close miss of the two filaments. So close in fact that a change of direction of the red filament towards the direction of the black filament is sterically hindered, such that the angular diffusion into anti-alignment is favored. The most important observation in the dry case is, however, that a maximal alignment is quickly reached around $t \approx L/v_0$, i.e. when the filaments have travelled a full length. The seeming relaxation towards $\mathcal{S} = 0$ can be attributed to an imperfect compensation of the angular diffusion.

Likewise, in the case with hydrodynamic interaction we find a strong shift of the polarization index $\mathcal{S}$ towards more negative values, which again is in accordance to our discussion above. In particular, also for $b = L$ where there was no angle change in the dry case, the interaction

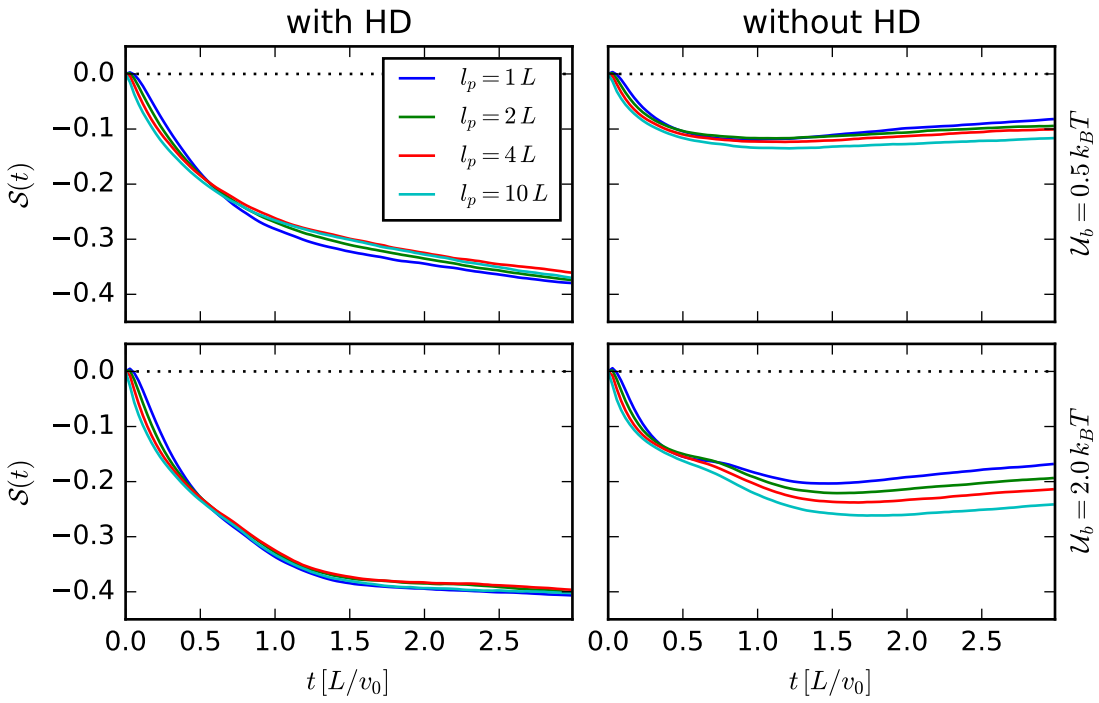

Figure 3.12 | Comparison of the polarization index $\mathcal{S}$ as defined in (3.8) for different l_p and $\mathcal{U}_b$. With hydrodynamics (left), the polarization index $\mathcal{S}$ is nearly independent of l_p, especially at longer times. On the other hand for pure contact interaction (right), $\mathcal{S}$ becomes more negative for stiffer filaments and therefore $\mathcal{S}$ *does* depend on l_p.

is about as polar as for smaller b. However, the biggest difference to the dry case is the much longer duration of the interaction showing in a decrease of $\mathcal{S}$ even at times much greater than $t \approx L/v_0$. It is clear that this long-term effect must come from the long range of hydrodynamic interactions compared to the short-ranged contact interaction mediated by the potential barrier. Furtermore, the difference in $\mathcal{S}$ between weak and strong $\mathcal{U}_b$ becomes rather small after longer times. This is an important insight because it means that at long time scales, the pair-wise contact interaction is dominated by the much weaker hydrodynamic interaction. Likewise, even the bending stiffness l_p has virtually no impact on the resulting angle at long times Fig. 3.12, which is in stark contrast to the dry case.

In summary, we have found that on top of the short-ranged aligning interaction due to contact interaction, the hydrodynamic interaction adds a further aligning force. In contrast to the short-ranged strong contact interaction, the hydrodynamic alignment is weaker, but has a long range such that it dominates the alignment of two filaments on longer time-scales.

3.2.3 Comparison to the actomyosin motility assay

In a recent work, Suzuki et al. have determined the scattering statistics of the motility assay experiment [57]. Because this experiment inspired our model, we will compare our results to their findings in the following.

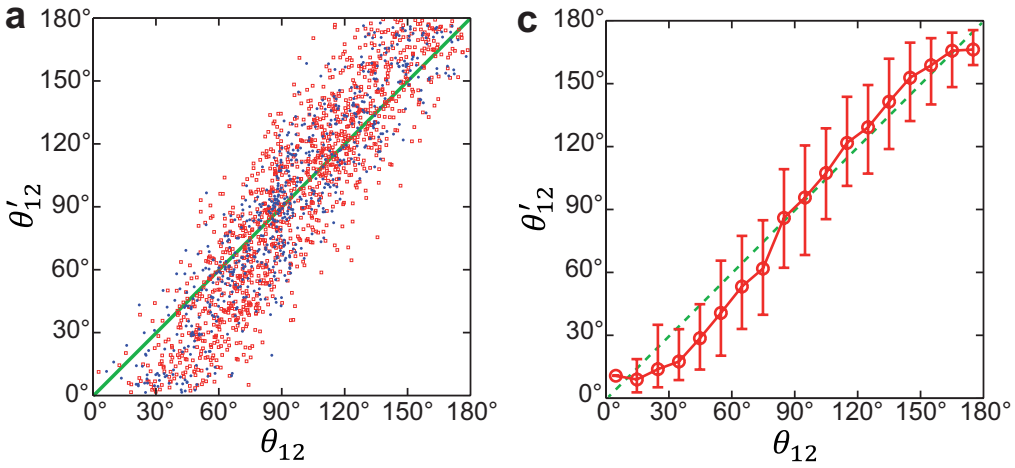

Figure 3.13 | Experimentally obtained binary-collision statistics for the actomyosin motility assay from [57]. **Left:** Scatter plot of incoming angle Θ_{12} versus outgoing angle Θ'_{12}. Red open squares and blue solid circles represent data for different filament densities. **Right:** Mean plot via binning by Θ_{12}. Indication of weak polar bias where $\Theta'_{12} < \Theta_{12}$ for highly acute Θ_{12}. Error bars: Standard deviation. Reprinted by permission from Macmillan Publishers Ltd: Nat. Phys. [57], ©2015.

Suzuki et al. looked at the actomyosin motility assay with very low filament densities, where no collective motion is observed. At such low densities, it is possible to identify binary filament collisions and determine the incoming and outgoing angle between the actin filaments. From these data, they estimated the scattering function $\Theta'_{12}(\Theta_{12})$ which directly compares to our $\Theta_{out}(t|\Theta_{in}, b, \mathcal{U}_b)$ from (3.6). Their measured $\Theta'_{12}(\Theta_{12})$ shows mostly a nematic signature with $\Theta'_{12}(\Theta_{12}) \gtrless \Theta_{12}$ for $\Theta_{12} \gtrless \pi/2$, and only a minuscule scattering polarity $\mathcal{S} < 0$ (see Fig. 3.13). The hydrodynamic drag which strongly polarizes the scattering statistics for in our model (e.g. Fig. 3.11), is therefore apparently irrelevant for binary collision of actin filaments. Consequently, the dry case has more similarity with the experimental scattering statistics. However even without hydrodynamics, our filaments collisions are more polar than observed by Suzuki et al. A reason for this could be the surface roughness of our filaments, because they are represented by a chain of spherical beads. Apart from this stronger polarity, the best matching amplitude to $\Theta'_{12}(\Theta_{12})$ is at rather low $\mathcal{U}_b$ below $1\,k_BT$.

In summary, the experimental measurements of binary actin filament collisions by Suzuki et al. are best reproduced by our dry simulations at small $\mathcal{U}_b$. In general, our binary filament interactions are stronger polar and less nematic than the measured collisions. An extension of our filament model to a more nematic contact interactions is left for future work.

4 Many filaments in a dry environment

The previous chapter has established that a single filament describes a persistent random walk and that binary filament collisions are aligning. Large systems of propelled semi-flexible filaments with contact interactions are novel, therefore this chapter will first consider systems of filaments without hydrodynamic interactions. In particular, we only consider systems with identical filaments of length L, persistence length l_p, and interaction strength $\mathcal{U}_b$.

In addition to these microscopic parameters, there is now an additional macroscopic parameter, the density of filaments ρ. One can give a very simple argument why ρ matters: in between collisions, the filaments lose their memory of direction due to angular diffusion. The filament density controls how often filaments collide, because by a very crude estimate, the average time between collisions is $t \propto \left(r_c^{d-1}\, v_0\, \rho\right)^{-1}$. Because v_0 and r_c remain unchanged, the filament density ρ controls whether the next collision occurs before or after the memory of direction is lost. Therefore, if collisions happen frequently enough, the alignment of one collision can carry through to the next collision, so that correlations build up.

All simulations in this chapter had a periodic box of size $80\,L \times 80\,L$ and filament densities between $0.47\,n/L^2 \leq \rho \leq 4.69\,n/L^2$ (3000–30 000 filaments). Such high numbers of filaments are computationally only viable through our scalable implementation of this model. Even then, a single run can easily take up to 500 hours compute time, resulting in about 63 hours runtime on an eight-core machine. For that reason, we only generated a single realization for every parameter combination. Although this causes considerable realization noise, the trends become sufficiently clear when considering the whole parameter set.

Data are acquired as follows: we start from random initial conditions where both the location and the direction of filaments are uniformly initialized. From these random initial conditions, we evolve the system of filaments as described in chapter 2 up to $t_{max} = 2^{22}\, h_{MPC} \approx 4.2 \cdot 10^6\, h_{MPC}$ iterations, corresponding to about $t_{max} \approx 1200\, L/v_0$ filament lengths. Data are only saved to disk at intervals of 512 iterations, corresponding to about $0.44\, L/v_0$.

This chapter is structured as follows: Section 4.1 sets the stage and gives a phenomenological overview of the system. Section 4.2 then quantifies these findings by looking at two different order parameters (4.2.1 & 4.2.2), the number fluctuations of the density (4.2.2), the density in the gas phase (4.2.3), and the clustering behavior (4.2.4). Finally, section 4.3 briefly summarizes the findings of this chapter.

4.1 Phenomenology

We find a plethora of different behaviour as the density ρ and filament parameters ($\mathcal{U}_b$ and l_p) are changed. To avoid confusion in the following sections, it is therefore necessary to first give an overview of the phenomenology and establish a simple nomenclature of the observed

features. To that end, we will show snapshots of the simulation at various points in time. Of course, the full time evolution can not be displayed in a printed form, however a central question is whether the system has become quasi-periodic. Here, quasi-periodic means that from a macroscopic point of view, the system repeatedly attains a very similar state. To address this question, we present a method that gives a two-dimensional representation for the time evolution of the system of filaments and thus allows to determine whether the system has become quasi-periodic.

4.1.1 The tSNE method

For a better understanding of the system of filaments, we want to give a visualization of the complete time evolution of our system. The time evolution of the system can be thought of as a sequence of points in the state space of the whole system, which is very high-dimensional. We are therefore looking for a two-dimensional representation of high-dimensional data. The tSNE-method is a general-purpose visualization method for high-dimensional data given by x_i [92, 93], which is well suited for our goal.

Any mapping of high-dimensional $x_i \in \mathbb{R}^n$ onto $y_i \in \mathbb{R}^2$ must discard a lot of information, so that no embedding can be perfect. For example, a typical embedding that physicists are familiar with, is the principal component analysis, where the points x_i are projected along some axis onto y_i in a 2D-plane. The projection axis is chosen in such a way that the variance of the y_i becomes maximal. In that way, the principal component analysis preserves the global structure of the points x_i for the two preserved dimensions, but on the other hand the local structure of the other $n-2$ dimensions is completely lost. The aim of the tSNE method is an embedding that preserves the *local* structure of the x_i for *all* dimensions, while ignoring the global structure of x_i for the most part.

The approach taken by tSNE is to go from a deterministic embedding to a stochastic embedding (the SNE in the name stands for "Stochastic Neighbor Embedding") by defining a measure of similarity between two points by

$$p_{j|i} = \begin{cases} \exp\left(-\|x_i - x_j\|^2/2\sigma_i^2\right) / \sum_{k\neq i} \exp\left(-\|x_i - x_k\|^2/2\sigma_i^2\right) & \text{for } j \neq i \\ 0 & \text{for } j = i \end{cases} . \tag{4.1}$$

The gaussian weight ensures that points which are close together have a large similarity, whereas widely separated points have no similarity. The width of the gaussian distribution σ_i has to be adjusted appropriately, so that points in dense and sparse regions both have a reasonable number of similar neighbors. Likewise, the image points y_i receive a similarity measure

$$q_{j|i} = \begin{cases} \left(1 + \|y_i - y_j\|^2\right)^{-2} / \sum_{k\neq i} \left(1 + \|y_i - y_k\|^2\right)^{-2} & \text{for } j \neq i \\ 0 & \text{for } j = i \end{cases} , \tag{4.2}$$

which is given by a Student-t distribution for reasons that are explained below[1].

[1] The "t" in tSNE stands for the Student-t distribution of the image points, so that the full name is Student-t distributed Stochastic Neighbor Embedding

Both similarities can be understood as the probabilities to find point x_j in the neighborhood of x_i or y_j in the neighborhood of y_i. A measure of the similarity of the two distributions is given by the Kullback-Leibler divergence [94]

$$D_{KL}(P|Q) = \sum_i \sum_j p_{j|i} \log \frac{p_{j|i}}{q_{j|i}} \ . \tag{4.3}$$

Minimizing $D_{KL}(P|Q)$ by adjusting the positions y_i appropriately gives the best embedding of the x_i in two dimensions. This minimization procedure is rather complex and requires intelligently chosen simplifications in order to be feasible[2]. The advantage of this embedding is that a pair of close-by points x_j and x_i has a high chance of being mapped to a pair of points y_j and y_i which are again neighbors in the image. If this were followed strictly, the image points y would always be very dense, because the volume of an n-dimensional sphere grows much faster than the area of a circle. To avoid this crowding, the Student-t distribution is employed for the image points, so that long distances in the image may be vastly exaggerated due to the heavy tail of the distribution. As a consequence, the embedding preserves the local structure of the x_i by putting their image points close together, but as the distance in the source increases, the image point may end up much further away. Of course, the image points y are no faithful representation, but it allows to determine whether the x_i have no structure, dense regions, or periodic orbits.

In our case, the dimensionality is rather high, specifically we have $N \times 2d \times N_b$ degrees of freedom for our N polymers with N_b beads, each of which has position and velocity in $d = 2$ dimensions. For N of the order of 10^4 this is even too much for a sophisticated method such as tSNE. As a first step, we can ignore the velocity of the filaments, because every filament usually moves with the same speed. Because filaments align in dense regions, even the direction of filaments becomes irrelevant so that we can be sure that this does not lose essential information. Furthermore, if filaments only exchange their location, we should consider these states as equivalent, because filaments are indistinguishable. Instead of individual filaments, we should therefore use the filament density instead. A very elegant way to achieve this is to generate a picture of the simulation and take the grey-values of each pixel as a degree of freedom. For every point in time[3] we generate a picture of the current state of the simulation. In order to keep the number of degrees of freedom low, we use only pictures of 10×10 pixels, resulting in 100 degrees of freedom.

There is one last obstacle; because the tSNE-method aims at preserving the local structure and subsequent frames are so similar, it only generates a linear sequence of image points y_i from our input data. The solution is to make the input image data d_{ij} artificially fuzzy. To that end, we apply a radial smoothing kernel with a density $k_{ij} = \max\big(0, 1-(i^2+j^2)/r^2\big)$ and a radius r of five pixels to the input images, effectively blurring the image. This smears out the small-scale features, so that a recurring state is already categorized as similar if its large-scale configuration is similar, although its small-scale features are different. However, this even increases the tendency of tSNE to group subsequent states together, because subsequent states mostly differ by their small-scale features and they are blurred out. To overcome this

[2] For the tSNE-plots shown below we performed the minimization with the publicly available implementation from [93]

[3] In fact, we store only a fraction of 1/512 of the simulation states and discard the rest. However, between stored states a filament typically moves only $0.15\,L$, so that the motion of a filament is still captured very well.

drawback, we added a uniformly distributed random noise on top of the image data. In that way, the sequence of images in image space is no longer a sharply defined path, but a blurry point cloud along this path, which can overlap with a recurring state. The noise level had to be adjusted in each of the examples below and was in the range of 2-6 signal to noise ratio[4].

In summary, we have introduced a method that allows to depict the time evolution of the large-scale filament density distribution in our system. The stochastic nature of the tSNE-embedding places similar states close together while ignoring the global configuration for the most part. We stress that discrete jumps or discontinuities in the path are possible, and cannot be avoided due to the dimensional reduction.

4.1.2 Observations

In the following we will present typical simulation snapshots and introduce terms for the observed features. The main part of this section are the plots which should stand on its own and the text is merely a description with some explanations. For easy reference, we therefore highlight new terms in bold.

To avoid misunderstandings, we first give a few remarks how to read the tSNE-plots. The tSNE-plots are a two-dimensional representation of the time evolution of the entire simulation, so that each dot corresponds to a particular state. In color and luminosity of the dots encodes the simulation time of the state, such that early points in time are dark (violet) whereas towards the end of the simulation, the dots are bright (yellow). As explained above, the tSNE-plot arranges the dots in such a way that close-by dots most likely correspond to similar states, where similar refers to a similar density distribution. On the other hand, if dots are separated by a large distance, they are likely different. Note that due to the construction of the plot, it is more likely that widely separated dots are similar, than close-by dots are dissimilar. It is therefore important not to misinterpret the plot in a geometric sense, instead it should be understood as a topological depiction of the path in the phase space.

The first example in Fig. 4.1 (top) shows the simulation at a rather low density ($\rho = 1.41\, n/L^2$) and low interaction strength ($\mathcal{U}_b = 0.4\, k_B T$). Note that a single filament is so small compared to the box size that it merely appears as a dot in the printed version. In the center of this figure is a tSNE-plot of the simulation, which in this case looks just like a random point cloud. In fact, early states (dark) and late states (bright) are mixed up randomly without showing any structure, so that the final state and beginning state have to be similar. Indeed, the snapshots of the filament distribution show no apparent density fluctuations and the initial state (top left) looks just like the final state (bottom right). It follows that for low density and interaction strength, the filaments form an unordered **gas**.

When the density is increased, the filaments start to cluster locally, as Fig. 4.1 (bottom) shows. In this case, both the density and the interaction strength were increased ($\rho = 2.34\, n/L^2$ and $\mathcal{U}_b = 2.8\, k_B T$). The snapshots show local clustering up to a length scale that remains much smaller than the size of the simulation box (in the following just **system size**). The tSNE-plot now has a few arcs and blobs that do not mix with the remaining states, which clearly indicates that the filaments are no longer completely randomly distributed. Because

[4] In other words, for a normalized input data $d_{ij} \in [0, 1]$ the noise variance was uniformly distributed from $[0, \eta]$ with $\eta \in [0.1, 0.5]$

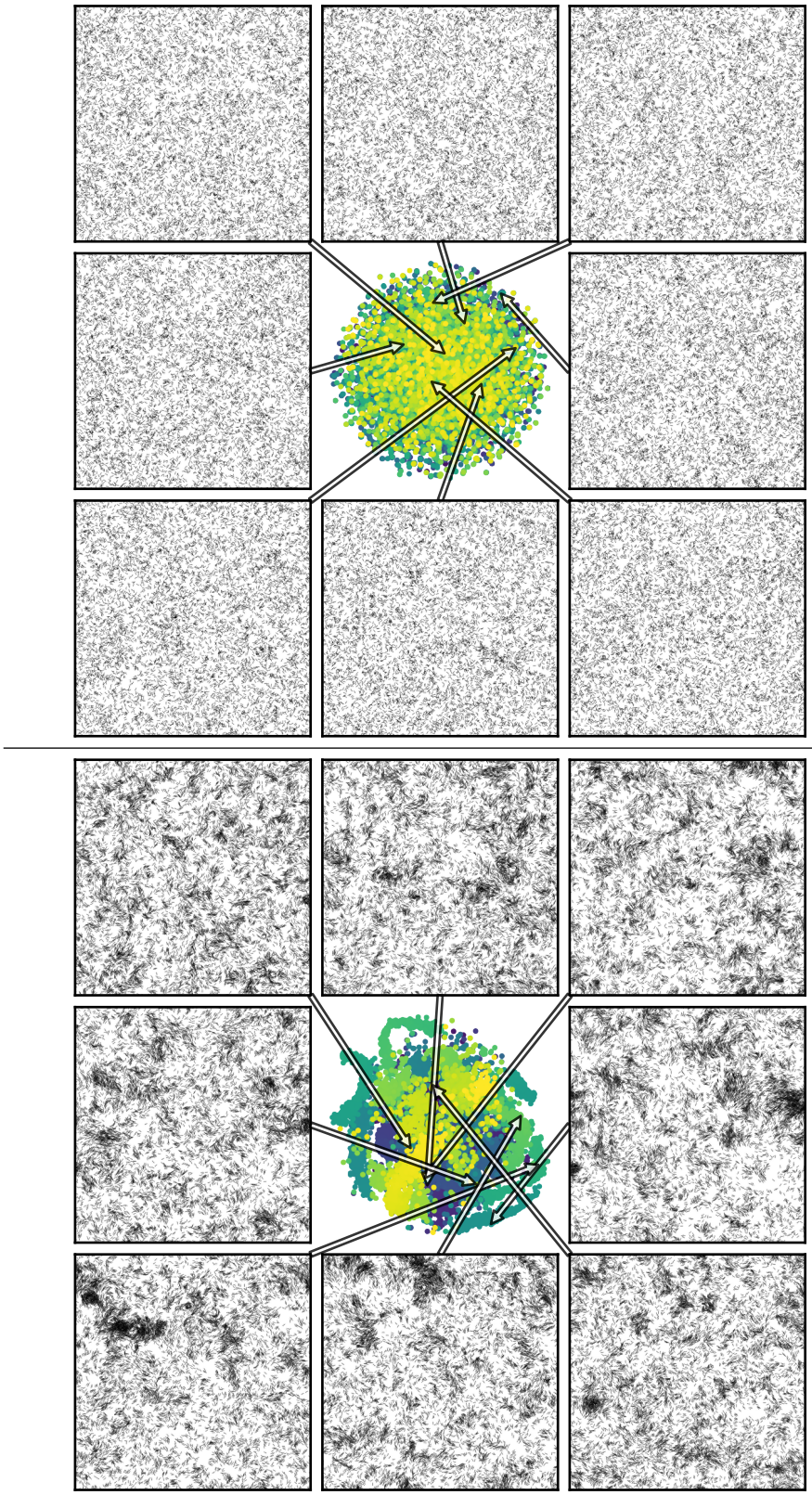

Figure 4.1 | Top: $\rho = 1.41\, n/L^2$, $\mathcal{U}_b = 0.4\, k_B T$, $l_p = 2\, L$ **Bottom:** $\rho = 2.34\, n/L^2$, $\mathcal{U}_b = 2.8\, k_B T$, $l_p = 2\, L$. More explanation about these plots is found in Appendix A.2.1 on page 156.

some states are grouped in lines, we can follow that there is a strong correlation among the states along this line. In fact, the lines in the tSNE plot correspond to the coherent movement of large clusters of the filaments. We note that widely separated start and end point mean uncorrelated density distributions, whereas along the line the correlation is strong, therefore the points are grouped together. At some point these clusters disintegrate and the line in the tSNE plot stops. As will be explained below, the clusters remain so small and disintegrate, because $\mathcal{U}_b$ is so large that the clusters can not permeate each other when colliding, which causes them to disassemble instead.

Upon further increasing the density of filaments, collisions among the filaments become so frequent that the direction between two collisions starts to be correlated. As a consequence, two filaments can align without direct interaction, but by collisions with a third filament. In particular, the alignment of two filaments can also propagate in the direction orthogonal to the direction of movement. Under such circumstances, an occasional density fluctuation has a drastic chain effect. Figure 4.2 (top) shows how an initially homogeneous system spontaneously produces a density fluctuation ($\rho = 3.75\, n/L^2$, $\mathcal{U}_b = 0\, k_B T$, and $l_p = 2\, L$). In this dense seed region, the filaments align through direct interactions and start moving in one direction. Because filaments to the sides of such a cluster are not re-aligned with the cluster, such a cluster splays to its side, thereby creating a spherical wave-shaped cluster of aligned filaments. As this cluster propagates through the system, it eventually spans the whole simulation box. Due to the wave-like behaviour of this system size cluster, such a cluster will be called **density wave** in the following. Such a density wave sweeps the simulation box and collects filaments at its front. It is essential that the un-aligned filaments which collide with the density wave do not disturb the filament alignment in the density wave too strongly, otherwise the density wave would not emerge at all. Towards the rear of the density wave, the density of the filaments drops so that filaments are no longer effectively realigned with the density wave. As a result, the density wave loses filaments at its rear end. Figure 4.2 (top) also shows that the density wave starts as a spherical wave, but as it propagates several times through the system, it basically flattens out over time. The tSNE-plot for this run shows a dark blob of unordered initial states with a trail leading away from it which corresponds to states where the density wave develops. After the density wave has established itself, the system repeatedly attains very similar states, so that the tSNE-plot shows a closed loop (greenish and yellow region). As a final remark to the alert reader, we note that the interaction potential is actually zero, so that filaments should not interact at all. This is however not correct, because in addition to the contact interaction, there is a spurious interaction between two filament beads, if they share the same collision cell. This interaction is however much weaker than the contact interaction via $\mathcal{U}_b$ and only has an effect, because the density in this example is extremely high.

If the interaction strength $\mathcal{U}_b$ of two filaments is increased, the onset of the density wave is in general at much earlier times. For example, Fig. 4.2 (bottom) shows the density wave for $\rho = 1.88\, n/L^2$ and $\mathcal{U}_b = 1.2\, k_B T$. Here, the filaments quickly form small locally aligned patches and merge to bigger clusters, until the density wave forms. The lower left panel of this figure nicely shows that the density wave usually has a **sharp front** and becomes more fuzzy and less dense towards the end. Besides, one can see that the density in the density wave also has a large variability, a feature that is found in most realizations. Similarly to the previous case, the tSNE-plot shows a blob of unordered initial states out of which partially

ordered states emerge. After the onset of the density wave, the system states form a closed loop, which means that the system has become quasi-periodic.

The similar pattern is found, if the density is further increased, with the difference that the width of the density wave grows with the total density ρ (Fig. 4.3 top). Intuitively, we may conjecture that the rate at which filaments are lost at the rear of a density wave is dominated by the microscopic filament parameters. Consequently, the density of all filaments which are not part of the density wave should be constant for the same combination of l_p and $\mathcal{U}_b$. We call the region of freely moving disordered filaments the **gas phase**. Therefore, the remaining filaments have to be in the density wave and its width must grow with ρ. Another notable and not so obvious difference to Fig. 4.2 (bottom) is that the onset of the density wave shifts towards later times as $\mathcal{U}_b$ increases. As already stated above, the reason is that cluster collisions at large $\mathcal{U}_b$ are often fatal, and result in the complete disintegration of the cluster.

The trend that the density wave emerges at later times becomes even more expressed if ρ is even further increased (Fig. 4.3 bottom, $\rho = 4.69\, n/L^2$, $\mathcal{U}_b = 3.6\, k_B T$). Only the lower three panels of this figure are in the quasi-periodic state as their localization on the tSNE-plot shows. In contrast, local clustering is much more efficient, so that even the first snapshot shows strong clustering. However, collisions of small clusters for such high $\mathcal{U}_b$ often lead to complete disintegration of the clusters, as will be discussed below. Another observation is that the fuzziness of the rear of the density wave becomes less fuzzy and increasingly sharper as $\mathcal{U}_b$ increases. This has an important consequence for the density in the **gas phase**, ρ_{gas}. Consider the gas phase in Figs. 4.2 & 4.3, where $\mathcal{U}_b$ increases from $0 - 4\, k_B T$, and which clearly show that the density in the gas phase varies drastically.

So far, we have only shown examples with a **single density wave**. The reason for that is that the run-length of a density seed is of the same order as the system size and that our system has periodic boundary conditions. Even if two density waves form, their paths will cross unless they are perfectly aligned. However, two crossing density waves merge to one big density wave, unless the interaction strength is so low that they may pass through each other. In the latter case, the density waves would still partially align and potentially form two distinct aligned density waves. It follows that **multiple density waves** can only form in parameter regions where the propensity to form clusters is large (high ρ and $\mathcal{U}_b$ big enough), but cluster collisions are not fatal (small $\mathcal{U}_b$).

Figure 4.4 (top) shows an example where the periodic final state shows two density waves. In accordance to our discussion above, the simulation parameters are at large density ($\rho = 4.69\, n/L^2$) and intermediate interaction strength ($\mathcal{U}_b = 1.2\, k_B T$). Another exotic example shows Fig. 4.4 (bottom) where a *single* density wave winds around the toroidal simulation box in such a way that it winds twice around the vertical axis and once around the horizontal axis. Even though it looks like two density waves, it is actually a single one from a topological point of view. We note, however, that a wave with multiple winding numbers is most likely observed in a region where multiple waves form, because it is less stable than a wave with a single winding and therefore easily destroyed by fluctuations.

The examples of Fig. 4.4 are however exceptions for two reasons. First, as already mentioned, a single density wave in the final state is much more likely than multiple density waves. Second, because multiple density waves only appear at parameters where the density waves

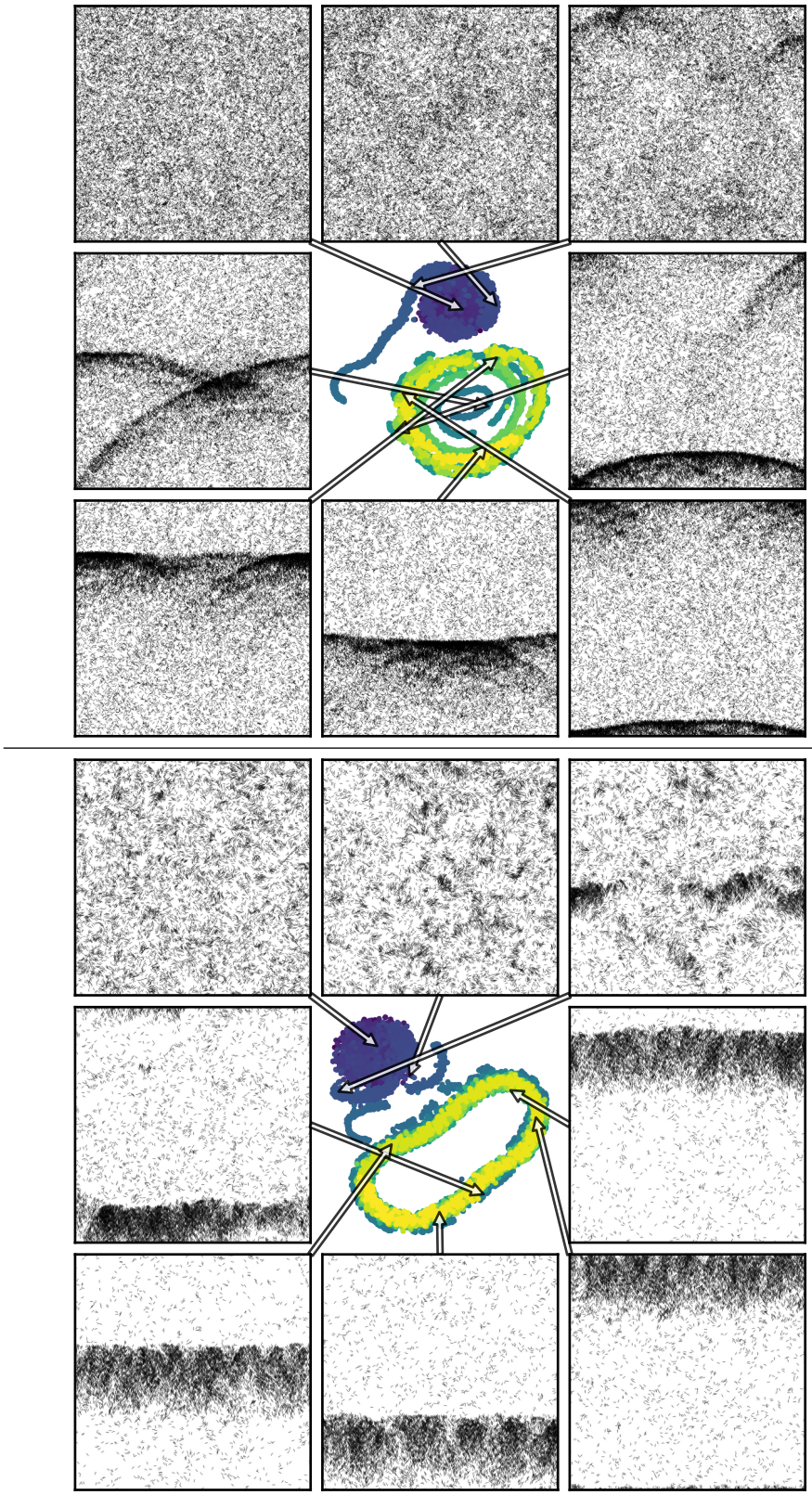

Figure 4.2 | Top: $\rho = 3.75\, n/L^2$, $\mathcal{U}_b = 0\, k_B T$, $l_p = 2\, L$ **Bottom:** $\rho = 1.88\, n/L^2$, $\mathcal{U}_b = 1.2\, k_B T$, $l_p = 2\, L$ (wave moving upwards). More explanation about these plots is found in Appendix A.2.1 on page 156.

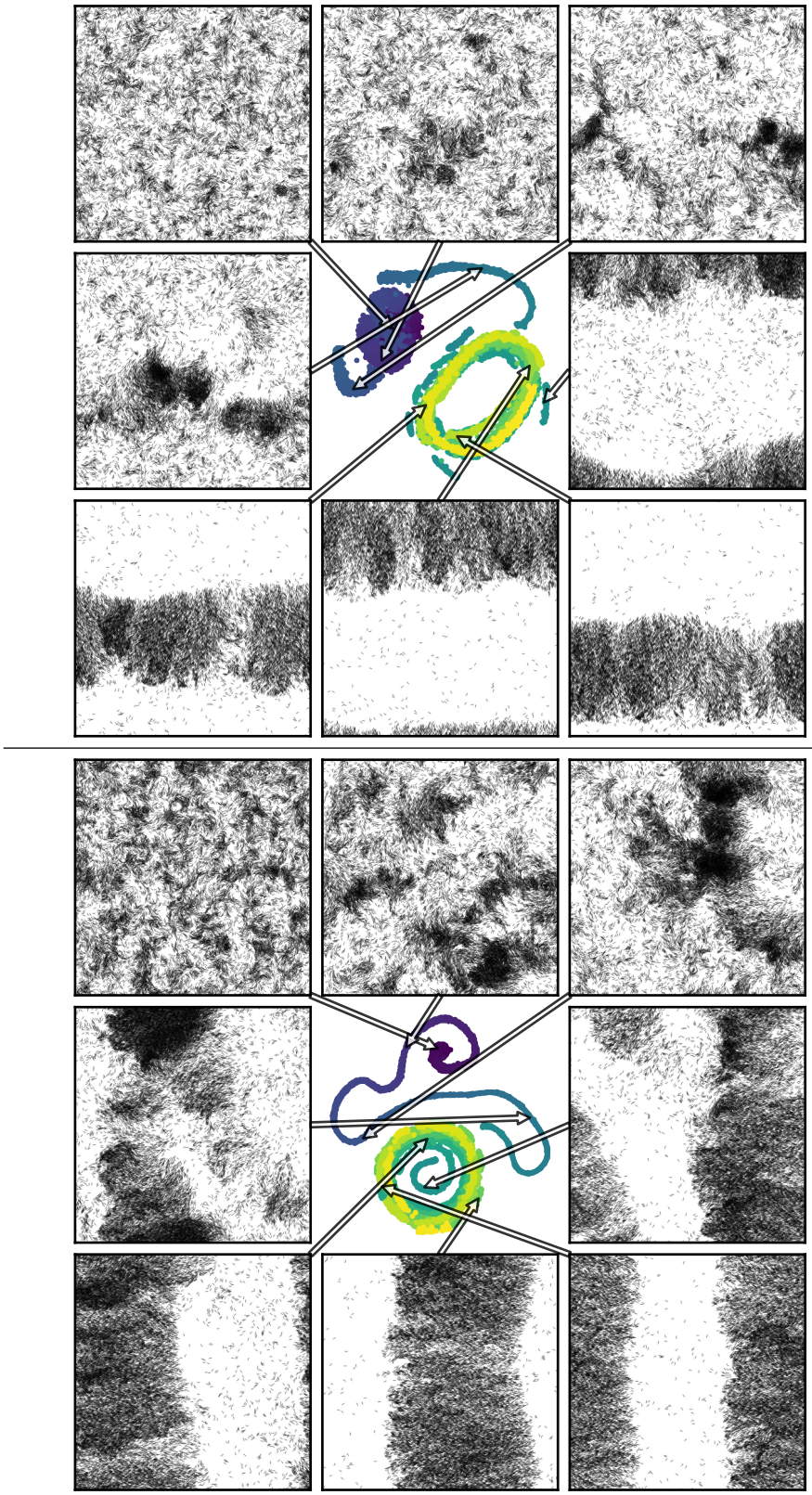

Figure 4.3 | Top: $\rho = 2.81\, n/L^2$, $\mathcal{U}_b = 4.0\, k_B T$, $l_p = 2\, L$ (wave moving downwards) **Bottom:** $\rho = 4.69\, n/L^2, \mathcal{U}_b = 3.6\, k_B T$, $l_p = 2\, L$ (wave moving leftwards). More explanation about these plots is found in Appendix A.2.1 on page 156.

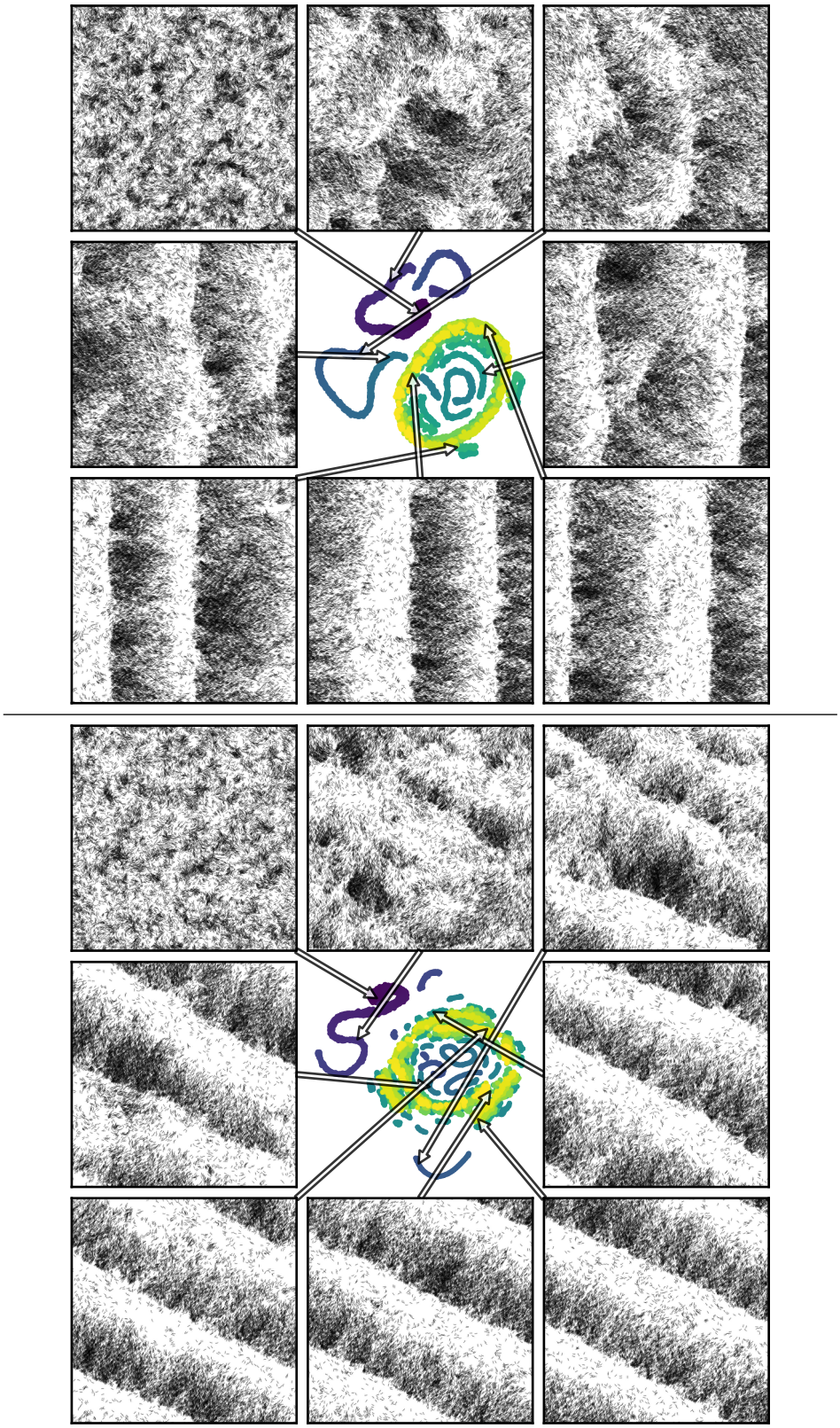

Figure 4.4 | Top: $\rho = 4.69\, n/L^2$, $\mathcal{U}_b = 1.2\, k_B T$, $l_p = 2\, L$ (waves moving leftwards) **Bottom:** $\rho = 3.75\, n/L^2$, $\mathcal{U}_b = 1.2\, k_B T$, $l_p = 2\, L$ (wave moving towards the lower left). Note that this is a *single* wave, because of the toroidal topology of the simulation box. More explanation about these plots is found in Appendix A.2.1 on page 156.

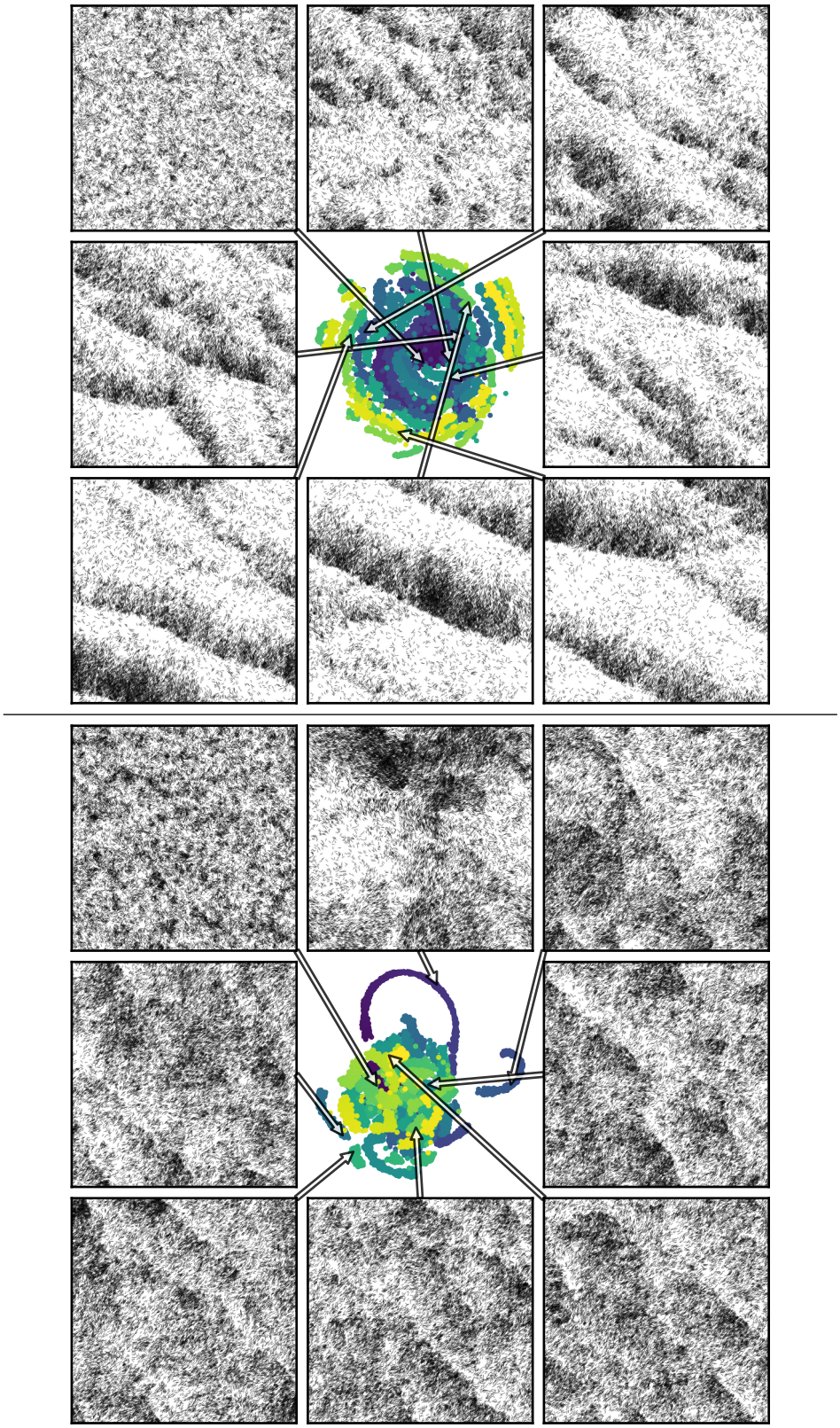

Figure 4.5 | Top: $\rho = 2.81\, n/L^2$, $\mathcal{U}_b = 0.8\, k_B T$, $l_p = 2\, L$ (waves moving towards the lower left) **Bottom:** $\rho = 4.69\, n/L^2$, $\mathcal{U}_b = 0.5\, k_B T$, n.b. $l_p = 7\, L$ (filaments moving towards the upper right). More explanation about these plots is found in Appendix A.2.1 on page 156.

are weakly interacting, the stationary state is achieved at much later times than normal. The stationary state is only reached, if all density waves have aligned their direction of movement. However, if one interaction is not enough to align the waves — and it is not because otherwise the cluster would merge — then the angle between the two density waves shrinks. But if the angle between the density waves shrinks, the period of their interaction grows. As a consequence, a typical final state in our simulations with **multiple distinct** density waves is one where the waves have a small non-zero angle. It follows that our simulation time had not been enough to reach a steady (quasi-periodic) state. Figure 4.5 (top) shows a typical example for such a situation. The tSNE-plot clearly shows multiple distinct lines, which means that these states are dissimilar to all others, and the plot has no closed loop, so that the system is not periodic.

Finally, multiple waves can also appear in a different flavor. Figure 4.5 (bottom) shows weakly interacting filaments at very high density ($\rho = 4.69\, n/L^2$, $\mathcal{U}_b = 0.5\, k_B T$) and n.b. $l_p = 7\, L$ (all previous examples were at $l_p = 2\, L$). We have discussed above that smaller $\mathcal{U}_b$ also makes the rear of the density wave move fuzzy, so that effectively the density wave also becomes more elongated. At these parameters, the density wave is in fact so elongated that it overlaps with the next one or itself. So instead of a distinct high- and a low-density gas phase, we observe a single phase with large density fluctuations which are typical for the high-density phase. In particular, all filaments in this joint phase move roughly in the same direction, so that there is no gas phase anymore where the filaments move in random directions. In contrast to multiple distinct density waves, we can assume that **multiple overlapping** density waves have reached a stationary state which is however non-periodic. The tSNE-plot in Fig. 4.5 (bottom) shows how in the beginning, a large density blob forms, leading the system far away from the initial density distribution. At later times (4^{th} snapshot), the density is again much more evenly distributed and stays like that until the end. Because the image points of different times are so mixed and there is no closed orbit, the tSNE-plot tells us that the system has a non-periodic stationary state.

In summary we have observed a gas-like disordered state at low filament densities. As the filament density increases, larger clusters of correlated filaments form and when these clusters reach system size, a density wave propagates through the system. The separation of the filaments into a coherently moving high-density region, the density wave, and a disordered low-density gas phase is a defined phase transition. The density wave itself also shows large density variations. The density in the gas phase varies drastically with the microscopic filament parameters or, in other words, the alignment strength of binary filament collision. Multiple distinct density waves are possible, but an exception. Where distinct density waves form, the system becomes quasi-periodic in the long run. The density waves can become so spread out that they even overlap with the subsequent wave. In that case, there is a *single* phase with large density variations where all filaments are mostly aligned. This is another phase transition, which is however much more difficult to quantify.

4.2 Quantitative analysis of the simulation data

The phenomenological findings of the previous section will now be quantified in the following. For that, we performed parameter sweeps over the parameters $\mathcal{U}_b$, l_p, and ρ, for constant

$\mathcal{U}_b$ and varying ρ/l_p (for $\mathcal{U}_b = 0.5\,k_BT$, $1\,k_BT$, $2\,k_BT$, and $4\,k_BT$), and also for constant l_p and varying $\rho/\mathcal{U}_b$(for $l_p = 2\,L$ and $9\,L$). As mentioned above, we only generated a single realization for every parameter combination, which makes it impossible to estimate the error range for our measurements. The limited time-series also prohibits to quantitatively evaluate the fluctuations over time. As we will become apparent, the relevant trends are nevertheless obvious.

4.2.1 Order parameter and angular distribution

The phenomenological overview showed that the system of filaments transitions from a homogeneous gas-like state into a state with large density fluctuations, as ρ increases. In addition, the figures suggest that the filaments become aligned and walk into the same direction. Consequently, the direction of filaments is not only locally aligned, but on a system-size length scale. This section will quantitatively investigate the degree of global directional order of the filaments in the simulation. To that end, we present two different approaches how order can be measured. The goal is to understand whether global directional order coincides with the appearance of the density wave.

Binary collisions of filaments show that filaments on average emerge polarly aligned, from a collision (see 3.2.1). If collisions among the filaments are frequent enough, so that the filament direction is correlated between subsequent collisions, we can expect that many collisions lead at least to a good local alignment of the filaments. Furthermore, as the filament density increases, so does the collision rate, and one can expect that with increasing density the filaments become better aligned. In particular, the frequency of collisions can become so high that the patches where the filaments are aligned grow up to system size. This is what we will refer to as "global order" or just "order" in the following. Global order is particularly easy to measure and easy to interpret. In the following, we present two alternative ways to measure order in our system and quantify our findings.

Polarization as order parameter

A very simple way to determine global order is to measure whether the filaments point into the same direction. Measuring the direction of a filament requires an unambiguous definition of its direction, which is unfortunately not trivial for filaments that may bend. Possible choices are the normalized end-to-end vector $\boldsymbol{r}(0) - \boldsymbol{r}(L)$ or the tangent at some position l along the contour of the filament, $\partial_s \boldsymbol{r}(s)|_{s=l}$. For our model, the tangent method taken at the far end of the head worked best, because it showed the smallest thermal noise. Because each filament is represented by a sequence of beads and not by a continuous line, the tangent on the filament has to be approximated by the normalized vector connecting two subsequent beads. So for a filament with N_b beads at positions $\{\boldsymbol{r}_1, \ldots, \boldsymbol{r}_{N_b}\}$ where its head bead is at position one, we defined the filament direction as

$$\boldsymbol{t} \equiv \frac{\boldsymbol{r}_{N_b-1} - \boldsymbol{r}_{N_b}}{|\boldsymbol{r}_{N_b-1} - \boldsymbol{r}_{N_b}|} \,. \tag{4.4}$$

The average polarization is then given by the length of the tangent vector averaged over the ensemble of filaments,

$$\mathcal{P}(t) \equiv \left| \sum_{i=1}^{N} \boldsymbol{t}_i(t) \right| . \tag{4.5}$$

In order to avoid shot noise, we average the polarization over a period of $1/64$ of our simulation duration or $57L/v_0$. This duration should be read as *57 times travelled the filament length*, which in most cases is much bigger than the persistence length of the persistent random walk. Therefore, the duration is long enough to sample statistically independent realisations in the region of the current state. In summary, the full expression for the averaged polarization is

$$\langle \mathcal{P}(t) \rangle \equiv \frac{1}{\Delta t} \int_{t}^{t+\Delta t} \mathrm{d}s \left| \sum_{i=1}^{N} \boldsymbol{t}_i(s) \right| . \tag{4.6}$$

For the current analysis, we are interested in the steady state of the system. Therefore, Fig. 4.6 shows the observed polarization at the end of the simulation for varying filament density ρ and persistence length l_p. Every data point was acquired from a single realisation of the system, so that the evident noise in the data contains realization artifacts. In order to reduce this error and get an estimate of the noise, several realizations for the same parameter set would be necessary. Although this is a simple procedure, the long compute time of up to $500\,h$ for a single realization prohibits that. Because the trend is already quite clear, this would be a waste of compute time.

Despite the shortcoming of a single realization, it is evident from Fig. 4.6 that there is a transition from an unordered state with a rather small polarization to an ordered state with non-zero polarization. This transition shows virtually no dependence on the persistence length of the filaments for $l_p \geq 2\,L$, which is surprising, because the persistence length determines how long the alignment of two filaments remains stable. Figure 3.6 for example shows that floppy filaments lose their respective orientation much quicker than stiff ones. A possible explanation for this peculiar is that the high-density regions contain many filaments of which only a minor fraction is at the boundary. Because in the high-density region the filaments are aligned, and collisions happen frequently, every deviation is suppressed by collisions with aligned neighbors. Only at the boundary can disalignments lead to a loss of filaments, because when a filament strays away into the low-density phase, it does not get re-aligned. Only for the low range of l_p we find a small dependency in the system polarization. The general picture seems to be that at small persistence lengths the filament density must be higher in order to find an ordered state.

On the other hand the dependence of $\mathcal{P}$ the filament density ρ is much more evident. For every interaction strength $\mathcal{U}_b$ there is a minimal density below which the polar state does not form. This threshold density shifts towards higher densities when $\mathcal{U}_b$ increases.

Kullback-Leibler divergence as order parameter

The polar order parameter as defined in (4.6) is in essence a mean of the angular distribution of the filaments. As such, it is best suited to answer the question “has the system polar order?”. However, there are partially ordered systems for example with mixtures of polarized

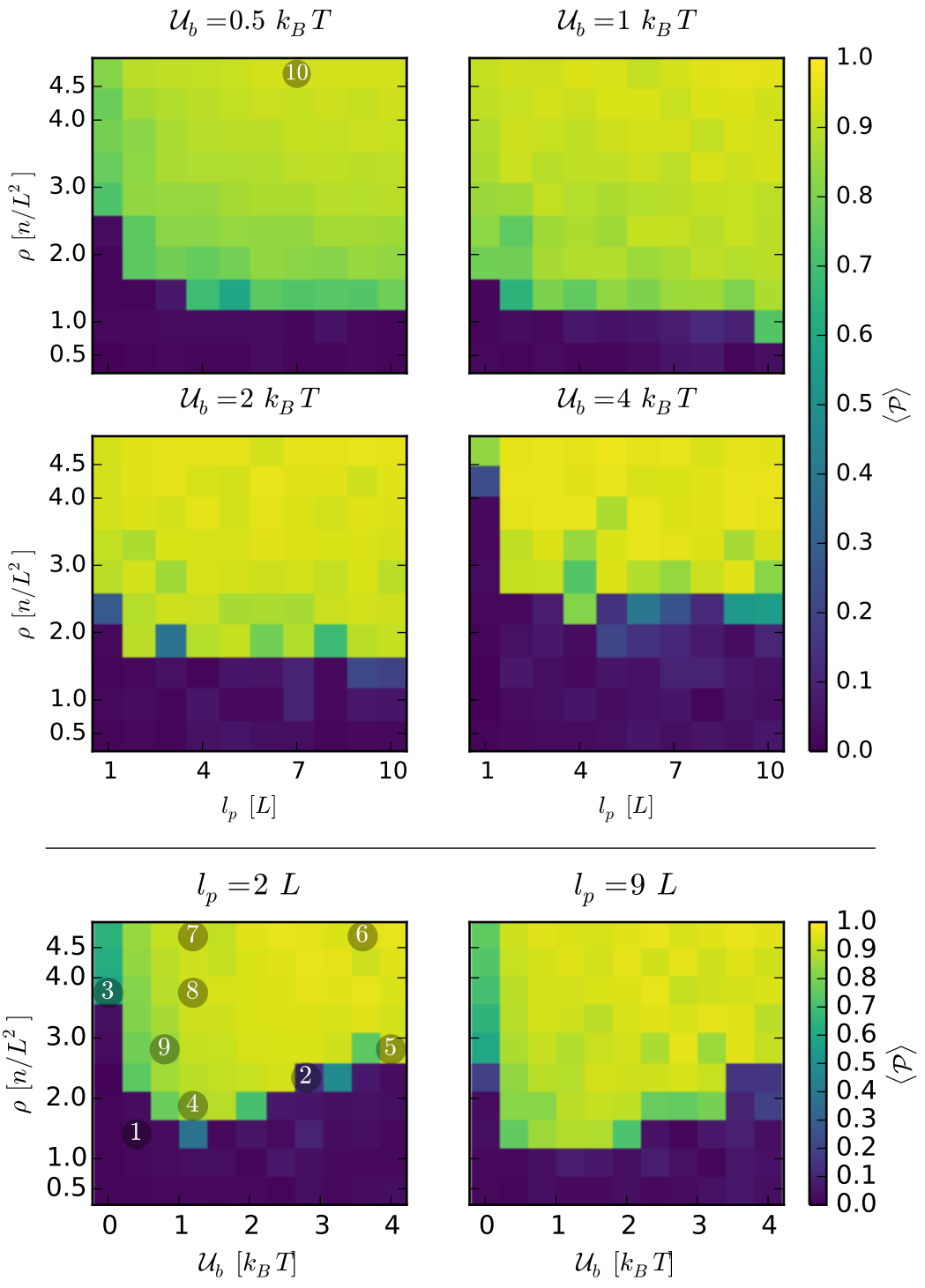

Figure 4.6 | Top panels: The observed polarization as defined by (4.6) scanned over persistence length l_p and filament density ρ. The panels show the same setup for different contact interaction strengths $\mathcal{U}_b$. **Bottom panels:** Analogous to the top panels but for fixed l_p and scanned over interaction strength $\mathcal{U}_b$ and filament density ρ. Because one data point took up to 500 hours compute time, each data point was acquired from only one realisation, such that the evident noise contains realization artifacts. As a consequence, the error range is unknown. The numbers mark the location of the examples from Figs. 4.1–4.5.

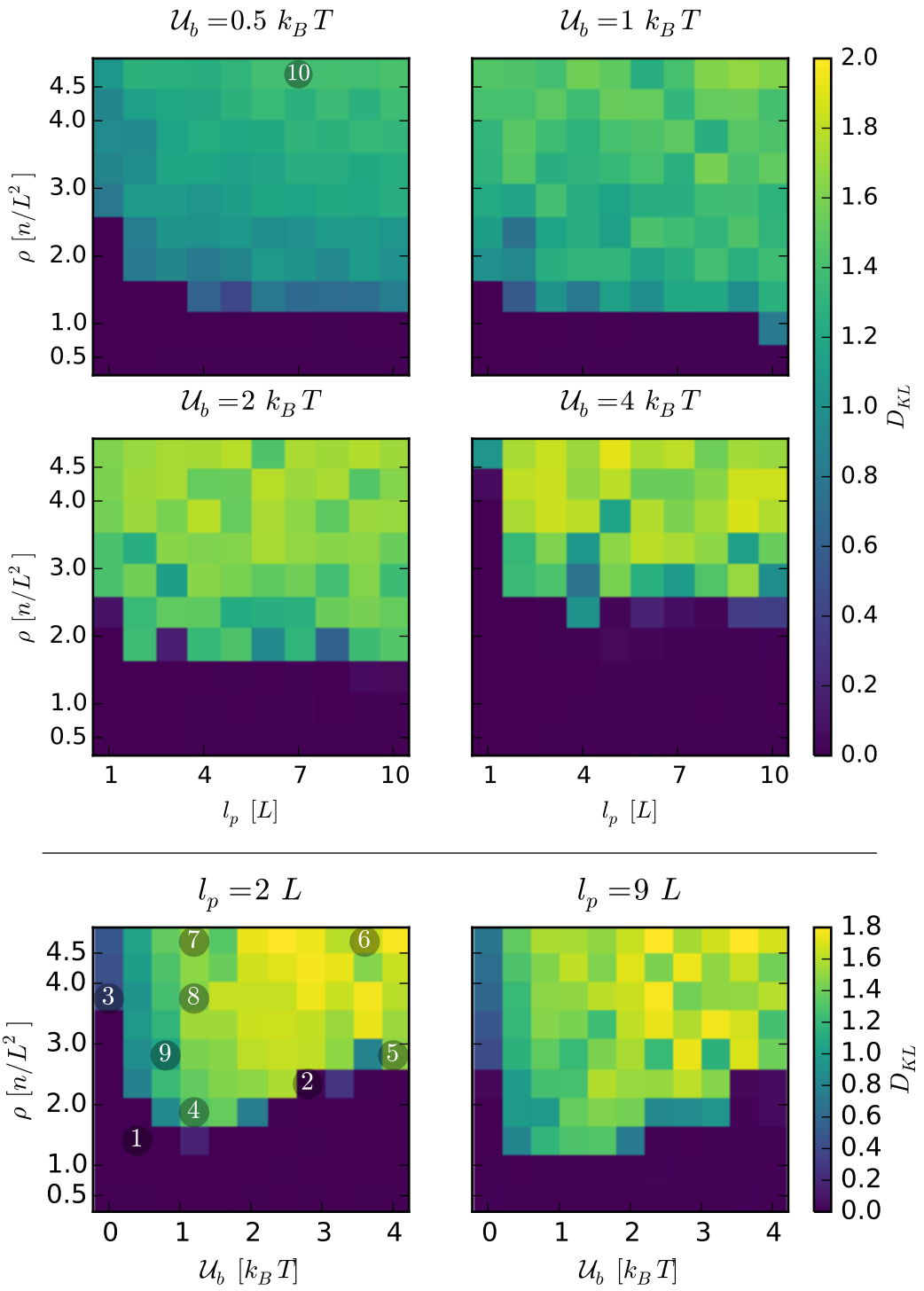

Figure 4.7 | Top panels: The observed Kullback-Leibler divergence of the measured angular distribution from a flat distribution as defined in (4.8) scanned over persistence length l_p and filament density ρ. The panels show the same setup for different contact interaction strengths $\mathcal{U}_b$. **Bottom panels:** Analogous to the top panels but for fixed l_p and scanned over interaction strength $\mathcal{U}_b$ and filament density ρ. Because one data point took up to 500 hours compute time, each data point was acquired from only one realisation, such that the evident noise contains realization artifacts. As a consequence, the error range is unknown. The numbers mark the location of the examples from Figs. 4.1–4.5.

sub-populations[5] which are not well captured by the polarization. In such cases, the question "is the system disordered" is better suited. To overcome these deficiencies of the polarization, we will develop a method where the whole angular distribution is taken into account. The idea is to compare the angular distribution with a flat distribution via the Kullback-Leibler divergence.

In order to do so, we measured the probability distribution $P(\varphi)$ of the angle φ between the filaments and an arbitrary reference axis. If the system is disordered, this distribution should be flat, $P_f(\varphi)\mathrm{d}\varphi = \frac{1}{2\pi}\mathrm{d}\varphi$, which will serve as the reference distribution. A standard measure to test how well a measured distribution matches a is the Kullback-Leibler divergence

$$D_{KL}(P|Q) \equiv \int \mathrm{d}x\, P(x) \log\left(\frac{P(x)}{Q(x)}\right) , \tag{4.7}$$

which can easily be adapted to a discrete setting. One can show that D_{KL} becomes zero only if P and Q are identical, otherwise the Kullback-Leibler divergence is positive. As for the polarization, we averaged the Kullback-Leibler divergence over a period of 1/64 of our simulation duration or $57L/v_0$

$$\langle D_{KL}(t)\rangle \equiv \frac{1}{\Delta t}\int_t^{t+\Delta t} \mathrm{d}s\, D_{KL}\big(P(s)|P_f\big) , \tag{4.8}$$

where $P(s)$ is the measured distribution at time s and P_f the flat angular distribution.

Figure 4.7 shows the Kullback-Leibler divergence for the same simulations as in Fig. 4.6. In agreement with Fig. 4.6 one finds a transition from a disordered state ($D_{KL} \approx 0$) to a non-disordered state ($D_{KL} > 0$) for the same parameters where the polarization $\mathcal{P}$ shows a transition to a polar ordered state. As a consequence, it follows that the system has no intermediate states with ordered subpopulations when transitioning from disorder to polar order. Furthermore, figure 4.7 shows a significant change of D_{KL} in the ordered phase when $\mathcal{U}_b$ is increased. This increase comes from a stronger peaked angular distribution of the filaments which can be explained by the more efficient alignment of filament interactions (see 3.2.1).

In summary, we have shown two different measures to determine the order in the system, where the first – standard – method was based on the average direction of the filaments and the second method took the full angular distribution into account. Using these measures of order, we found a sharp transition from an unordered state at low filament densities into an ordered state as the density was increased. Both measures gave qualitatively identical results, however the Kullback-Leibler based approach gave more information about the peakedness of the angular distribution. Surprisingly, the order transition showed almost no dependence on the persistence length l_p. On the other hand, we found that with increasing $\mathcal{U}_b$ the onset of order shifts towards lower densities, as long as $\mathcal{U}_b < 1k_BT$, but towards higher densities beyond this threshold.

4.2.2 Number fluctuations

The maximization principle of entropy forbids large density fluctuations in systems which are in equilibrium. In other words, a system with large density fluctuation cannot be in

[5] For example, the analogous system with hydrodynamic interactions often has a two sub-regions with different polarizations.

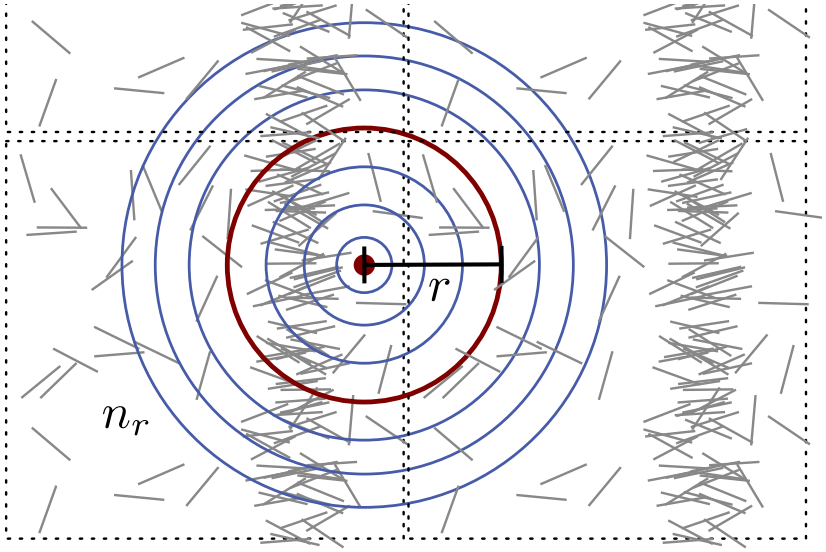

Figure 4.8 | Illustration how the density fluctuations were measured. After choosing a random pivot p (red dot), we count the number of filaments n_r contained in concentric circles around this point with increasing radius r. In every following state, a new random pivot is chosen so that the statistical independence subsequent measurements of n_r increases.

equilibrium. Possible reasons for being out of equilibrium are that the evolution of the system has slowed down so drastically that it appears to be frozen, which happens for example in glasses. Another possibility is that via a steady input of energy the system is actively pushed out of equilibrium, so that the system remains non-static and constantly changing. Clearly, the system of filaments belongs to the second class, because the filaments are actively pushed at all times. Indeed, it is a generic feature of systems where the order parameter is also a velocity to have large density fluctuations [19, 42]. In this section, we will measure density fluctuations of the filaments in our simulation and quantify to what extent they are abnormal.

Density fluctuations can be measured in a robust way by evaluating the number fluctuations on different length scales. The great advantage of the number fluctuations is that they are easy to measure, however there are a few caveats. Figure 4.8 illustrates the process how we measured the number fluctuations. First we choose a random pivot point p. Around this pivot point we then draw concentric circles of increasing radius r and count the number of filaments in each circle n_r. It greatly improves the independence of subsequent measurements of n_r, if the pivot point is chosen randomly. This is because subsequent pivot points can be so far apart that the regions around these points are spatially uncorrelated, and so will be n_r for small r. Furthermore, it is important to count the number fluctuations in circles and not square boxes, as other authors have proposed [42]. The problem with boxes is that they have an orientation and are therefore not isotropic. This orientation can cause artifacts if the underlying density field itself has an orientation as well. As the snapshots of the simulation show (e.g. Figs. 4.2 & 4.3), this is indeed the case for our system.

In equilibrium when the system has a constant well-defined density, density correlations are absent and therefore the placement of the particles is independent of each other. As a consequence, $\langle n_r \rangle$ is proportional to the area of the circle. Likewise, the law of large numbers dictates that the number fluctuations $\Delta n_r^2 \equiv \langle n_r^2 \rangle - \langle n_r \rangle^2$ are proportional to $\langle n_r \rangle$.

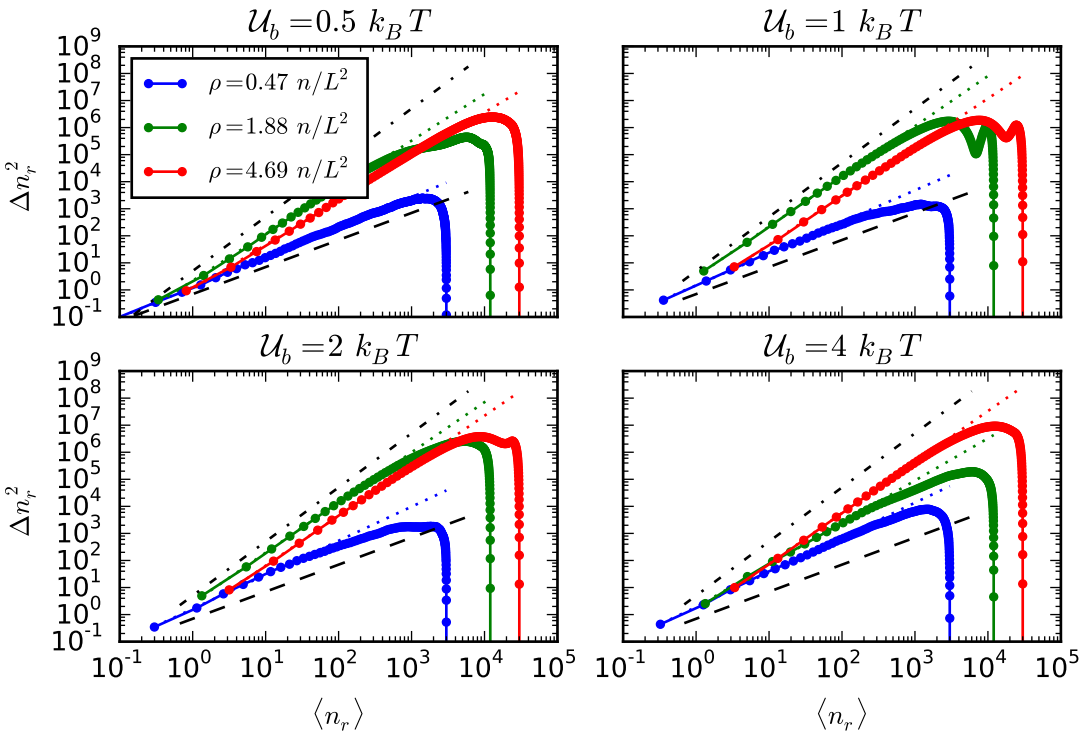

Figure 4.9 | Example for the number fluctuations at different densities (colors) and $\mathcal{U}_b$ as indicated in the panel titles. Linear and quadratic slope are indicated by the dashed and dash-dotted line, respectively. The dotted lines indicate the slope of the number fluctuations in the lower range. The slope bigger than one indicates density fluctuations that are not reconcilable with an equilibrium density distribution. The reason for the vanishing numbers fluctuations at high numbers is that fluctuations become impossible when the radius of the circle approaches system size. Errors are missing due to the fact that the data were taken from a single realisation. The persistence length of the polymers is $l_p = 7\,L$.

Consequently, in order to check whether a system has a defined density, one can measure Δn_r^2 and $\langle n_r \rangle$ and plot these in double-logarithmic scaling. Figure 4.9 shows the number fluctuations for a few selected parameters, which were chosen such that different regimes are displayed. First of all, it is striking that the number fluctuations drop to zero for high $\langle n \rangle$. However, this must necessarily happen, because the number of filaments in the simulation is fixed. As a consequence, number fluctuations are no longer possible when the circle diameter approaches system size.

The low density curve (blue) in Fig. 4.9 is from a region where the order parameters indicated disorder. For that case, the number fluctuations show ordinary scaling with ≈ 1 for all $\mathcal{U}_b$. It follows that the filaments in this phase have not only no polar order, but also no spatial structure. In other words, the filaments are almost randomly distributed, much like in a gas. We say that it is almost randomly distributed, because the scaling exponent is slightly larger than 1[6], especially for $\mathcal{U}_b = 4\,k_B T$. This already hints a non-equilibrium filament distribution.

[6]For completeness, we list the measured scaling exponents: for the low-density case, the fit of the scaling exponent is 1.11, 1.17, 1.26 and 1.27 for $\mathcal{U}_b$ $0.5 k_B T$, $1 k_B T$, $2 k_B T$, and $4 k_B T$, respectively.

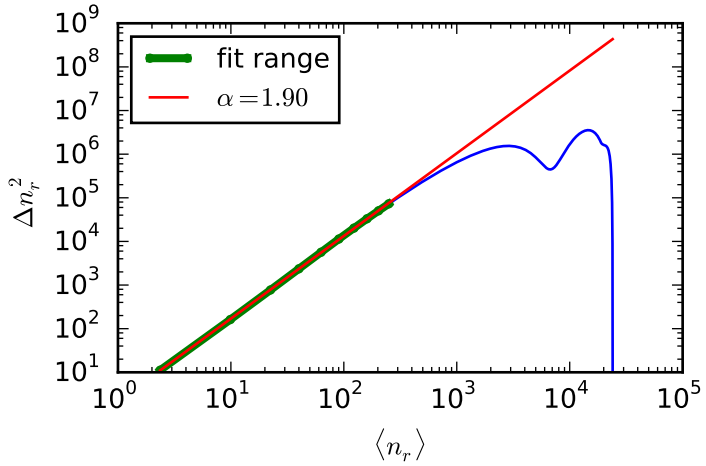

Figure 4.10 | Sample number fluctuation data (blue) with the range highlighted from which the scaling exponent is determined (green). Only the first ten data points are used when fitting with the linear function $b + \alpha\, x$ (red) to the loglog transformed data.

The high density curve (red) is in a region where the polarization is close to one. Here, the number fluctuations reveal a scaling exponent close to two for all $\mathcal{U}_b$, so-called giant number fluctuations[7]. This shows that the system has no flat density profile and indicates the existence of high-density regions with length scales comparable to the system size.

Finally, the intermediate density (green) was chosen such that the polarization jumps from ≈ 1 to ≈ 0 from $\mathcal{U}_b = 2k_BT$ to $\mathcal{U}_b = 4k_BT$. As for the high density, one finds a scaling exponent of ≈ 2 for $\mathcal{U}_b \leq 2k_BT$, and a significantly smaller scaling exponent for $\mathcal{U}_b = 4k_BT$[8]. So this case is a bit peculiar and deserves more explanation. At a closer look, the number fluctuations for $\rho = 1.88\, n/L^2$ and $\mathcal{U}_b = 4k_BT$ indicate a crossover from a ≈ 2 regime to a ≈ 1 regime at $\langle n \rangle \approx 200$. This means that the high-density phase only grows up to a length scale l_c that is much smaller than the system size. Consequently, the number fluctuations show approximately quadratic scaling up to l_c, but above this length scale the high-density clusters are randomly distributed, leading to the ≈ 1 scaling. Unfortunately, the data from these giant number fluctuations are not perfectly reliable, because the linear scaling only appears at rather large numbers where finite-size effects may already play a role. However, this explanation is supported by video material.

Although the discussion so far was insightful, it has only shown a few cases out of a few hundred simulations. Therefore, a more compact presentation of the essential information of the giant number fluctuations is needed. The main information we extract from such a scaling plot is the scaling exponent α, as already mentioned above. We determine α by a linear fit $b + \alpha\, x$ to the loglog-data where every point gets the same weight. In order to avoid any finite size effects which suppress number fluctuations, we used only the first ten data points for the fit (see Fig. 4.10).

[7] For the high-density case, the fit of the scaling exponent is 1.63, 1.80, 1.85 and 1.88 for $\mathcal{U}_b$ $0.5k_BT$, $1k_BT$, $2k_BT$, and $4k_BT$, respectively.

[8] For the intermediate density case, the fit of the scaling exponent is 1.72, 1.85, 1.85 and 1.56 for $\mathcal{U}_b$ $0.5k_BT$, $1k_BT$, $2k_BT$, and $4k_BT$, respectively.

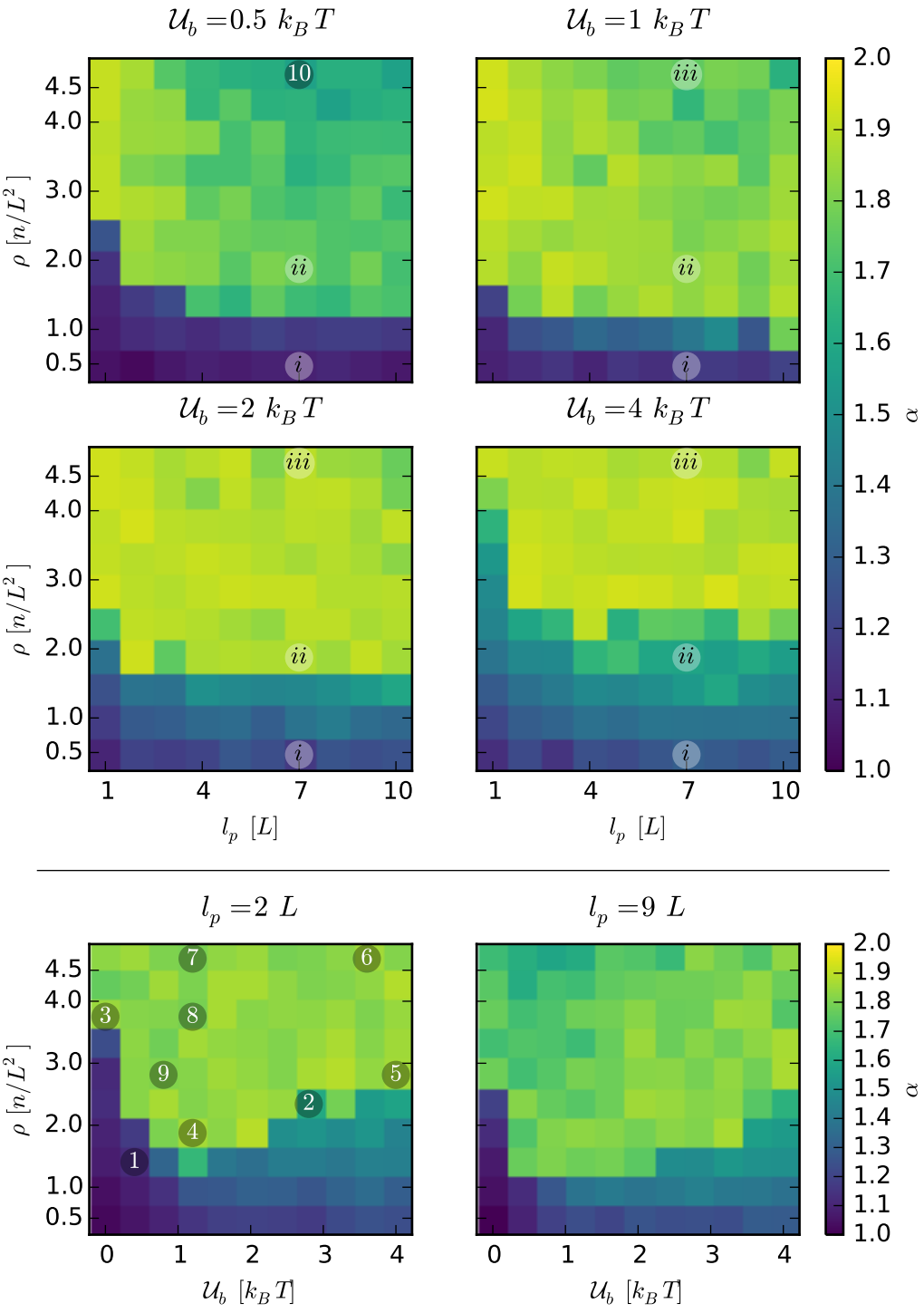

Figure 4.11 | The observed scaling exponents of the number fluctuations scanned over persistence length l_p and filament density ρ. The panels show the same setup for different contact interaction strengths $\mathcal{U}_b$. Because one data point took up to 500 hours compute time, each data point was acquired from only one realisation, such that the evident noise contains realization artifacts. As a consequence, the error range is unknown. The arabic (roman) numbers mark the location of the examples from Figs. 4.1–4.5 (4.9).

Using this procedure, we thus determined the scaling exponents for all our simulations. Figure 4.11 shows the scaling exponents of the giant number fluctuations for the same data as for the order parameters. In agreement with our previous findings, there is a sharp increase of the scaling exponent for the parameters where order emerges, such that the overall appearance is very similar to our previous findings. However, the match is not one-to-one and there are important differences.

First, the distribution of filaments is only random ($\alpha \approx 1$) for very low $\mathcal{U}_b$ and low densities. As the interaction strength increases and with it the alignment efficiency (see 3.2.1), the filaments are no longer randomly distributed, showing in an increase of α. In addition, the scaling exponent increases with the density of the system, as the panel for $\mathcal{U}_b = 4k_BT$ shows best. As for the order parameters, the persistence length of the filaments seems to play a subordinate role, because the scaling exponents are virtually independent of l_p. Only the lowest persistence length $l_p = L$ shows divergent behavior. As a consequence, we follow that even in the disordered state some local clustering is happening for the larger $\mathcal{U}_b$ values.

As a second big difference to previous results, for small $\mathcal{U}_b$ we find in the region of high ρ and large l_p a significant decrease of the scaling exponent. This is rather counter-intuitive because all previous results seem to suggest that high densities and high persistence lengths favor the emergence of high-density polar clusters. The key to understand this is that the high-density region becomes larger for smaller $\mathcal{U}_b$, because the alignment of filaments is less efficient there. With increasing density, the high-density region starts to fill the whole simulation volume, so that a low density region can no longer emerge. However, because the high-density region itself has no constant density, the number fluctuations stay at a level above $\alpha = 1$ but significantly below $\alpha = 2$. Of course this does not change the polar order of the system, therefore the polarization shows no signature of this subtle change.

In summary, the giant number fluctuations are abnormally large with a scaling exponent close to $\alpha = 2$ in almost the entire region where the polarization is non-zero. In contrast to the polarization, the system shows clustering at small scales even in the unordered state, where the scaling of the number fluctuations becomes $1 < \alpha < 2$. This trend with anomalous scaling is most expressed for large $\mathcal{U}_b$, whereas for small $\mathcal{U}_b$ both the scaling exponent α and the polarization show a sudden jump. In addition, we have found downturn of the scaling exponent of the number fluctuations in regions where distinct density waves are impossible, which is in accordance to the more homogeneous distribution of filaments at these parameters (see Fig. 4.5 bottom).

4.2.3 Density in the gas phase

The phenomenological overview in 4.1.2 has shown that the filaments form a high- and low-density region, which we call gas phase. The filament density in this gas phase holds important information about the collective interaction mechanisms. However, estimating the density of the gas phase is difficult, because in order to measure the density in a high- or low-density region, these regions need to be separated first. Because the way in which the two regions are separated has great impact on the result, an unbiased method is of paramount importance. Below, we will develop such an unbiased method to measure the density in the gas phase and apply it to our data.

When trying to separate the high- and low-density regions, one quickly realizes that there is no standard way to cut one region from the other. Further, the resulting density in one cut-out region sensitively depends on the chosen procedure. Therefore, a more robust approach is needed than separating the two regions by some – maybe intelligently – chosen cutoff. In the following, we propose a robust method to measure the density of low-density regions if there is a mixture of low and high density regions. The idea is to partition the simulation volume into equal-sized boxes and evaluating the count statistics of the filaments in the boxes. The aim is to choose the box sizes in such a way that the count statistics for nearly empty boxes is dominated by the low-density region.

Under this pre-condition, it is possible to give an analytic formula for the density in the low-density phase. Consider a density field $\rho(\boldsymbol{x})$, so that we can define a *conditional density* by

$$R(\rho_0) \equiv \frac{\int_V \mathrm{d}V\, \rho(\boldsymbol{x})\, \mathbf{1}_{\rho(\boldsymbol{x})\leq\rho_0}}{\int_V \mathrm{d}V\, \mathbf{1}_{\rho(\boldsymbol{x})\leq\rho_0}} \ , \tag{4.9}$$

which is the *average* density in the region where the *local* density is smaller than ρ_0. In a simulation, this conditional density can be estimated by partitioning the simulation volume into equal-sized boxes of length l_b and counting the contained filaments. Then the conditional density becomes

$$R(n) \equiv \frac{\sum_i n_i \Theta(n - n_i)}{l_b^d \sum_i \Theta(n - n_i)} \ , \tag{4.10}$$

where Θ is the Heaviside-theta function and n_i the number of filaments in box i. Now let's assume that the system has a low-density region with an average number of m filaments per box. In our simulation, this average number m is so small that collisions in the gas phase are rare and therefore we may assume that the filaments in the gas phase are in equilibrium. Consequently, we may assume that the average over a single state of the simulation approaches the ensemble average, if the simulation volume is large. Hence it follows that the ratio in (4.10) approaches the probability to find a box with n_i filaments. This probability is a classic application of the Poisson distribution, so that (4.10) becomes

$$R(n|\lambda) = \frac{\sum_{i\leq n} i\mathcal{P}(i|\lambda)}{l_b^d \sum_{i\leq n} \mathcal{P}(i|\lambda)} \ , \tag{4.11}$$

where $\mathcal{P}(i|\lambda)$ is the Poisson distribution with mean λ. The great advantage is that this expression has an analytic solution:

$$R(n|\lambda) = \lambda - \frac{e^{-\lambda}}{E_{-n}(\lambda)} \ , \tag{4.12}$$

where $E_n(x)$ is the exponential integral function[9].

In the limit, $R(n)$ approaches λ for $n \to \infty$ and 0 for $n \to 0$. Furthermore, we can expect that $R(n = \lambda) \approx \lambda$ if the number of filaments per box is large, because a surplus of filaments becomes rather unlikely then. Therefore, we expect that the function $R^*(n^*|\lambda) \equiv R(\lambda\, n^*|\lambda)/\lambda$ has a crossover to a constant value at ≈ 1, which becomes sharper for increasing λ. This is indeed the case, as Fig. 4.12 shows.

[9]The exponential integral function is defined by $E_n(z) \equiv \int_1^\infty \mathrm{e}^{-z\,t} t^{-n} \mathrm{d}t$ and is implemented in common math libraries.

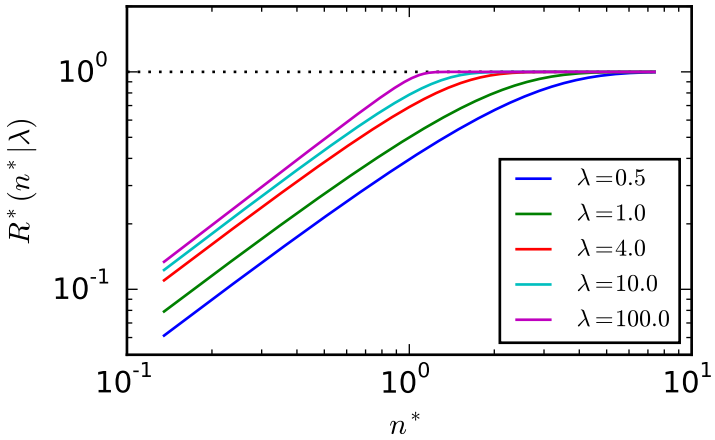

Figure 4.12 | Rescaled conditional density function as defined in (4.12) for various λ. As expected, the conditional density approaches λ for $n^* \approx 1$, if the average number of filaments per box, λ, becomes larger. Furthermore, one can show that the scaling exponent for $n^* \ll 1$ is approximately 1.

In a simulation, we can measure $R(n)$ so that we need to invert equation (4.12) for λ. Unfortunately, this is not possible for arbitrary n, however there are simple analytic expressions for the first few values of R,

$$R(1) = \frac{\lambda}{1+\lambda} \qquad R(2) = \frac{2\lambda(1+\lambda)}{2+\lambda(2+\lambda)} \,. \tag{4.13}$$

For these two values, analytic expressions for λ are therefore easily found,

$$\lambda = \frac{R(1)}{1-R(1)} \qquad \lambda = \frac{1-R(2)-\sqrt{2-\big(R(2)-1\big)^2}}{R(2)-2} \,. \tag{4.14}$$

These two expressions can be used as bias-free estimators for the density in the low-density phase, if the high-density phase only contributes little to the empty, single, or double occupied boxes. The great advantage of this method is that it does not depend on an arbitrary choice of some cutoff, but only on the box size. For proper results, one therefore has to make sure that the high-density phase does not contribute to the nearly empty boxes. Consequently, the box size l_b must be large enough to avoid this but still small enough to ensure a large number of nearly empty boxes. This number depends both on the density of the low-density phase and the simulation volume, therefore it is essential that the simulation volume is large.

Of course, nothing would be won if equations (4.14) would yield different results for different box sizes. We therefore generated mock data with densities in the same range as our simulation and compared the predicted density with the actual one. Thus we found that for box sizes in the range from $\approx 1\,L$ to $\approx 4\,L$[10] the predicted density differed from the actual one by only $\approx 1\%$. Furthermore, we found that the expression for $R(2)$ gave in general more accurate results than the expression for $R(1)$. Therefore, we used a box size of $2\,L$ in the following and obtained the density by inversion of (4.14) for $R(2)$.

[10] These box sizes correspond to a number of 6400 and 400 boxes, respectively.

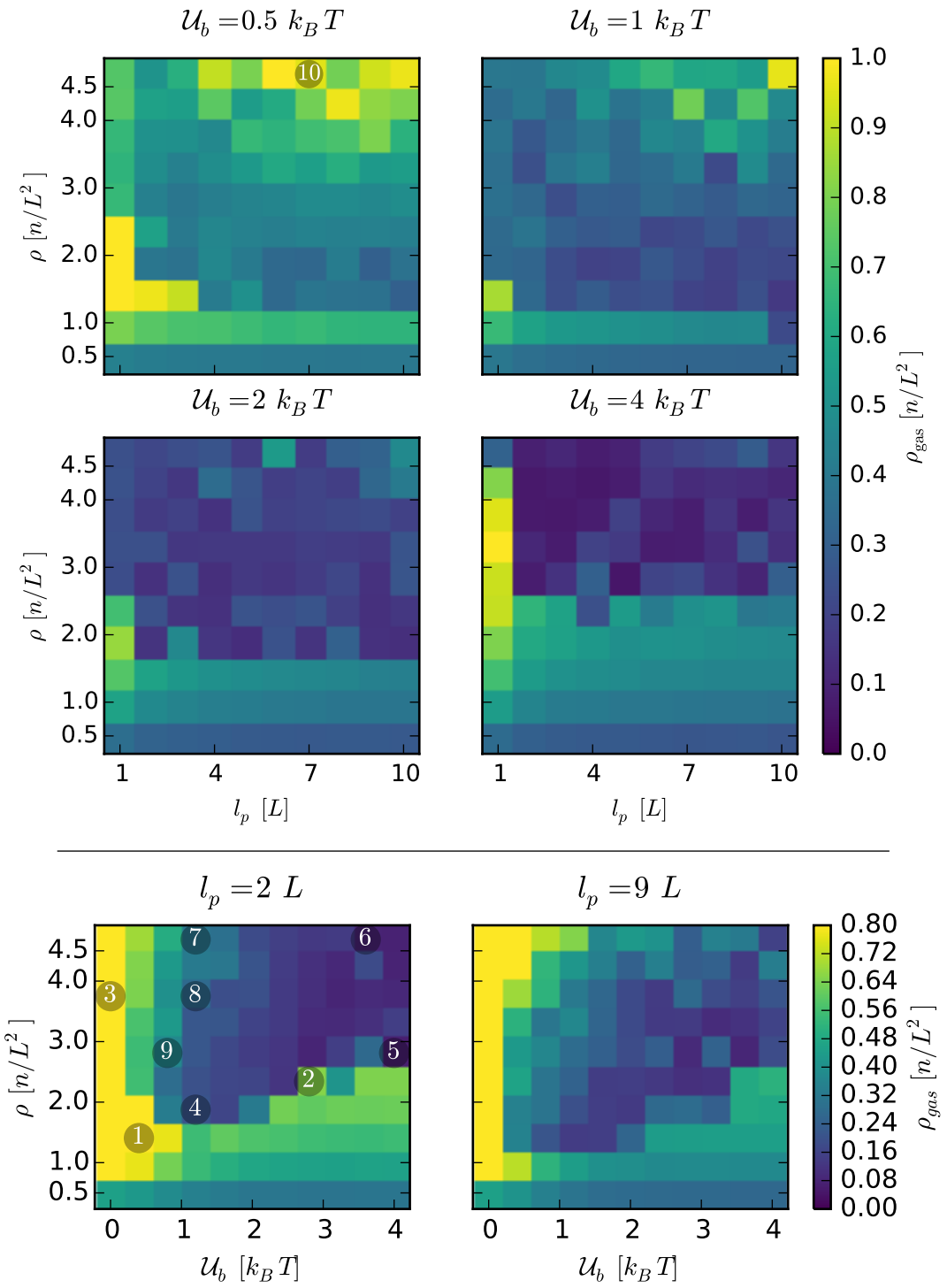

Figure 4.13 | Top panels: The density in the gas phase determined via (4.14) scanned over persistence length l_p and filament density ρ. The panels show the same setup for different contact interaction strengths $\mathcal{U}_b$. **Bottom panels:** Analogous to the top panels but for fixed l_p and scanned over interaction strength $\mathcal{U}_b$ and filament density ρ. Because one data point took up to 500 hours compute time, each data point was acquired from only one realisation, such that the evident noise contains realization artifacts. As a consequence, the error range is unknown. The numbers mark the location of the examples from Figs. 4.1–4.5.

Figure 4.13 shows the measured filament density in the gas phase scanned over persistence length and filament density for different $\mathcal{U}_b$. All panels show a significant drop of ρ_{gas} at the emergence of order and large clusters (see also figs. 4.10 & 4.6). For densities below this transition, ρ_{gas} increases, although the increase of ρ_{gas} remains far below the total filament density ρ. This is in accordance with the increase of the scaling exponent of the number fluctuations, because filament clustering on small scales reduces the gas phase density and likewise increases the number fluctuations. As the clustering is more stable and thus stronger for larger l_p, the increase of ρ_{gas} with the total density ρ is slightly larger for small l_p.

Interestingly, the gas phase density is approximately constant in the whole ordered region, except for parameters with low $\mathcal{U}_b$ and high l_p. The increase of ρ_{gas} in this region is connected to the decrease of the scaling exponent of the number fluctuations there. Above, we already explained that the high-density phase becomes system spanning in this region, so that the disordered gas phase no longer exists. Hence, the method of measuring the density of a low-density phase must break down here. Our results indicates that the lowest density increases which means that overall the system shows smaller density variations. Yet this has to be taken with a grain of salt, because the high-density region is ordered and therefore not gas-like, so that the equilibrium assumption on which our method builds is no longer fulfilled. Apart from this peculiar region however, the density in the gas phase is surprisingly low and flat. In particular, ρ_{gas} stays constant even if the total density ρ is increased, which allows to determine $\rho_{gas} = 0.22 \pm 0.01 \left[n/L^2\right]$ ($\mathcal{U}_b = 2k_BT$) and $\rho_{gas} = 0.14 \pm 0.01 \left[n/L^2\right]$ ($\mathcal{U}_b = 4k_BT$). It follows that all the added filaments are accumulated in the ordered high-density phase which therefore grows in size, whereas the low-density region shrinks. The mechanism how this works is that the density wave has a direction and periodically sweeps the system from one side to the other, thereby hoovering up all filaments in the gas phase. The density in the gas phase is therefore only replenished by filaments that are lost at the trailing end end of the density wave. It is reasonable to assume that the rate of lost filaments at the trailing end only depends on the filament properties and is therefore independent of the total filament density. This explains why the density in the gas phase is independent of the total density.

However, ρ_{gas} also shows little to no dependence on l_p, as far as the noisy data allow this conclusion. We have shown that the alignment characteristics depend only very weakly on the persistence length l_p, whereas the persistence length of the random walk L_p is approximately equal to l_p. Therefore, the independence of ρ_{gas} on l_p shows that aligning collisions in the dense phase and its tail are much more frequent than L_p/v_0, otherwise it should make a difference how long L_p is. If collisions are frequent, ρ_{gas} may however depend on the polarity of binary collisions. However, Fig. 3.8 shows, if at all, little dependence of the alignment for two filaments if the collision angle is small. As filament collisions in the ordered phase happen frequently, the incoming collision angel Θ_{in} is usually small, so that l_p makes virtually no difference. Consequently, also the density of the gas phase becomes virtually independent of l_p.

In summary, we have developed an unbiased estimator for the density in the gas phase, which is based on the count statistics of filaments in a partition of the simulation into equal-sized boxes. Applying this method to our data showed that ρ_{gas} increases with ρ as long as no density wave has formed. However, as soon as the density wave appeared, the gas density dropped drastically and remained independent of both ρ and l_p as far as our data allow that

conclusion. On the other hand, ρ_{gas} drops drastically with increasing $\mathcal{U}_b$. These observations allowed the conclusion that the gas density is determined by the alignment efficiency of binary filament interactions.

4.2.4 Clustering of the filaments

The density fluctuations in the simulation have shown (see 4.2.2) that the system has large density fluctuations which are impossible in equilibrium. Although the number fluctuations are a robust method to measure out-of-equilibrium density fluctuations, they are a rather crude measure which is most appropriate for experimental data. For a simulation where data acquisition is no obstacle, the clustering behavior can be examined in more detail. This section will therefore quantitatively examine the clustering behavior of the filaments in our system. For that, we establish a procedure how to determine the cluster sizes at any point in time and thus measure the cluster size distribution. In addition, we will present equations which qualitatively reproduce the features of the measured cluster size distribution.

The first step in this analysis is to define a unique cluster set for every given snapshot of the simulation. This requires to partition the set of filaments $F = \{f_1, f_2, \ldots, f_n\}$ into disjoints subsets $\mathcal{C}_i$ which we call clusters, such that the following conditions are met,

$$F = \mathcal{C}_1 \cup \mathcal{C}_2 \cup \ldots \cup \mathcal{C}_m \qquad\qquad \mathcal{C}_i \cap \mathcal{C}_j = \emptyset \quad \forall i \neq j \ .$$

Further, we call two filaments f_1 and f_2 clustered, if they are in the same cluster $f_1, f_2 \subset \mathcal{C}$. This partition into clusters form a new set,

$$C = \{\mathcal{C}_1, \mathcal{C}_2, \ldots, \mathcal{C}_m\} \ , \tag{4.15}$$

which we call cluster set. Of course, this partition has to be built in a way that it corresponds to our understanding of clusters. Here, we are mainly interested in spatial clusters, that is, filaments should be clustered if their distance is smaller than some cutoff distance $d(f_1, f_2) \leq r_c$. However, even if filaments are close together, we would not consider them clustered, if they are walking into different directions and are thus close together only by chance. In addition to the spatial criterion, we therefore also require that the angle between two filaments is below some cutoff angle $\sphericalangle(f_1, f_2) \leq \alpha_c$.

These criteria enable us to define a unique cluster set. For any two filaments f_1 and f_l in the same $\mathcal{C}_i$, we require that there exists a sequence of filaments $f_1, f_2, \ldots, f_l$ such that subsequent filaments fulfill our clustering criteria. We call this property of $\mathcal{C}_i$ path-connected. Furthermore, for every filament f_i in $\mathcal{C}_i$ we require that no other cluster $\mathcal{C}_j$ contains some filament f_j such that f_i and f_j fulfill the clustering criteria. In other words, f_i may not be path-connected to any filament in any cluster other than $\mathcal{C}_i$. It is easy to see that this defines a unique cluster set, because assume there are two cluster sets C and B. Then there has to be at least one cluster $\mathcal{C}_i \in C$ that is not in B and without loss of generality we may assume that $|\mathcal{C}_i| > 1$. Therefore there exists a pair of filaments $\{f_1, f_l\} \subset \mathcal{C}_i$ which are in different clusters in B, $\mathcal{B}_1$ and $\mathcal{B}_l$. Because f_1 and f_l are clustered in $\mathcal{C}_i$, there exists a sequence of filaments $f_1, f_2, \ldots, f_l$, such that along the sequence every filament fulfills the clustering criteria. Some part of this sequence $f_1, \ldots, f_b$ has to be contained in $\mathcal{B}_1$, but it has to be broken somewhere, otherwise f_l would be in $\mathcal{B}_1$. Consequently, $f_{b+1} \ni \mathcal{B}_1$ although f_b and

f_{b+1} fulfill the clustering criteria, which is a contradiction. Therefore, the partition into the cluster set C must be unique.

The spirit of this definition is that a filament belongs to a cluster, if there is at least one filament in this cluster which fulfill the clustering criteria. This makes sense, because a filament can only sense its immediate environment, however it has the drawback that big blobs of filaments can be connected via a thin thread of filament, like a bridge. It depends on the questions one tries to answer if this is a concern or not, for our purposes this is fine. However in such a situation with a bridge, the noise in our system often leads to flickering cluster partitions, because it may happen frequently that the path over the bridge fulfills the clustering criteria or not. So in essence, this problem arises if filaments were clustered but then no longer fulfill the clustering criteria. Hence, we make use of the sequence $C_0, C_1, \ldots, C_i$ of previous cluster sets and when building C_{i+1} we relax the clustering criteria for two filaments, if they were already clustered in C_i. The uniqueness of the partition into a cluster set follows along the same line of arguments as above, but one has to keep in mind that it also depends on the sequence of cluster sets, so that individual states cannot be processed independently. For the relaxed clustering criteria we use both distance and angle again, but the cutoff thresholds are higher. It is clear that these cutoff values are to some extent arbitrary, and the resulting cluster partition depends on the particular cutoff values. Therefore, it is important to carefully choose the cutoff values that make sense. In practice, a rather strict alignment cutoff and a distance cutoff in the order of the filament length have proven to work best. All cluster partitions below were constructed with a (relaxed) cutoff distance $\frac{2}{3}L$ ($1\,L$) and a (relaxed) angle of 10° (15°).

In the following, we describe the procedure how the cluster set is built in practice. Given cluster set C_i of the previous step, we start with an initial cluster set $C = \{\{f_1\}, \{f_2\}, \ldots, \{f_n\}\}$, which already fulfills the disjointedness and path-connectedness that is required for the cluster set. What is missing is the requirement that different $\mathcal{C}_i$ are *not* path-connected. To achieve this, two clusters $\mathcal{C}_i, \mathcal{C}_j \in C$ are joined, if there exists an $f_i \in \mathcal{C}_i$ and $f_j \in \mathcal{C}_j$ which fulfill the strong clustering criteria, or the relaxed ones, if $\{f_j, f_i\} \subset \mathcal{C}_k \in C_i$ for some k. This joined cluster is disjoint to all other clusters in C and also path-connected, because any two filaments in $\tilde{f}_i, \tilde{f}_j \in \mathcal{C}_i \cup \mathcal{C}_j$ can be connected via f_i and f_j which are connected. This joined cluster replaces $\mathcal{C}_i$ and $\mathcal{C}_j$ in C, and it is ensured that the disjointedness and path-connectedness remains valid for the updated cluster set C. This procedure is repeated, until no connected pairs of filaments in two different clusters can be found, so that the remaining requirement of the cluster partition is fulfilled. The so-constructed cluster set C becomes the next C_{i+1}.

In summary, the above procedure defines an algorithm to partition the filaments into a set of disjoint clusters. The above proof shows that the partition is in fact unique. The algorithm is also efficient with a complexity linear in the number of filaments, if properly implemented. In the following, we will discuss particular features of this cluster set.

Largest cluster

The cluster partition can answer important non-trivial questions about our system. A very fundamental question for example is, how many filaments are in the largest high-density region in our system. Because our clustering criteria also require an alignment of the filaments in a cluster, this question is related to the polarization. With clusters, on the other hand, the

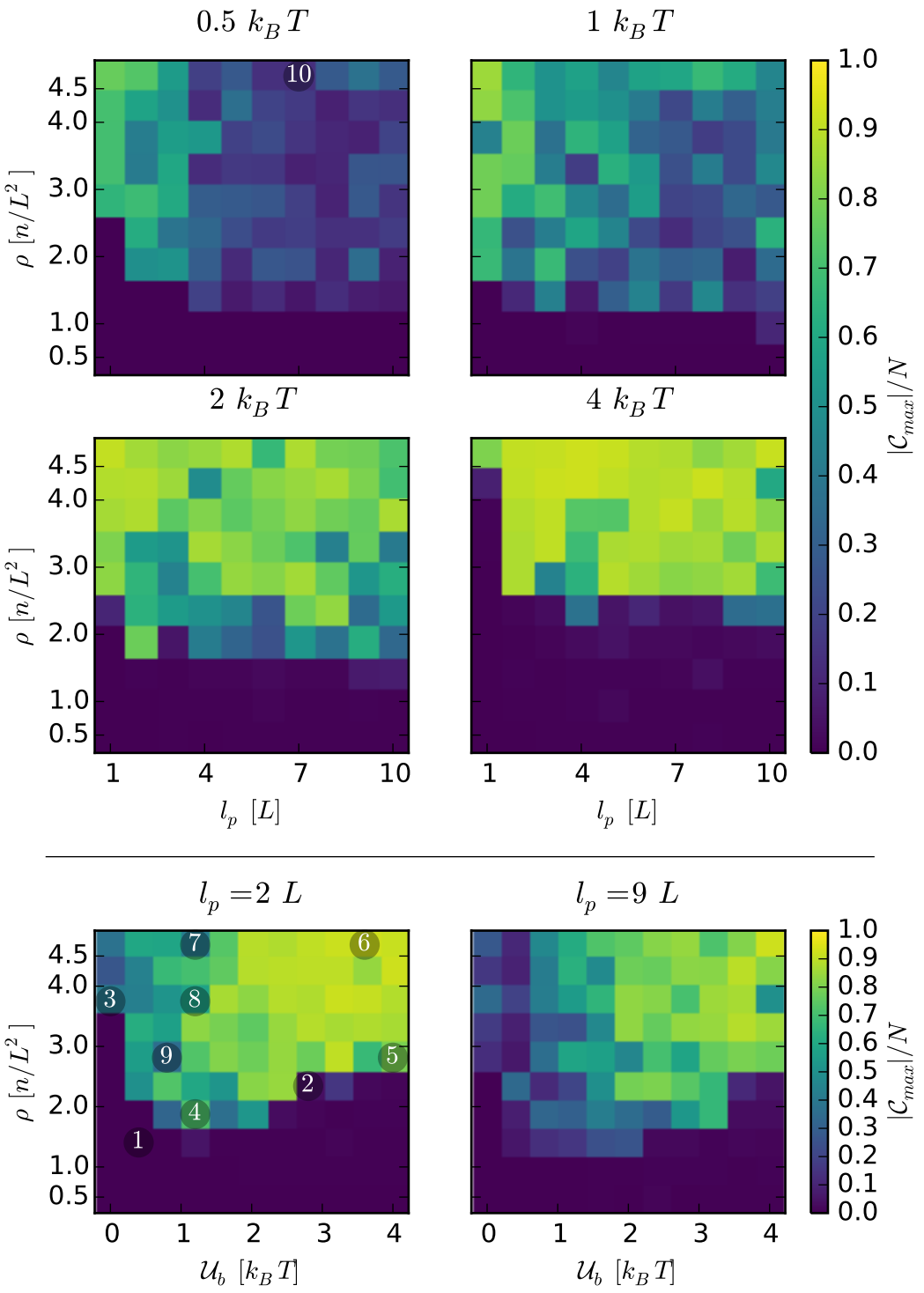

Figure 4.14 | Top panels: The relative cluster size of the largest cluster in the system, $|C_{max}|/N$, scanned over persistence length l_p and filament density ρ. The panels show the same setup for different contact interaction strengths $\mathcal{U}_b$. **Bottom panels:** Analogous to the top panels but for fixed l_p and scanned over interaction strength $\mathcal{U}_b$ and filament density ρ. Because one data point took up to 500 hours compute time, each data point was acquired from only one realisation, such that the evident noise contains realization artifacts. As a consequence, the error range is unknown. The numbers mark the location of the examples from Figs. 4.1–4.5.

emphasis is on being connected and high-density and not only aligned. As a consequence, the largest cluster size can be small even if the polarization is large, for example if the filaments are distributed homogeneously but all point into the same direction. In the following, we will investigate the question, if a large polarization necessarily implies the existence of a large cluster.

With the definition of our cluster size distribution from above, it is straight-forward to extract the size of the largest cluster, $|C_{max}|$. Yet we have to expect that the cluster size of the largest cluster also depends on the total number of filaments N, so that it makes no sense to compare cluster sizes at different densities. To compensate for this undesired dependence, we rescale the cluster size by the total number of filaments, $|C_{max}|/N$. Thus, this relative cluster is a measure for the fraction of filaments contained in the largest cluster which is independent of the filament density ρ.

Figure 4.14 displays the relative cluster size of the largest cluster for various parameter combinations. A first observation is that $|C_{max}|/N$ can be close to one which means there is a huge cluster that contains nearly all filaments. This trend is most expressed for large $\mathcal{U}_b$, for which the alignment of filaments is most efficient, but less pronounced for small $\mathcal{U}_b$. Considering that the density in the gas phase changes by almost one order of magnitude from $\mathcal{U}_b = 0.5k_BT$ to $\mathcal{U}_b = 4k_BT$, this dependence makes perfect sense. Of course, the relative size of the largest cluster is not always large. Concretely, wherever the polarization is small, also the size of the largest cluster must necessarily be small, as the low-ρ region in Fig. 4.14 shows. If this were not the case, a considerable fraction of the filaments would form an orientated structure whose contribution to the polarization cannot be balanced by the remaining filaments. Therefore, the polarization must be non-zero which is a contradiction. On the other hand, a large polarization does not imply that the largest cluster must contain most of the filaments. Indeed, Fig. 4.14 shows a rather small fraction of filaments in the largest cluster for large l_p and ρ. In contrast, Fig. 4.6 shows a very large polarization in that region. There are two possible explanations for this anomaly; either the density of the ordered phase is too low so that the clustering criteria split the density wave into several clusters, or there are multiple distinct density waves in the system. A visual inspection of the data shows that both situations apply in in different regions (e.g. Fig. 4.5 bottom). Specifically, we find multiple waves for low ρ which become more and more elongated as ρ grows. At some point, when ρ is large enough, the density waves start to overlap, so that nearly all filaments point into the same direction which explains the large polarization[11]. However, the density in this region varies drastically, so that the filaments form no coherent cluster according to our definition. In general, multiple density waves seem to be favored at large l_p and we find them almost exclusively at low $\mathcal{U}_b$.

Overall, the cluster size of the largest cluster shows a behavior that is in good agreement with our previous findings. In the region where the polarization is large, we found for $\mathcal{U}_b \gtrapprox 1k_BT$ that a large cluster forms which accumulates nearly all filaments in the system. We can identify this giant cluster as the density wave which was described in 4.1.2. In contrast at low $\mathcal{U}_b$, the fraction of filaments in the largest cluster only reaches 30% of the filaments. This is in perfect agreement with 4.1.2 where we found that multiple distinct density waves form in this parameter region.

[11] Note that the giant number fluctuations also showed an anomaly for these parameters, which had the same reasons.

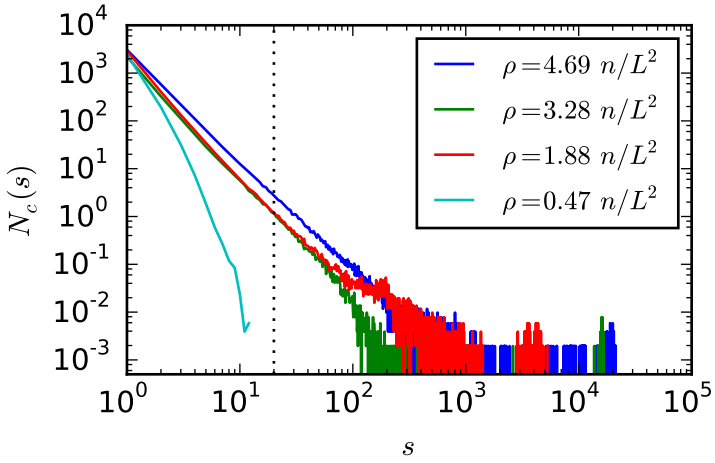

Figure 4.15 | Cluster size distribution for $l_p = 2\,L$, $\mathcal{U}_b = 1 k_B T$, and different densities. The data is shown in loglog-scale, so that it becomes evident that the cluster size distribution drops approximately algebraically. At high densities where the ordered phase forms, the size distribution shows an outlier at very high cluster size which corresponds to the orientated density wave. To determine the power law exponent, only cluster sizes up to 20 are used (dotted black line).

Cluster size distribution

Instead of considering just a single cluster, the cluster set as defined in 4.2.4 can also yield a distribution of cluster sizes. This cluster size distribution allows to address the question, how the clustering propensity of the filaments changes with the simulation parameters. In particular, it tells how the balance of large and small clusters changes. In the following, we will discuss typical cluster size distributions as they are found in our simulation and compare them to an analytic model for the cluster size distribution.

The abundance of clusters with a specific size s is easily calculated by counting,

$$N_c(s|C_i) \equiv \left| \{\mathcal{C} \,|\, \mathcal{C} \in C_i \wedge |\mathcal{C}| = s\} \right| . \tag{4.16}$$

Similarly to other observables from above, we averaged the cluster size distribution for over a duration of 1/64 of our simulation duration and only show data at the final state of our simulation. Figure 4.15 gives an example of the cluster size distributions for arbitrarily chosen parameters. The plot shows a few notable features which are generic for our measured cluster size distributions: First, because the plot has loglog scaling, it reveals that the cluster number distribution approximately drops algebraically with the cluster size up to intermediate cluster sizes. Second, this scaling only applies at large enough filament densities, because for $\rho = 0.47\, n/L^2$ the cluster size distribution deviates from the algebraic scaling. Third, very large cluster sizes are much more abundant than a strict algebraic scaling would predict In particular, there are extreme outliers which correspond to the density wave which encompasses a major fraction of all filaments. Furthermore, some cluster size distributions show a kink at intermediate cluster sizes, for example at 100 for a density $\rho = 1.88\, n/L^2$. These features can be explained by a clustering model first presented by Peruani et al. [95].

Theoretic model for the cluster size distribution Inspired by Master equation approaches to understand nucleation in gases, Peruani et al. found a simplified model for cluster growth [95, 96], which we outline in the following. Take the average number of clusters with size i at time t, $n_i(t)$, so that free filaments are just clusters of size 1. An individual cluster can either shrink by losing filaments, or grow by colliding with another cluster and absorbing its filaments. The loss of filaments can either come from a splay of the whole cluster, so that the whole cluster breaks up at once, or by losing individual filaments. Because splay can also be viewed as a repeated loss of single filaments on a faster time-scale, we assume that a cluster only shrinks by losing one filament at a time. A filament breaks away from its cluster, if its direction of movement is not aligned with its cluster and therefore with its neighboring filaments. Because a single filament in the interior of a cluster is quickly re-aligned by collisions with its neighbors, it follows that only filaments at the boundary of the cluster can effectively leave the cluster. As a consequence, the rate B_i at which filaments in a cluster of size i leave the cluster is proportional to the cluster circumference, so that we approximate $B_i \propto \sqrt{i}$. Similarly, the collision rate $A_{i,j}$ of two clusters can be estimated by the collision rate of two spherical disks, which has been shown to be proportional to the relative speed and the sum of the disk radii [97]. In fact, not every collision leads to a merger of two clusters, but for simplicity we can assume assume that a constant fraction of collisions results in a merger, so that $A_{i,j} \propto (\sqrt{i} + \sqrt{j})$. Of course, the collision rate A also depends on the relative cluster speed v_0 and quadratic on the overall density of clusters. We now make the simplifying assumption that cluster collisions are only binary, so that the time evolution of the average cluster size n_i is given by

$$\begin{aligned}
\dot{n}_1 &= 2B_2 n_2 + \sum_{k=3}^{N} B_k n_k - \sum_{k=1}^{N-1} A_{k,1} n_k n_1 \\
\dot{n}_N &= -B_N n_N + \frac{1}{2} \sum_{k=1}^{N-1} A_{k,N-k} n_k n_{N-k} \qquad (4.17) \\
\dot{n}_j &= B_{j+1} n_{j+1} - B_j n_j - \sum_{k=1}^{N-j} A_{k,j} n_k n_j + \frac{1}{2} \sum_{k=1}^{j-1} A_{k,j-k} n_k n_{j-k} \quad \text{for } j = 2, \ldots, N-1 \ , \qquad (4.18)
\end{aligned}$$

where N is the total number of filaments. Here, we are only interested in the stationary state of this equation system, therefore the absolute value of the rates $A_{i,j}$ and B_k are irrelevant, because they only affect how fast the equilibrium is reached. On the other hand, the relative magnitude of of the rates determines the balance of clusters breaking up (B) and re-forming due to mergers (A). Hence, by transforming time to an unknown time-scale, the rates become

$$B_k = \sqrt{k} \qquad\qquad A_{i,j} = P\left(\sqrt{i} + \sqrt{j}\right) \ , \qquad (4.19)$$

where P is the ratio of the rates of cluster merging and disassembly. In principle, the assembly ratio P can be estimated from microscopic filament parameters, however these microscopic parameters are not well-known for our filament model. Therefore, a quantitative comparison of the predicted cluster size distribution makes no sense and we focus on the question, whether this model describes cluster formation qualitatively.

These equations have to be integrated numerically for a duration that is long enough so that the fixed point of the equation system is reached. Numerical accuracy and computing

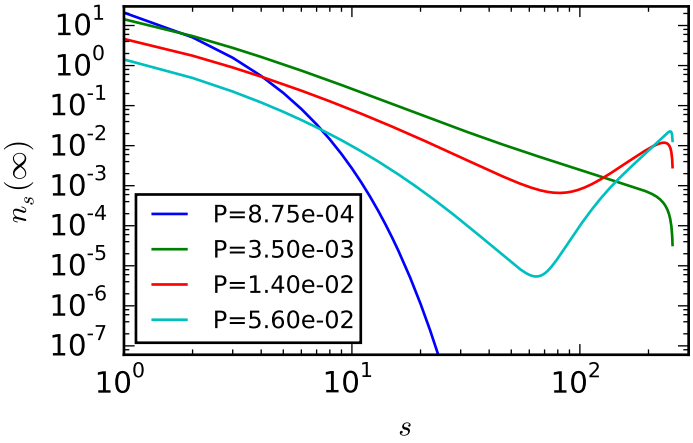

Figure 4.16 | Fixed point solutions of the equations (4.18) for $N = 256$ and various assembly ratios P. The equation system was integrated numerically using Mathematica.

power limit the feasible range of the number of filaments to $N \approx 250$, which is twice as much as was possible at the time of Peruani's original work. Still, this is substantially smaller than the number of filaments in our simulation (up to 30 000), however we find that the solutions for smaller N are qualitatively similar to the one at large N. Therefore, assuming that the behaviour does not change drastically up to $N = 10^4$, we may assume that the comparison with our data is nevertheless valid.

Figure 4.16 shows the so-obtained cluster size distribution for different assembly ratios P. At small assembly ratio P, the filaments can not cluster fast enough, before the loss of filaments on the surface destroys the cluster (blue curve). In that case, the cluster size distribution is not a power law, and we find a similar behavior in our data at small densities. At increased P, the cluster size distribution then shows a power law that deviates only at very large cluster sizes (green curve). Upon further increase of the assembly ratio, the power law remains only valid up to intermediate cluster sizes of about 50 filaments, and for very large cluster sizes the model predicts an excess of clusters (red curve). For even higher P, the transition from power law to excess of clusters shifts towards smaller cluster sizes (turquoise curve).

Comparison the measured cluster size distribution and the theoretic model A comparison of the theoretic model with the data shows strikingly similar features (Figs. 4.16 & 4.15). As mentioned above, the assembly rate grows with the total filament density, because the density of clusters increases alike. Consequently, the low-density data correspond to small P values, whereas the high density data correspond to larger P values. In that regard, the model predictions are in good agreement with the observed cluster size distribution, despite the considerable simplifications of the model. However, there are a few discrepancies in the qualitative behavior. For example, our data do not show the steep increase in the cluster abundance for large cluster sizes, as predicted by the model. Deviations at large cluster sizes have to be expected because the density wave has peculiar properties compared to smaller clusters. To understand this, consider a square-shaped cluster with one edge as the front. Filaments cannot outrun the cluster, therefore filament loss at the leading edge is impossible. On the sides, filaments can easily leave the cluster by a small angular deviation pointing

away from the cluster center, because in the long run even a small angular difference adds up. The rear of the cluster is special, because small angular deviations are re-aligned with the direction of movement of the cluster, of the filament density is large enough. So a filament at the rear can only escape from the cluster, if the density in its vicinity is rather thin, or the angular misalignment is so large that neighboring filaments cannot outbalance the difference. From this discussion follows that filament loss at the rear is slow compared to the sides. This has no impact on the scaling of the decay rate B_k of a cluster, because we can assume that the length of the sides still scales with $\sqrt{k}$. However, this is wrong if the cluster has no sides. Due to the toroidal topology of our simulation, this is indeed the case, if the cluster width reaches system size. The density wave does indeed span the whole system and is therefore much more stable than the model predicts. This also impacts on the cluster distribution of the intermediate clusters, because they are long-lived enough to eventually collide with the density wave. Therefore, we have to expect that the model only fits well for cluster sizes where the life-time is smaller than a sweep of the density wave.

So far, we have found that the measured cluster size distribution shows a falloff that is stronger than algebraic at small densities and a near perfect algebraic decrease over about two orders of cluster size for higher densities. These findings are in good qualitative agreement with a theoretic cluster model by Peruani et al. The major difference between model and theory concerns the clustering at the largest cluster sizes. Instead of the predicted surplus over a wide range of large cluster sizes, we merely found a single outlier from the density wave, which we could explain by the increased lifetime of the density wave.

Scaling exponents of the cluster size distribution

Although the full cluster size distribution contains most information, it allows no easy comparison of the clustering behaviour for different parameters. However, it is possible to extract the scaling exponent of the cluster size distribution which is a measure for the propensity to form clusters. Our data only allow to measure the scaling exponent for small cluster sizes, therefore this scaling exponent measures clustering of small clusters. In the following we address the question, how the clustering propensity changes with the filament parameters.

The scaling exponent α makes only sense for distributions where the cluster size distribution is proportional to $N_c(s) \propto s^\alpha$, in other words if the cluster size distribution is algebraic. A large scaling exponent then favors the buildup of large clusters, whereas a small scaling exponent shifts the distribution towards small clusters. To measure the scaling exponent from our data, we transformed both cluster size and cluster abundance to a logarithmic scale and fitted a linear function to the transformed data. In order to circumvent the stronger noise at higher cluster sizes and other deviations from the algebraic scaling due to the influence of the density wave, we limited the range of N_c to a maximal cluster size of 20. In the parameter region where the cluster size distribution fits a power law well (see Fig. 4.15), we typically found scaling exponents α in the range from -2.8 to -2.2. This is a remarkably good agreement with the typical scaling exponent found in the theoretic model ranging from -2.7 to -2.3, despite the considerable simplifications of the model. Consequently, we may assume that the clustering model proposed by Peruani et al. can even make quantitative predictions about the cluster size distribution of small clusters.

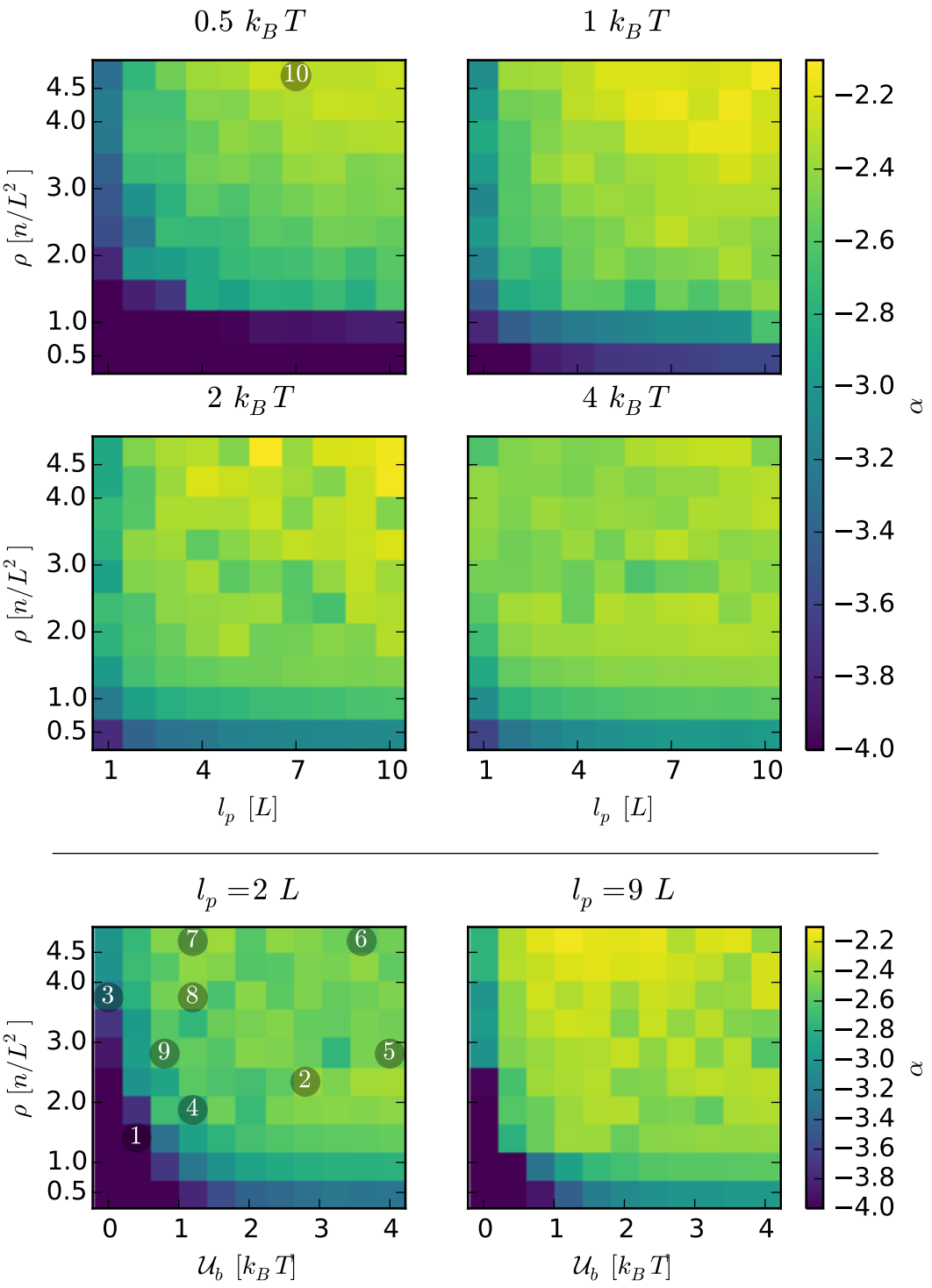

Figure 4.17 | Top panels: The measured scaling exponents α of the cluster size distribution as defined by (4.16) scanned over persistence length l_p and filament density ρ. The panels show the same setup for different contact interaction strengths $\mathcal{U}_b$. **Bottom panels:** Analogous to the top panels but for fixed l_p and scanned over interaction strength $\mathcal{U}_b$ and filament density ρ. Because one data point took up to 500 hours compute time, each data point was acquired from only one realisation, such that the evident noise contains realization artifacts. As a consequence, the error range is unknown. The numbers mark the location of the examples from Figs. 4.1–4.5.

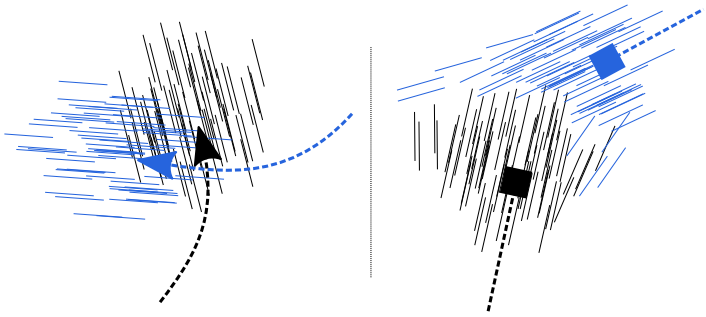

Figure 4.18 | Illustration of cluster collisions with low $\mathcal{U}_b$ (left) and high $\mathcal{U}_b$ (right). If $\mathcal{U}_b$ is small, filaments may easily cross each other so that two colliding clusters may permeate and either merge or change their direction. If $\mathcal{U}_b$ is large, filaments can no longer cross each other, because the potential barrier is too high. As a consequence, two colliding clusters do not permeate but come to a halt and disintegrate over time.

In order to have a more systematic overview, Fig. 4.17 shows the scaling exponents for all our data in the familiar heat map. In general, the bottom panels show that the scaling exponent α increases with the density ρ, which is expected, because the collision rate $A_{i,j}$ grows with the density. Additionally, we find that α also increases with $\mathcal{U}_b$, which comes from the better alignment of the binary collisions with increasing $\mathcal{U}_b$. Consider now the regions where α is small (dark regions in Fig. 4.17). Because large clusters emerge from collisions of small clusters, it is a necessary condition that a dense ordered phase can only build up, if the clustering propensity at small scales is strong. Hence it is consistent that the regions where α is small do not show an ordered phase (compare to Fig. 4.6). However, it is rather surprising that in general the scaling exponent is even quite large in regions where no ordered phase is found. Especially for large $\mathcal{U}_b$ the difference is quite stark, because the scaling exponent is around -2.4 for almost the entire parameter space, but the ordered phase is only found in the upper half. At least, this discrepancy between the scaling exponent and the polarization is no contradiction, because α only measures the propensity to cluster at small scales.

Figure 4.17 suggests that at low $\mathcal{U}_b$, the ordered phase is limited by clustering on small scales, and on the other hand for high $\mathcal{U}_b$ it is not. Because small clusters do form for the entire parameter range of high $\mathcal{U}_b$, it follows that cluster growth must be inhibited at a length scale which is large compared to the filament size, but still smaller than system size. Indeed, video material shows that as $\mathcal{U}_b$ increases, collisions of two clusters become more and more fatal in a sense that the clusters destroy each other. Figure 4.18 illustrates the underlying problem. If $\mathcal{U}_b$ is small enough, filaments may easily cross each other so that two colliding clusters may permeate and either merge or change their direction. On the other hand, if $\mathcal{U}_b$ is large, filaments can no longer cross each other, because the potential barrier is too high. Because our model is constructed in a way that filaments cannot be pushed away, the two clusters are in a stalemate which resolves over time by disintegration of both clusters. As a consequence, the rate at which clusters collide $A_{i,j}$ is no longer proportional to the rate at which clusters merge.

In summary, we found a good quantitative agreement of the scaling exponent of the cluster size distribution between data and the theoretic cluster model. The scaling exponent of the measured cluster size distribution increased with filament density or $\mathcal{U}_b$ and approached a scaling exponent around -2.3 (see Fig. 4.17). At small $\mathcal{U}_b$ where clusters rather merge

instead of destroying each other, the scaling exponent showed a sudden increase at the same parameters where order emerges. On the other hand for large $\mathcal{U}_b$ where clusters can *not* permeate, the scaling exponent shows a completely different behavior than the polarization. We explained this by an increased trend towards fatal cluster collision that destroy two clusters rather than merging them. Consequently, we inferred that clustering at small scales does not necessarily imply an ordered phase.

4.3 Summary of the dry system

In this chapter we examined a system of many filaments that interacted solely via a short-ranged contact interaction. In particular, we looked at the dependence on filament density ρ, persistence length l_p, and interaction strength $\mathcal{U}_b$.

For low enough filament densities ρ we found a disordered gas-phase of almost homogeneously distributed filaments. At such low densities, the filaments only align locally.

With increasing ρ, the filaments started to cluster locally, resulting in an increase of the number fluctuations of the filament density. At some filament density threshold, which depends on the filament parameters l_p and $\mathcal{U}_b$, the disordered system undergoes a phase transition where the filaments start to form two distinct phases: first, a disordered gas phase much like the gas phase at low filament densities. Second, a tightly packed high-density phase where all filaments point into the same direction. This high-density phase periodically sweeps the simulation volume — therefore "density wave" — and encompasses most of the filaments. Interestingly, the density of the gas phase remains independent of the total filament density, so that additional filaments are simply taken up by the density wave.

Additional filaments in the density wave also increase the width of the density wave. Therefore, at very large filament densities there is another phase transition where the disordered gas phase ceases to exist because the density wave spans the whole system.

These findings are akin to the Vicsek model of point particles with a polar alignment by Grégoire et al. who find a similar clustering before the onset of a density wave [32]. Because their particles only have an attractive interaction, their density waves do not spread out as the filaments in our model. Consequently, they observe no mostly homogeneous ordered phase at very high densities (see Fig. 4.5 bottom), although the Vicsek model could be readily extended to that case. In a completely different approach, Thüroff et al. considered a numerical solution of the Boltzmann equation for self-propelled particles with polar alignment [31]. Similarly to our system, they find a disordered phase at low densities and an ordered phase at high densities. In addition, they also report an intermediate regime where multiple density waves occupy different lanes and travel in opposite directions which was absent in our simulations.

The density wave from our simulations is similar to the phenomenology of the actomyosin motility assay as reported by Schaller et al. [10]. Like in our simulation, they find a disordered phase at low filament densities ρ, and the formation of system-spanning density waves above a critical density ρ^*. However, for intermediate densities $\rho_c < \rho < \rho^*$, they also report the formation of long-lived compact clusters that are substantially smaller than a density wave. Although we also find cluster formation on intermediate scales at high persistence length l_p and interaction strength $\mathcal{U}_b$, these clusters are always short-lived in our simulation. We

cannot exclude that other simulation settings will also produce such long-lived structures, but given the fact that the clusters in the experiment also interact hydrodynamically [58], it seems much more likely that the dry system lacks essential details.

5 Many filaments in a wet environment

The previous chapter has examined the collective behavior of self-propelled filaments without hydrodynamic interactions — in other words a "dry" system. This chapter deals with the wet case, where the filaments interact via both a contact *and* hydrodynamic interaction. Because the dry and wet systems are identical up to the hydrodynamic interaction, this approach allows to directly deduce the consequences of long-ranged interactions on the collective phenomena that were observed in the dry system. Apart from the added hydrodynamic interactions, the whole procedure of initialization and data acquisition is the same as in 4.

The chapter is structured as follows: Section 5.1 discusses the phenomenology of wet systems with many filaments for purely two-dimensional setups. These observations are then quantified in section 5.2 in a broadly analogous manner to the dry system: section 5.2.1 looks at the order parameters, section 5.2.2 is new and examines the flow patterns, section 5.2.3 shows the number fluctuations, and section 5.2.4 examines the clustering behavior. Finally, section 5.3 then extends the purely two-dimensional fluid in two different ways. First, by an effective friction (5.3.1) and then by a fully three-dimensional fluid (5.3.2). Our findings are then briefly summarized in section 5.4.

5.1 Phenomenology

In analogy to the case without hydrodynamic interactions in section 4.1, this section presents the phenomenology of a system of many filaments with both contact *and* hydrodynamic interactions. For now, we only consider two-dimensional systems with 2D hydrodynamics, so that the hydrodynamic interactions are rather long-ranged and strong. For further details about the tSNE-method that is used in the following, we refer to section 4.1.1.

The following plots are analogous to Figs. 4.1–4.5, however they also depict the flow field of the fluid via streamlines. The first example in Fig. 5.1 (top) shows at a very low number density of filaments ($\rho = 0.94\, n/L^2$), where the filaments in the dry system were at most locally ordered, but globally disordered. In the wet system on the other hand, the filaments initially also align locally in small packs of a few filaments. For the formation of small packs, the hydrodynamic interaction should play no role, because a single filaments only have a weak flow field that is usually dominated by thermal noise. In contrast to a single filament, these packs of filaments generate enough drag to move the surrounding fluid. As a result, these packs interact over a long range via their induced hydrodynamic flow, so that the large-scale motion of the filaments becomes more and more dominated by the fluid flow. This coordinated movement initially shows in small swirls of filaments, which over time merge into larger swirls. The merging of vortices with an anti-vortex[1] happens on rather long time-scales as it has to be

[1] It is standard nomenclature to refer to points with a winding number of $+1$ as vortices. In analogy, we refer to singular points with a winding number of -1 as anti-vortices or saddles.

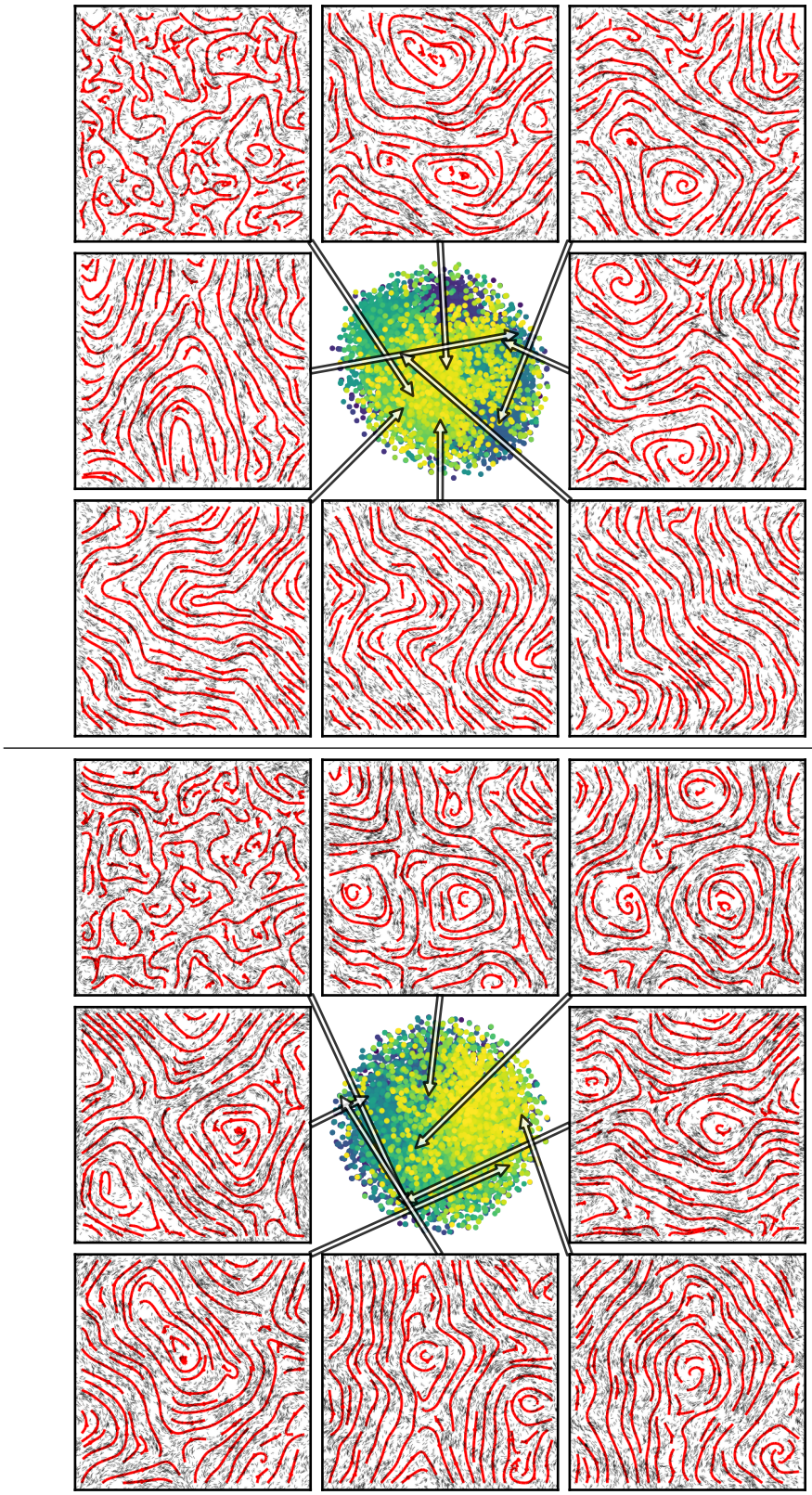

Figure 5.1 | Top: $\rho = 0.94\, n/L^2$, $\mathcal{U}_b = 2\, k_B T$, $l_p = 4\, L$ **Bottom:** $\rho = 1.41\, n/L^2$, $\mathcal{U}_b = 2\, k_B T$, $l_p = 2\, L$. More explanation about these plots is found in Appendix A.2.2 on page 156.

expected of global conformation changes such as vortex diffusion. As the number of vortices shrinks, the movement of the filaments becomes more and more coherent over long length-scales. Thus, the final state in the example of Fig. 5.1 (top) is a globally polar state, where all filaments walk into the same direction. Nearly global polar order was also observed in the dry case, albeit at much higher filament densities. However, the important difference to the dry case is that here the filaments show *no* apparent density modulations. The lack of density modulations also shows in the unstructured tSNE-plot.

The second example in Fig. 5.1 (bottom) for a slightly higher density ($\rho = 1.41\, n/L^2$) shows a completely analogous behavior. However, in that case the evolution of the vortex dynamic is so slow that the final state still has two pairs of vortices and saddles. In all the cases where such a state formed it was very long-lived. Despite long-range order, a final state with vortices has no global order so that its polarization should be rather small.

As the density of filaments increases further, the initial density fluctuations become more pronounced, as Fig. 5.2 (top) shows. This density modulation shows up as an arc in the tSNE-plot (protruding dark arc), however at later times the density profile levels out and the tSNE-plot takes the form of an amorphous blob. The quasi-stationary order of the filaments in this example is two regions where the filaments stream downwards and upwards, separated by two sharp turning lines. This zig-zag flow is the most predominant quasi-stationary state at high densities. However, this flow pattern is only quasi-stationary and not stationary, because the turning lines move over time. The speed at which these turning lines shift is not necessarily the same, so that the two turning lines may hit and annihilate. Another way how this state decays is by a gradual reduction of the amplitude of the zig-zag motion. Figure 5.2 (bottom) shows an example where two flow regions coexist over a long time, until one direction wins over the other and the flow becomes almost perfectly parallel.

Upon further increase of the filament density, the general behavior remains the same although small-scale fluctuations become more and more suppressed. There is one major difference at high densities, where the locations of vortices are depleted of filaments. This depletion is plausible because in order for a filament to stay close to the vortex center, it has to be strongly curved. Yet the bending rigidity of the filaments forbids too strongly bent filaments, so that the filament inevitably wanders away from the center. Besides, the vortex is kept stable by the large number of filaments that move about the vortex center in stable orbits, so that small numbers of filaments in the eye of the vortex can not perturb the vortex and render it unstable. For example, Fig. 5.3 (top) shows an example with apparent depletion of the vortices. In this example, the vortices annihilate with anti-vortices at about half the simulation time, which shows nicely in the red stream lines. It is quite common that after the last vortex annihilation the system of filaments remains in the zig-zag stream pattern for a long time. Apparently, in this zig-zag pattern the filament density flattens out even if it was non-uniform in the beginning. Consequently, the tSNE-plot has some structure at early times where the vortices are depleted of filaments, whereas at later times, it becomes amorphous. It is no coincidence that the path in the tSNE-plot returns to where it started off, because the initial density distribution was also uniform as is the final state.

Finally, Fig. 5.3 (bottom) shows an example with a very weak density wave travelling from bottom left to top right. Due to the travelling density waves, the tSNE-plot also shows a (broken) yellow ring. This example proves that density waves can actually form with hydrodynamic interactions, although their density profile is much flatter than without hy-

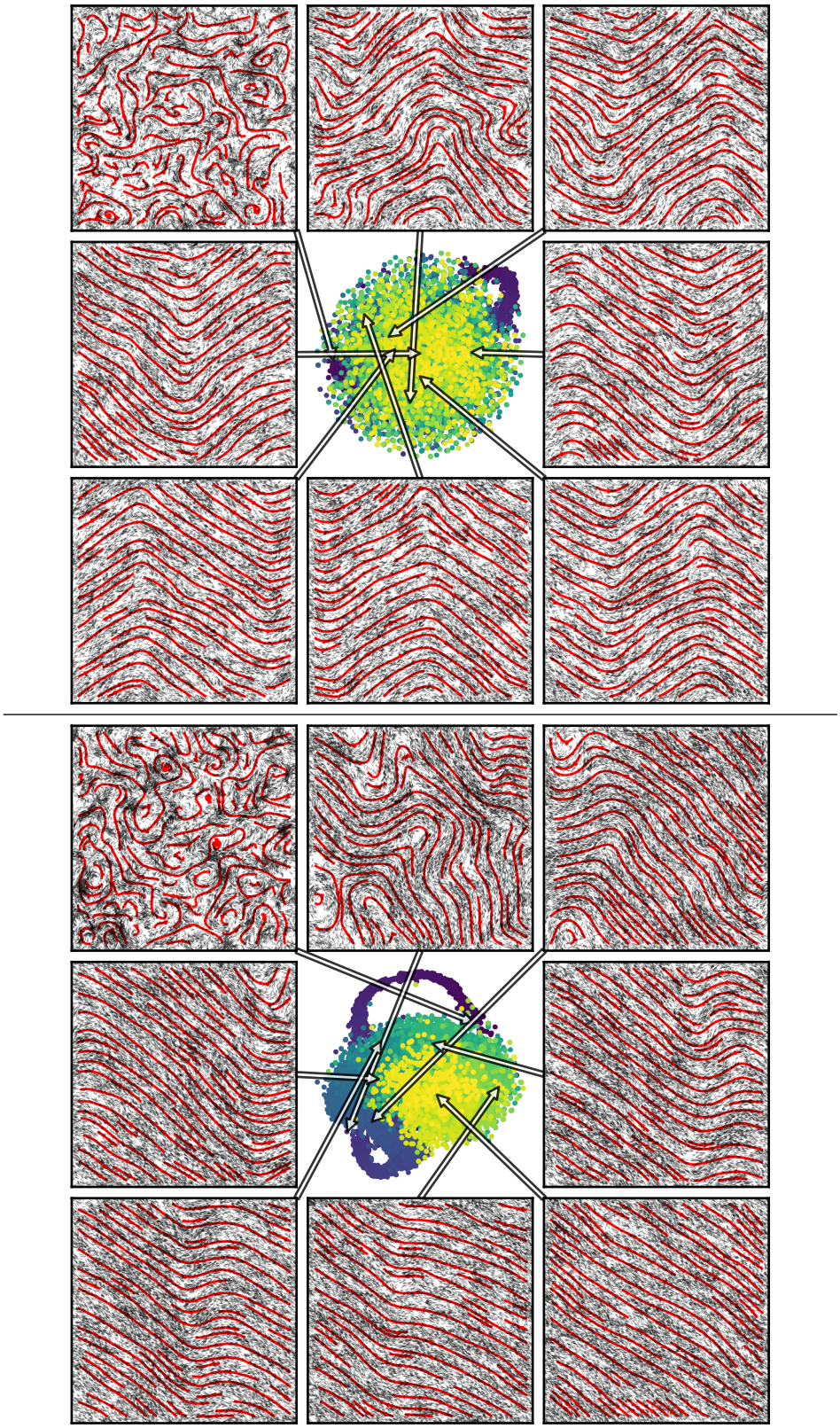

Figure 5.2 | Top: $\rho = 2.81\, n/L^2$, $\mathcal{U}_b = 2\, k_B T$, $l_p = 3\, L$ **Bottom:** $\rho = 3.75\, n/L^2$, $\mathcal{U}_b = 2\, k_B T$, $l_p = 5\, L$. More explanation about these plots is found in Appendix A.2.2 on page 156.

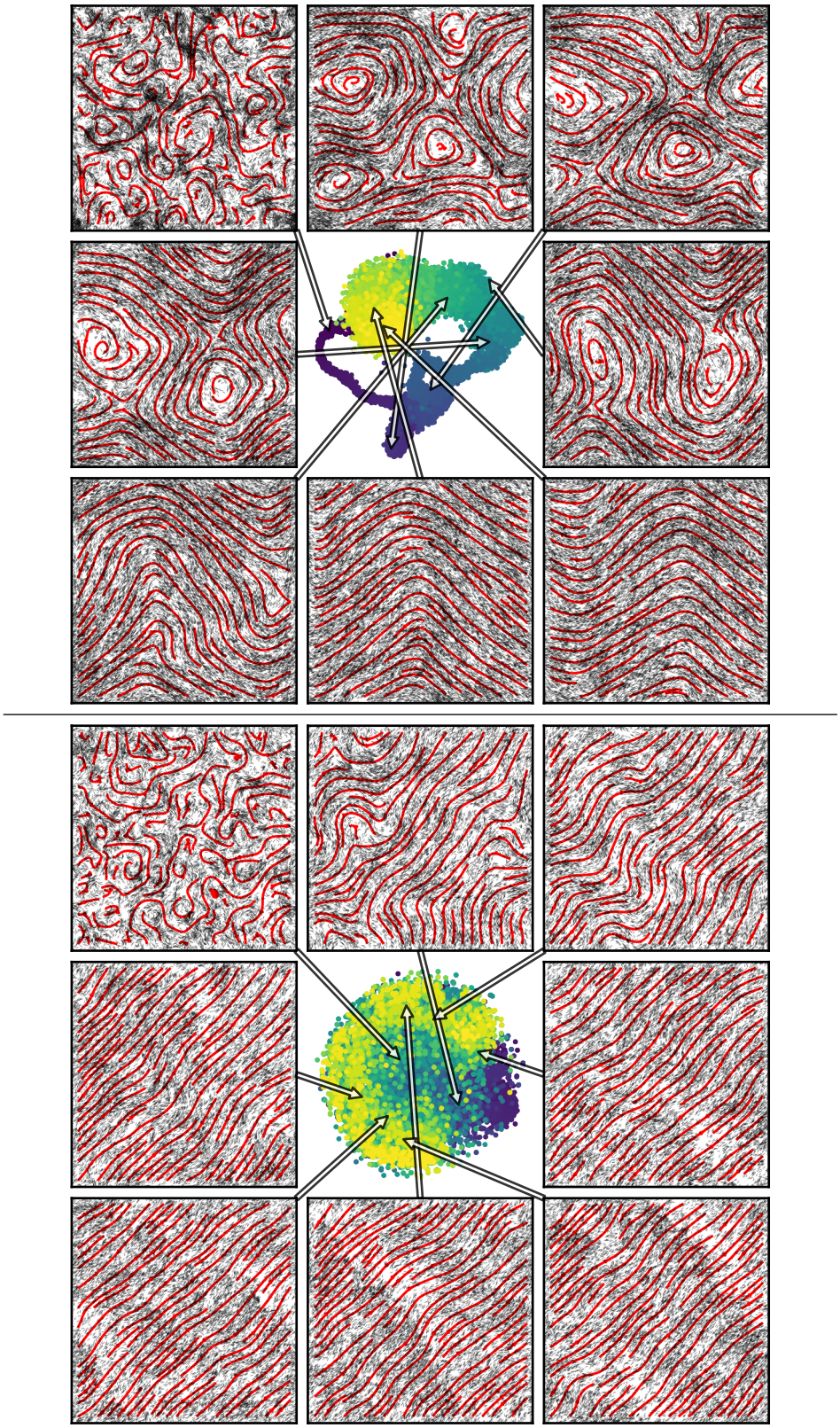

Figure 5.3 | Top: $\rho = 4.22\,n/L^2$, $\mathcal{U}_b = 2\,k_BT$, $l_p = 4\,L$ **Bottom:** $\rho = 2.81\,n/L^2$, $\mathcal{U}_b = 2.4\,k_BT$, $l_p = 2\,L$. More explanation about these plots is found in Appendix A.2.2 on page 156.

drodynamic interactions. From its phenomenological appearance, the best matching example from the dry cases is 4.5 (bottom) where the system was globally ordered and had similar overlapping density bands. However, in the dry case the density waves were very robust and formed nearly always above a certain filament density, whereas the rather faint density wave from this example (Fig. 5.3) with hydrodynamic interactions is only found in rare cases. Therefore there are two possibilities: either the density waves are suppressed in favor of a flat density profile, or the other systems from above without a density wave have not yet fully equilibrated.

In summary, we have found that the systems of multiple filaments with hydrodynamic interactions always have long-range orientation correlations. Three very long-lived orientation states were found: *global order* where all filament point into the same direction, *vortices* where the filaments move in circular orbits, and *zig-zag* where at least two stripe regions form in which the filaments move into the same direction. Because the states other than global order evolve slowly, they are only quasi-stationary and may eventually transition into global order. The observed density profiles of the final states were usually flat and had almost no apparent density variations. Only the vortex centers (if any) were depleted of filaments and in rare cases we also found faint density waves. In short, the density modulations that were observed in the dry case were flattened out by the hydrodynamic interactions.

5.2 Quantitative analysis of the simulation data

The findings from the phenomenological overview of the previous section will now be quantified in the following. For that, we performed two parameter sweeps over the parameters $\mathcal{U}_b$, l_p, and ρ, where either the persistence length $l_p = 2\,L$ or interaction strength $\mathcal{U}_b = 2\,k_BT$ was kept constant. As mentioned in the introduction of chapter 4, we only generated a single realization for every parameter combination, which makes it impossible to estimate the error range for our measurements. The following analysis uses the observables from section 4.2, so that the results are fully compatible and comparable.

5.2.1 Order parameter and angular distribution

The phenomenological overview has indicated that the filaments order on large length scales even for very small filament densities. In the following, this observation will be quantified using the measures that were developed in 4.2.1.

The easiest way to measure global alignment is to evaluate the average direction $\mathcal{P}(t) \equiv \left|\sum_{i=1}^{N} \boldsymbol{t}_i(t)\right|$, as introduced in (4.5) on page 52. Figure 5.4 shows the polarization $\langle \mathcal{P}(t_{final}) \rangle$ for two parameter scans over filament density ρ versus interaction strength $\mathcal{U}_b$ and persistence length l_p. Except for a few dark speckles of bad alignment, the polarization is indeed quite large for the entire parameter range. In fact, the polarization is so large for most runs that for example the zig-zag states (e.g. #3) do not separate cleanly from the more ordered states (e.g. #4). To understand the reason for this small variability in the polarization, imagine a mixture of two equal-sized sub-populations of filaments which are aligned, but off by an angle of α. Then the polarization will be $\langle \mathcal{P} \rangle = \cos \frac{\alpha}{2}$, which is still ≈ 0.7 for an angle of $\alpha = \pi/4$.

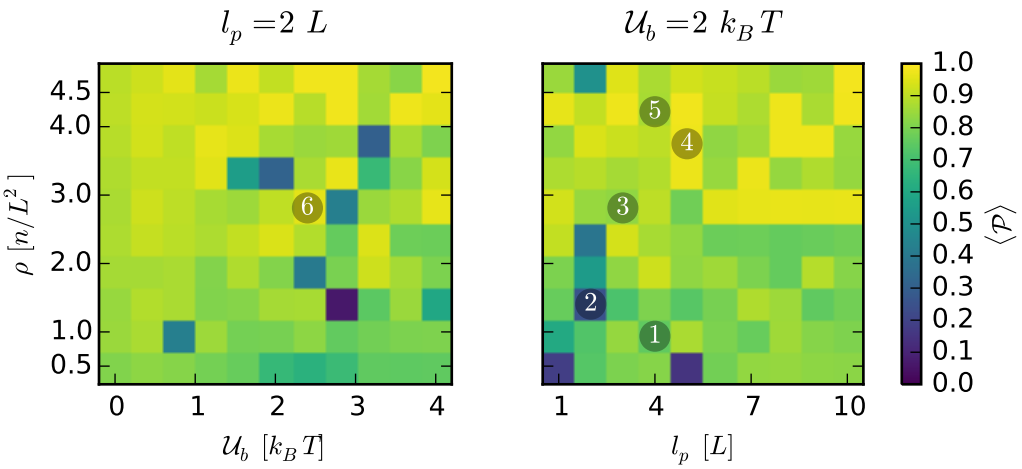

Figure 5.4 | Left: The observed polarization as defined by (4.6) for constant $l_p = 2\,L$ scanned over interaction strength $\mathcal{U}_b$ and filament density ρ. **Right:** Analogous to the left panel but for fixed $\mathcal{U}_b = 2\,k_B T$ and scanned over persistence length l_p and filament density ρ. Because one data point took up to 500 hours compute time, each data point was acquired from only one realisation, such that the evident noise contains realization artifacts. As a consequence, the error range is unknown. The numbers mark the location of the examples from Figs. 5.1–5.3.

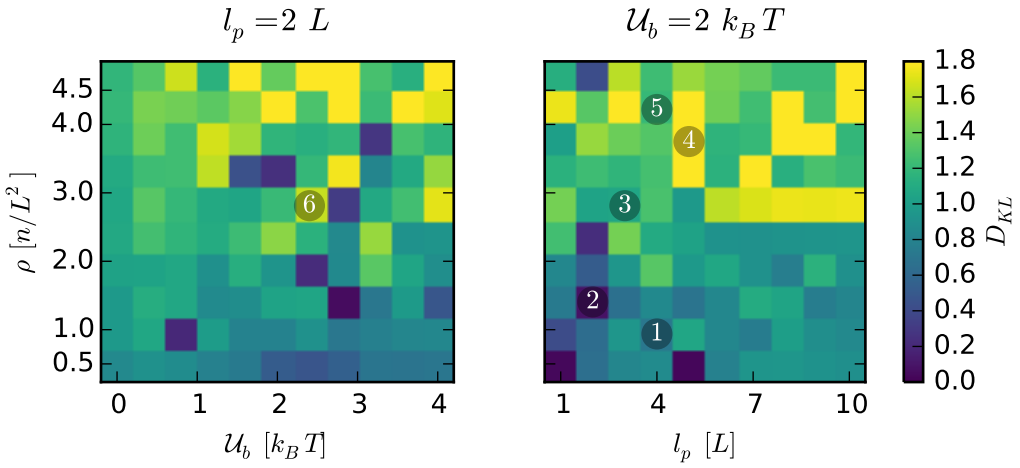

Figure 5.5 | Left: The observed Kullback-Leibler divergence of the measured angular distribution from a flat distribution as defined in (4.8) for constant $l_p = 2\,L$ scanned over interaction strength $\mathcal{U}_b$ and filament density ρ. **Right:** Analogous to the left panel but for fixed $\mathcal{U}_b = 2\,k_B T$ and scanned over persistence length l_p and filament density ρ. Because one data point took up to 500 hours compute time, each data point was acquired from only one realisation, such that the evident noise contains realization artifacts. As a consequence, the error range is unknown. The numbers mark the location of the examples from Figs. 5.1–5.3.

In other words, the polarization $\mathcal{P}$ recognizes the relatively good alignment within each of the two sub-populations, but it fails to punish the mutual misalignment between those two sub-regions.

This situation is where the Kullback-Leibler divergence approach to measure global order shines. Compare Fig. 5.5 to Fig. 5.4, showing D_{KL} and $\langle \mathcal{P} \rangle$ for the same dataset. The two measures qualitatively agree on the non-ordered[2] states (dark spots) and the very well ordered states (bright yellow). The range in between looks however quite different: the whole region where the $\mathcal{P}$ has values around $0.8 \times \mathcal{P}_{max}$ has shifted towards the region $0.5 \times D_{KL,max}$. In other words, the Kullback-Leibler divergence penalizes the misalignment of the two regions stronger. We can estimate the difference of the Kullback-Leibler divergence of a single peak versus two peaks by

$$\Delta D_{KL} \approx 1 \cdot \log \frac{p}{q} - 2 \times \frac{1}{2} \log \frac{p/2}{q} = \log(2) \approx 0.7 \ ,$$

which well matches the difference in the observed Kullback-Leibler divergence from the ordered ($D_{KL} \approx 1.8$) and the zig-zag states ($D_{KL} \approx 1$). So the Kullback-Leibler divergence is better suited than $\mathcal{P}$ to separate ordered from zig-zag states. Because the Kullback-Leibler divergence is also more sensitive to orientational fluctuations of the filaments, it also shows a slight gradient from small filament densities towards high filament densities, indicating a stabler alignment at higher filament densities.

Finally, we need to elucidate the nature of the non-ordered states (dark spots), which seem to be scattered randomly over the parameter range. Figure 5.1 suggests that the global order in these states is so low, because the filaments revolve around vortices, so that every direction becomes equally likely and the polarization is thus small. Such a vortex has a topological and therefore global nature, such that even small displacements of a vortex center require a global rearrangement of all filaments. Due to this large-scale reorganization, the evolution of these vortex states is very slow, and the vortex states become long-lived. Apparently, the life-time of these vortex states is comparable to our simulation window, so that some final states still have such vortices.

In summary, our analysis of the order parameters has shown that the systems of filaments with hydrodynamic interactions have strong global order throughout the parameter range, we looked at. This is in stark contrast to the dry system where the there was a sharp transition from disordered to ordered systems. Despite the long-range order in all cases, we found states where the wet system was trapped in long-lived vortex states, whose polarization is necessarily small. Last but not least, the most prevalent final state was not perfectly ordered, but rather one with an intermediate global order. It will be the goal of the next section to further elucidate the nature of these states.

5.2.2 Streaming patterns

The last section has established that the filaments order on a large scale, however not in all cases and usually not perfectly. In the following, we will provide further evidence that the streaming pattern for the filaments is indeed linear, zig-zag, or in vortices.

[2]For brevity we say non-ordered, because those systems usually have swirls and thus no preferred direction, although they are locally ordered.

First, we focus on the non-ordered cases, for which the comparison to simulation snapshots has shown that the filaments move in swirls. Our conjecture that the non-ordered systems are always systems with swirls in their final state is so far solely based on the comparison to these examples. To support this claim for the remaining non-ordered cases, we want to measure the total vorticity in the fluid field $\boldsymbol{v}(\boldsymbol{r})$. The local vorticity of such a vector field can be measured by the curl of the fluid flow field, $\partial_x v_y(\boldsymbol{x}) - \partial_y v_x(\boldsymbol{x})$. For a total measure of vorticity, a first guess could therefore be to integrate the curl over the simulation area A,

$$\tilde{\mathcal{V}}[\boldsymbol{v}] = \int_A \Big(\partial_x v_y - \partial_y v_x\Big)\,\mathrm{d}A \ .$$

However, via the Stokes law this definition can be re-written as a line integral and one can calculate

$$\begin{aligned}\tilde{\mathcal{V}}[\boldsymbol{v}] &= \int_A \Big(\partial_x v_y - \partial_y v_x\Big)\,\mathrm{d}A = \int_{\partial A} \boldsymbol{v}\,\mathrm{d}\boldsymbol{l} \\ &= -\int_{A^C} \Big(\partial_x v_y - \partial_y v_x\Big)\,\mathrm{d}A = \int_{\emptyset} \cdots = 0 \ .\end{aligned}$$

Here we have used the Stokes law twice and rewritten the integral as an integral over the complement of A, which is the empty set and therefore the integral must be zero. To remedy this situation, we define our global measure for the vorticity as

$$\mathcal{V}[\boldsymbol{v}] = \int_A \Big|\partial_x v_y - \partial_y v_x\Big|\mathrm{d}A \ . \tag{5.1}$$

By taking the absolute value of the local curl, we basically count left- and right-turning vortices as the same, which is fine for our aim. For a better intuition of what features this measure of vorticity is sensitive to, Fig. A.1 shows the vorticity field of the examples in Figs. 5.1–5.3.

Figure 5.6 shows this measure of vorticity, $\mathcal{V}$, for the same data as in Fig. 5.4. It is apparent that both measures are somewhat complementary to each other. In particular, the vorticity measure is especially large at all the spots where the polarization was small. In conjunction with our direct observation of vortices, this is a strong indicator for vortices being the cause of a small polarization. Consequently, the small polarization for these isolated spots must not be interpreted as disordered systems, but rather as states with large-scale order that contain vortices. Furthermore, Fig. 5.6 shows a very low vorticity measure for the regions with very high order parameter. This means that the fluid streams in those examples have no bends and thus stream in a laminar fashion. Last but not least, we observe a general trend towards larger vorticity at small densities or high interaction potential $\mathcal{U}_b$. The small level of vorticity at small $\mathcal{U}_b$ is a hint that the contact interaction of filaments causes irregular stream patterns and thus creates vorticity. On the other hand the decrease of vorticity with the filament density ρ is a sign that the fluid flow alone cannot keep the filaments perfectly on track. However, as the filament density rises, the contact interaction of the filaments suppresses directional fluctuations, while the hydrodynamic interaction ensures the coherent motion on longer length and time scales.

Finally, we want to support the claim that the most common final state is a zig-zag state and not a laminar stream pattern. To that end, we consider the angular distribution $P(\varphi)$

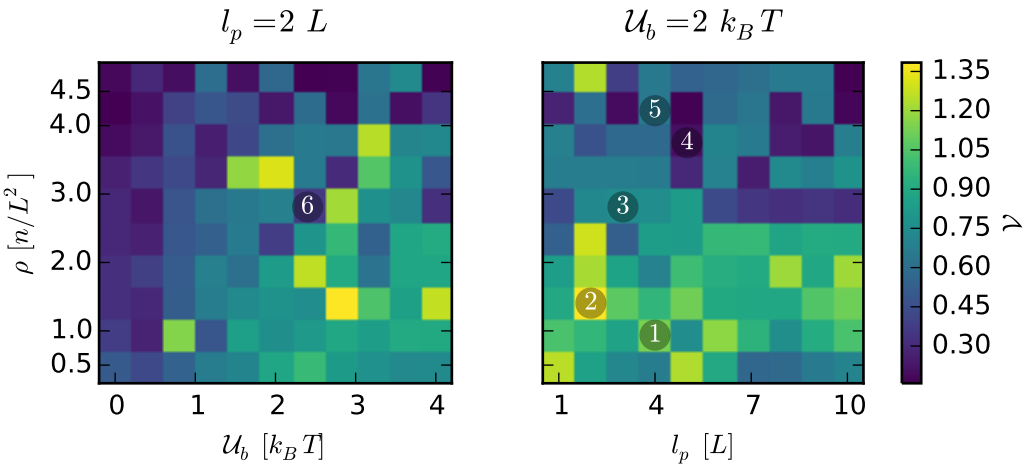

Figure 5.6 | Left: The vorticity measure $\mathcal{V}$ as defined by (5.1) for constant $l_p = 2\,L$ scanned over interaction strength $\mathcal{U}_b$ and filament density ρ. **Right:** Analogous to the left panel but for fixed $\mathcal{U}_b = 2\,k_B T$ and scanned over persistence length l_p and filament density ρ. Because one data point took up to 500 hours compute time, each data point was acquired from only one realisation, such that the evident noise contains realization artifacts. As a consequence, the error range is unknown. The numbers mark the location of the examples from Figs. 5.1–5.3.

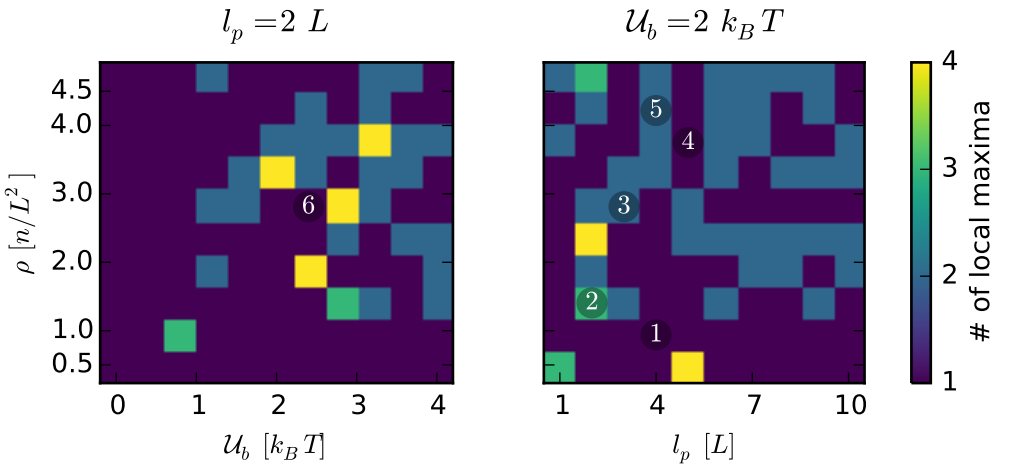

Figure 5.7 | Left: The number of peaks of the angular distribution $P(\varphi)$ for constant $l_p = 2\,L$ scanned over interaction strength $\mathcal{U}_b$ and filament density ρ. **Right:** Analogous to the left panel but for fixed $\mathcal{U}_b = 2\,k_B T$ and scanned over persistence length l_p and filament density ρ. Because one data point took up to 500 hours compute time, each data point was acquired from only one realisation, such that the evident noise contains realization artifacts. As a consequence, the error range is unknown. The numbers mark the location of the examples from Figs. 5.1–5.3.

of the filaments and count the number of peaks. For a laminar stream, the filament angles should be distributed over a single peak around the average direction, whereas for the zig-zag pattern we expect two peaks. We determined the angle distribution by averaging all filament directions over a period of 1/64 of our simulation duration or $57L/v_0$. Because these data still had some noise, we performed an order-3 Savitzky-Golay smoothing with a window width of 17 points [3] to reduce the number of candidate maxima [98]. In the next step we determined all maxima of the smoothed probability distribution $P^{SG}(\varphi)$, which correctly contains all peak maxima, but still some spurious local maxima in φ-regions where $P^{SG}(\varphi)$ is close to zero. To avoid counting these unwanted artifacts, we additionally required that each valid peak must have at least 2% the height of the largest peak.

Figure 5.7 shows the number of peaks of $P^{SG}(\varphi)$ for the same dataset as in Fig. 5.4. It is remarkable that the vortex states light up with three or more peaks. Two features catch the eye: first, below a filament density of $\rho \approx 1\, n/L^2$ there are no double-peaked states, but only singly-peaked angular distributions or vortex states. Second, below $\mathcal{U}_b = 1\, k_B T$ there are no double-peaked states. Both these observations indicate that the contact interaction between filaments plays an important role for the stability of the zig-zag states, because in the first case direct collisions are rare, and in the second the collisions are not very effective because filaments may cross each other. This suggests the following mechanism for the stability of the zig-zag states: when a filament enters a band where the direction changes, it is forced by the already present filaments to bend as well. Because the filament density is high enough that new filaments are almost guaranteed to run into other (bent) filaments, the band is in a way self-sustaining. This process is of course only effective, if the filament-filament interactions are strong enough, which apparently is above $\mathcal{U}_b \approx 1\, k_B T$. Finally, it is palpable how the cases with high order parameter and low vorticity also correspond to singly-peaked angular distributions. It is clear that these states must have a laminar order. The figure also shows that double-peaked or zig-zag states are rather common.

In summary, this discussion has shown that the filaments either flow in a laminar fashion, in zig-zag patterns, or around vortices. Because zig-zag states were only found above a certain filament density and contact interaction strength $\mathcal{U}_b$, it seems likely that the steric interaction of filaments is the mechanism that causes the bending bands of the zig-zag states.

5.2.3 Number fluctuations

Large density variations are a generic sign for being out of equilibrium. This section evaluates the number fluctuations of the filament density in the wet system. It is thus analogous to 4.2.2 where we found large number fluctuations in the dry case.

Figure 5.8 shows the scaling coefficient of the number fluctuations in the wet system, which were obtained via the identical procedure as in 4.2.2. Ordinary uniformly distributed densities would have a scaling exponent of one, whereas non-uniformly distributed have larger scaling exponents. The first thing to note is that the range of scaling exponents is only [1, 1.5] here, whereas for the dry system we found a range of [1, 2] (see Fig. 4.11). This means that the density fluctuations in the system of filaments are far less pronounced if the long-

[3] The Savitzky-Golay smoothing procedure calculates an n-th order polynomial of the data points in the moving window and uses the interpolation for the midpoint of the window as the smoothed data point.

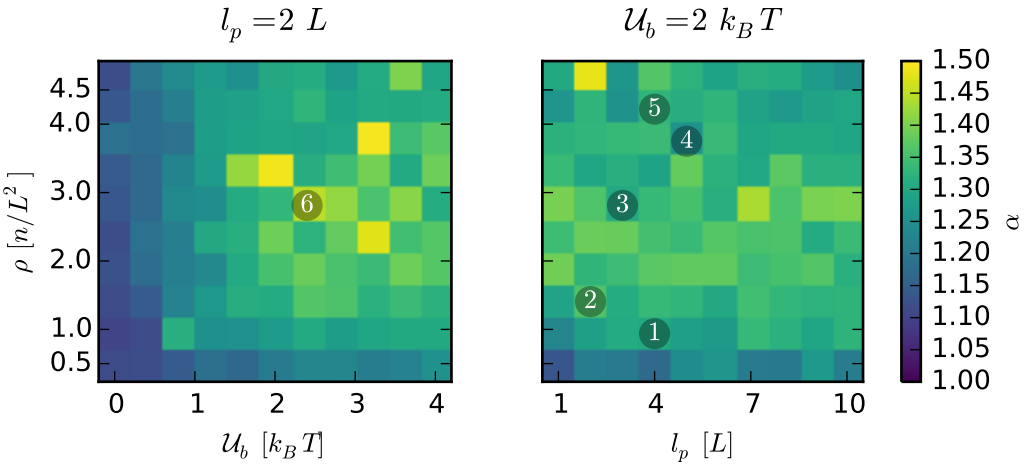

Figure 5.8 | The observed scaling exponents of the number fluctuations scanned over persistence length l_p and filament density ρ. The panels show the same setup for different contact interaction strengths $\mathcal{U}_b$. Because one data point took up to 500 hours compute time, each data point was acquired from only one realisation, such that the evident noise contains realization artifacts. As a consequence, the error range is unknown. The numbers mark the location of the examples from Figs. 5.1–5.3.

ranged hydrodynamic interaction is relevant. On the other hand, the scaling exponent of the number fluctuations is still significantly larger than one, so that the filaments cannot be randomly distributed either. One should note here that the scaling exponent for very low $\mathcal{U}_b$ is rather small, and rises with increasing $\mathcal{U}_b$ up to $\mathcal{U}_b \approx 1.5\, k_B T$ (Fig. 5.8 left). Because the hydrodynamic interaction is unaffected by $\mathcal{U}_b$, it follows that it is the contact interaction what causes the density anomaly, and not the hydrodynamic interaction. On the contrary, because the density fluctuations in the dry system were much stronger, it follows that the hydrodynamic interaction actually suppresses the density waves. Note that the cases with the strongest number fluctuations are states with vortices, where the vortex centers are depleted of filaments. As noted above, the depletion of the vortex centers is caused by the filament stiffness which makes it impossible for filaments to circle around the vortex center in a stable orbit.

In summary, the number fluctuations of the filament density in the wet system showed that the filaments are not uniformly distributed. However, the density fluctuations in the wet case are greatly reduced compared to the dry case.

5.2.4 Clustering of the filaments

One very characteristic feature of the dry system was the emergence of a traveling high-density wave. We have however not found such density waves in our phenomenological overview, therefore the goal of this chapter is to confirm that there are no density waves in the wet system.

A very reliable indicator for the density wave in the dry case was the size of the largest cluster in the system. Figure 5.9 shows the size of the largest cluster where the clustering

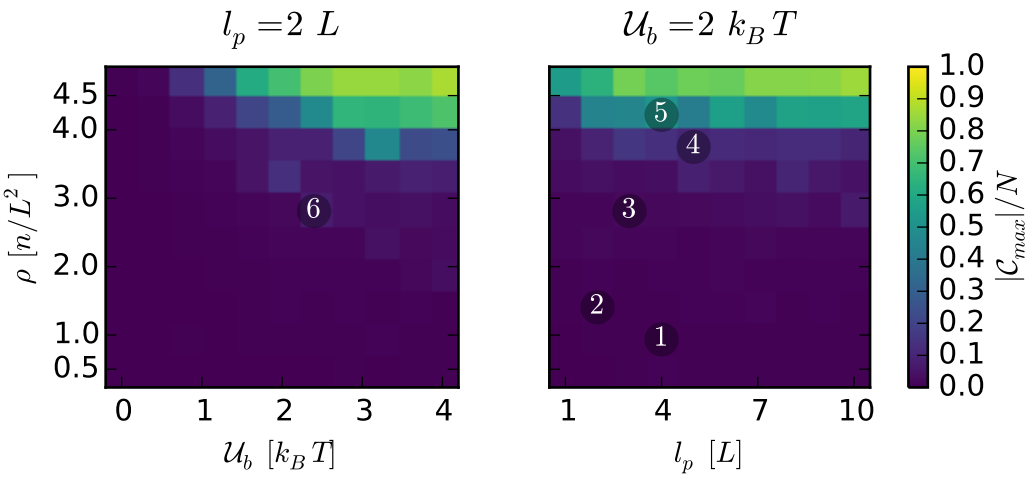

Figure 5.9 | Left: The relative cluster size of the largest cluster in the system, $|C_{max}|/N$, as defined in 4.2.4 for constant $l_p = 2\,L$ scanned over interaction strength $\mathcal{U}_b$ and filament density ρ. **Right:** Analogous to the left panel but for fixed $\mathcal{U}_b = 2\,k_BT$ and scanned over persistence length l_p and filament density ρ. Because one data point took up to 500 hours compute time, each data point was acquired from only one realisation, such that the evident noise contains realization artifacts. As a consequence, the error range is unknown. The numbers mark the location of the examples from Figs. 5.1–5.3.

criteria are identical to the clustering criteria in 4.2.4[4]. Apparently, there are no fat clusters in wet systems. Only at very high densities $\rho \approx 4\,n/L^2$ there is a stripe region where the largest cluster becomes fat. However, at this density it is quite likely that the next filament is less than $2/3\,L$ away – even if most filaments are part of small dense clusters. In other words, our clustering criteria make one big cluster out of the (more or less) homogeneously distributed filaments, because the hydrodynamic interaction also creates order on long length-scales.

Another important quantity that derives from the cluster size distribution is the scaling exponent of the cluster size distribution. As before, we only use the first 20 data points to derive the scaling exponent from the cluster size distribution. The scaling exponent is therefore mostly a measure for the cluster distribution of small clusters. Figure 5.10 shows the scaling exponents for the wet system. A comparison to the results for the dry system in Fig. 4.17 shows a very similar behavior, albeit the scaling exponents tend to be a bit larger in the wet system. The crucial point is, however, that the cluster size distribution is almost unaffected by the hydrodynamic interaction. This is a strong indication that the small-scale clustering of filaments is solely due to the contact interaction and that the hydrodynamic interaction plays almost no role in clustering. An explanation for this similarity is that the hydrodynamic interaction only becomes effective for long-lived large clusters which create a strong hydrodynamic flow field. For single filaments or clusters of only a few filaments, the hydrodynamic interaction is too feeble to counteract the thermal fluctuations of the polymers.

In summary, we found that the small-scale clustering of filaments is almost unaffected by the hydrodynamic interactions. Despite the similar clustering behavior at small scales, the

[4]This means that two filaments are considered as clustered, if their distance is less than $\frac{2}{3}L$ and their angle is less than 10°. If the filaments were clustered in the last step, these criteria are relaxed to $1\,L$ and 15°.

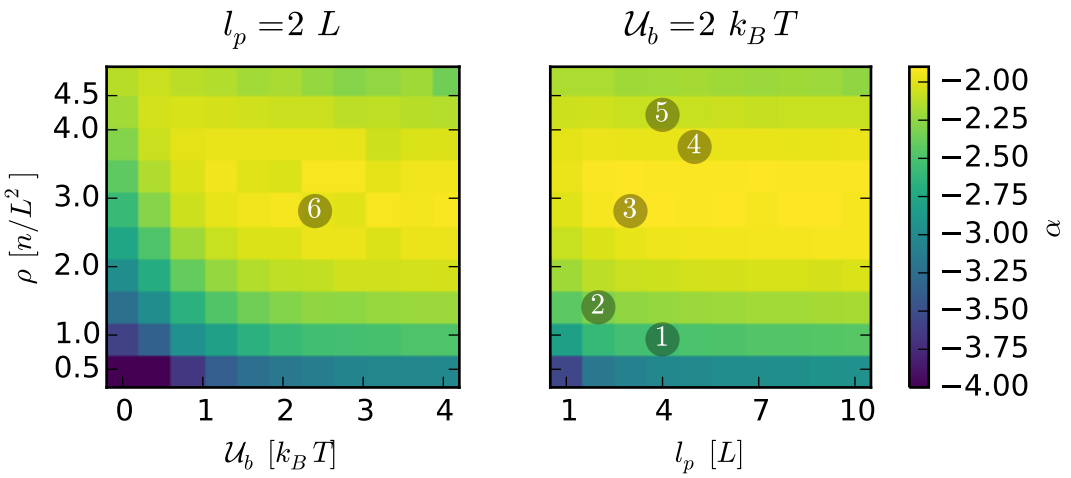

Figure 5.10 | Left: The measured scaling exponents α of the cluster size distribution as defined by (4.16) for constant $l_p = 2\,L$ scanned over interaction strength $\mathcal{U}_b$ and filament density ρ. **Right:** Analogous to the left panel but for fixed $\mathcal{U}_b = 2\,k_B T$ and scanned over persistence length l_p and filament density ρ. Because one data point took up to 500 hours compute time, each data point was acquired from only one realisation, such that the evident noise contains realization artifacts. As a consequence, the error range is unknown. The numbers mark the location of the examples from Figs. 5.1–5.3.

hierarchy of cluster growth breaks at some point and fat clusters that contain almost all filaments do not form. In other words, there was no evidence for a density wave.

5.3 Recovering density waves with hydrodynamic interaction

It is puzzling that our wet system does not form a density wave, given that there are numerous experimental realizations of similar setups where the filaments are in aqueous solution. In fact, the dimensionless numbers characterizing the hydrodynamic interactions would mean even stronger hydrodynamic interactions in real systems. The lack of density waves in our wet systems of filaments therefore raises the question, what went wrong in our model. The goal of the next two subsections is to extend the wet model so that density waves re-emerge.

5.3.1 Wet systems with 2D hydrodynamics and finite range

One major difference between the contact interaction and the hydrodynamic interaction is the long range of the latter [99]. Because in real experiments the filaments are in close proximity to a no-slip boundary, the hydrodynamic flow field of the filaments falls off much faster due to the presence of the wall [100]. If the two-dimensional fluid can be augmented so that it effectively models three-dimensional fluid interactions, one would have a computationally pretty efficient interaction mechanism. In the following we therefore emulate a screened fluid flow by a modified collision kernel of the multi particle collision method, and study the effect on the emergence of a density wave.

One should always keep in mind that our two-dimensional model is only an approximation of an actual three-dimensional system, where the filaments are confined to a quasi two-dimensional layer close to a no-slip boundary. Due to the proximity to this no-slip wall, the fluid feels a strong drag from the stationary wall. So imagine an initially moving fluid streaming over this no-slip wall, then the fluid would quickly[5] come to a halt. In other words, the initial momentum of the fluid particles dissipates out of the system — into the no-slip wall. It is possible to emulate this dissipation of momentum in the collision step of the MPC hydrodynamics. Remember the general form of the MPC collision in (2.7) from section 2.1.1,

$$\boldsymbol{p}_i' = \frac{m_i}{M_c}\boldsymbol{P}_c + \boldsymbol{\Omega}\big[\boldsymbol{p}_i\big] \ .$$

The crucial point of the collision operator was to conserve the fluid momentum on the level of a collision cell. Now we modify this collision prescription to

$$\boldsymbol{p}_i' = \gamma\frac{m_i}{M_c}\boldsymbol{P}_c + \boldsymbol{\Omega}\big[\boldsymbol{p}_i\big] \ , \tag{5.2}$$

where γ is a friction coefficient in the range $\gamma \in \,]0,\,1]$. Effectively, this amounts to a wall friction that is proportional to the local speed of the fluid, which is very similar to the dissipated momentum in an actual three-dimensional fluid layer. Note that this modified collision kernel dissipates kinetic energy, so that the fluid temperature would decrease without a thermostat. The Andersen-thermostat variant of MPC that is used throughout this thesis, has such a thermostat implicit in its collision operator $\boldsymbol{\Omega}$.

For a more intuitive understanding of the friction coefficient we would like to express the friction coefficient as a length l_h which corresponds to the range of the hydrodynamic interaction. We define this length to be

$$l_h \equiv -\log\gamma/v_T \qquad \text{or} \qquad \gamma \equiv \mathrm{e}^{-v_T/l_h} \tag{5.3}$$

where v_T is the thermal speed of a particle $v_T \approx \sqrt{k_BT/m_f}$, and m_f is the mass of a fluid particle. This definition aims to be the length after which the speed of a thermal particle of speed v_T has dropped down to v_T/e. Figure 5.11 shows the measured flow speed between two boundaries moving up and down (so-called Lees-Edwards boundary condition), where a linear velocity profile is expected (black dotted line) [101]. By (5.3), the intersection of the data with the dashed horizontal line corresponds to the actual hydrodynamic range l_h. The data show that the hydrodynamic range l_h of the shear flow is only approximately correct for very small $l_h \approx 3$, whereas the flow range for large l_h is apparently overestimated by (5.3). Yet, for large l_h this discrepancy is expected, because the drag from the opposing wall becomes relevant. These details are irrelevant here, because for our purposes it is only important that the range is indeed finite.

In addition, Fig. 5.12 shows the flow field of the fluid around a disk that is dragged at a constant speed through a fluid with $l_h = 3\,a$. Due to the effective friction of the fluid, the flow in remote regions remains small, leading to vortices with backflow of fluid. The range of the induced flow field becomes larger when the hydrodynamic range l_h increases, and becomes completely laminar when $l_h \to \infty$ (see Appendix A.5 on p. 162). To sum up, the modified

[5] How quick depends on the viscosity of the fluid. Because we are at small Reynolds numbers, we may assume that this dissipation of momentum happens rapidly.

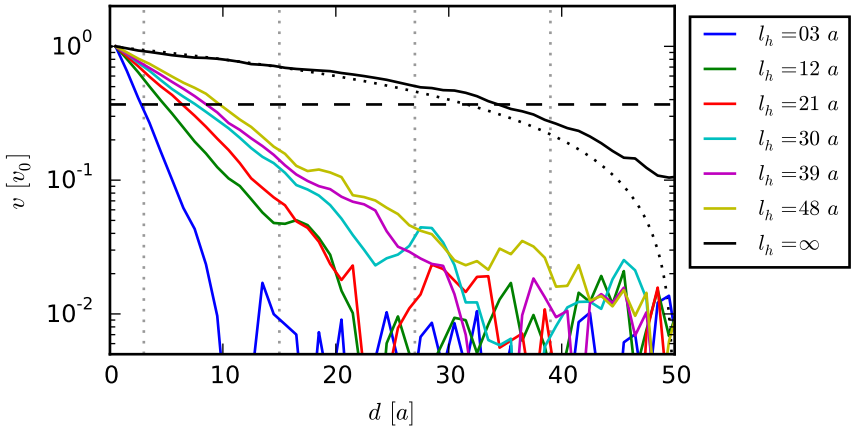

Figure 5.11 | The measured fluid speed for different hydrodynamic range l_h between to walls spaced $100\,a$ apart, moving up and down at a speed v and $-v$, respectively. The black (dotted) line shows the measured (theoretic) velocity profile for $l_h = \infty$ or $\gamma = 1$. The intersection of the data with the dashed lines give the actual hydrodynamic range l_h, which in general is smaller than predicted by (5.3). Note the logarithmic scale for the velocity axis.

collision kernel with a finite hydrodynamic range yields flow fields with a finite range, as was intended. The effects of l_h on the fluid properties such as its viscosity were not explored, but as a first approximation, we may assume that the fluid transport coefficients remain approximately constant.

We applied this modified hydrodynamic interaction with a finite range to our system of driven filaments in order to see if a density wave as in the dry case can be recovered. Figure 5.13 shows the scaling exponents of the number fluctuations, which have proven as a robust measure for the existence of a density wave in the preceding sections. The data show that both cases with hydrodynamic interactions have only modest density fluctuations with $\alpha \leq 1.3$, regardless of the hydrodynamic interaction range. In contrast, the dry case shows a significant jump to large scaling coefficients $\alpha > 1.8$. This finding is surprising, because one could expect that for the extreme case with $l_h = L/3 = 1\,a$ the hydrodynamic interaction becomes weak and the filament interactions are dominated by the contact interactions via $\mathcal{U}_b$. Despite the shorter range, the hydrodynamic interactions are therefore still strong enough to destroy the patterns that were found in the dry case.

In fact, the data for both $l_h = L/3$ and $l_h = \infty$ hardly differ at all, raising the question whether the proposed mechanism to reduce the hydrodynamic range is effective for the system of filaments. Although we have no definite answer, we can speculate about why this may not be the case. So consider a fluid package in front of a propelled disc, and assume it has the same flow speed as the disc, v. The effective friction then decelerates this fluid package so that its speed decreases, $v' < v$. However, because the disc is pushing the fluid by its constant speed, the volume of fluid between the package and the disc shrinks, so that an excess of fluid particles builds up in front of the disc. In two dimensions, this excess of particles can only evade in-plane, leading to a strong in-plane fluid flow with vortices in the proximity of the sphere. Note that the strong drag and backflow must also emerge with finite l_h.

It seems reasonable that the flow pattern between such vortices acts aligning on filaments. This leads to a self-reinforcing cluster growth, because a slightly larger cluster would push its

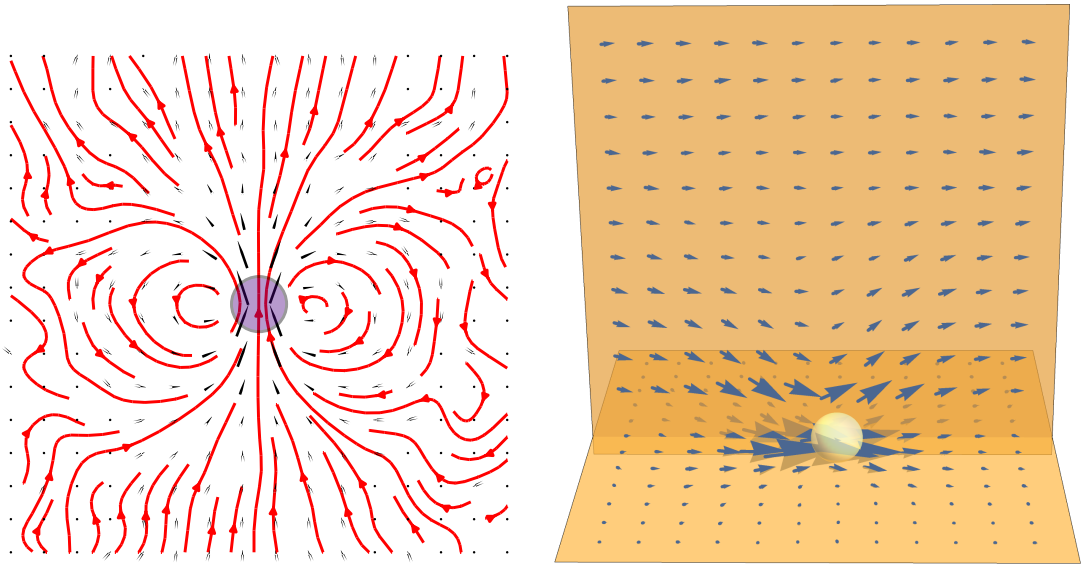

Figure 5.12 | Simulations of a sedimenting sphere of diameter $5\,a$ in a box of side-length $48\,a$. **Left:** The flow field (black arrows) and streamlines (red) for two-dimensional hydrodynamics with a range $l_h = 3\,a$. Note the strong backflow of fluid in the far region of the disc. **Right:** The flow field (blue arrows) of a three-dimensional setup in a parallel and orthogonal plane. The sphere moves close to a no-slip boundary (bottom), whereas the top boundary has slip conditions. The fluid flow at the lower fluid layer is marginal, because the fluid flow can evade into the third dimension.

swirls even farther out, thus aligning even more filaments. However, if the cluster has crossed a certain threshold size, the cluster of filaments would push the whole fluid in its direction. As soon as the fluid flow becomes global, *all* filaments become aligned, regardless how far they were away from the seed cluster. In particular, the filaments are not required to interact with a high-density filament region.

In summary, we have shown an MPC variant that generates hydrodynamics with a finite range. Despite the finite range however, the long-ranged hydrodynamic interaction remains the dominant interaction mechanism between filaments, so that the density waves from the dry case do not emerge.

5.3.2 Wet systems with full 3D hydrodynamics

The complete lack of density waves in our two-dimensional system with hydrodynamic interactions is unsatisfactory, because it contradicts the motility assay experiment which *is* in aqueous solution. However, the preceding section discussed that two-dimensional hydrodynamics is peculiar, because a fluid flow must necessarily stay in the same plane as the filaments. This chapter will therefore consider true three-dimensional simulations of the fluid layer, to see if density waves can be recovered.

Section 2.1.2 already discussed the simulation setup with a focus on the technical detail, so we need only briefly recapitulate the setup. Similarly to the two-dimensional setup, the filaments are confined to a plane $z = 0.5\,a$ close to the lower boundary. The in-plane motion

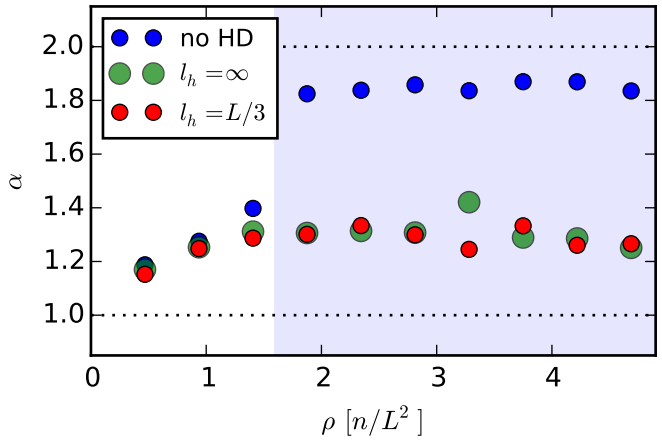

Figure 5.13 | Scaling exponents α of the number fluctuations as a function of filament density ρ for $l_p = 2\,L$, $\mathcal{U}_b = 1.6\,k_BT$, and $l_h = L/3$. In the dry case (blue dots), a density wave consistently forms for $\rho \gtrsim 1.6\,n/L^2$ (shaded region) so that α jumps to values close to 2. In the wet cases of $l_h = \infty$ (green dots) and $l_h = L/3$ (red dots), the number fluctuations remain much smaller than 2, showing that no density wave formed.

then closely resembles the two-dimensional setup, because the simulation volume is again periodic in the x and y directions. In contrast, the z-direction is bounded by two solid walls, where the upper wall has slip boundary conditions, and was chosen to emulate the behavior of a much larger fluid bulk. The lower wall on the other hand should have a large drag because it corresponds to a real no-slip boundary in the experiment. For the lowest possible slip velocities, we employ the bounce-back boundary condition in conjunction with virtual ghost particles (see 2.1.2 for details).

Because it is computationally rather expensive to model the increased number of fluid particles which are necessary to model the three-dimensional fluid, we only looked at a few examples instead of a full parameter sweep. In addition, we only considered simulation boxes of $120 \times 120 \times 10$ collision cells, which is only half as many in the x and y direction as in the two-dimensional case. Figures 5.14 & 5.15 (top) show tSNE-plots of the filament systems at three different densities. Each of these examples shows the emergence of a density wave. In fact, it seems that the density waves even emerge at earlier simulation times than in the dry case. More importantly, the density waves also emerge at much smaller filament densities. For example, in Fig. 5.14 (top) the density is only $\rho = 0.94\,n/L^2$ where in the dry case no density wave formed (see e.g. Fig. 4.11 on p. 59). Consequently, these examples not only demonstrate the existence of density waves in systems with fully three-dimensional hydrodynamic interactions, but also show that these density waves are more stable than in the dry case.

Now consider the streamlines of the fluid flow in these examples. The fluid in the filament layer (red streamlines) only co-moves with the cluster in high filament density regions. On the other hand, where the filament density is low, the fluid flow stops and becomes random, showing as entangled and broken streamlines. Such a broken fluid flow in the plane is only possible in three dimensions, where the fluid flow can evade into the third dimension. Although not visible in the figures, the fluid flow in the top z-layer (blue streamlines) is also aligned with the cluster movement and not anti-aligned. Therefore, there is no a back-flow

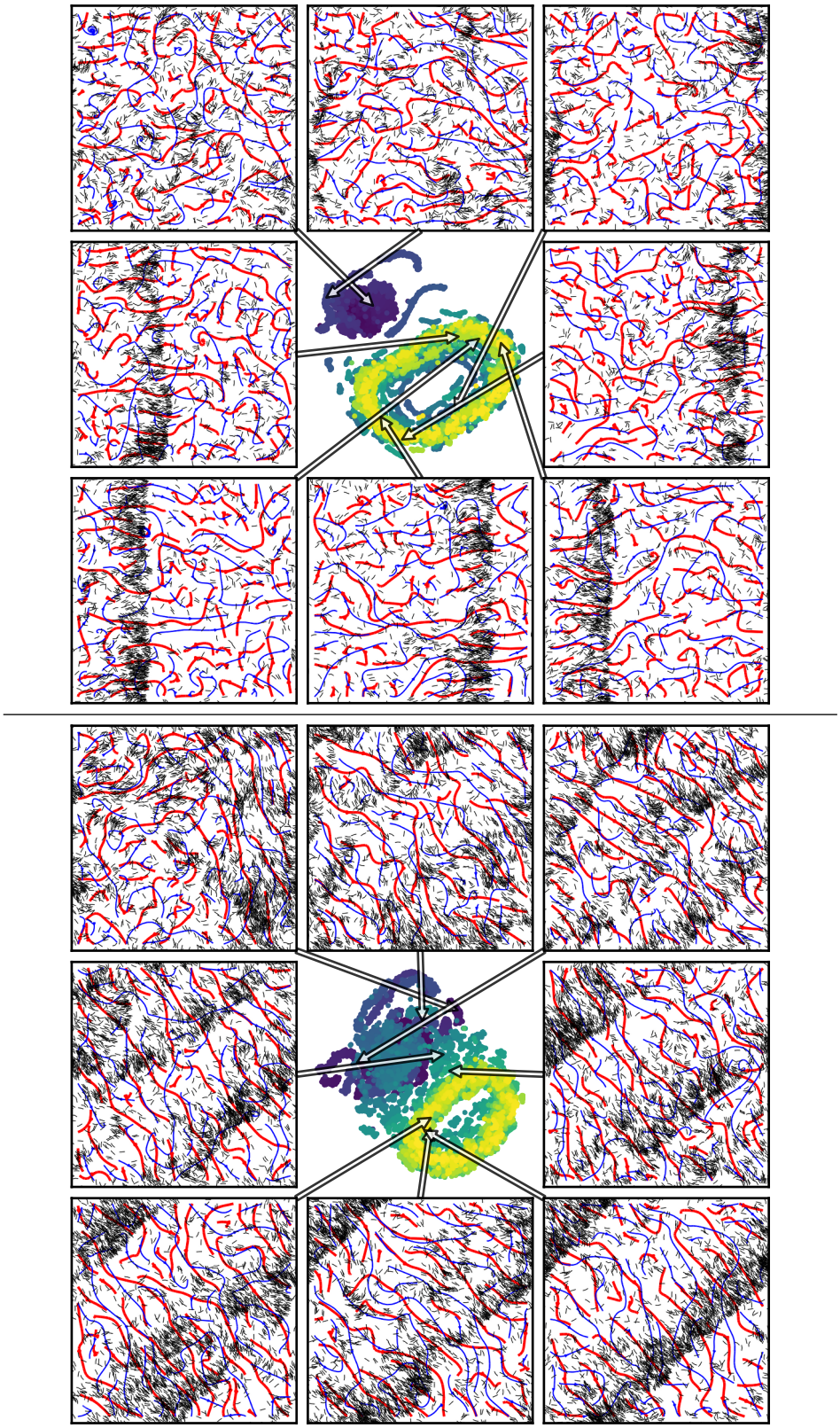

Figure 5.14 | Top: $\rho = 0.94\, n/L^2$, $\mathcal{U}_b = 1.6\, k_B T$, $l_p = 2\, L$ **Bottom:** $\rho = 1.88\, n/L^2$, $\mathcal{U}_b = 1.6\, k_B T$, $l_p = 2\, L$. More explanation about these plots is found in Appendix A.2.3 on page 157.

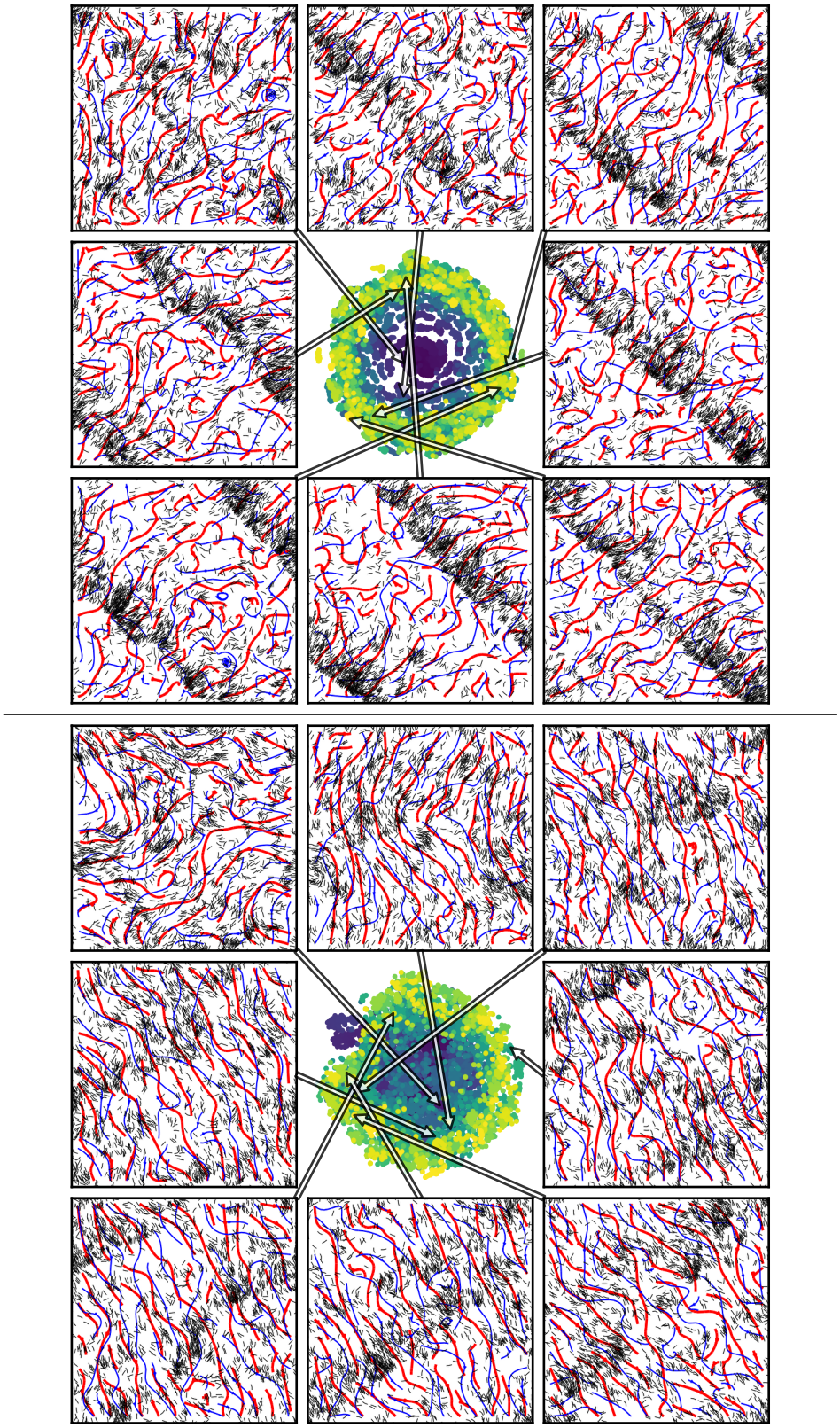

Figure 5.15 | Top: $\rho = 1.41\, n/L^2$, $\mathcal{U}_b = 1.6\, k_B T$, $l_p = 2\, L$ **Bottom:** Same as the top panel, but with increased fluid slip at the boundary (no ghost particles). More explanation about these plots is found in Appendix A.2.3 on page 157.

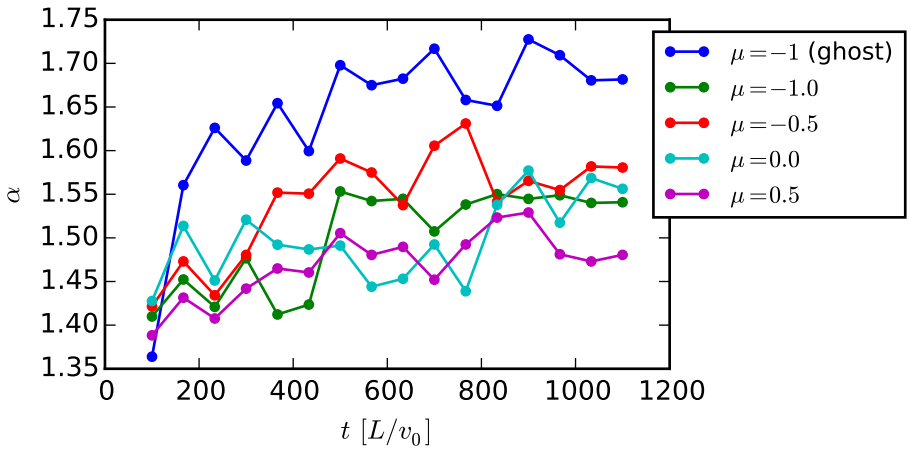

Figure 5.16 | The observed scaling exponents of the number fluctuations in a three-dimensional setup scanned over time for different different slip boundary conditions. The factor μ controls the momentum that is transfered to the boundary when a fluid particle collides with the wall via $\boldsymbol{p}'_{\parallel} = \mu\, \boldsymbol{p}_{\parallel}$ (see Fig. 2.3 for details). The line labeled by *ghost* uses ghost particle to further reduce the slip velocity (see Fig. 2.4 for details). Note that there is a synchronous overshoot at small times that is a consequence of the random orientation initial condition.

of fluid in the top layers, but the fluid rather funnels over the obstructing non-moving fluid region. The in-plane vortex of a sedimenting disc in two dimensions (Fig. 5.12 left) therefore becomes a revolving fluid tube over the density wave.

Unfortunately, the thermal noise in the available data made it impossible to properly measure the fluid flow that is generated by a moving density wave. Therefore, for a better understanding of the flow field we instead measured the flow field of a sphere that moves at a constant speed along a no-slip boundary. Figure 5.12 (right) shows that the in-plane flow field quickly drops to zero when moving away from the sphere, which is in accordance to our observations of the streamlines in Fig. 5.14. In addition, the vertical cut of the simulation volume reveals that the fluid which is pushed by the sphere moves upwards into higher layers where the wall drag is smaller. Likewise, on the rear end of the sphere, the fluid is pulled down to from higher layers. For the large-scale flow it does not matter whether the fluid is pushed by a sphere or dragged along by a cluster of moving filaments. Therefore, the flow field of the filaments must resemble this example of a moving sphere.

Having demonstrated that a density wave emerges with no-slip boundary conditions, this immediately raises the question how important the no-slip boundary condition is. Without a strict no-slip boundary condition at the lower wall, one has to expect that the flow field extends further in-plane. In other words, a larger slip velocity should make the hydrodynamic interactions more similar to the two-dimensional fluid and thus interpolates between these two cases. Consequently, with increased slip the hydrodynamic interactions among filaments become more long-ranged and stronger, so that the density wave could become unstable. Our MPC simulation can test this hypothesis, by gradually allowing for larger slip velocities at the lower boundary. For example, a rather large increase of slip velocity is obtained when no ghost particles are inserted at wall cell. Furthermore, the drag can be fine-controlled by

gradually increasing μ in the boundary condition $\boldsymbol{p}'_{\parallel} = \mu\,\boldsymbol{p}_{\parallel}$ for fluid particles that hit the wall (see 2.1.2).

We therefore focused on the case $\rho = 1.41\,n/L^2$ from Fig. 5.15 and varied μ from -1 to $+1/2$. For example, Fig. 5.15 (bottom) shows the observed density pattern for $\mu = -1$ but without ghost particles. Note that apart from the slip velocity, all simulation parameters are identical in the top and bottom example of this figure. Indeed, the plot shows that the increased slip velocity also makes the density wave more unstable and the filaments are much more spread out. Furthermore, as expected, the fluid streamlines extend much further, especially in the filament fluid layer.

To quantify the reduction in filament clustering, we used the number fluctuations as defined in 4.2.2. Figure 5.16 shows the scaling exponents of the number fluctuations for different μ over time. Although the data fluctuate over time, there is an apparent drop of the number fluctuations when ghost particles are omitted, which is in accordance to our observation from Fig. 5.15. With further increasing μ, there is no conclusive trend up to $\mu \approx 0$, but it seems that for $\mu > 0$ the number fluctuations decrease further. It seems reasonable that for $\mu = 1$, the system behaves similar to the two-dimensional setup where the number fluctuations for otherwise identical parameters are $\alpha \approx 1.3$.

In summary, we have demonstrated that the density waves, which were absent in two-dimensional hydrodynamics, are recovered when the fluid is modelled in three dimensions. In fact, the density wave emerged quickly and even formed at filament densities where we found no density wave at all in the dry system. In contrast, the large-scale flow states (vortex and zig-zag) could not form, because the boundary drag inhibits stable hydrodynamic flows. By increasing the slip velocity at the lower boundary, we found that the number fluctuations of the filament density drop considerably and the filaments were much more evenly distributed. This shows that non-confined long-range hydrodynamic interactions among filaments are incompatible with large density fluctuations.

5.4 Summary of the wet system

In this chapter, we examined a system of many filaments that interacted both via a short-ranged contact interaction *and* via a long-randed hydrodynamic interaction. As for the dry system, we looked at the dependence on filament density ρ, persistence length l_p, and interaction strength $\mathcal{U}_b$. In addition, we also considered different variants of the hydrodynamic interaction, namely two- and three-dimensional fluids and a two-dimensional fluid with a finite range.

A full parameter scan was computationally only feasible for two-dimensional fluids. Regardless of the filament density ρ and filament properties (l_p and $\mathcal{U}_b$) the filaments were always mostly homogeneously distributed with a small scaling coefficient in the number fluctuations around 1.3. For comparison, the number fluctuations of the dry system had a scaling coefficient around 1.9. Apart from that, the filaments always moved in a coordinated fashion, for example completely laminar or in vortices. Beside these two expectable flow patterns, we also found a surprising zig-zag flow pattern. This zig-zag pattern may be related to the instability of ordered self-propelled particles with hydrodynamic interactions reported by [36, 102, 103].

For example, Aditi Simha et al. predict wavelike excitations in ordered suspensions of self-propelled particles and a convective instability of low Reynolds number suspensions [102]. To what extent their work applies to extended filaments as in our model, and why both zig-zag and laminar flow seem to be stable is left for future investigation.

One could argue that a faithful representation of the fluid interactions must also respect the conservation of angular momentum, which is violated by the MPC variant which was employed above [72, 73]. However, Appendix A.4 presents the results for an angular momentum conserving MPC-variant, which are virtually identical to the above presented data.

Because the lack of density waves stands in contrast to the actomyosin motility assay, we extended the two-dimensional fluid by an effective wall drag that yields a finite hydrodynamic range. Despite a very short hydrodynamic range, this two-dimensional variant gave virtually identical results as the conventional 2D fluid.

Finally, with a three-dimensional fluid, the density wave pattern from the dry system was recovered. Here, the density wave even formed faster and at lower densities than in the dry system. By allowing for larger slip velocities at the boundaries, we found that the density wave becomes unstable and the filaments become more evenly spread out. We concluded that a non-confined long-range hydrodynamic interaction among filaments is incompatible with large density fluctuations.

Nevertheless, this shows that hydrodynamic interactions could be the essential aligning mechanism between actin filaments in the actomyosin motility assay. In light of the marginal collision polarity of binary filament encounters [57], this would require primordial nucleations to trigger the emergence of a density wave [104]: Only a nucleation of a critical size may create a flow field which is strong enough to recruit further filaments to the cluster. At this stage this hypothesis is however only speculative and requires further evidence.

6 Discussion & outlook

In this part, we developed a model of driven filaments that is inspired by the actomyosin motility assay [10, 58]. Our model allows to selectively enable hydrodynamic interactions between the filaments, thereby allowing to explore the consequences of a long-ranged hydrodynamic interaction on collective effects. The filaments in this model are represented by worm-like chains with FENE bonds and a soft repulsion of strength $\mathcal{U}_b$. By construction, these filaments move in a snake-like fashion at a constant speed.

To characterize the filament motion, we first looked at the path of a single filament. We found that the path of an isolated filament can be understood as a persistent random walk whose persistence length L_p roughly equals the persistence length of a free filament, l_p. This is similar to the actomyosin motility assay where the persistence length of the path is also in the same order as the persistence length of actin filaments.

As a next step towards systems of many filaments, we examined binary filament collisions in two-dimensional setups. Without hydrodynamic interactions, the signature of the filament collisions had a nematic component with $\Theta_{out} \gtrless \Theta_{in}$ for $\Theta_{in} \gtrless \pi/2$, but also an aligning polar component. The overall angular change depended on the interaction strength $\mathcal{U}_b$ and was vanishingly small for $\mathcal{U}_b = 0\,k_BT$. Our findings showed that for $\mathcal{U}_b \lesssim 1\,k_BT$, two filaments can easily cross each other. When enabling hydrodynamic interactions, the nematic signature of the direct filament collision remained almost unchanged, while the polarity of the interaction was greatly amplified. Furthermore, we saw that the hydrodynamic interaction remains effective over a much greater range than the contact interaction. Comparing these results to the measurements of Suzuki et al. showed that binary actin interactions of the actomyosin motility assay are best reproduced by the dry system [57].

Finally, we examined systems with up to 30 000 filaments to explore the collective effects of the filaments therein. To the best of our knowledge, these are the largest simulations of driven semi-flexible filaments so far. For the analysis of these large systems, we used standard measures such as the polarity of the filaments or the number fluctuations of the density distribution. In addition to these standard measures, we also introduced a new measure for the order in the system via the Kullback-Leibler divergence. Furthermore, to measure the density of the low-density phase, we invented an estimator that is based on count statistics in equally-sized regions. Finally, for a qualitative representation of the time-evolution of these systems, we adapted the tSNE-method, which is a stochastic embedding method that visualizes high-dimensional data in two dimensions, to the analysis of time series. The tSNE-method can also be used for pattern characterization in other biological contexts.

To this end, we first examined systems *without* hydrodynamic interactions, which are almost equivalent to Langevin dynamics. At low filament density, the filaments in these systems were disordered and mostly homogeneously distributed. With growing filament density, the filaments increasingly clustered into bigger packages of aligned filaments. At a certain density

threshold, which depends on the microscopic filament parameters, the filaments underwent a phase transition where a disordered low-density gas phase separated from an ordered, system-spanning, tightly-packed high-density region that swept the system — in short, a density wave. This density wave encompassed the major fraction of all filaments, so that the total polarity became very high. More filaments then only increased the width of this density wave, whereas the density of the low-density region stayed constant. At a second, larger density threshold, the density wave became so spread out that the disordered gas phase completely vanished. This second phase transition goes along with a decrease in the number fluctuations in the density of the filaments.

Second, we examined systems *with* hydrodynamic interactions, where the fluid was modelled via Multiparticle Collision dynamics (MPC). For numerical feasibility, we first considered two-dimensional MPC fluids. In contrast to the dry systems, we found no large density fluctuations for two-dimensional fluids — regardless of the filament density and filament properties. However, all filaments moved in a coordinated fashion, be it as a laminar flow or in vortices. Beside these expectable flow patterns, there was also a surprising zig-zag flow pattern where the filaments and the fluid flow abruptly changed their direction. Which of these flow patterns emerged, seemed to be random. These results remained virtually the same with angular momentum conserving variants of MPC (Appendix A.4).

To see how density waves can be recovered, we modified the MPC method so that the hydrodynamic interactions are screened. However, even with strongly screened hydrodynamics, the screened and unscreened two-dimensional systems had an identical phenomenology. Even quantitatively, the number fluctuations of the density were virtually the same.

Finally, we made the fluid fully three-dimensional, while the filaments remained confined to a two-dimensional plane close to a no-slip wall. In that case, we recovered the density waves of the dry system, which even formed faster and at lower filament densities than in the dry system. Thus we showed that hydrodynamic interactions do stabilize the density wave. Furthermore, our simulation allowed to gradually increase the fluid slip velocity at the walls, upon which the density wave destabilized and the filaments became much more evenly spread out. We concluded that a non-confined long-range hydrodynamic interaction among filaments is incompatible with large density fluctuations.

Because our model is inspired by the actomyosin motility assay, this begs a comparison to the phenomenology of the experiment. Schaller et al. report two critical densities [10]: below a critical density ρ_c, the driven actin filaments are disordered and homogeneous. Above a second threshold ρ^*, the actin filaments separate into density waves and a disordered low-density phase. In addition, for intermediate actin densities $\rho_c < \rho < \rho^*$, they report another regime with compact, long-lived clusters having diameters of 50–200 μm (corresponding to $\approx$ 5–20 L).

With respect to the density wave, this phenomenology is similar to our model without hydrodynamic interactions or with the three-dimensional fluid. However, the intermediate regime with long-lived compact clusters was not found. Even though there was clustering on a small scale in the dry system (high $\mathcal{U}_b$ and low densities, e.g. Fig. 4.1 bottom), these clusters were only transient and not long-lived as in the experiment. Because we currently lack data for very low densities with the three-dimensional fluid, there is nevertheless a chance that these clusters can be found there.

It is peculiar that the phenomenology of our two-dimensional hydrodynamic systems is so vastly different from the dry and three-dimensional case. We presume this to be due to the unscreened long-ranged fluid interactions in two-dimensional fluids. Consequently, collective systems with a truly long-range interaction are a completely different class than systems with only short-ranged interactions. So why are systems with two- and three-dimensional fluid interactions apparently in different classes, even though three-dimensional hydrodynamics is also long-ranged? The reason is that in three dimensions, a fluid flow can evade into the third dimension so that the hydrodynamic flow close to a no-slip boundary remains negligible. Only at very short ranges, the hydrodynamic interaction therefore plays a role. These findings imply that in the actomyosin motility assay, the hydrodynamic interactions must also be screened. Indeed, Schaller et al. report hydrodynamic interactions in the cluster phase $\rho_c < \rho < \rho^*$ where the clusters come very close before being deflected [58]. This finding can be well explained by a screened hydrodynamic flow field.

Furthermore, one may speculate that the hydrodynamic interactions in the actomyosin motility assay are actually essential. Remember that Suzuki et al. reported an almost entirely nematic interaction in binary filament encounters, which necessarily means that the flow field of a single actin filament is marginal. However, if a primordial nucleation of filaments is large enough to create a relevant flow field, the hydrodynamic interaction could recruit further filaments to the cluster and stabilize the structure [104].

Our model can and should be extended in a few obvious ways that were out of scope of this current work. First, the most obvious question — which does not even require further work — is whether the regime with compact long-lived clusters can be reproduced using the three-dimensional fluid. Another important check is to consider the three-dimensional case without contact interactions, to see if the same phenomenology is observed. If it is not, this can finally answer the question whether it is contact or hydrodynamic interactions that cause the density waves in the actomyosin motility assay. At the time of writing, these results were unfortunately not available. Next, we have only considered a single filament length in this work. It will be interesting to see whether longer filaments have other consequences than only a mere rescaling of length. Furthermore, due to the spherical potential around the filament beads, our filaments had a considerable roughness that made filament collisions aligning. Because Suzuki et al. report a mostly nematic interaction, the current filament model should be extended to a more nematic character. Last but not least, the three-dimensional case can also improved by a more realistic filament propulsion that is based on forces instead of an imposed propulsion speed.

Apart from modifying the filament properties, this model can also be used to investigate questions of a different kind. For example, the density profiles of the density waves could be analyzed and compared to other works [30, 31]. Furthermore, one can examine the behavior of binary mixtures with filaments of different properties, as has been explored for a similar system [47]. Besides, we have only considered the emergence of density waves from a disordered initial state. In a next step, the stability of artificially prepared ordered states should be determined, which should be possible to compare to theoretic predictions [102].

Finally, we can also speculate about our two-dimensional wet system. We argued that this system is of a completely different class due to its truly long-range interactions. It would be ideal to have an experimental counterpart to this situation, but unfortunately, we do not know

of any matching experiment. Maybe a clever experimentalist will one day realize analogous conditions in an experiment.

The ultimate goal, however, is to establish a comprehensive theory of active matter. Until such a theory is found, simulations such as these give us clues what to look out for.

Bibliography Part I

[1] N.D. Mermin and H. Wagner. *Absence of Ferromagnetism or Antiferromagnetism in One- or Two-Dimensional Isotropic Heisenberg Models*. In: **Physical Review Letters** 17.22 (Nov. 1966), pp. 1133–1136. DOI: 10.1103/PhysRevLett.17.1133 (cit. on p. 3).

[2] P.C. Hohenberg. *Existence of Long-Range Order in One and Two Dimensions*. In: **Physical Review** 158.2 (June 1967), pp. 383–386. DOI: 10.1103/PhysRev.158.383 (cit. on p. 3).

[3] T. Vicsek et al. *Novel Type of Phase Transition in a System of Self-Driven Particles*. In: **Physical Review Letters** 75.6 (Aug. 1995), pp. 1226–1229. DOI: 10.1103/PhysRevLett.75.1226 (cit. on pp. 3, 4).

[4] J. Toner and Y. Tu. *Long-Range Order in a Two-Dimensional Dynamical* XY *Model: How Birds Fly Together*. In: **Physical Review Letters** 75.23 (Dec. 1995), pp. 4326–4329. DOI: 10.1103/PhysRevLett.75.4326 (cit. on pp. 3, 4).

[5] J. Toner and Y. Tu. *Flocks, herds, and schools: A quantitative theory of flocking*. In: **Physical Review E** 58.4 (Oct. 1998), pp. 4828–4858. DOI: 10.1103/PhysRevE.58.4828 (cit. on p. 3).

[6] J. Toner, Y. Tu, and S. Ramaswamy. *Hydrodynamics and phases of flocks*. In: **Annals of Physics**. Special Issue 318.1 (July 2005), pp. 170–244. DOI: 10.1016/j.aop.2005.04.011 (cit. on p. 3).

[7] T. Vicsek and A. Zafeiris. *Collective motion*. In: **Physics Reports**. Collective motion 517.3–4 (Aug. 2012), pp. 71–140. DOI: 10.1016/j.physrep.2012.03.004 (cit. on p. 3).

[8] M.C. Marchetti et al. *Hydrodynamics of soft active matter*. In: **Reviews of Modern Physics** 85.3 (July 2013), pp. 1143–1189. DOI: 10.1103/RevModPhys.85.1143 (cit. on pp. 3, 4).

[9] J. Elgeti, R.G. Winkler, and G. Gompper. *Physics of microswimmers—single particle motion and collective behavior: a review*. In: **Reports on Progress in Physics** 78.5 (2015), p. 056601. DOI: 10.1088/0034-4885/78/5/056601 (cit. on p. 3).

[10] V. Schaller et al. *Polar patterns of driven filaments*. In: **Nature** 467.7311 (Sept. 2010), pp. 73–77. DOI: 10.1038/nature09312 (cit. on pp. 3, 4, 7, 14, 26, 75, 101, 102).

[11] Y. Sumino et al. *Large-scale vortex lattice emerging from collectively moving microtubules*. In: **Nature** 483.7390 (Mar. 2012), pp. 448–452. DOI: 10.1038/nature10874 (cit. on pp. 3, 4).

[12] T. Sanchez et al. *Spontaneous motion in hierarchically assembled active matter*. In: **Nature** 491.7424 (Nov. 2012), pp. 431–434. DOI: 10.1038/nature11591 (cit. on p. 3).

[13] F.C. Keber et al. *Topology and dynamics of active nematic vesicles*. In: **Science** 345.6201 (Sept. 2014), pp. 1135–1139. DOI: 10.1126/science.1254784 (cit. on p. 3).

[14] K. H. Nagai et al. *Collective Motion of Self-Propelled Particles with Memory*. In: **Physical Review Letters** 114.16 (Apr. 2015), p. 168001. DOI: 10.1103/PhysRevLett.114.168001 (cit. on p. 3).

[15] J. Palacci et al. *Sedimentation and Effective Temperature of Active Colloidal Suspensions*. In: **Physical Review Letters** 105.8 (Aug. 2010), p. 088304. DOI: 10.1103/PhysRevLett.105.088304 (cit. on p. 3).

[16] M. Enculescu and H. Stark. *Active Colloidal Suspensions Exhibit Polar Order under Gravity*. In: **Physical Review Letters** 107.5 (July 2011), p. 058301. DOI: 10.1103/PhysRevLett.107.058301 (cit. on p. 3).

[17] A. Bricard et al. *Emergence of macroscopic directed motion in populations of motile colloids*. In: **Nature** 503.7474 (Nov. 2013), pp. 95–98. DOI: 10.1038/nature12673 (cit. on p. 3).

[18] A. Bricard et al. *Emergent vortices in populations of colloidal rollers*. In: **Nature Communications** 6 (June 2015), p. 7470. DOI: 10.1038/ncomms8470 (cit. on p. 3).

[19] S. Ramaswamy, R. A. Simha, and J. Toner. *Active nematics on a substrate: Giant number fluctuations and long-time tails*. In: **EPL (Europhysics Letters)** 62.2 (Apr. 2003), p. 196. DOI: 10.1209/epl/i2003-00346-7 (cit. on pp. 3, 56).

[20] V. Narayan, S. Ramaswamy, and N. Menon. *Long-Lived Giant Number Fluctuations in a Swarming Granular Nematic*. In: **Science** 317.5834 (July 2007), pp. 105–108. DOI: 10.1126/science.1140414 (cit. on p. 3).

[21] A. Kudrolli et al. *Swarming and Swirling in Self-Propelled Polar Granular Rods*. In: **Physical Review Letters** 100.5 (Feb. 2008), p. 058001. DOI: 10.1103/PhysRevLett.100.058001 (cit. on p. 3).

[22] J. Deseigne, O. Dauchot, and H. Chaté. *Collective Motion of Vibrated Polar Disks*. In: **Physical Review Letters** 105.9 (Aug. 2010), p. 098001. DOI: 10.1103/PhysRevLett.105.098001 (cit. on p. 3).

[23] C. Dombrowski et al. *Self-Concentration and Large-Scale Coherence in Bacterial Dynamics*. In: **Physical Review Letters** 93.9 (Aug. 2004), p. 098103. DOI: 10.1103/PhysRevLett.93.098103 (cit. on p. 3).

[24] L. H. Cisneros et al. *Fluid dynamics of self-propelled microorganisms, from individuals to concentrated populations*. In: **Experiments in Fluids** 43.5 (Oct. 2007), pp. 737–753. DOI: 10.1007/s00348-007-0387-y (cit. on p. 3).

[25] H. H. Wensink et al. *Meso-scale turbulence in living fluids*. In: **Proceedings of the National Academy of Sciences** 109.36 (Sept. 2012), pp. 14308–14313. DOI: 10.1073/pnas.1202032109 (cit. on p. 3).

[26] J. Dunkel et al. *Fluid Dynamics of Bacterial Turbulence*. In: **Physical Review Letters** 110.22 (May 2013), p. 228102. DOI: 10.1103/PhysRevLett.110.228102 (cit. on p. 3).

[27] V. Bratanov, F. Jenko, and E. Frey. *Self-organization in active fluids: A new class of turbulence*. In: (2015). Submitted (cit. on pp. 3, 4).

[28] J. Toner. *Reanalysis of the hydrodynamic theory of fluid, polar-ordered flocks*. In: **Physical Review E** 86.3 (Sept. 2012), p. 031918. DOI: 10.1103/PhysRevE.86.031918 (cit. on p. 3).

[29] S. Ramaswamy. *The Mechanics and Statistics of Active Matter*. In: **Annual Review of Condensed Matter Physics** 1.1 (2010), pp. 323–345. DOI: 10.1146/annurev-conmatphys-070909-104101 (cit. on p. 3).

[30] T. Ihle. *Invasion-wave-induced first-order phase transition in systems of active particles*. In: **Physical Review E** 88.4 (Oct. 2013), p. 040303. DOI: 10.1103/PhysRevE.88.040303 (cit. on pp. 4, 103).

[31] F. Thüroff, C. A. Weber, and E. Frey. *Numerical Treatment of the Boltzmann Equation for Self-Propelled Particle Systems*. In: **Physical Review X** 4.4 (Nov. 2014), p. 041030. DOI: 10.1103/PhysRevX.4.041030 (cit. on pp. 4, 75, 103).

[32] G. Grégoire and H. Chaté. *Onset of Collective and Cohesive Motion*. In: **Physical Review Letters** 92.2 (Jan. 2004), p. 025702. DOI: 10.1103/PhysRevLett.92.025702 (cit. on pp. 4, 75).

[33] K. Kruse et al. *Generic theory of active polar gels: a paradigm for cytoskeletal dynamics*. In: **The European Physical Journal E** 16.1 (Jan. 2005), pp. 5–16. DOI: 10.1140/epje/e2005-00002-5 (cit. on p. 4).

[34] J. Dunkel et al. *Minimal continuum theories of structure formation in dense active fluids*. In: **New Journal of Physics** 15.4 (2013), p. 045016. DOI: 10.1088/1367-2630/15/4/045016 (cit. on p. 4).

[35] J. Słomka and J. Dunkel. *Generalized Navier-Stokes equations for active suspensions*. In: **The European Physical Journal Special Topics** 224.7 (July 2015), pp. 1349–1358. DOI: 10.1140/epjst/e2015-02463-2 (cit. on p. 4).

[36] L. Giomi and M. C. Marchetti. *Polar patterns in active fluids*. In: **Soft Matter** 8.1 (Dec. 2011), pp. 129–139. DOI: 10.1039/C1SM06077E (cit. on pp. 4, 98).

[37] E. Bertin, M. Droz, and G. Grégoire. *Boltzmann and hydrodynamic description for self-propelled particles*. In: **Physical Review E** 74.2 (Aug. 2006), p. 022101. DOI: 10.1103/PhysRevE.74.022101 (cit. on p. 4).

[38] E. Bertin, M. Droz, and G. Grégoire. *Hydrodynamic equations for self-propelled particles: microscopic derivation and stability analysis*. In: **Journal of Physics A: Mathematical and Theoretical** 42.44 (2009), p. 445001. DOI: 10.1088/1751-8113/42/44/445001 (cit. on p. 4).

[39] T. Ihle. *Kinetic theory of flocking: Derivation of hydrodynamic equations*. In: **Physical Review E** 83.3 (Mar. 2011), p. 030901. DOI: 10.1103/PhysRevE.83.030901 (cit. on p. 4).

[40] H. Chaté et al. *Collective motion of self-propelled particles interacting without cohesion*. In: **Physical Review E** 77.4 (Apr. 2008), p. 046113. DOI: 10.1103/PhysRevE.77.046113 (cit. on p. 4).

[41] M. R. D'Orsogna et al. *Self-Propelled Particles with Soft-Core Interactions: Patterns, Stability, and Collapse*. In: **Physical Review Letters** 96.10 (Mar. 2006), p. 104302. DOI: 10.1103/PhysRevLett.96.104302 (cit. on p. 4).

[42] H. Chaté, F. Ginelli, and R. Montagne. *Simple Model for Active Nematics: Quasi-Long-Range Order and Giant Fluctuations*. In: **Physical Review Letters** 96.18 (May 2006), p. 180602. DOI: 10.1103/PhysRevLett.96.180602 (cit. on pp. 4, 56).

[43] F. Ginelli et al. *Large-Scale Collective Properties of Self-Propelled Rods*. In: **Physical Review Letters** 104.18 (May 2010), p. 184502. DOI: 10.1103/PhysRevLett.104.184502 (cit. on p. 4).

[44] F. Peruani et al. *Polar vs. apolar alignment in systems of polar self-propelled particles*. In: **Journal of Physics: Conference Series** 297.1 (2011), p. 012014. DOI: 10.1088/1742-6596/297/1/012014 (cit. on p. 4).

[45] F. Peruani, A. Deutsch, and M. Bär. *Nonequilibrium clustering of self-propelled rods*. In: **Physical Review E** 74.3 (Sept. 2006), p. 030904. DOI: 10.1103/PhysRevE.74.030904 (cit. on p. 4).

[46] Y. Yang, V. Marceau, and G. Gompper. *Swarm behavior of self-propelled rods and swimming flagella*. In: **Physical Review E** 82.3 (Sept. 2010), p. 031904. DOI: 10.1103/PhysRevE.82.031904 (cit. on p. 4).

[47] M. Abkenar et al. *Collective behavior of penetrable self-propelled rods in two dimensions*. In: **Physical Review E** 88.6 (Dec. 2013), p. 062314. DOI: 10.1103/PhysRevE.88.062314 (cit. on pp. 4, 103).

[48] S.R. McCandlish, A. Baskaran, and M.F. Hagan. *Spontaneous segregation of self-propelled particles with different motilities*. In: **Soft Matter** 8.8 (Feb. 2012), pp. 2527–2534. DOI: 10.1039/C2SM06960A (cit. on p. 4).

[49] F.D.C. Farrell et al. *Pattern Formation in Self-Propelled Particles with Density-Dependent Motility*. In: **Physical Review Letters** 108.24 (June 2012), p. 248101. DOI: 10.1103/PhysRevLett.108.248101 (cit. on p. 4).

[50] J. Barré et al. *Motility-Induced Phase Separation of Active Particles in the Presence of Velocity Alignment*. In: **Journal of Statistical Physics** 158.3 (May 2014), pp. 589–600. DOI: 10.1007/s10955-014-1008-9 (cit. on p. 4).

[51] M.E. Cates and J. Tailleur. *Motility-Induced Phase Separation*. In: **Annual Review of Condensed Matter Physics** 6.1 (2015), pp. 219–244. DOI: 10.1146/annurev-conmatphys-031214-014710 (cit. on p. 4).

[52] S.N. Weber, C.A. Weber, and E. Frey. *Binary Mixtures of Particles with Different Diffusivities Demix*. In: **ArXiv e-prints** (May 2015). arXiv: 1505.00525 [cond-mat.soft] (cit. on p. 4).

[53] G.S. Redner, M.F. Hagan, and A. Baskaran. *Structure and Dynamics of a Phase-Separating Active Colloidal Fluid*. In: **Physical Review Letters** 110.5 (Jan. 2013), p. 055701. DOI: 10.1103/PhysRevLett.110.055701 (cit. on p. 4).

[54] S. Weitz, A. Deutsch, and F. Peruani. *Self-propelled rods exhibit a phase-separated state characterized by the presence of active stresses and the ejection of polar clusters*. In: **Physical Review E** 92.1 (July 2015), p. 012322. DOI: 10.1103/PhysRevE.92.012322 (cit. on p. 4).

[55] T.J. Pedley. *Collective Behaviour of Swimming Micro-organisms*. In: **Experimental Mechanics** 50.9 (Oct. 2010), pp. 1293–1301. DOI: 10.1007/s11340-010-9406-7 (cit. on p. 4).

[56] A. Zöttl and H. Stark. *Hydrodynamics Determines Collective Motion and Phase Behavior of Active Colloids in Quasi-Two-Dimensional Confinement.* In: **Physical Review Letters** 112.11 (Mar. 2014), p. 118101. DOI: 10.1103/PhysRevLett.112.118101 (cit. on p. 4).

[57] R. Suzuki et al. *Polar pattern formation in driven filament systems requires non-binary particle collisions.* In: **Nature Physics** advance online publication (Aug. 2015). DOI: 10.1038/nphys3423 (cit. on pp. 4, 7, 37, 38, 99, 101, 103).

[58] V. Schaller et al. *Polar pattern formation: hydrodynamic coupling of driven filaments.* In: **Soft Matter** 7.7 (Mar. 2011), pp. 3213–3218. DOI: 10.1039/C0SM01063D (cit. on pp. 4, 76, 101, 103).

[59] A. Ott et al. *Measurement of the persistence length of polymerized actin using fluorescence microscopy.* In: **Physical Review E** 48.3 (Sept. 1993), R1642–R1645. DOI: 10.1103/PhysRevE.48.R1642 (cit. on pp. 4, 7).

[60] F. Gittes et al. *Flexural rigidity of microtubules and actin filaments measured from thermal fluctuations in shape.* In: **The Journal of Cell Biology** 120.4 (Feb. 1993), pp. 923–934. DOI: 10.1083/jcb.120.4.923 (cit. on pp. 4, 7).

[61] L. Le Goff et al. *Tracer Studies on F-Actin Fluctuations.* In: **Physical Review Letters** 89.25 (Dec. 2002), p. 258101. DOI: 10.1103/PhysRevLett.89.258101 (cit. on pp. 4, 7).

[62] H.H. Wensink et al. *Controlling active self-assembly through broken particle-shape symmetry.* In: **Physical Review E** 89.1 (Jan. 2014), p. 010302. DOI: 10.1103/PhysRevE.89.010302 (cit. on p. 4).

[63] J.E. Molloy et al. *Single-molecule mechanics of heavy meromyosin and S1 interacting with rabbit or Drosophila actins using optical tweezers.* In: **Biophysical Journal** 68.4 Suppl (Apr. 1995), 298S–305S (cit. on p. 7).

[64] X. Liu and G.H. Pollack. *Mechanics of F-Actin Characterized with Microfabricated Cantilevers.* In: **Biophysical Journal** 83.5 (Nov. 2002), pp. 2705–2715. DOI: 10.1016/S0006-3495(02)75280-6 (cit. on p. 7).

[65] O. Kratky and G. Porod. *Röntgenuntersuchung gelöster Fadenmoleküle.* de. In: **Recueil des Travaux Chimiques des Pays-Bas** 68.12 (Jan. 1949), pp. 1106–1122. DOI: 10.1002/recl.19490681203 (cit. on p. 9).

[66] N. Saitô, K. Takahashi, and Y. Yunoki. *The Statistical Mechanical Theory of Stiff Chains.* In: **Journal of the Physical Society of Japan** 22.1 (Jan. 1967), pp. 219–226. DOI: 10.1143/JPSJ.22.219 (cit. on p. 9).

[67] C. Bustamante, Z. Bryant, and S.B. Smith. *Ten years of tension: single-molecule DNA mechanics.* In: **Nature** 421.6921 (Jan. 2003), pp. 423–427. DOI: 10.1038/nature01405 (cit. on p. 9).

[68] H.R. Warner. *Kinetic Theory and Rheology of Dilute Suspensions of Finitely Extendible Dumbbells.* In: **Industrial & Engineering Chemistry Fundamentals** 11.3 (Aug. 1972), pp. 379–387. DOI: 10.1021/i160043a017 (cit. on p. 9).

[69] A. Malevanets and R. Kapral. *Mesoscopic model for solvent dynamics.* In: **The Journal of Chemical Physics** 110.17 (May 1999), pp. 8605–8613. DOI: 10.1063/1.478857 (cit. on pp. 10, 11).

[70] C.-C. Huang, G. Gompper, and R. G. Winkler. *Hydrodynamic correlations in multiparticle collision dynamics fluids*. In: **Physical Review E** 86.5 (Nov. 2012), p. 056711. DOI: 10.1103/PhysRevE.86.056711 (cit. on pp. 10, 11).

[71] T. Ihle and D. M Kroll. *Stochastic rotation dynamics: A Galilean-invariant mesoscopic model for fluid flow*. In: **Physical Review E** 63.2 (Jan. 2001), p. 020201. DOI: 10.1103/PhysRevE.63.020201 (cit. on p. 10).

[72] H. Noguchi, N. Kikuchi, and G. Gompper. *Particle-based mesoscale hydrodynamic techniques*. In: **EPL (Europhysics Letters)** 78.1 (2007), p. 10005. DOI: 10.1209/0295-5075/78/10005 (cit. on pp. 11, 99, 158).

[73] I. O. Götze, H. Noguchi, and G. Gompper. *Relevance of angular momentum conservation in mesoscale hydrodynamics simulations*. In: **Physical Review E** 76 (4 Oct. 2007), p. 046705. DOI: 10.1103/PhysRevE.76.046705 (cit. on pp. 11, 99, 162).

[74] E. Allahyarov and G. Gompper. *Mesoscopic solvent simulations: Multiparticle-collision dynamics of three-dimensional flows*. In: **Physical Review E** 66.3 (Sept. 2002), p. 036702. DOI: 10.1103/PhysRevE.66.036702 (cit. on p. 12).

[75] R. G. Winkler et al. *Rod-like colloids and polymers in shear flow: a multi-particle-collision dynamics study*. In: **Journal of Physics: Condensed Matter** 16.38 (2004), S3941. DOI: 10.1088/0953-8984/16/38/012 (cit. on p. 12).

[76] C.-C. Huang, G. Gompper, and R. G. Winkler. *Effect of hydrodynamic correlations on the dynamics of polymers in dilute solution*. In: **The Journal of Chemical Physics** 138.14 (Apr. 2013), p. 144902. DOI: 10.1063/1.4799877 (cit. on p. 12).

[77] A. Lamura et al. *Multi-particle collision dynamics: Flow around a circular and a square cylinder*. In: **EPL (Europhysics Letters)** 56.3 (2001), p. 319 (cit. on pp. 14, 15).

[78] A. Lamura and G. Gompper. *Numerical study of the flow around a cylinder using multi-particle collision dynamics*. In: **The European Physical Journal E** 9.1 (2002), pp. 477–485 (cit. on pp. 14, 15).

[79] T. Ihle and D. M Kroll. *Stochastic rotation dynamics. I. Formalism, Galilean invariance, and Green-Kubo relations*. In: **Physical Review E** 67.6 (June 2003), p. 066705. DOI: 10.1103/PhysRevE.67.066705 (cit. on p. 17).

[80] T. Ihle and D. M Kroll. *Stochastic rotation dynamics. II. Transport coefficients, numerics, and long-time tails*. In: **Physical Review E** 67.6 (June 2003), p. 066706. DOI: 10.1103/PhysRevE.67.066706 (cit. on p. 17).

[81] N. Kikuchi et al. *Transport coefficients of a mesoscopic fluid dynamics model*. In: **The Journal of Chemical Physics** 119.12 (Sept. 2003), pp. 6388–6395. DOI: 10.1063/1.1603721 (cit. on pp. 17–19).

[82] T. Ihle, E. Tüzel, and D. M Kroll. *Equilibrium calculation of transport coefficients for a fluid-particle model*. In: **Physical Review E** 72.4 (Oct. 2005), p. 046707. DOI: 10.1103/PhysRevE.72.046707 (cit. on pp. 17–19).

[83] L. Verlet. *Computer "Experiments" on Classical Fluids. I. Thermodynamical Properties of Lennard-Jones Molecules*. In: **Physical Review** 159.1 (July 1967), pp. 98–103. DOI: 10.1103/PhysRev.159.98 (cit. on p. 20).

[84] W.C. Swope et al. *A computer simulation method for the calculation of equilibrium constants for the formation of physical clusters of molecules: Application to small water clusters*. In: **The Journal of Chemical Physics** 76.1 (1982), pp. 637–649. DOI: http://dx.doi.org/10.1063/1.442716 (cit. on p. 20).

[85] M. Matsumoto and T. Nishimura. *Mersenne twister: a 623-dimensionally equidistributed uniform pseudo-random number generator*. In: **ACM Transactions on Modeling and Computer Simulation (TOMACS)** 8.1 (1998), pp. 3–30 (cit. on p. 20).

[86] M. Saito and M. Matsumoto. „SIMD-Oriented Fast Mersenne Twister: a 128-bit Pseudorandom Number Generator". In: *Monte Carlo and Quasi-Monte Carlo Methods 2006*. Ed. by A. Keller, S. Heinrich, and H. Niederreiter. Springer Berlin Heidelberg, 2008, pp. 607–622. DOI: 10.1007/978-3-540-74496-2_36 (cit. on p. 20).

[87] M. Saito and M. Matsumoto. „A PRNG Specialized in Double Precision Floating Point Numbers Using an Affine Transition". In: *Monte Carlo and Quasi-Monte Carlo Methods 2008*. Ed. by P. L' Ecuyer and A.B. Owen. Springer Berlin Heidelberg, 2009, pp. 589–602. DOI: 10.1007/978-3-642-04107-5_38 (cit. on p. 20).

[88] G. Marsaglia and W.W. Tsang. *The Ziggurat Method for Generating Random Variables*. In: **Journal of Statistical Software** 5.8 (Oct. 2, 2000), pp. 1–7 (cit. on p. 20).

[89] C.H. Hamilton and A. Rau-Chaplin. „Compact Hilbert indices for multi-dimensional data". In: *Complex, Intelligent and Software Intensive Systems, 2007. CISIS 2007. First International Conference on*. IEEE. 2007, pp. 139–146 (cit. on p. 21).

[90] F. Pérez and B.E. Granger. *IPython: a System for Interactive Scientific Computing*. In: **Computing In Science & Engineering** 9.3 (May 2007), pp. 21–29. DOI: 10.1109/MCSE.2007.53 (cit. on p. 21).

[91] J.D. Hunter. *Matplotlib: A 2D graphics environment*. In: **Computing In Science & Engineering** 9.3 (2007), pp. 90–95 (cit. on p. 21).

[92] L. Van der Maaten and G. Hinton. *Visualizing data using t-SNE*. In: **Journal of Machine Learning Research** 9.2579-2605 (2008), p. 85 (cit. on p. 40).

[93] L. Van Der Maaten. *Accelerating t-sne using tree-based algorithms*. In: **The Journal of Machine Learning Research** 15.1 (2014), pp. 3221–3245 (cit. on pp. 40, 41).

[94] S. Kullback and R.A. Leibler. *On information and sufficiency*. In: **The annals of mathematical statistics** 22 (1951), pp. 79–86. DOI: 10.1214/aoms/1177729694 (cit. on p. 41).

[95] F. Peruani, L. Schimansky-Geier, and M. Bär. *Cluster dynamics and cluster size distributions in systems of self-propelled particles*. In: **European Physical Journal Special Topics** 191 (Dec. 2010), pp. 173–185. DOI: 10.1140/epjst/e2010-01349-1. arXiv: 1404.6806 [physics.bio-ph] (cit. on pp. 69, 70, 72).

[96] F. Peruani, L. Schimansky-Geier, and M. Bär. *Cluster dynamics and cluster size distributions in systems of self-propelled particles*. In: **The European Physical Journal Special Topics** 191.1 (Feb. 2011), pp. 173–185. DOI: 10.1140/epjst/e2010-01349-1 (cit. on p. 70).

[97] F. Reif. **Fundamentals of Statistical and Thermal Physics**. Waveland Press, 1965 (cit. on p. 70).

[98] A. Savitzky and M. J. Golay. *Smoothing and differentiation of data by simplified least squares procedures.* In: **Analytical chemistry** 36.8 (1964), pp. 1627–1639 (cit. on p. 87).

[99] H. Lamb. *XV. On the uniform motion of a sphere through a viscous fluid.* In: **The London, Edinburgh, and Dublin Philosophical Magazine and Journal of Science** 21.121 (1911), pp. 112–121 (cit. on p. 90).

[100] J. Blake. „A note on the image system for a stokeslet in a no-slip boundary". In: *Mathematical Proceedings of the Cambridge Philosophical Society.* Vol. 70. 02. Cambridge Univ Press. 1971, pp. 303–310 (cit. on p. 90).

[101] A. W. Lees and S. F. Edwards. *The computer study of transport processes under extreme conditions.* In: **Journal of Physics C: Solid State Physics** 5.15 (1972), p. 1921 (cit. on p. 91).

[102] R. Aditi Simha and S. Ramaswamy. *Hydrodynamic Fluctuations and Instabilities in Ordered Suspensions of Self-Propelled Particles.* In: **Physical Review Letters** 89.5 (July 2002), p. 058101. DOI: 10.1103/PhysRevLett.89.058101 (cit. on pp. 98, 99, 103).

[103] R. A. Simha and S. Ramaswamy. *Statistical hydrodynamics of ordered suspensions of self-propelled particles: waves, giant number fluctuations and instabilities.* In: **Physica A: Statistical Mechanics and its Applications**. Invited Papers from the 21th IUPAP International Conference on St atistical Physics 306 (Apr. 2002), pp. 262–269. DOI: 10.1016/S0378-4371(02)00503-4 (cit. on p. 98).

[104] C. A. Weber et al. *Nucleation-induced transition to collective motion in active systems.* In: **Physical Review E** 86.3 (Sept. 2012), p. 030901. DOI: 10.1103/PhysRevE.86.030901 (cit. on pp. 99, 103).

Part II

Swimmer

7 Swimming at low Reynolds numbers

Swimming at small scales is very different to what we are used when going to the pool — welcome to the world of Aristotle, where nothing moves without a pushing force.

Theorists have begun to investigate the unfamiliar physics of low Reynolds numbers more than 60 years ago, including the pioneering works by Taylor [1–3]. In his seminal talk "*Life at low Reynolds number*", Purcell put this physics into perspective [4]. In particular, he coined the so-called "scallop theorem", which states that in a highly viscous Newtonian fluid, a reciprocal or time-reversible motion does not lead to propulsion [4–6].

The restrictions posed by the scallop theorem can be overcome in a number of different ways [7–9]. In order to move, a swimmer must in essence have more than one degree of freedom that can change alternately and independently. For example, Purcell suggested a three-link swimmer that moves by alternately waving one of its two arms, but the full analysis of this swimmer is quite complex [4, 10]. Therefore, a similar but simpler to analyze toy model was suggested that consists of three spheres in a line whose distances alternately shorten and widen [11, 12]. This model can be further reduced to only two spheres, if the sphere radii can grow and shrink [13]. However, these toy models are neither very efficient nor can they be built in experiment.

For practical examples of swimmers, one may have a look at nature, which has evolved highly optimized swimming strategies in basically all animals. For example, unicellular organisms often have to search for food in aqueous environments for which they have to propel [14, 15], and higher order animals reproduce via sperm cells that have to find the egg [16]. These swimming strategies form two major categories [17]: on the one hand, there are passive, stiff flagella, which are actuated at one end and are found in procaryotes. On the other hand, there are actively beating flagella which deform via motors along the flagellum and can be found in eucaryotes. Interestingly enough, the structure of these appendages has been highly conserved during the evolution [18].

Analyzing the propulsion mechanisms of bacteria requires appropriate tools, because the equations governing low Reynolds number motion are notoriously difficult. This has sparked the development of several very successful methods and approximations. Among these is the slender body approximation that estimates the hydrodynamic drag on an elongated body and thereby renders the full solution of the hydrodynamic equations unnecessary [17, 19–21]. Another approach is to use the fundamental solutions of the Stokes equation for the flow of point-like particles, the so-called Stokeslets [22–24]. These fundamental solutions can be used to calculate the flow field of complex bodies by distributing point sources of fluid flow over their surface so that the boundary conditions of the fluid flow are met [25–27]. Because in most cases, such complex bodies have to be approximated by many Stokeslets — with the notable exception of the tree-sphere swimmer from above [11, 12] — this method has to be considered as semi-analytic. Beside these analytic approaches, there are numerous simulation methods,

among which is the Multiparticle Collision dynamics (MPC) which has been employed in the first part of this thesis [28].

These tools allowed to analytically examine the swimming strategies of living microorganism. For active eucaryotic flagella, the hydrodynamic analysis was done for both Newtonian [17, 29–31] and viscoelastic fluids [32, 33], but a quantitative comparison to experiments is challenging because the swimming depends on the details of the beat shape. The beat shape, on the other hand, depends on the driving of the molecular motors, for which various models exist, but the parameters of these models are unknown [34, 35]. Furthermore, engineering active flagella is even more challenging than it is to build passive flagella, which explains why swimming with passive flagella has received much more attention.

The prototypic example for a passive procaryotic flagellum are the helical flagella found in Escherichia Coli [14, 15]. E. Coli is particularly suited as a model bacterium for swimming, because it is easy to cultivate, often harmless, and an excellent swimmer with a speed of $\approx 30\,\mu m/s$ at $\approx 10\,\mu m$ body length [14]. It swims by rotating its helical flagella at the base, which is a well-understood problem in both Newtonian and viscoelastic fluids [36–39]. In terms of swimming efficiency, E. Coli is close to the maximally attainable efficiency of $\approx 1\%$ [40–42]. One particularly interesting aspect of E. Coli is its ability to bundle its multiple helical flagella and to run fast or unbundle the flagella and tumble. This bundling and unbundling can be explained solely by hydrodynamic interactions of the filaments and is caused by a change of the sense of rotation in one of the filaments [43–47].

It is the helical shape of the flagella of E. Coli that makes this bacterium such a good swimmer. However, Purcell already realized that even swimming with a flexible oar is enough to break the time-reversibility [4]. This becomes clear when considering a flexible oar that is fixed at one end while rotating on a cone. The hydrodynamic drag of the fluid then bends the oar such that it gains an induced helicity, an effect that has been studied in several works [48–51]. In terms of the equation of motion, the crucial point of a flexible oar is that the boundary condition of the hydrodynamic problem, in other words the current shape of the oar, is itself a function of the fluid flow [52]. For the motion of a micro-swimmer, this was first exploited by Wiggins et al. [53, 54], although the relevant hyper-diffusive equation of motion had already been reported much earlier by Machin [55].

This theory gave rise to the first micro-swimmer with an artificial flagellum, where a large cell was decorated with a flagellum made from flexibly linked magnetic micro-particles which could be actuated by an external magnetic field [56–58]. Since then, the advances in micro-fabrication have made ever more sophisticated micro-swimmers possible. For example, a whip-like swimmer with a flexible tail and a magnetic head [59], micro-screws with a magnetic head [60, 61], and an exotic hybrid made from an inorganic structure with contractile bacteria as motor [62].

None of the above-mentioned examples had an appendage with variable bending stiffness which explains why all theoretic approaches have so far ignored the consequences from a variable stiffness when swimming with a flexible appendage. However, in a collaboration with the group of Prof. Tim Liedl we designed and realized a microswimmer based on DNA-flagella attached to a magnetic bead (see Fig. 7.1) [63]. When rotated by an external magnetic field, this microswimmer forms a flagella bundle whose number of flagella decreases towards its end. This thinning number of flagella results in a decreasing bending stiffness of the flagella

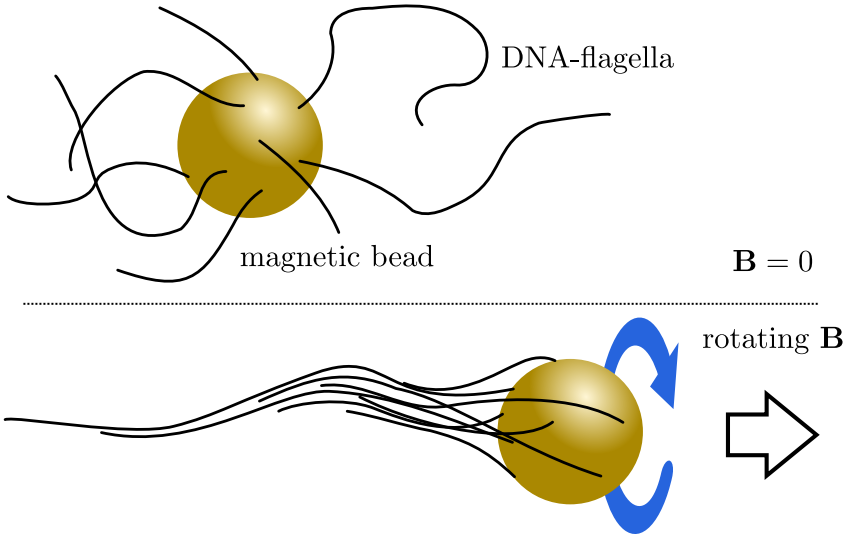

Figure 7.1 | Schematic of the experimental microswimmer. **Top:** Multiple DNA-flagella of different length are chemically attached to a magnetic bead. Without a magnetic field, the DNA-flagella stick out randomly from the bead. **Bottom:** An external magnetic field rotates the magnetic bead, thereby entangling the DNA-flagella to a bundle. If the bundle only forms on one side, the induced helical shape of the bundle propels the hybrid swimmer through the surrounding fluid. Note the thinning number of flagella towards the end of the bundle.

bundle. This work fills the gap in the theoretic treatment of swimming with a passive flexible oar of variable stiffness by extending an earlier work by Lauga [52].

This work is structured as follows: Section 8.1 describes the model and the necessary simplifications to make the problem feasible and derives a generalized hyper-diffusion equation for the tail shape. This equation will be solved analytically in 8.1.3. Section 8.1.4 and the following finally derive a formula for the swimming speed. This formula is discussed in general and examined for special cases in 8.1.4. Finally, section 8.3 applies our model to a self-assembled swimmer with artificial DNA flagella, which was realized by Alexander Maier from the group of Prof. Tim Liedl.

8 Swimming with a variable bending modulus

8.1 A model for swimmers with a variable bending modulus

This section introduces a model for swimming with a flexible oar that has a variable bending stiffness. After establishing a shape-determining equation for the tail, we use that equation to derive an expression for the swimming speed of such a swimmer.

Our swimmer model aims to reflect a micro-swimmer that has been conceived in collaboration with and realized by Maier et al. [63]. This swimmer will be discussed in detail in 8.3, but for our discussion below we reduce its structure to the most basic description. The swimmer consists of a magnetic micro-particle to which straight artificial flagella are attached (see Fig. 7.1). Upon rotation of the bead, the flagella form a bundle that extends from the rear side of the swimmer. For the following theoretic treatment, we consider the bundle of flagella as a *single* filament that is attached to a rotating bead (see Fig. 8.1). We will argue in 8.3 that the local stiffness of the flagella bundle decreases away from the bead due to the thinning number of flagella towards the end. Consequently, the single coarse-grained filament representing the bundle must also have a decreasing local bending stiffness.

This model closely resembles a swimmer model by Lauga, who discussed these swimmers in-depth, however only for tails with constant stiffness [52]. In the following, we generalize this work to tails with variable stiffness. Because the following line of argument is similar to the steps taken in Lauga's work, we try to be brief and focus on the differences.

Solving the equations of motion in a hydrodynamic setting is notoriously difficult, rendering adroit simplifications inevitable for an analytic treatment. As a first step, we neglect hydrodynamic fluctuations so that the model becomes deterministic. Without noise, any notion of diffusion is lost, but since we are mainly interested in active swimming here, this is acceptable. The following section introduces the shape-determining equation for the tail alone, and only in 8.1.2 will the swimmer head come into play.

8.1.1 The shape-determining equation for the tail

This section establishes the equation of motion for only the tail in three steps. Below, we introduce the general equation of motion for the tail via the slender body approximation and discuss its boundary conditions. The following subsections then apply a small amplitude approximation and finally switch to a better suited unit system.

Above, we introduced our swimmer model as a *single* inextensible elastic filament with a bending stiffness $A(s)$ that changes with the arc length position s along the filament. The elastic energy of the filament with length-dependent bending modulus $A(s)$ is given by

$$\mathcal{E} = \frac{1}{2}\int_0^L \big((A(s)\partial_s^2\boldsymbol{r})^2 + (\sigma(s)\partial_s\boldsymbol{r})^2\big)\mathrm{d}s \ , \tag{8.1}$$

where $\sigma(s)$ is a Lagrange multiplier ensuring the in-extensibility of the filament. We stress that both $A(s)$ and $\sigma(s)$ depend on the position s along the filament. From the energy (8.1) the force density due to bending and constraint forces is obtained via variation of the contour path. In the low-Reynolds number regime where inertia plays no role, this force needs to balance with the anisotropic friction forces on the filament from the fluid as given by standard slender body theory [19, 64, 65],

$$\big(\xi_\parallel \boldsymbol{t}\otimes\boldsymbol{t} + \xi_\perp(1-\boldsymbol{t}\otimes\boldsymbol{t})\big)\boldsymbol{u} = -\partial_s^2(A(s)\partial_s^2\boldsymbol{r}) + \partial_s(\sigma(s)\partial_s\boldsymbol{r}) \ . \tag{8.2}$$

Here $\boldsymbol{t}(s) = \partial_s\boldsymbol{r}(s)$ is the local tangent to the filament and $\boldsymbol{u}(s) = \dot{\boldsymbol{r}}(s)$ is the local speed of the filament with respect to the surrounding fluid. Note the difference on the RHS to the original work of Lauga [52], where the term $\partial_s^2(A(s)\partial_s^2\boldsymbol{r})$ is replaced by the simpler much simpler term $A\,\partial_s^4\boldsymbol{r}$. An equation for the Lagrange multiplier which ensures the constraint $|\boldsymbol{t}^2| = 1$ is given in an implicit form by

$$\boldsymbol{t}\cdot\partial_s\boldsymbol{u} = 0 \ . \tag{8.3}$$

These two equations have the boundary conditions

$$\boldsymbol{F}_{\mathrm{ext}} = \quad \partial_s(A\,\partial_s^2\boldsymbol{r}) - \sigma\partial_s\boldsymbol{r}, \qquad \boldsymbol{T}_{\mathrm{ext}} = -\boldsymbol{t}\times A\,\partial_s^2\boldsymbol{r} \quad \text{at } s=0, \tag{8.4a}$$

$$\boldsymbol{F}_{\mathrm{ext}} = -\partial_s(A\,\partial_s^2\boldsymbol{r}) + \sigma\partial_s\boldsymbol{r}, \qquad \boldsymbol{T}_{\mathrm{ext}} = +\boldsymbol{t}\times A\,\partial_s^2\boldsymbol{r} \quad \text{at } s=L, \tag{8.4b}$$

where $\boldsymbol{F}_{\mathrm{ext}}$ and $\boldsymbol{T}_{\mathrm{ext}}$ are externally applied forces and torques on the filament, respectively. We remark that a drag force from the bead is also called "external" in this nomenclature.

Small amplitude approximation

The compound head-tail object is torqued into a steady rotation by the externally applied rotating homogeneous magnetic field. The rotation of the head creates a rotating fluid flow around the head that falls off with $1/r$. This is true for both externally and internally actuated swimmers, though the head of externally actuated swimmers co-rotates with the tail whereas for internally actuated swimmers it counter-rotates. In both cases however, this rotational fluid flow is small over the major part of the bundle, so it will be neglected in what follows.

After the swimmer has established a stationary shape, the magnetic field rotates the head about the axis in which it propels himself and the attachment point of the bundle follows a circular path on the bead surface. We choose this rotation axis as the $\hat{\boldsymbol{e}}_x$ direction and arbitrary orthogonal vectors $\hat{\boldsymbol{e}}_y$ and $\hat{\boldsymbol{e}}_z$ as the local coordinate system that co-rotates with the head (Fig. 8.1). As long as the rotations about the y and z axes are small, it is straightforward to find this coordinate system. The origin of this coordinate system is placed at the projection of the attachment point on the rotation axis of the swimmer. Consequently, the

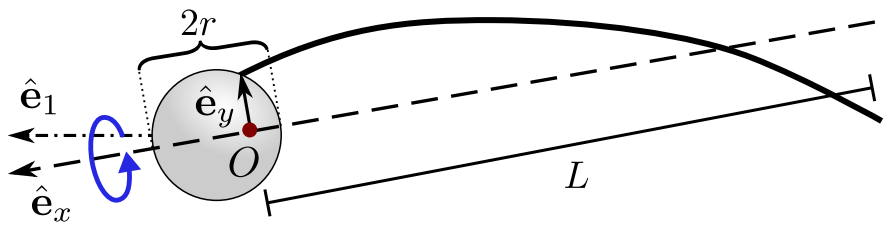

Figure 8.1 | Coordinate system of the swimmer. The local coordinate system of the swimmer is indicated by $\hat{\boldsymbol{e}}_x$ and $\hat{\boldsymbol{e}}_y$. The origin of this coordinate system is at the projection of the attachment point on the x-axis, indicated by O (red dot). The swimmer rotates around the $\hat{\boldsymbol{e}}_x$ axis (blue arrow). The effective swimming direction $\hat{\boldsymbol{e}}_1$ is slightly off the $\hat{\boldsymbol{e}}_x$ axis, because the $\hat{\boldsymbol{e}}_x$ axis precesses with a small opening angle around the $\hat{\boldsymbol{e}}_1$ axis. The arrows indicate the direction of the coordinate directions.

origin does not coincide with the center of the head, but is offset by some distance in the range $[0,\, r_h]$ where r_h is the bead radius.

The actuation of the bundle is about the x-axis in this coordinate system. In the following we assume small actuations of the bundle about the x-axis, such that $s \approx x$ and

$$\boldsymbol{r} \approx x\,\hat{\boldsymbol{e}}_x + y(x,t)\,\hat{\boldsymbol{e}}_y + z(x,t)\,\hat{\boldsymbol{e}}_z \ , \tag{8.5}$$

where $y(s,t)$ and $z(s,t)$ are the small amplitudes along the contour. The error inflicted by this approximation is small, as experiments have shown [66]. Equations (8.2) and (8.3) written in this coordinate frame become with the definitions $\gamma = \xi_\perp/\xi_\parallel$ and $\boldsymbol{r}_\perp(x,t) = y(x,t)\,\hat{\boldsymbol{e}}_y + z(x,t)\hat{\boldsymbol{e}}_z$,

$$\xi_\parallel u_x + (\xi_\parallel - \xi_\perp)(u_y y' + u_z z') = \sigma' \tag{8.6a}$$

$$u_y\left(\xi_\perp - (\xi_\parallel - \xi_\perp)z'^2\right) + (\xi_\parallel - \xi_\perp)(u_x + u_z z')\,y' = -\partial_x^2(A\,y'') + \partial_x(\sigma\,y') \tag{8.6b}$$

$$u_z\left(\xi_\perp + (\xi_\parallel - \xi_\perp)z'^2\right) + (\xi_\parallel - \xi_\perp)(u_x + u_y y')\,z' = -\partial_x^2(A\,z'') + \partial_x(\sigma\,z') \tag{8.6c}$$

$$A\cdot\Big(\big(\frac{1}{\gamma}-1\big)\boldsymbol{r}_\perp''\boldsymbol{r}_\perp^{(4)} - \boldsymbol{r}_\perp'\boldsymbol{r}_\perp^{(5)}\Big) - \big(\frac{2}{3\gamma}+\frac{7}{3}\big)\boldsymbol{r}_\perp'\boldsymbol{r}_\perp^{(4)}A' - \big(\frac{1}{\gamma}+2\big)\boldsymbol{r}_\perp'\boldsymbol{r}_\perp^{(3)}A'' + \frac{1}{\gamma}\boldsymbol{r}_\perp'\boldsymbol{r}_\perp^{(3)}\sigma + \sigma'' = 0\ . \tag{8.6d}$$

Here and in the following a prime denotes a derivative with respect to x. Note the appearance of terms with A' and A'' in the equation for σ.

This set of equations is greatly simplified by an order of magnitude analysis. If $\boldsymbol{r}_\perp$ is of order ε, σ must be of order ε^2 by (8.6d). Likewise by (8.6a–8.6c) u_x is of order ε^2 and $u_\perp$ of order ε. Keeping only terms of leading order, equations (8.6) simplify to

$$\xi_\parallel u_x + (\xi_\parallel - \xi_\perp)(u_y y' + u_z z') = \sigma' \tag{8.7a}$$

$$\xi_\perp u_y + \partial_x^2(A\,y'') = 0 \tag{8.7b}$$

$$\xi_\perp u_z + \partial_x^2(A\,z'') = 0\ . \tag{8.7c}$$

The corresponding small-amplitude approximation of the boundary conditions (8.4) for a bundle of length L are

$$\boldsymbol{F}_{\text{ext}} = \ \partial_x(A\partial_x^2\boldsymbol{r}_\perp) - \sigma\hat{\boldsymbol{e}}_x, \qquad T_{\text{ext},y} = -A\,\partial_x^2 z \qquad T_{\text{ext},z} = \ A\,\partial_x^2 y \quad \text{at } s = 0 \tag{8.8a}$$

$$\boldsymbol{F}_{\text{ext}} = -\partial_x(A\partial_x^2\boldsymbol{r}_\perp) + \sigma\hat{\boldsymbol{e}}_x, \qquad T_{\text{ext},y} = \ A\,\partial_x^2 z \qquad T_{\text{ext},z} = -A\,\partial_x^2 y \quad \text{at } s = L. \tag{8.8b}$$

Natural units

It is convenient to use intrinsic units such that all pre-factors are numbers. The externally applied magnetic field revolves in the yz-plane with an angular speed ω and periodically actuates the swimmer. Hence, time is best measured in multiples of ω^{-1}.

Next, we look for a natural unit of length for our swimmer, which is a bit more contrived. Without friction forces but only thermal activity, a natural length scale for a slender body is given by its persistence length $l_p = A/k_BT$. However, the tail is not force-free but experiences a drag from being pulled through the fluid. For such elasto-hydrodynamic equations an intrinsic bending length

$$\ell_\omega \equiv \left(A/\omega\xi_\perp\right)^{1/4} \tag{8.9}$$

is a natural unit for the length [25, 53, 67]. Because in our case, A is not constant but a function of the arc length position, we need to choose at which point of the filament the bending stiffness should be taken. Below we will argue that an experimentally realisable way to obtain a variable bending stiffness is by attaching multiple filaments to a bead, it seems most natural to take the bending stiffness of a single filament as the typical scale for the bending stiffness. Hence, we define A_s as the bending stiffness of a single filament, so that in dimensionless $A(x)$ corresponds to the number of filaments making up the bundle at position x. Forces and torques are measured by $\xi_\perp\ell_\omega$ and $\xi_\perp\ell_\omega^3$, respectively. In the following we will only refer to the dimensionless quantities but use the same symbols as before.

In particular, we will consider the swimming speed of the swimmer. To convert swimming speeds from our choice of units back into physical units, the result has to be multiplied by $\ell_\omega \cdot 2\pi f$ where f is the rotation frequency of the external magnetic field. The extra factor of 2π is necessary because the natural unit of time is given by the *angular* frequency ω^{-1} and not frequency f^{-1}.

8.1.2 Attaching the tail to a sphere

In the preceding sections we developed the determining equations for the shape of the tail in the small amplitude approximation. The next step is to choose appropriate boundary conditions in the equations for the tail such that one end of the tail is free and the other attached to a movable sphere. This equation will then be cast into a single complex differential equation with complex boundary conditions.

The motion of the bead shall be given by the velocity $\boldsymbol{U}(t)$ and rotation speed $\boldsymbol{\Omega}(t)$. Given the current speed of the bead, the total speed with respect to the fluid $\boldsymbol{u}$ of any point on the bundle is then a superposition of the velocity and rotation of the bead coordinate system and the local bundle velocity in the reference frame of the bead:

$$u_x = U_x + z\Omega_y - y\Omega_z \qquad u_y = U_y + x\Omega_z - z\Omega_x + \dot{y} \qquad u_z = U_z + y\Omega_x - x\Omega_y + \dot{z} \tag{8.10}$$

Because the local coordinate system co-rotates with the head, the tail shape becomes static in these coordinates, such that $\dot{y} = \dot{z} = 0$. In the low-Reynolds number regime drag through motion and rotation must balance with external force and torque,

$$\tilde{\boldsymbol{F}}_{\text{ext}} = -\begin{pmatrix} \mathcal{R}_{\parallel}^{FU} & 0 & 0 \\ 0 & \mathcal{R}_{\perp}^{FU} & 0 \\ 0 & 0 & \mathcal{R}_{\perp}^{FU} \end{pmatrix} \tilde{\boldsymbol{U}} \qquad \tilde{\boldsymbol{T}}_{\text{ext}} = -\begin{pmatrix} \mathcal{R}_{\parallel}^{L\Omega} & 0 & 0 \\ 0 & \mathcal{R}_{\perp}^{L\Omega} & 0 \\ 0 & 0 & \mathcal{R}_{\perp}^{L\Omega} \end{pmatrix} \tilde{\boldsymbol{\Omega}} \,,$$

when taken with respect to the center of mass of the bead. When expressed in the shifted local coordinate system these equations become

$$\boldsymbol{F}_{\text{ext}} = -\begin{pmatrix} \mathcal{R}_{\parallel}^{FU} & 0 & 0 \\ 0 & \mathcal{R}_{\perp}^{FU} & 0 \\ 0 & 0 & \mathcal{R}_{\perp}^{FU} \end{pmatrix} \cdot \boldsymbol{U} + \begin{pmatrix} 0 & 0 & 0 \\ 0 & 0 & a\mathcal{R}_{\perp}^{FU} \\ 0 & -a\mathcal{R}_{\perp}^{FU} & 0 \end{pmatrix} \cdot \boldsymbol{\Omega} \tag{8.11a}$$

$$\boldsymbol{T}_{\text{ext}} = \begin{pmatrix} 0 & 0 & 0 \\ 0 & 0 & -a\mathcal{R}_{\perp}^{FU} \\ 0 & a\mathcal{R}_{\perp}^{FU} & 0 \end{pmatrix} \cdot \boldsymbol{U} - \begin{pmatrix} \mathcal{R}_{\parallel}^{L\Omega} & 0 & 0 \\ 0 & \mathcal{R}_{\perp}^{L\Omega} + a^2\mathcal{R}_{\perp}^{FU} & 0 \\ 0 & 0 & \mathcal{R}_{\perp}^{L\Omega} + a^2\mathcal{R}_{\perp}^{FU} \end{pmatrix} \cdot \boldsymbol{\Omega} \,, \tag{8.11b}$$

where a is the offset of the origin from the center of the head (see Fig. 8.1). Because the external magnetic field is strong enough to ensure a phase-locked rotation of the head, we take $\Omega_x = -1$ as given. However, for the remaining components, the forces need to balance out. Therefore with (8.8) we find for the attached end of the tail

$$\mathcal{R}_{\parallel}^{FU} U_x = \quad \sigma(0) \tag{8.12a}$$

$$\mathcal{R}_{\perp}^{FU} U_y - a\mathcal{R}_{\perp}^{FU} \Omega_z = -\partial_x (A(x)\, y''(x,t))\big|_{x=0} \tag{8.12b}$$

$$\mathcal{R}_{\perp}^{FU} U_z + a\mathcal{R}_{\perp}^{FU} \Omega_y = -\partial_x (A(x)\, z''(x,t))\big|_{x=0} \tag{8.12c}$$

$$a\mathcal{R}_{\perp}^{FU} U_z + (\mathcal{R}_{\perp}^{L\Omega} + a^2\mathcal{R}_{\perp}^{FU})\Omega_y = -A(0)\, z''(0) \tag{8.12d}$$

$$-a\mathcal{R}_{\perp}^{FU} U_y + (\mathcal{R}_{\perp}^{L\Omega} + a^2\mathcal{R}_{\perp}^{FU})\Omega_z = \quad A(0)\, y''(0) \tag{8.12e}$$

and for the free end at $x = L$ where no external force applies

$$y''(L) = z''(L) = y^{(3)}(L) = z^{(3)}(L) = \sigma(L) = 0 \,. \tag{8.13}$$

With the driving of the bundle

$$y(0) = \Re[\varepsilon_1] \qquad y'(0) = \Re[\varepsilon_2] \tag{8.14a}$$

$$z(0) = \Im[\varepsilon_1] \qquad z'(0) = \Im[\varepsilon_2] \tag{8.14b}$$

there are eight boundary conditions (8.14, 8.13) for the two fourth order equations for y and z and two boundary conditions 8.12a, 8.13 for the second order equation for σ. For each of the unknowns y, z, σ, U_x, U_y, U_z, Ω_y, Ω_z there is a determining function 8.6, 8.12b–8.12e. As long as the rotation about the y and z axes remains small, we can safely assume that the swimmer revolves mainly about the x-axis with an angular speed ω. We will argue below that this condition is well met in our experiment.

Rewriting equations 8.7b, 8.7c in natural units and using (8.10) yields

$$U_y + x\Omega_z + z + \partial_x^2 (A\, y'') = 0 \tag{8.15a}$$

$$U_z - x\Omega_y - y + \partial_x^2 (A\, z'') = 0 \tag{8.15b}$$

where we have used $\Omega_x = -1$. With the definitions $\zeta = y + \imath z$, $U = U_y + \imath U_z$ and $\Omega = \Omega_y + \imath \Omega_z$ these two equations can be combined into one complex equation

$$U + \imath x\Omega - \imath\zeta + \partial_x^2(A\,\zeta'') = 0 \tag{8.16}$$

with boundary conditions corresponding to (8.13, 8.14)

$$\zeta(0) = \varepsilon_1 \qquad \zeta'(0) = \varepsilon_2 \qquad \zeta''(L) = 0 \qquad \zeta^{(3)}(L) = 0\ . \tag{8.17}$$

Inversion of the equation system 8.12b and 8.12e determines U and Ω in terms of x and y:

$$U_y = -\frac{\mathcal{R}_\perp^{L\Omega} + a^2\mathcal{R}_\perp^{FU}}{\mathcal{R}_\perp^{L\Omega}\mathcal{R}_\perp^{FU}}\,\partial_x\big(A(x)\,y''(x,t)\big)\big|_{x=0} + \frac{aA(0)}{\mathcal{R}_\perp^{L\Omega}}y''(0) \tag{8.18a}$$

$$U_z = -\frac{\mathcal{R}_\perp^{L\Omega} + a^2\mathcal{R}_\perp^{FU}}{\mathcal{R}_\perp^{L\Omega}\mathcal{R}_\perp^{FU}}\,\partial_x\big(A(x)\,z''(x,t)\big)\big|_{x=0} + \frac{aA(0)}{\mathcal{R}_\perp^{L\Omega}}z''(0) \tag{8.18b}$$

$$\Omega_y = \frac{a}{\mathcal{R}_\perp^{L\Omega}}\,\partial_x\big(A(x)\,z''(x,t)\big)\big|_{x=0} - \frac{A(0)}{\mathcal{R}_\perp^{L\Omega}}z''(0) \tag{8.18c}$$

$$\Omega_z = \frac{-a}{\mathcal{R}_\perp^{L\Omega}}\,\partial_x\big(A(x)\,y''(x,t)\big)\big|_{x=0} + \frac{A(0)}{\mathcal{R}_\perp^{L\Omega}}y''(0) \tag{8.18d}$$

With the abbreviations

$$\beta = A(0)\frac{\mathcal{R}_\perp^{L\Omega} + a^2\mathcal{R}_\perp^{FU}}{\mathcal{R}_\perp^{L\Omega}\mathcal{R}_\perp^{FU}} \qquad \sigma = A(0)\frac{a}{\mathcal{R}_\perp^{L\Omega}}$$

$$\lambda = -A(0)\frac{a}{\mathcal{R}_\perp^{L\Omega}} + A'(0)\frac{\mathcal{R}_\perp^{L\Omega} + a^2\mathcal{R}_\perp^{FU}}{\mathcal{R}_\perp^{L\Omega}\mathcal{R}_\perp^{FU}} \qquad \mu = -A(0)\frac{1}{\mathcal{R}_\perp^{L\Omega}} + A'(0)\frac{a}{\mathcal{R}_\perp^{L\Omega}}$$

these relations can be written in a more compact form

$$U = -\big(\beta\zeta^{(3)}(0) + \lambda\zeta''(0)\big) \qquad \Omega = -\imath\big(\sigma\zeta^{(3)}(0) + \mu\zeta''(0)\big)\ . \tag{8.19}$$

Using this result in (8.16) yields the final form

$$-\imath\zeta + \partial_x^2(A\,\zeta'') = (\beta + \sigma x)\zeta^{(3)}(0) + (\lambda + \mu x)\zeta''(0)\ . \tag{8.20}$$

The major challenge is to find a solution ζ for variable $A(x)$.

In summary, the preceding subsections have established a single equation of motion for the tail of the swimmer (8.20). The boundary conditions of this equation express the drag and torque forces that the attached sphere exerts on the one end of the tail. We note that the fluid flow field of the head was ignored in this approach.

8.1.3 Analytic solution for the swimmer shape

Lauga has presented an analytic solution for the tail shape (8.20) when A is constant. Here, we extend this analytic solution to variable $A(x)$.

For that, we assume the existence of an analytic solution of the homogeneous equation

$$-\imath\zeta + \partial_x^2(A\,\zeta'') = 0\ . \tag{8.21}$$

Therefore, assume the ζ_1, ζ_2, ζ_3, and ζ_4 are four independent solutions of (8.21). Because equation (8.20) is linear, also any superposition of those fundamental solutions is a solution of the homogeneous equation. We notice that the full solution has an inhomogeneity of the form $B\,x+C$, where $B=\sigma\zeta^{(3)}(0)+\mu\zeta^{(2)}(0)$ and $C=\beta\zeta^{(3)}(0)+\lambda\zeta^{(2)}(0)$. Therefore, we make the ansatz for the full solution

$$\zeta(x)=\sum_{i=1}^{4}\alpha_i\zeta_i(x)+b\,x+c\ , \tag{8.22}$$

where the coefficients $\alpha_1,\dots,\alpha_4,b,c$ are to be determined. It is very convenient that the second derivative of $b\,x+c$ is zero, so that upon substitution of our ansatz (8.22) into (8.20), we find

$$-\imath(b\,x+c)\overset{!}{=}\sum_{i=1}^{4}\Big(\beta\,\zeta_i^{(3)}(0)+\lambda\,\zeta_i^{(2)}(0)\Big)\alpha_i+\sum_{i=1}^{4}\Big(\sigma\,\zeta_i^{(3)}(0)+\mu\,\zeta_i^{(2)}(0)\Big)\alpha_i\cdot x\ , \tag{8.23}$$

where we have used that the left-hand side applied to ζ_i is zero according to (8.21). This equation can only be fulfilled, if it holds that

$$0=\sum_{i=1}^{4}\Big(\beta\zeta_i^{(3)}(0)+\lambda\zeta_i^{(2)}(0)\Big)\alpha_i+\imath b \tag{8.24}$$

$$0=\sum_{i=1}^{4}\Big(\sigma\zeta_i^{(3)}(0)+\mu\zeta_i^{(2)}(0)\Big)\alpha_i+\imath c\ . \tag{8.25}$$

In addition, the solution has to obey the boundary conditions from (8.17), which can be written as a matrix equation:

$$\begin{pmatrix}
\zeta_1(0) & \zeta_2(0) & \zeta_3(0) & \zeta_4(0) & 0 & 1\\
\zeta_1'(0) & \zeta_2'(0) & \zeta_3'(0) & \zeta_4'(0) & 1 & 0\\
\zeta_1''(L) & \zeta_2''(L) & \zeta_3''(L) & \zeta_4''(L) & 0 & 0\\
\zeta_1^{(3)}(L) & \zeta_2^{(3)}(L) & \zeta_3^{(3)}(L) & \zeta_4^{(3)}(L) & 0 & 0\\
\beta\zeta_1^{(3)}+\lambda\zeta_1^{(2)} & \beta\zeta_2^{(3)}+\lambda\zeta_2^{(2)} & \beta\zeta_3^{(3)}+\lambda\zeta_3^{(2)} & \beta\zeta_4^{(3)}+\lambda\zeta_4^{(2)} & 0 & 0\\
\sigma\zeta_1^{(3)}+\mu\zeta_1^{(2)} & \sigma\zeta_2^{(3)}+\mu\zeta_2^{(2)} & \sigma\zeta_3^{(3)}+\mu\zeta_3^{(2)} & \sigma\zeta_4^{(3)}+\mu\zeta_4^{(2)} & 0 & 0
\end{pmatrix}\cdot\begin{pmatrix}\alpha_1\\ \alpha_2\\ \alpha_3\\ \alpha_4\\ b\\ c\end{pmatrix}=\begin{pmatrix}\varepsilon_1\\ \varepsilon_2\\ 0\\ 0\\ 0\\ 0\end{pmatrix} \tag{8.26}$$

Here, the first four lines are the boundary conditions (8.17), and the lower two lines correspond to the consistency conditions (8.25). Solving this matrix equation for the coefficients α_i, b, c yields a fully analytic solution for the tail shape of the tail, as given by equation (8.22).

Below, we will use an exponential stiffness profile for the tail, so that $A(x)=A_0\mathrm{e}^{-x/\chi}$. In that case, an analytic solution of (8.21) can be given in terms of the Meijer-G functions [68],

$$\zeta_1(x)=G_{0,4}^{1,0}\left(\begin{matrix}\\ 1,0,0,1\end{matrix}\,\middle|\,\frac{-\imath\chi^4}{A_0}\,\mathrm{e}^{x/\chi}\right)\qquad \zeta_2(x)=G_{0,4}^{2,0}\left(\begin{matrix}\\ 1,1,0,0\end{matrix}\,\middle|\,\frac{\imath\chi^4}{A_0}\,\mathrm{e}^{x/\chi}\right) \tag{8.27a}$$

$$\zeta_3(x)=G_{0,4}^{3,0}\left(\begin{matrix}\\ 0,1,1,0\end{matrix}\,\middle|\,\frac{-\imath\chi^4}{A_0}\,\mathrm{e}^{x/\chi}\right)\qquad \zeta_4(x)=G_{0,4}^{4,0}\left(\begin{matrix}\\ 0,0,1,1\end{matrix}\,\middle|\,\frac{\imath\chi^4}{A_0}\,\mathrm{e}^{x/\chi}\right)\ . \tag{8.27b}$$

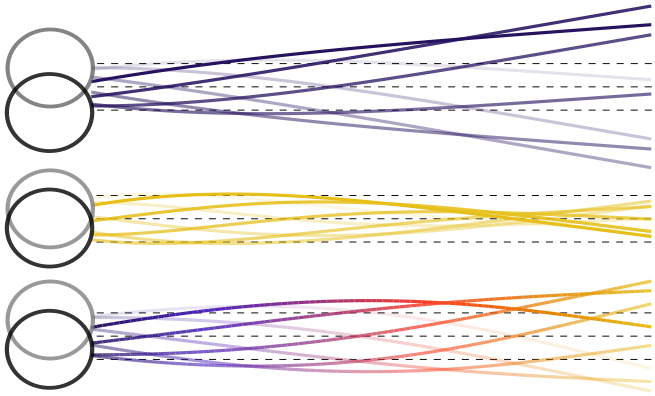

Figure 8.2 | Tail shape for a swimmer with optimal tail parameters $L = 4.1\,\ell_\omega$, $r_h = 1.7\,\ell_\omega$, and exponential stiffness for constant tail stiffness $A = 25 \cdot A_s$ (top) and variable tail stiffness $A(x) = A_s \cdot 25^{1-x/L}$ (bottom) at eight time points over one beat period. The line opacity fades at each step, so that each line can be discerned. The color indicates the local tail stiffness and ranges from $a = 25$ (dark blue) to $a = 1$ (yellow). In addition, the middle shows a swimmer with constant tail stiffness and $a = 1$. The black dashed lines indicate the amplitude of ε_1 and serve as a relative scale for the different cases. **Active content:** In a flash enabled player, a click reveals an interactive 3D model showing the predicted tail shape and movement for typical swimmer parameters (swimmer #2 in table 8.1). Although the tail looks to be actively beating, this is indeed not the case as can be seen in the back view.

The Meijer-G functions themselves are a generalization of the generalized hyper-geometric functions and can be defined in a closed form by

$$G^{m,n}_{p,q}\left(\begin{matrix} a_1, \ldots, a_p \\ b_1, \ldots, b_q \end{matrix} \middle| (-1)^{m+n+p}\, x \right) = \frac{1}{2\pi\imath} \int_L \frac{\prod_{j=1}^{n} \Gamma(1 - a_j + s) \cdot \prod_{i=1}^{m} \Gamma(b_i - s)}{\prod_{j=n+1}^{p} \Gamma(a_j - s) \cdot \prod_{i=m+1}^{q} \Gamma(1 - b_i + s)} x^s \mathrm{d}s \ . \tag{8.28}$$

Here, the integration contour L has to be chosen appropriately, so that it encloses all residuals of the integrand in the complex plane [69].

As one may imagine, the Meijer-G functions are not easily evaluated. In fact, the computer algebra software Mathematica is very slow when evaluating the Meijer-G functions for numerical values. In addition, the accuracy of the return values is not particularly good. The first problem can be tackled by using an interpolating function, so that the function evaluation becomes very fast. However, this does not ameliorate the problems concerning the accuracy of the solution, but on the contrary makes the situation even worse. Because in the following we need a very accurate solution that has small errors even in the derivatives, this renders the analytic solution unusable. Instead, we had to resort to direct numerical solvers of the differential equation (8.20) using the computer algebra system Mathematica. Due to the dependence of the right-hand side on derivatives of ζ at zero, this required a small trick. We first solved the equation system numerically with the values $\zeta^{(2)}(0)$ and $\zeta^{(3)}(0)$ as parameters κ_2 and κ_3, respectively. In a second step, we used a root-finding algorithm to match the κ_i to the desired derivatives of ζ. A complete listing of the Mathematica routine for this task

can be found in Appendix B.1. Despite its numerical nature, the so-obtained solution had a much higher accuracy than the analytic one. For example, the integrated residual

$$\int_0^L \left| -\imath\zeta + \partial_x^2(A\,\zeta'') - \Big((\beta+\sigma x)\zeta^{(3)}(0) + (\lambda+\mu x)\zeta''(0)\Big)\right| \mathrm{d}x \tag{8.29}$$

was typically of the order of 10^{-1} for the analytic solution as opposed to 10^{-7} for the numerical solution. In addition, this numerical method is more versatile, because it can deal with nearly arbitrary stiffness models and is not restricted to cases where an analytic solution of the homogeneous equation exists. Figure 8.2 shows typical solutions of the swimmer shape.

In summary, we have presented an analytical solution for the shape of the swimmer tail, as determined by equation (8.20). This full solution requires solutions of the homogeneous equation (8.21), which in turn depend on the stiffness profile $A(x)$. For an exponential stiffness profile, the solutions of the homogeneous problem are given by Meijer-G functions. Because the numerical evaluation of the Meijer-G functions is rather inaccurate, we found that a direct numerical differential equation solver yields better numerical results than the above analytical solution.

8.1.4 Determining the swimming speed

This section derives an expression for the swimming speed of our swimmer, if the tail shape of the swimmer is known. As we will see, this result has to be transformed into the laboratory system, which will be done at the end of this section.

From the tail shape the swimming speed will be determined in the following. For this equations 8.7b and 8.7c are substituted into (8.7a) which reads in natural units

$$u_x - (1-\gamma)\big(y'\partial_x^2(A\,y'') + z'\partial_x^2(A\,z'')\big) = \gamma\sigma' \ . \tag{8.30}$$

Here $\gamma = \xi_\perp/\xi_\parallel$ is the ratio of the drag coefficient perpendicular and parallel to the bundle. Using (8.12a) and (8.10), integration along the contour of the bundle yields

$$\begin{aligned}(\gamma\mathcal{R}_\parallel^{FU} + L)U_x = \Omega_z\int_0^L y\,\mathrm{d}x - \Omega_y\int_0^L z\,\mathrm{d}x + (1-\gamma)\\ \left(A(0)|\boldsymbol{r}_\perp''(0)|^2 - \boldsymbol{r}_\perp'(0)\cdot\Big(A(0)\boldsymbol{r}_\perp^{(3)}(0) + A'(0)\boldsymbol{r}_\perp''(0)\Big) + \int_0^L A(x)\,\boldsymbol{r}_\perp''(x)\cdot\boldsymbol{r}_\perp^{(3)}(x)\mathrm{d}x\right) .\end{aligned} \tag{8.31}$$

Note that with our choice of coordinates, this relation is time-independent. It is straightforward to express this equation in terms of the complex quantities

$$\begin{aligned}(\gamma\mathcal{R}_\parallel^{FU} + L)U_x = \Im\left[\Omega^*\int_0^L \zeta\,\mathrm{d}x]\right] + (1-\gamma)\\ \Re\left[A(0)|\zeta''(0)|^2 - \zeta'(0)^*\Big(A(0)\zeta^{(3)}(0) + A'(0)\zeta''(0)\Big) + \int_0^L A(x)\,\zeta''(x)\zeta^{(3)}(x)^*\mathrm{d}x\right] .\end{aligned} \tag{8.32}$$

Integration along the bundle of (8.16) with the boundary conditions (8.12b, 8.12c) yields the relation

$$\int_0^L \zeta\,\mathrm{d}x = \imath\big(\mathcal{R}_\perp^{FU} + L\big)U + \big(a\mathcal{R}_\perp^{FU} - \frac{L^2}{2}\big)\Omega \ , \tag{8.33}$$

therefore $\Im[\Omega^* \int_0^L \zeta \,\mathrm{d}x] = (\mathcal{R}_\perp^{FU} + L)\,\Re[\Omega^* U]$. With the expressions for Ω and U from (8.19) one finds

$$\Re[\Omega^* U] = \frac{A(0)^2}{\mathcal{R}_\perp^{FU}\mathcal{R}_\perp^{L\Omega}} \Im[\zeta''(0)\zeta^{(3)}(0)^*] \,. \tag{8.34}$$

Collecting the previous results, the final expression for the swimming speed in the local frame of reference becomes

$$\begin{aligned}(\gamma\mathcal{R}_\parallel^{FU} + L)U_x =& A(0)^2 \frac{\mathcal{R}_\perp^{FU} + L}{\mathcal{R}_\perp^{FU}\mathcal{R}_\perp^{L\Omega}} \Im[\zeta''(0)\zeta^{(3)}(0)^*] + \\ & (1-\gamma)\,\Re\Big[A(0)|\zeta''(0)|^2 - \zeta'(0)^*\Big(A(0)\zeta^{(3)}(0) + A'(0)\zeta''(0)\Big) + \int_0^L A(x)\,\zeta''(x)\zeta^{(3)}(x)^* \mathrm{d}x\Big] \,.\end{aligned} \tag{8.35}$$

It is instructive to look at the limiting behavior of this equation for long L. Because the excitation of the tail is only locally at the origin, the amplitude $|\zeta(x)|$ must go to zero for large x. Therefore, the second term on the right-hand side of (8.35) must remain finite as $L \to \infty$. It follows that

$$U_x \approx \frac{A(0)^2}{\mathcal{R}_\perp^{FU}\mathcal{R}_\perp^{L\Omega}} \Im[\zeta''(0)\zeta^{(3)}(0)^*] \tag{8.36}$$

remains non-zero as $L \to \infty$. However, this must be wrong because the drag from the tail grows with L whereas the pushing portion of the tail remains bounded. The solution to this contradiction is that U_x is the bead speed in the local coordinate system of the swimmer. In contrast, the observed speed with respect to the fluid is measured from the laboratory system. Therefore, the result from (8.35) must be transformed into the lab system, which will be dealt with in the following section.

Transformation into the lab system

The swimming speed in (8.35) refers to a local coordinate system that co-rotates with the swimmer's head. Therefore, it must be transformed into the laboratory system. We define the lab frame along the orthogonal vectors $\hat{\boldsymbol{e}}_1$, $\hat{\boldsymbol{e}}_2$, $\hat{\boldsymbol{e}}_3$, where $\hat{\boldsymbol{e}}_1$ points along the average swimming direction. The swimmer revolves at constant angular velocity $\{\Omega_x = -1, \Omega_y, \Omega_z\}$ about its local axes. Hence, in the lab system the local coordinate vectors change according to

$$\frac{\mathrm{d}}{\mathrm{d}t}\boldsymbol{e}_{xyz} = \begin{pmatrix} 0 & -\Omega_z & \Omega_y \\ \Omega_z & 0 & -1 \\ -\Omega_y & 1 & 0 \end{pmatrix} \cdot \boldsymbol{e}_{xyz} \,. \tag{8.37}$$

The analytical solution of this rotation is given through the matrix exponential $\Re[\exp(M\,t)] \cdot \boldsymbol{e}_{xyz}$ where M is the above rotation matrix. Dropping all terms of second order in Ω one finds

$$\hat{\boldsymbol{e}}_x = \hat{\boldsymbol{e}}_1 - \Re[\Omega(1-\mathrm{e}^{\imath t})]\,\hat{\boldsymbol{e}}_2 - \Im[\Omega(1-\mathrm{e}^{\imath t})]\,\hat{\boldsymbol{e}}_3 \tag{8.38a}$$

$$\hat{\boldsymbol{e}}_y = -\Re[\Omega(1-\mathrm{e}^{-\imath t})]\,\hat{\boldsymbol{e}}_1 + \cos t\,\hat{\boldsymbol{e}}_2 + \sin t\,\hat{\boldsymbol{e}}_3 \tag{8.38b}$$

$$\hat{\boldsymbol{e}}_x = -\Im[\Omega(1-\mathrm{e}^{-\imath t})]\,\hat{\boldsymbol{e}}_1 - \sin t\,\hat{\boldsymbol{e}}_2 + \cos t\,\hat{\boldsymbol{e}}_3 \tag{8.38c}$$

which is exact up to order $|\Omega|^2$. The total swimming velocity of the head is given by $\boldsymbol{U} = U_x\hat{\boldsymbol{e}}_x + U_y\hat{\boldsymbol{e}}_y + U_z\hat{\boldsymbol{e}}_z$ of which we are only interested in the $\hat{\boldsymbol{e}}_1$ component. Hence,

$$U_1 = U_x - \Re[\Omega(1-\mathrm{e}^{-\imath t})]U_y - \Im[\Omega(1-\mathrm{e}^{-\imath t})]U_z \,. \tag{8.39}$$

In contrast to the velocity in co-rotating coordinates, this expression depends on time due to the oscillating motion of the bead. However, the time-dependent terms average out over one period, such that

$$\langle U_1 \rangle = U_x - \Re[\Omega^* U] \ . \tag{8.40}$$

With the previous results from (8.34,8.35) this yields the swimming speed in the lab system

$$\langle U_1 \rangle = \frac{1}{\gamma \mathcal{R}_{\parallel}^{FU} + L} \Bigg(A(0)^2 \frac{\mathcal{R}_{\perp}^{FU} - \gamma \mathcal{R}_{\parallel}^{FU}}{\mathcal{R}_{\perp}^{FU} \mathcal{R}_{\perp}^{L\Omega}} \Im[\zeta''(0)\zeta^{(3)}(0)^*] + (1-\gamma)\,\Re\Big[A(0)|\zeta''(0)|^2 - \zeta'(0)^* \Big(A(0)\zeta^{(3)}(0) + A'(0)\zeta''(0) \Big) + \int_0^L A(x)\,\zeta''(x)\zeta^{(3)}(x)^* \mathrm{d}x \Big] \Bigg) \ . \tag{8.41}$$

Because the experimentally implemented swimmer has a spherical head for which $\mathcal{R}_{\perp}^{FU} = \mathcal{R}_{\parallel}^{FU}$ and $\mathcal{R}_{\perp}^{L\Omega} = \mathcal{R}_{\parallel}^{L\Omega}$, this expression simplifies further to

$$\langle U_1 \rangle = \frac{1-\gamma}{\gamma \mathcal{R}^{FU} + L} \Bigg(\frac{A(0)^2}{\mathcal{R}^{L\Omega}} \Im[\zeta''(0)\zeta^{(3)}(0)^*] + \Re\Big[A(0)|\zeta''(0)|^2 - \zeta'(0)^* \Big(A(0)\zeta^{(3)}(0) + A'(0)\zeta''(0) \Big) + \int_0^L A(x)\,\zeta''(x)\zeta^{(3)}(x)^* \mathrm{d}x \Big] \Bigg) \ . \tag{8.42}$$

For $A = const$ this result is consistent with the one from the work of Lauga.

As in the previous section, consider $\langle U_1 \rangle$ in the limit of $L \to \infty$. In contrast to (8.35) which has a linear term in L, all terms on the right-hand side of (8.41) are bounded. Consequently, as $L \to \infty$ the swimming speed approaches zero. This is in accordance to our intuition that as the tail grows, the hydrodynamic drag increases, so that the swimmer becomes slower and less efficient. Hence, there must be an optimal tail length up to which the pushing force of the tail grows faster[1] than the hydrodynamic drag of the filament.

8.2 Swimming performance of our swimmer model

8.2.1 General discussion of the swimming speed

The formula for the swimming speed (8.42) in conjunction with the analytic solution (8.22) allows a few general remarks about swimming with a passive tail.

First of all, we remark that the swimming speed as given by (8.41) is the travelled distance of the swimmer after one complete revolution. Apparently, this distance has no explicit time dependence, which is typical for locomotion at small Reynolds number [4]. Consider the conformations of the swimmer in an abstract phase space, where the swimmer starts at some point A in this conformation space and takes a path $\mathcal{P}$ to point B. In doing so, the swimmer translates in its physical space by some distance l, but this distance is solely a function of the path taken and does *not* depend on how fast this path was traversed [70]. Swimming at low Reynolds number is a therefore a purely geometric question. In our case, this shows in the

[1] Depending on the chosen tail parameters, the pushing force can also be negative, so that the swimmer swims backwards.

above-mentioned independence of the swimmer displacement over one rotation and the driving frequency. There is however an indirect linear dependence on time, because revolutions of the swimmer have a faster sequence, if the frequency increases. This indirect dependence is hidden by the choice of our unit system and becomes apparent when transforming the swimming speed into physical units by multiplying with $\ell_\omega \cdot 2\pi f$ (see 8.1.1). Furthermore, there is an additional non-trivial dependence on the driving frequency, because ℓ_ω is a function of ω. As a consequence, a higher frequency changes the relevant length scales of the swimmer, leading to an entirely different tail shape. Intuitively, it is clear that the tail receives a stronger drag from the fluid if driven faster, so that it bends more. This dependence will be the subject of the next section (8.2.2).

Equation (8.41) also shows that for isotropic friction where $\mathcal{R}_\perp^{FU} = \mathcal{R}_\parallel^{FU}$ and $\gamma = 1$ there is no propulsion. This is an important consistency check, because propulsion at low Reynolds number can only be achieved by anisotropic friction and not by inertial effects [4]. In addition, there is a subtlety in (8.41) that is easily overlooked. Consider therefore the shape equation (8.2)

$$\Gamma \boldsymbol{u} = -\partial_s^2(A(s)\partial_s^2 \boldsymbol{r}) + \partial_s(\sigma(s)\partial_s \boldsymbol{r}) \ ,$$

where we have abbreviated the friction tensor on the left-hand side by Γ. The left-hand side sets the scale of typical friction forces that act on the tail by $\Gamma\boldsymbol{u}$. It follows that the typical curvature of the tail is then in the order of $|\partial_s^2 \boldsymbol{r}| \approx |\Gamma \boldsymbol{u}| L^2/A$. Consequently, as A becomes large, the curvature of the tail becomes negligibly small. However, $\zeta^{(2)}$ or $\zeta^{(3)}$ appear in every single term of (8.41), so that the swimming speed becomes zero. What we have recovered was the scallop theorem from [4], which states that a time-reversible motion does not lead to propulsion. The motion of a straight rod is however always time-reversible.

Finally, we look at the functional form of the swimming speed (8.41). We note that every single term is quadratic in ζ, so that the swimming speed scales quadratic with the amplitude of the tail shape. This is a generic feature of low Reynolds number swimming as can be shown in a simplified setup [70]. The tail shape on the other hand depends linearly on the excitation parameters ε_1 and ε_2 (see 8.26).

In summary, we have found that our formula for the swimming speed scales linearly with the frequency of the external field and quadratic with the amplitude of the tail shape. Because the swimming mechanism is based on the anisotropic friction of a non time-reversible motion, the motion subsides if the friction anisotropy vanishes ($\gamma = 1$) or the rod becomes too stiff to bend. These findings are in accordance to fundamental considerations of swimming strokes at low Reynolds numbers.

8.2.2 Design principles for fast swimming with passive tails

The geometric nature of swimming at low Reynolds number implies that the swimming speed increases linearly with the rotation frequency ω — if the geometry stays the same. Because the swimmer geometry determines the swimming speed, we examine the impact of various geometrical parameters on the swimming speed. Before doing so, we limit the number of free parameters and focus on the interesting ones in the following. The swimming speed as function of these swimmer parameters will then be discussed in the next subsections.

The parameters determining the tail shape and therefore the swimmer speed are the (variable) tail stiffness $A(x)$, the tail length L, the driving frequency ω, the head diameter r_h, and the excitation amplitudes ε_1, ε_2. As this list of parameters is rather long, we reduce the number of parameters to the most interesting ones. First, we choose $\varepsilon_1 = \varepsilon \mathrm{e}^{-\imath\pi/4}$ and $\varepsilon_2 = \varepsilon$, so that $\varepsilon_{1,2}$ contribute equally to the swimming speed. Remember that $\boldsymbol{r}(x) = x\hat{\boldsymbol{e}}_x + \Re\zeta(x)\hat{\boldsymbol{e}}_y + \Im\zeta(x)\hat{\boldsymbol{e}}_z$, so that a phase shift of $-\pi/4$ of ε_1 versus ε_2 means that the tail direction at $x = 0$ lags behind the direction of the point of attachment. The equality of $|\varepsilon_1| = |\varepsilon_2| = \varepsilon$ allows to scale our results of the swimming speed by ε^2, so that the results become independent of the amplitude ε. Furthermore as already mentioned above, our main focus for the stiffness model $A(x)$ is an exponential profile for reasons that will be explained below (see 8.3.2 on p. 142). Unless explicitly stated otherwise, a *variable stiffness* will in the following always refer to an exponential stiffness profile. To be precise, we use the stiffness model $A(x) = A_s \cdot a^{1-x/L}$ where a is the number of attached filaments to the bead. Because A_s is one in our unit system, for brevity we refer to a as the stiffness.

In addition to the variable parameters, we have to specify the friction coefficients of the tail and the head. For the tail, the friction coefficients can be estimated by slender body theory [19, 71]

$$\gamma_\perp = 4\pi\eta / \left(\log(L/d) - \frac{1}{2} + \log(2) - \frac{1 - \frac{\pi^2}{12}}{\log(L/d)} \right) \tag{8.43a}$$

$$\gamma_\parallel = 2\pi\eta / \left(\log(L/d) - \frac{3}{2} + \log(2) - \frac{1 - \frac{\pi^2}{12}}{\log(L/d)} \right) \tag{8.43b}$$

where η is the dynamic viscosity of water and L/d is the aspect ratio of the tail. Because the dominant L/d-dependence is $1/\log(L/d)$ and therefore logarithmic, the results below change only slightly when varying L/d. In the following, we only use an aspect ratio of $L/d = 200$, so that $\gamma \equiv \gamma_\perp/\gamma_\parallel \approx 1.63$. Where necessary, we used the dynamic viscosity of water at $20°C$, which is $\eta = 1.00\, mPa \cdot s$ [72].

Finally, we restrict our considerations to swimmers with a spherical head of radius r_h, for which the friction coefficients are [73]

$$\mathcal{R}^{FU} = \mathcal{R}^{FU}_\parallel = \mathcal{R}^{FU}_\perp = 6\pi\eta\, r_h/\xi_\perp \qquad [\xi_\perp \ell_\omega] \tag{8.44a}$$

$$\mathcal{R}^{L\Omega} = \mathcal{R}^{L\Omega}_\parallel = \mathcal{R}^{L\Omega}_\perp = 8\pi\eta\, r_h^3/\xi_\perp \qquad [\xi_\perp \ell_\omega^3]\ . \tag{8.44b}$$

The brackets are a reminder that the friction coefficients in natural units are simply numbers, which have to be multiplied by the factor in the brackets to transform into physical units. There is however a caveat. Consider the swimmer being rotated by an external field, e.g. a magnetic field, so that it feels hydrodynamic drag forces from its movement through the surrounding fluid. Because these drag forces apply also on the tail, they are asymmetric with respect to the center of mass of the swimmer, so that they tilt the swimmer along its x- or z-axis. Although this is fine for our theory, it is not what would happen in an experiment if driven by a magnetic field that rotates around the x-axis. To understand this, remember that the head must have a magnetic momentum to be rotated by the external magnetic field. This momentum exerts a torque that rotates the bead along the x-axis so that its magnetic moments points along a perpendicular direction, say the y direction. This also

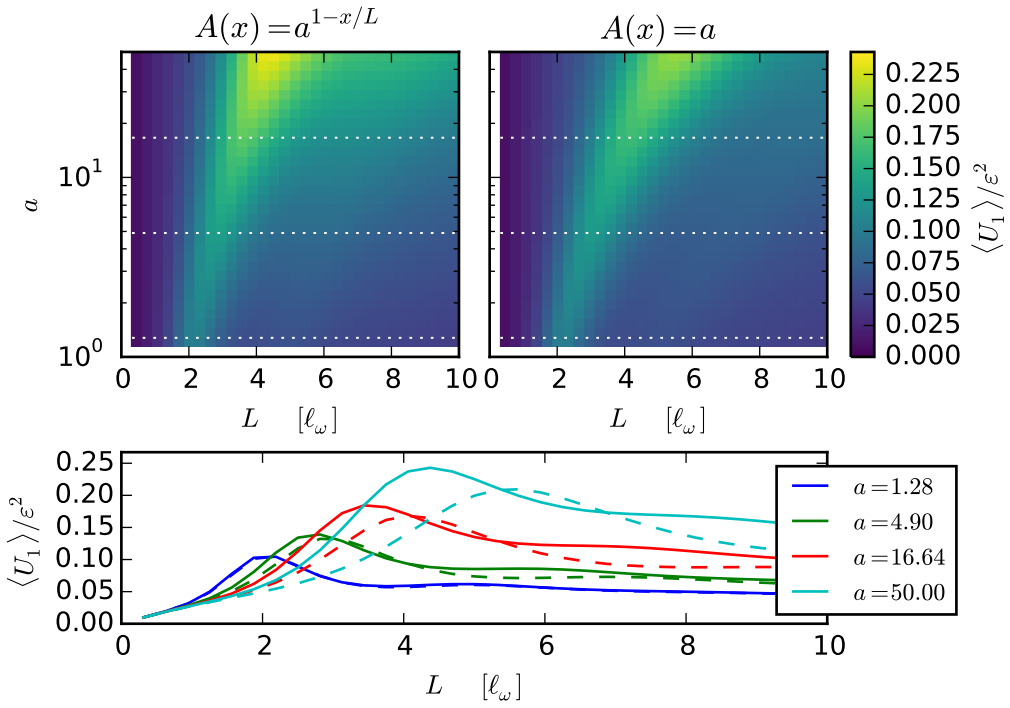

Figure 8.3 | Swimming speeds $\langle U_1 \rangle$ of a swimmer with head size $r_h = 1\,\ell_\omega$ for constant (**top right**) and variable (**top left**) stiffness model as a function of tail length L and tail stiffness a. As explained in 8.2.2, $\mathcal{R}^{L\Omega}$ was 500-fold increased. Note that the scale bar of the a-axis is logarithmic. The **bottom** panel shows the same data for selected a-values with variable (solid lines) and constant (dashed lines) stiffness model. The corresponding cuts through the parameter space are indicated by dotted lines in the top panels.

means, however, that the bead cannot rotate along the z-axis, because this rotation has to work against the external torque. In practice, there will be a force balance of drag forces which effectively lead to a suppression of rotations about the y- and z-axes. We can account for this effect by using an effective torque $\mathcal{R}^{L\Omega}$ that is multiplied by an arbitrary large factor, which we refer to as **fixated**.

Altogether, we have seen that there are three parameters of particular interest: the stiffness a, the tail size L, and the head diameter r_h. All other parameters can either be ignored, or we use reasonable generic values. In the following, we will discuss design principles concerning the above-mentioned free parameters for swimmers with passive tails.

Constant head size $r_h = 1\,\ell_\omega$

First, we discuss the interplay of tail length L and tail stiffness a[2] with the swimming speed. The results are exemplary and were obtained for $r_h = 1\,\ell_\omega$.

Figure 8.3 shows the swimming speed as a function of tail length L and tail stiffness a for a swimmer with 500-fold increased $\mathcal{R}^{L\Omega}$. In accordance to our general discussion above, the swimming speed in general decreases for long tails. Besides, for very short tails, the swimming

[2]Remember that for brevity we refer to a stiffness model $A(x) = A_s \cdot a^{1-x/L}$ simply as a.

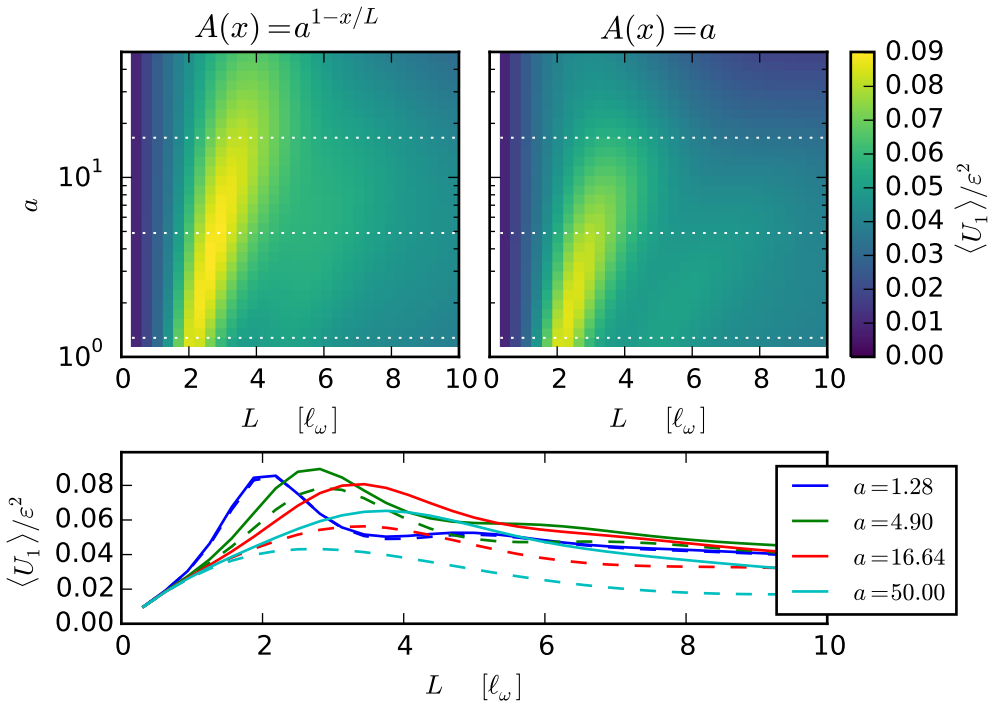

Figure 8.4 | Swimming speeds $\langle U_1 \rangle$ of a swimmer with head size $r_h = 1\,\ell_\omega$ for constant (**top right**) and variable (**top left**) stiffness model as a function of tail length L and tail stiffness a. Here, $\mathcal{R}^{L\Omega}$ was left unchanged. Note that the scale bar of the a-axis is logarithmic. The **bottom** panel shows the same data for selected a-values with variable (solid lines) and constant (dashed lines) stiffness model. The corresponding cuts through the parameter space are indicated by dotted lines in the top panels.

speed approaches zero, because an undecorated bead does not propel when rotated. However, in between those limiting points, the swimming speed is non-zero and must therefore have a maximum. As Fig. 8.3 shows, the qualitative behaviour for variable stiffness is similar to a constant stiffness, but the peak speed is higher and shifts towards smaller tail lengths. Indeed, the maximum speed of the variable stiffness swimmer is about 15% faster (0.24 versus 0.21).

At first sight it may be surprising to find an increase of the swimming speed even for very high tail stiffness. The reason for this behavior is the strongly increased $\mathcal{R}^{L\Omega}$, which has the effect of suppressing any rotations[3] of the swimmer. Because our boundary conditions ε_1 and ε_2 have a phase shift, a completely straight tail points outward in a chiral fashion, so that the swimming speed remains non-zero for arbitrarily large a.

If the rotation about the y- and z-axes is not suppressed, this picture changes significantly (Fig. 8.4). In contrast to the fixated[4] case, the swimming speed indeed decreases if a becomes too large. This behavior is as expected from our general discussion of the swimming speed. Furthermore, the swimming speed of the variable stiffness swimmer is in general faster than the corresponding swimmer with constant stiffness. Indeed, the fastest swimmer with constant stiffness is found for $a = 1$, which has almost the same speed as the fastest swimmer with

[3] Of course, the driven rotation of along the swimming axis is unaffected of the increased $\mathcal{R}^{L\Omega}$
[4] See 8.2.2

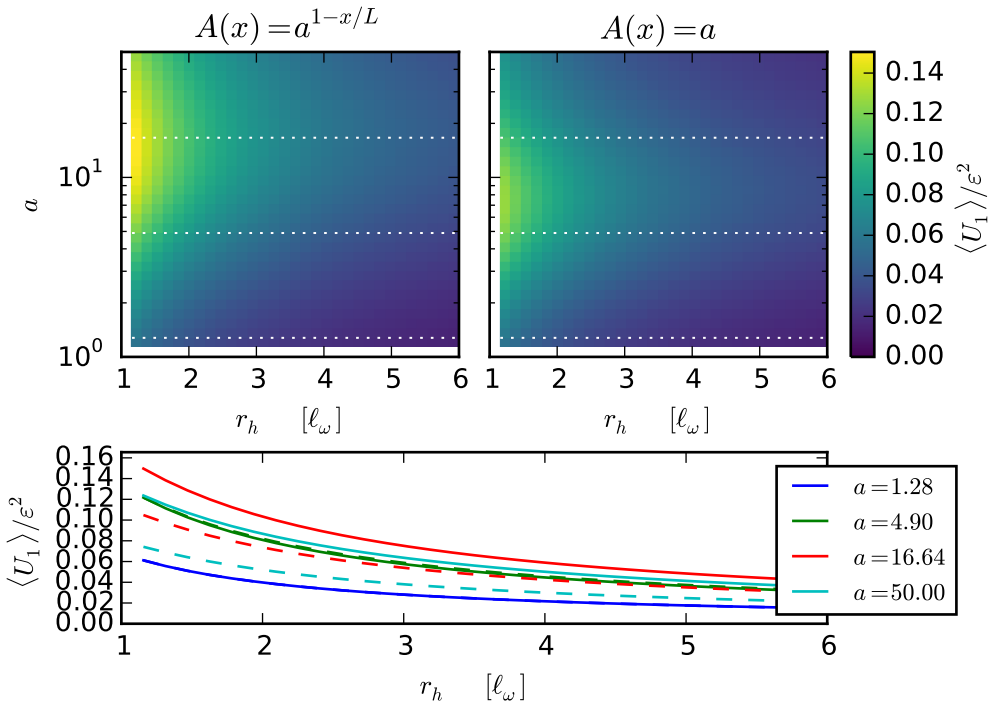

Figure 8.5 | Swimming speeds $\langle U_1 \rangle$ of a swimmer with tail length $L = 3\,\ell_\omega$ for constant (**top right**) and variable (**top left**) stiffness model as a function of head size r_h and tail stiffness a. As explained in 8.2.2, $\mathcal{R}^{L\Omega}$ was 500-fold increased. Note that the scale bar of the a-axis is logarithmic. The **bottom** panel shows the same data for selected a-values with variable (solid lines) and constant (dashed lines) stiffness model. The corresponding cuts through the parameter space are indicated by dotted lines in the top panels.

variable stiffness (0.090 versus 0.086). However, for a constant stiffness the swimming speed quickly decreases with a, whereas the variable stiffness swimmer achieves significantly higher speeds for a very large a-region (remember that the a-scale is logarithmic).

In summary, this example shows that the swimming speed of a swimmer with variable stiffness is generally higher than that of a constant stiffness swimmer. The suppression of rotations about the axes perpendicular to the swimming axis makes swimming with stiffer tails effective, whereas non-fixated swimmers swim best at low tail stiffness. In all cases, for any given stiffness a there is an optimal tail length where the swimming speed has a pronounced optimum. In short, a variable stiffness tail is nearly always beneficial.

Constant tail length $L = 3\,\ell_\omega$

In the following, we discuss the interplay of head size r_h and tail stiffness a with the swimming speed. The results are exemplary and were obtained for $L = 3\,\ell_\omega$.

Figure 8.5 shows the swimming speed as a function of head size r_h and tail stiffness a for a swimmer with 500-fold increased $\mathcal{R}^{L\Omega}$. It is apparent from the lower panel of Fig. 8.5 that the swimming speed has a rather regular dependence on the head size r_h. The reason for this regularity becomes apparent when considering the geometry of the swimmer. Because the

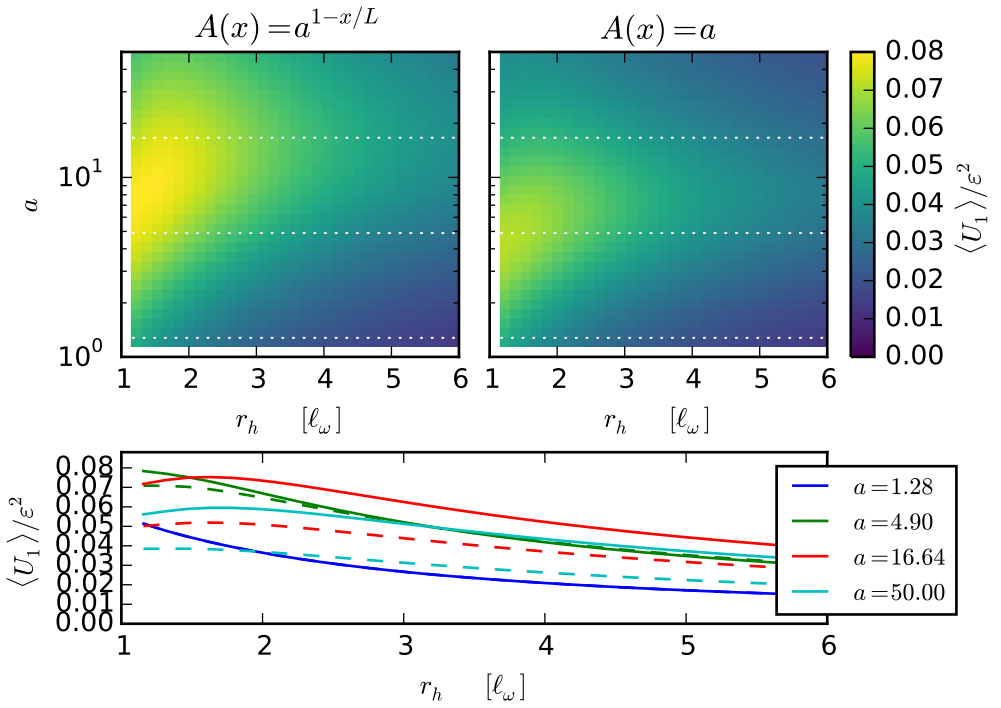

Figure 8.6 | Swimming speeds $\langle U_1 \rangle$ of a swimmer with tail length $L = 3\,\ell_\omega$ for constant (**top right**) and variable (**top left**) stiffness model as a function of head size r_h and tail stiffness a. Here, $\mathcal{R}^{L\Omega}$ was left unchanged. Note that the scale bar of the a-axis is logarithmic. The **bottom** panel shows the same data for selected a-values with variable (solid lines) and constant (dashed lines) stiffness model. The corresponding cuts through the parameter space are indicated by dotted lines in the top panels.

rotations about the y- and z-axes are suppressed, the resulting beat shape of the swimmer does not change when increasing r_h. Therefore, the main effect of an increased r_h is an additional drag from the head. Because the head drag enters the swimming speed with $1/\mathcal{R}^{FU}$, the resulting swimming speed scales approximately with $1/r_h$. Therefore, the fastest swimmers are found for the smallest head radius. As for the stiffness axis, we find that for all bead sizes the swimming speed increases with tail stiffness up to some optimal stiffness and starts to decrease for even higher values. In general, the qualitative behaviour for variable stiffness and constant stiffness is similar, but the peak speed shifts towards higher tail stiffness and is higher for variable stiffness. Indeed, the maximum speed of the variable stiffness swimmer is about 19% faster (0.15 versus 0.13).

If the rotation about the y- and z-axes is not suppressed, this picture changes significantly (Fig. 8.6). Similarly to the other cases above, the swimming speed for a freely rotating head decreases by about a factor 2. In contrast to the fixated case, here the swimming speed has a non-trivial dependence on the head size. If the head size is too small, the tail acts like an anchor in the water and mainly the head moves, so that the overall swimming speed remains small. With increasing head size, the roles interchange such that the head becomes the anchor and the tail moves and the overall push by the tail increases. Because the drag from the head increases at the same time, there is an optimal head size where the swimming speed is maximized. A similar reasoning applies to the tail stiffness a: if the tail is too wiggly,

it always bends away when a drag applies and the pushing force is small. If on the other hand the tail is too stiff, the induced chirality of the tail is lost and the swimming speed decreases. In general, the swimming speed of the variable stiffness swimmer is faster than the corresponding swimmer with constant stiffness. Indeed, the fastest swimmer with variable stiffness is about 12% faster than the fastest swimmer with variable stiffness (0.080 versus 0.072).

In summary, the preceding example demonstrated that the swimming speed of a swimmer with variable stiffness is generally higher than that of a constant stiffness swimmer. The suppression of rotations about the axes perpendicular to the swimming axis allows efficient swimming with small heads, while for larger heads, the rotation lock is less important. For a fixated swimmer, the guideline for the optimal head size is "as small as possible", whereas for a freely rotating swimmer the optimal head size is non-zero. In all cases, for any given head size r_h there was an optimal tail stiffness where the swimming speed is largest. In general, a variable stiffness tail is nearly always beneficial.

Constant tail stiffness $a = 25$

In the following, we discuss the interplay of tail length L and head size r_h with the swimming speed. The results are exemplary and were obtained for $a = 25$.

Figure 8.7 shows the swimming speed as a function of tail length L and head size r_h for a swimmer with 500-fold increased $\mathcal{R}^{L\Omega}$. As already discussed above, the geometry of a fixated swimmer is almost independent of the bead size, so that the main effect of an increased r_h is an additional drag from the head. Because the head drag enters the swimming speed with $1/\mathcal{R}^{FU}$, the resulting swimming speed scales approximately with $1/r_h$. Therefore, the fastest swimmers are found for the smallest head radius. Again, for very short tails or long tails the swimming speed approaches zero, but is nonzero in between and therefore has a maximum. As Fig. 8.7 shows, the qualitative behaviour for variable stiffness and constant stiffness is similar, but the peak speed shifts towards smaller tail lengths and is higher for variable stiffness. Indeed, the maximum speed of the variable stiffness swimmer is about 12% faster (0.19 versus 0.17).

If the rotation about the y- and z-axes is not suppressed, this picture changes significantly (Fig. 8.8). Similarly to the other cases above, the swimming speed for a freely rotating head decreases by about a factor 2. In contrast to the fixated case, here the swimming speed has a non-trivial dependence on the head size. If the head size is too small, the tail acts like an anchor in the water and mainly the head moves and the overall swimming speed remains small. With increasing head size, the roles interchange such that the head becomes the anchor and the tail moves, so that the overall push by the tail increases. Because the drag from the head increases at the same time, there is an optimal head size where the swimming speed is maximized. A similar reasoning applies to the tail length L: if the tail is too short, it does not push. If on the other hand the tail is too long, it adds to the hydrodynamic drag, so that the swimming speed is highest for an intermediate tail length. In general, the swimming speed of the variable stiffness swimmer is faster than the corresponding swimmer with constant stiffness. Indeed, the fastest swimmer with variable stiffness is about 22% faster than the fastest swimmer with variable stiffness (0.090 versus 0.074).

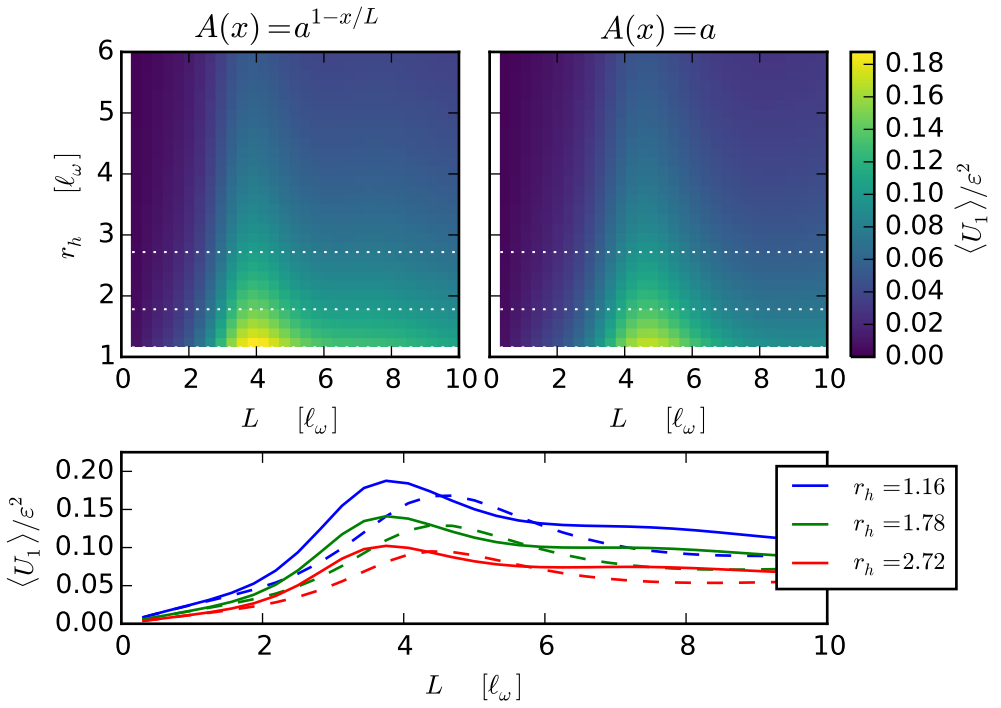

Figure 8.7 | Swimming speeds $\langle U_1 \rangle$ of a swimmer with tail stiffness $a = 25$ for constant (**top right**) and variable (**top left**) stiffness model as a function of tail length L and head size r_h. As explained in 8.2.2, $\mathcal{R}^{L\Omega}$ was 500-fold increased. The **bottom** panel shows the same data for selected head sizes with variable (solid lines) and constant (dashed lines) stiffness model. The corresponding cuts through the parameter space are indicated by dotted lines in the top panels.

In summary, this exemplifies that the swimming speed of a swimmer with variable stiffness is generally higher than that of a constant stiffness swimmer. The suppression of rotations about the axes perpendicular to the swimming axis allows efficient swimming with small heads, while for larger heads, the rotation lock is less important. For a fixated swimmer, the guideline for the optimal head size is "as small as possible", whereas for a freely rotating swimmer the optimal head size is non-zero. In all cases, for any given head size r_h there was an optimal tail length where the swimming speed has a pronounced optimum. In general, a variable stiffness tail is nearly always beneficial.

Optimized stiffness profile

So far, we have discussed the swimming performance for a particular stiffness model $A(x) = A_s \cdot a^{1-x/L}$ and discovered that a variable stiffness generally improves the swimming speed. Although there is an optimal combination of stiffness a, tail length L, and head size r_h, this optimum remains within the subclass of exponential stiffness profiles. In the following, we will consider a much bigger class of stiffness models and determine an optimal stiffness profile.

We now consider a swimmer with fixed tail length L and fixed head size r_h, but unknown stiffness profile $A(x)$. Because a comparison to a bad swimmer with exponential stiffness profile would be a bit unsportsmanlike, we take a parameter set where the exponential profile

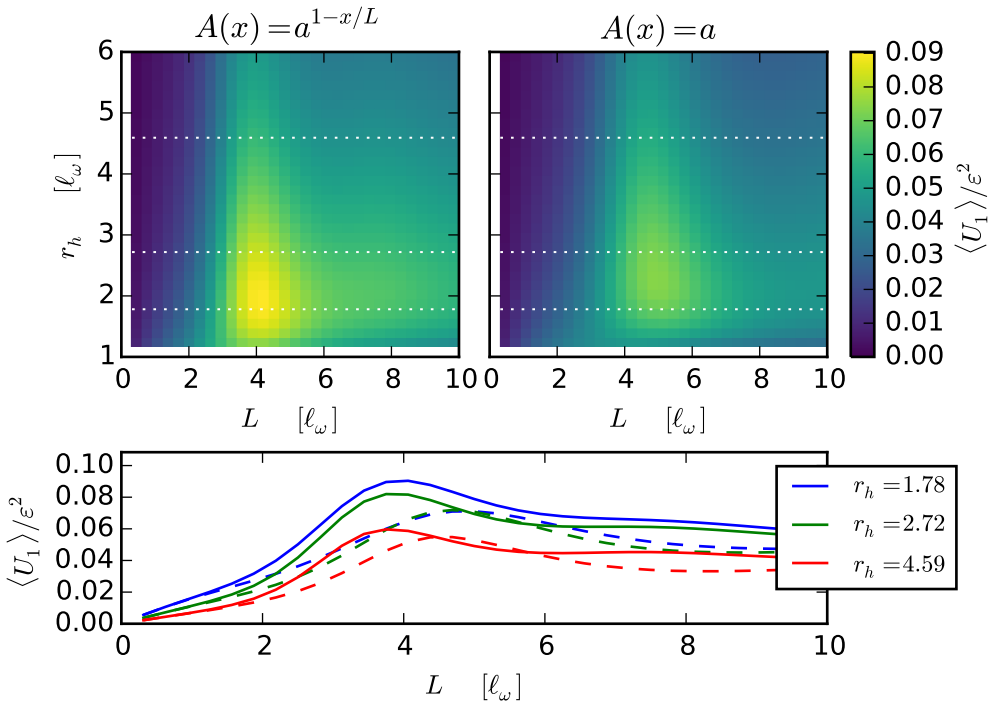

Figure 8.8 | Swimming speeds $\langle U_1 \rangle$ of a swimmer with tail stiffness $a = 25$ for constant (**top right**) and variable (**top left**) stiffness model as a function of tail length L and head size r_h. Here, $\mathcal{R}^{L\Omega}$ was left unchanged. The **bottom** panel shows the same data for selected head sizes with variable (solid lines) and constant (dashed lines) stiffness model. The corresponding cuts through the parameter space are indicated by dotted lines in the top panels.

swimmer was good at: $L = 4.1\,\ell_\omega$, $r_h = 1.7\,\ell_\omega$, and $a = 25$. Of course, the set of relevant stiffness functions $A(x)$ has to be restricted so that the problem becomes feasible. Because in experiments a variable stiffness is best achieved by attaching several thin filaments with different lengths, it is clear that the stiffness can decrease along the tail, but not increase. In addition to the monotonicity, we require that the stiffness has fixed values at the boundaries, because the preceding sections have shown that the maximum stiffness improves the swimming speed. Therefore, we limit our set of functions to monotonously decreasing ones that in addition fulfill the boundary conditions $A(0) = a$ and $A_s = 1$.

These conditions considerably restrict the set of possible stiffness profiles, but for a numerical optimization, the degrees of freedom have to be drastically reduced. This has to be done in a such way that every reasonable solution can be well approximated in this reduced function set. Spline interpolations are the ideal choice for this task, because they approximate smooth functions with very small error and are easy to handle [74]. Below we use an interpolating spline function with six suspension points and an interpolation order of 3. Altogether, the stiffness model then has four independent parameters $s_1, \ldots, s_4$, because the boundary values are fixed.

The reduction of the stiffness model $A(x|s_1, \ldots, s_4)$ allows to numerically maximize the swimming speed with respect to the suspension points of $A(x)$. The solver for the tail shape as presented in Appendix B.1 can easily be generalized to handle spline stiffness models.

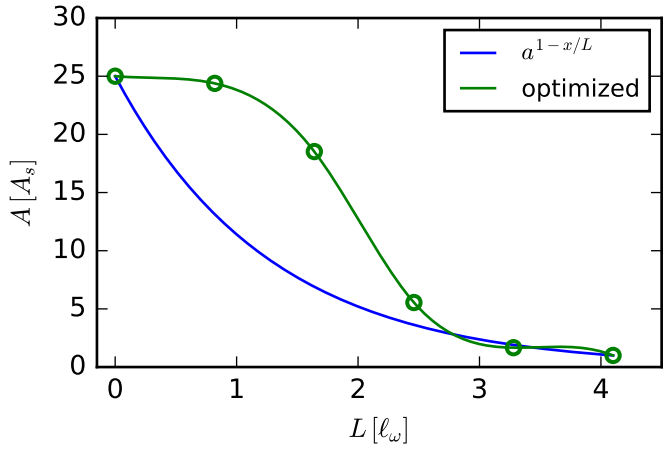

Figure 8.9 | Stiffness profile A for a swimmer with optimized stiffness profile (green) and the usual exponential stiffness profile (blue). The optimized stiffness profile was approximated using a cubic spline function with six suspension points (green circles). The swimming speed of the optimized swimmer is about 19% faster than with an exponential stiffness profile.

Because we can only calculate the swimming speed itself but not its gradient in the space of the spline parameters, the minimization procedure is computationally quite demanding. In addition, every evaluation of the swimming speed takes about $2\,s$, so that we have to stop the optimization procedure at a rather coarse accuracy. For the minimization, we used the differential evolution algorithm from the built-in Mathematica routines [75]. Figure 8.9 shows the result of this optimization effort. This optimal stiffness profile has a large stiffness close to the head and a small transition region at about half tail-length where it drops down to the minimally allowed stiffness. This step-like shape of the optimized stiffness profile is also found for other combinations of tail length, head stiffness, boundary conditions ε_1 & ε_2, and even maximal stiffness a. One can therefore assume that the shape of the optimal stiffness profile is rather generic. Compared to the exponential stiffness profile, the optimized stiffness profile results in a speed boost from $0.091\,\ell_\omega\omega/\varepsilon^2$ to $0.108\,\ell_\omega\omega/\varepsilon^2$ ($\approx 19\%$). This is a comparable improvement as from constant stiffness to an exponential stiffness profile.

The simple shape of the optimized stiffness profile even allows to realize this stiffness profile in experiments. In the next section, we will see how a variable stiffness profile can be realized in an experiment by attaching several filaments with different lengths to a head. Because without cross-links the local stiffness scales linearly with the number of filaments in the tail [76–78], monotonously decreasing stiffness profiles can be approximated by attaching the corresponding number of filaments

$$N(l) = \int_{A(0)}^{A(L)} \delta\Big(A^{-1}(a) - l\Big)\mathrm{d}a \ . \tag{8.45}$$

For self-assembled structures however, where the filaments attach at random, the number of attached filaments with a defined length can not be easily controlled. Yet, in the special case of a step-like function it is possible to mix many small filaments with a few long filaments. If done right, the short filaments bind much more often than the long ones, so that the step-like stiffness profile can be approximated.

In summary, by using a spline approximation of the stiffness profile, we determined an optimal stiffness profile for a swimmer whose other tail parameters were fixed. Although not rigorously proven, the obtained profile with a step-like transition from high stiffness to low stiffness at about half tail-length seems to be generic, because it was also found in other examples. Because of its simplicity, we argued that such a stiffness profile could even be realized by experiments with self-assembled swimmers.

Summary of the design principles

The preceding examples considered the swimming speed of a swimmer with variable stiffness profile when at least one parameter is fixed. In the following, these results will be combined and the most important guidelines will be highlighted.

In general, one has to distinguish between the two cases where the rotation of the head is free and only limited by its rotational friction $\mathcal{R}^{L\Omega}$ and where the rotation is suppressed due to external torques ("fixated"). In an experiment with a driving by a magnetic field, the latter usually applies better than the free rotation (see 8.2.2). For such a fixated swimmer, the swimming speed has a trivial dependence on the head size r_h, because a bigger head just means a larger drag while the tail shape remains the same. Therefore, the smaller r_h the higher is the swimming speed (Figs. 8.5 and 8.7). On the other hand, for a and L the swimming speed is a non-trivial function of these parameters, and the highest swimming speeds were found for the highest stiffness a (Fig. 8.3). Consequently, it is unclear whether the swimming speed would increase further for even higher stiffness values a. However, because the maximally achievable stiffness is usually limited, the guideline for the best performance is to make the stiffness as high as possible and adapt the tail length accordingly. For virtually any parameter set the variable stiffness swimmer is faster than the swimmer with constant stiffness.

On the other hand, when the swimmer head is not fixated and may rotate freely, the guidelines are quite different. In contrast to the fixated case, the swimmer head now influences the tail shape and the swimming speed has a non-trivial dependence on the head size. As a consequence, the optimal head size is in general no longer as small as possible but depends on the other tail parameters (Figs. 8.6 and 8.8). Like for the fixated swimmer, there is still an optimal tail length with a pronounced maximum (Figs. 8.4 and 8.8), so that the tail length is the most important handle for the swimming performance. In contrast to the fixated case, however, the stiffness a has a much smaller impact on the maximum speeds and in general, the best swimming speeds are found at small and intermediate stiffnesses ($a = 1 - 10$). In general, the swimming speed is only about half as big as in the fixated case. So if there is a choice, the head rotation should be suppressed by external forces. Also in this case, for virtually any parameter set, the variable stiffness swimmer is faster than the swimmer with constant stiffness.

Last but not least, we found that the optimized stiffness profile has the very simple form of step function. It is a mere coincidence that the shape of the optimal stiffness profile is so simple, but it should make it possible to approximate the optimal stiffness profile in experiments (see 8.2.2). Because the speed increase from an exponential to the optimized stiffness profile is comparable to the gain from constant stiffness to exponential, it is worth to consider. It is remarkable that the swimming speed for variable stiffness outperforms a

constant stiffness for all parameters shown. Indeed, this is a feature that we found in all stiffness profiles that we considered.

8.3 Application to an experimental micro-swimmer

The model presented above was developed in close collaboration to an experiment that realized microscopic swimmers [63]. The aim of this experiment was to use bottom-up DNA-based self-assembly techniques to build micro-scale oars that propel a rotating magnetic bead. Thereby it opens up the toolbox of DNA self-assembly to the construction of micro-swimmers and unravels a whole new class of versatile micro-swimmer designs. In the following, we will outline the construction principle of this micro-swimmer and compare the measured swimming speeds to the predicted ones.

8.3.1 Experimental micro-swimmer with variable bending stiffness

The bottom-up self-assembly of DNA into defined shapes is a powerful tool to construct a huge variety of micro-structures [79, 80]. In particular, this technique also allows to construct three-dimensional and curved structures with some control over their rigidity [81, 82]. Because the self-assembly happens without the need of external control, the yield of so created particles is huge. The versatility in shape and the high yield makes self-assembled DNA structures an ideal component for the construction of micro-swimmers. In the following we will outline the design for a DNA-based micro-swimmer that was developed in collaboration with the group of Tim Liedl [63].

As this experiment aimed to be a proof of principle, we used the simplest shape that generates propulsion: a flexible oar [4]. This oar is the centerpiece in the construction of a micro-swimmer, because it has to be several micrometers long and very stiff. These are requirements that can be met by self-assembled DNA structures. Usual DNA origami works by the controlled folding of a long single-stranded DNA scaffold via short DNA oligonucleotides — so-called "staple strands" — that tie different points of the scaffold strand together [79]. After folding, several of these structures can be concatenated if the staple strands at the ends stick out and complementarily match the staples at the other end. For example, it is possible to create tube-like structures that can be concatenated via staple binding. However, such links with staples create joints where the local stiffness of the tube differs from the target value. Therefore, a more uniform design for DNA tubes is required. Yin et al. have proposed a modified approach where the target structure is solely built from short DNA oligonucleotides that repeat like in a polymer [83]. Because no staple has an exceedingly long sequence (as the scaffold in DNA origami) and every staple type is repeated frequently along the tube, the stiffness of the resulting structure is much more uniform than for concatenated DNA origamis. In particular, this approach also allows to tune the diameter, stiffness and helicity of the resulting tube structure [83–85]. For the experimental swimmer, we settled with a straight twisted 8-helix structure [63] (in the following just "filament") with a persistence length of $l_p = 8.2\,\mu m$ [85].

As the motor of our swimmer we used a ferro-magnetic bead with about $1\,\mu m$ in diameter. This bead was rotated by means of an externally applied homogeneous magnetic field, so that

Figure 8.10 | Snapshot of swimmer #2 (table 8.1) as observed in the experiment. **Active content:** In a flash enabled viewer, clicking the image plays a movie of this swimmer. With courtesy of Alexander Maier

the bead receives a torque from the magnetic field. The head and tail were connected by biotin-streptavidin bonds [86, 87]. For that, we let staple strands stick out along the filament, which in turn were functionalized with biotin via the binding of complementary DNA strands. The magnetic particles were already supplied with streptavidin functionalization. Because the abundance of filaments was much higher than the abundance of beads, the number of attached filaments was random. In particular, the beads attached at random positions along the tail and the filaments covered the beads isotropically.

Upon rotation of the magnetic head via an external magnetic field, the filaments formed bundles along the rotation axis of the bead. In about 10% of the cases, the bundles formed only on one side of the bead and propelled the swimmer into the direction of the bead. Figure 8.10 shows a typical example of such an example as observed in the experiment.

8.3.2 Observed and predicted swimming speed

The preceding section has presented an experimental realization of a swimmer with a variable bending modulus. Above, we have presented a theory that exactly applies to this case, so this begs a comparison of theory and experiment. For that, we discuss how to determine the relevant model parameters and compare the predicted to the observed swimming speed.

The most direct way to compare theory and experiment would be to compare the observed tail shape to the predicted tail shape. However, the shape of the experimental swimmer is rather noisy so that it is hard to compare to a predicted shape. Therefore it is much cleaner to compare a time-averaged quantity such as the translation during some time interval, in other words the average speed. To apply the theoretic model, we must determine the whole set of model parameters $A(x)$, L, r_h, ε_1, ε_2, l_p, $\gamma_\perp$, η, and ω. Some of these parameters are well-known or well-controlled, such as the dynamic viscosity of water ($\eta \approx 1\,mPa\,s$ at $20°C$ [72]), the persistence length of a single filament ($8.2\,\mu m$, [85]), the frequency at which the magnetic field was rotated ($f = 1$–$3\,Hz$) and the head diameter ($1\,\mu m$). The remaining parameters on the other hand are parameters that have to be determined individually for each observed swimmer.

In particular, among the individual parameters is the stiffness profile $A(x)$ or the number of attached filaments a. For an estimate of the stiffness profile, we first have to understand the length distribution of the attached filaments. Because each filament in the bundle re-

sults from a linear polymerization process, we expect an exponential distribution of filament lengths [88]. Indeed, Yin et al. found an exponential length distribution in the lengths of unbound DNA filaments [83]. To verify this length distribution in the attached filaments, we furthermore measured the fluorescence intensity along the contour of the bundle, which we found to be exponentially decaying. Because we expect the fluorescence intensity to be proportional to the number of filaments present at the respective bundle position, this supports our assumption that the attached filaments have an exponential length distribution. If the attached filaments have an exponential length distribution, then the number of filaments present at a distance l away from the head is proportional to $\int_l^\infty P(l' > l)\,\mathrm{d}l'$, so again an exponential function. Therefore we assumed that the number of filaments present at the bundle position x is proportional to $a\,\mathrm{e}^{-x/\chi}$. Next we need to establish a relationship between the number of filaments present at a position x and the local stiffness of the bundle $A(x)$. Without crosslinks the stiffness scales linearly with the number of filaments in the tail [76–78, 89]. Because the twisted 8-helix tubes have no binding sites for linkers[5], we therefore we take $A(x) = A_s a\,\mathrm{e}^{-x/\chi}$ as the stiffness model, where A_s is the bending stiffness of a single filament. The parameters a and χ could be estimated by the ratio of the fluorescence intensity close to the head and at the far end, if we assume that only a single filament extends to the far end. Typical numbers of attached filaments a range from 7 to 25.

The individual parameters varied for different swimmers, so they had to be determined for each swimmer instance.

Next, we determined the bundle length, the amplitude parameters ε_1 & ε_2 and their respective phase from snapshots of the swimmer. The bundle length is easily measured by integrating the length along the contour of the tail and was typically in the range from 4.8–8.0 μm (Tab. 8.1). On the other hand the two amplitude parameters ε_1 and ε_2 have to be determined with great care, because the swimming speed scales quadratically with their amplitude (see 8.2.1). For that, we took snapshots of the video sequence where the tail was maximally deflected. This allowed to measure the amplitude of the attachment point, ε_1, in fractions of the head radius and we found values ranging from 0.1–1.0. Likewise, the opening angle α between tail and swimming direction was measured for which we found values ranging from 20–40 degrees. This opening angle α determines ε_2 via $\varepsilon_2 = \tan\alpha$. The relative phase of ε_1 and ε_2 corresponds to the torsion of the tail close to the head. From our data it was not possible to reliably determine the phase difference, therefore we have to supply a generic value. Because the tail is pulled through the fluid, it feels a drag directed against its current direction of movement and bends accordingly. This induced bending corresponds to a phase shift of $-\pi/2$ which we take as an estimate for the phase shift. We note that the phase shift has only a minor impact on the swimming speed of about 5%. Because of the small size of the swimmers and the coarseness of the data, this whole procedure is a source of a large unknown error.

Finally the friction coefficients of tail and head need to be estimated. For the tail, the friction coefficient can be calculated via slender-body theory (8.43) from the aspect ratio of the tail, for which we assumed a value of 200, resulting in $\gamma \approx 1.6$. The Stokes friction coefficients for the head are given by (8.44). In the experiment, translational motion is free,

[5] Although no linkers were present, it is nevertheless possible that staple strands from one filament loosen and bind to a neighboring filament that accidentally has a free complementary site. However, we assume that these spurious interlinks are rare.

swimmer	#1	#2	#3	#4	#5	#6	#7	#8	#9	#10
length $[\mu m]$	6.2	7.8	6.8	6.5	6.3	8.0	6.5	6.0	4.8	7.0
N_0	20	25	11	12	23	18	24	21	9	7
frequency $[Hz]$	1	1	1	2	1	1	1	2	2	1
$\varepsilon_1/\mathrm{e}^{-\imath\pi/2}$ $[r_h]$	0.9	1.	0.9	0.25	0.5	0.1	0.9	0.5	0.9	0.8
$\arctan(\varepsilon_2)$ $[deg]$	21	20	20	26	26	30	28	23	30	42
measured speed $[\mu m/s]$	0.12	0.12	0.17	0.19	0.20	0.22	0.25	0.27	0.31	0.42
predicted speed $[\mu m/s]$	0.21	0.18	0.14	0.23	0.26	0.21	0.36	0.29	0.50	0.44

Table 8.1 | Model parameters and swimming speeds for ten different swimmers that were found in the experiment. The agreement of measured and predicted swimming speed agrees up to a factor of two.

so that $\mathcal{R}^{FU}$ is a reasonable value for the translational friction. On the other hand, the head rotation is *not* free, because the external magnetic field aligns the magnetic moment of the head with its direction. As a consequence, a torques working against the magnetic field are suppressed and therefore lead to much smaller deflections. To emulate this suppressed rotation, we scaled the rotational friction coefficient by a large factor (500). Because the resulting values of the swimming speed differ by only 20% in the range $[200, \infty]$, the error inflicted by this arbitrariness is small.

Table 8.1 shows the model parameters and predicted swimming speeds for ten swimmers from the experiment. Note that the swimming speeds are converted into physical units by multiplying with $\ell_\omega \cdot 2\pi f$ where f is the rotation frequency of the external magnetic field (see 8.1.1). Typically, we measured swimming speeds around $0.2\,\mu m/s$, and our predicted swimming speeds were off by less than 40%. Differences between the model prediction and the experimental observations are attributed to errors in determining ε_1 & ε_2. Besides, the swimmers in the experiment are close to a cell wall with no-slip boundary conditions, leading to an additional drag that is neglected in the theoretic model. Despite these differences, the experimental observations agree remarkably well with the quantitative predictions from the model, despite the considerable simplifications that the model involves.

In summary, we have found good quantitative agreement of our prediction with the experimental observations. Interestingly, the proposed construction method for DNA-based microswimmers automatically yields swimmers with tails that have a decreasing bending stiffness. Our model has shown that such a decreasing stiffness profile improves the swimming speed of such a swimmer. In other words, a bead with a bundle of multiple filaments of different lengths surpasses one with a single filament, which is a feature that arises naturally in our method of construction. We note that the increased swimming speed is a generic feature of decreasing tail stiffness and is also found for other stiffness profiles.

9 Summary and outlook

In this part, we have developed a theory for low Reynolds number swimming with a flexible oar whose local stiffness decreases along its contour. This theory extends previous work by Lauga [52]. We applied our model to an experimentally realized swimmer and found good quantitative agreement of predicted and measured swimming speeds.

The swimmer model consists of a spherical bead, which is actuated from afar, and straight flexible rods attached to the bead. By the motion of the attached oar through the surrounding fluid, the fluid drag bends the oar and induces a chiral shape. It is by this chirality that our swimmer breaks the constraints for swimming at low Reynolds numbers imposed by the scallop theorem, which states that a swimming stroke must be non time-reversible to create propulsion.

In order to determine the swimming speed of our proposed swimmer, we had to determine the induced tail shape first. For that, we used the slender body approximation and simplified the equations of motion by a small amplitude approximation of the tail shape. The resulting differential equation is a generalized hyper-diffusion equation that was solved analytically for an exponentially decreasing tail stiffness. Because the evaluation of the involved functions has considerable numerical errors, the direct numerical solution of the differential equation gave more accurate results in practice.

This tool allowed us to study the swimming speed of swimmers with an exponentially decreasing tail stiffness as a function of their geometric parameters, such as its length, head size, and maximal tail stiffness. Surprisingly, a decreasing tail stiffness in general improved the swimming speed over a comparable swimmer with a constant tail stiffness. Our analysis showed a qualitatively similar dependence of the swimming speed on the swimmer parameters for both constant and variable tail stiffness. In addition, we discussed design principles for optimal swimmers, e.g. an optimal ratio of head and tail size. Last but not least, we determined that the optimal stiffness profile for the swimmer tail is given by a step-like function which remains at high stiffness up to the mid of the tail where it transitions to very low stiffness.

This model was applied to an experimentally realized swimmer made from self-assembled DNA flagella. The novel fabrication method of this micro-swimmer and its advantages are the subject of a joint publication by Alexander M. Maier, Cornelius Weig, Peter Oswald, Erwin Frey, Peer Fischer, and Tim Liedl [63]. The comparison of the observed and predicted swimming speed gave a good quantitative agreement.

There are a few open questions regarding the theory developed in this work. For example, we have neglected any noise acting on the swimmer, although diffusion for micro-meter sized particles is quite strong. A logical next step in the theory is therefore to include noise in the analysis and examine its effects. In particular, we would like to know the minimal swimmer size for which active swimming is viable [90], and below which the swimmer can only increase

its diffusion [91, 92]. Furthermore, we used a small amplitude approximation for the swimmer tail. Although experiments with a macroscopic realization of a constant stiffness tail have shown that the theory predicts the tail shape remarkably well [66], it is unclear whether this still applies for decreasing tail stiffness. It should however be easy to repeat this experiment with decreasing tail stiffness. Last but not least, our treatment ignored the flow field from the rotation of the head, which is common practice in this field, because it makes an analytic treatment possible. Still, the inflicted error is completely unknown. Due to the complexity of the problem, the validity of this approximation will best be checked via numerical simulations.

Apart from these consistency checks regarding the validity of our solution, the variable tail stiffness opens up a lot of new questions that had been answered for constant tail stiffness: Is there a better head shape than spherical [93]? What is the effect of large beat amplitudes [94]? How do close-by boundaries affect a swimmer with variable bending stiffness [95–98]? What happens if the fluid is viscoelastic [99]?

The ultimate goal is to use these insights for the construction of microscopic machines that pump fluid [100], switch the fluid viscosity [101, 102], or even perform medical tasks on the micro-scale [103, 104]. There is much to do.

Bibliography Part II

[1] G. Taylor. *Analysis of the Swimming of Microscopic Organisms*. In: **Proceedings of the Royal Society of London A: Mathematical, Physical and Engineering Sciences** 209.1099 (Nov. 1951), pp. 447–461. DOI: 10.1098/rspa.1951.0218 (cit. on p. 115).

[2] G.J. Hancock. *The Self-Propulsion of Microscopic Organisms through Liquids*. In: **Proceedings of the Royal Society of London A: Mathematical, Physical and Engineering Sciences** 217.1128 (Mar. 1953), pp. 96–121. DOI: 10.1098/rspa.1953.0048 (cit. on p. 115).

[3] G. Taylor. *The Action of Waving Cylindrical Tails in Propelling Microscopic Organisms*. In: **Proceedings of the Royal Society of London A: Mathematical, Physical and Engineering Sciences** 211.1105 (1952), pp. 225–239. DOI: 10.1098/rspa.1952.0035 (cit. on p. 115).

[4] E.M Purcell. *Life at low Reynolds number*. In: **American Journal of Physics** 45.1 (Jan. 1977), pp. 3–11. DOI: 10.1119/1.10903 (cit. on pp. 115, 116, 129, 130, 141).

[5] H. Brenner and J. Happel. **Low Reynolds number hydrodynamics**. Prentice-Hall, Englewood Cliffs, NJ, 1965 (cit. on p. 115).

[6] T. Qiu et al. *Swimming by reciprocal motion at low Reynolds number*. In: **Nature Communications** 5 (Nov. 2014). DOI: 10.1038/ncomms6119 (cit. on p. 115).

[7] E. Lauga and T.R. Powers. *The hydrodynamics of swimming microorganisms*. In: **Reports on Progress in Physics** 72.9 (Sept. 2009), p. 096601. DOI: 10.1088/0034-4885/72/9/096601 (cit. on p. 115).

[8] E. Lauga. *Life around the scallop theorem*. In: **Soft Matter** 7.7 (Mar. 2011), pp. 3060–3065. DOI: 10.1039/C0SM00953A (cit. on p. 115).

[9] J. Elgeti, R.G. Winkler, and G. Gompper. *Physics of microswimmers—single particle motion and collective behavior: a review*. In: **Reports on Progress in Physics** 78.5 (May 2015), p. 056601. DOI: 10.1088/0034-4885/78/5/056601 (cit. on p. 115).

[10] L.E. Becker, S.A. Koehler, and H.A. Stone. *On self-propulsion of micro-machines at low Reynolds number: Purcell's three-link swimmer*. In: **Journal of Fluid Mechanics** 490 (Sept. 2003), pp. 15–35. DOI: 10.1017/S0022112003005184 (cit. on p. 115).

[11] A. Najafi and R. Golestanian. *Simple swimmer at low Reynolds number: Three linked spheres*. In: **Physical Review E** 69.6 (June 2004), p. 062901. DOI: 10.1103/PhysRevE.69.062901 (cit. on p. 115).

[12] A. Najafi and R. Golestanian. *Propulsion at low Reynolds number*. In: **Journal of Physics: Condensed Matter** 17.14 (Apr. 2005), S1203. DOI: 10.1088/0953-8984/17/14/009 (cit. on p. 115).

[13] J. E. Avron, O. Kenneth, and D. H. Oaknin. *Pushmepullyou: an efficient micro-swimmer.* In: **New Journal of Physics** 7.1 (Nov. 2005), p. 234. DOI: 10.1088/1367-2630/7/1/234 (cit. on p. 115).

[14] H. C. Berg. **E. coli in Motion**. Springer Science & Business Media, 2004 (cit. on pp. 115, 116).

[15] H. C. Berg and R. A. Anderson. *Bacteria Swim by Rotating their Flagellar Filaments.* In: **Nature** 245.5425 (Oct. 1973), pp. 380–382. DOI: 10.1038/245380a0 (cit. on pp. 115, 116).

[16] L. J. Fauci and R. Dillon. *Biofluidmechanics of Reproduction.* In: **Annual Review of Fluid Mechanics** 38.1 (2006), pp. 371–394. DOI: 10.1146/annurev.fluid.37.061903.175725 (cit. on p. 115).

[17] J. Lighthill. *Flagellar Hydrodynamics.* In: **SIAM Review** 18.2 (Apr. 1976), pp. 161–230. DOI: 10.1137/1018040 (cit. on pp. 115, 116).

[18] I. Gibbons. *Cilia and flagella of eukaryotes.* In: **The Journal of cell biology** 91.3 (1981), 107s–124s (cit. on p. 115).

[19] J. B. Keller and S. I. Rubinow. *Slender-body theory for slow viscous flow.* In: **Journal of Fluid Mechanics** 75.04 (1976), pp. 705–714. DOI: 10.1017/S0022112076000475 (cit. on pp. 115, 120, 131).

[20] R. E. Johnson and C. J. Brokaw. *Flagellar hydrodynamics. A comparison between resistive-force theory and slender-body theory.* In: **Biophysical Journal** 25.1 (Jan. 1979), pp. 113–127. DOI: 10.1016/S0006-3495(79)85281-9 (cit. on p. 115).

[21] R. E. Johnson. *An improved slender-body theory for Stokes flow.* In: **Journal of Fluid Mechanics** 99.02 (July 1980), pp. 411–431. DOI: 10.1017/S0022112080000687 (cit. on p. 115).

[22] C. W. Oseen. **Über die Stoke'sche Formel und über eine verwandte Aufgabe in der Hydrodynamik: Mitteilung 2**. German. Almqvist & Wiksell, 1911 (cit. on p. 115).

[23] J. Rotne and S. Prager. *Variational Treatment of Hydrodynamic Interaction in Polymers.* In: **The Journal of Chemical Physics** 50.11 (June 1969), pp. 4831–4837. DOI: 10.1063/1.1670977 (cit. on p. 115).

[24] H. Yamakawa. *Transport Properties of Polymer Chains in Dilute Solution: Hydrodynamic Interaction.* In: **The Journal of Chemical Physics** 53.1 (July 1970), pp. 436–443. DOI: 10.1063/1.1673799 (cit. on p. 115).

[25] C. P Lowe. *Dynamics of filaments: modelling the dynamics of driven microfilaments.* In: **Philosophical Transactions of the Royal Society of London B: Biological Sciences** 358.1437 (Sept. 2003), pp. 1543–1550. DOI: 10.1098/rstb.2003.1340 (cit. on pp. 115, 122).

[26] R. Cortez, L. Fauci, and A. Medovikov. *The method of regularized Stokeslets in three dimensions: Analysis, validation, and application to helical swimming.* In: **Physics of Fluids (1994-present)** 17.3 (Mar. 2005), p. 031504. DOI: 10.1063/1.1830486 (cit. on p. 115).

[27] B. Delmotte, E. Climent, and F. Plouraboué. *A general formulation of Bead Models applied to flexible fibers and active filaments at low Reynolds number*. In: **Journal of Computational Physics** 286 (Apr. 2015), pp. 14–37. DOI: 10.1016/j.jcp.2015.01.026 (cit. on p. 115).

[28] A. Malevanets and R. Kapral. *Mesoscopic model for solvent dynamics*. In: **The Journal of Chemical Physics** 110.17 (May 1999), pp. 8605–8613. DOI: 10.1063/1.478857 (cit. on p. 116).

[29] C. Brennen and H. Winet. *Fluid Mechanics of Propulsion by Cilia and Flagella*. In: **Annual Review of Fluid Mechanics** 9.1 (1977), pp. 339–398. DOI: 10.1146/annurev.fl.09.010177.002011 (cit. on p. 116).

[30] J.J.L. Higdon. *A hydrodynamic analysis of flagellar propulsion*. In: **Journal of Fluid Mechanics** 90.04 (Feb. 1979), pp. 685–711. DOI: 10.1017/S0022112079002482 (cit. on p. 116).

[31] H. Gadêlha et al. *Nonlinear instability in flagellar dynamics: a novel modulation mechanism in sperm migration?* In: **Journal of The Royal Society Interface** (May 2010). DOI: 10.1098/rsif.2010.0136 (cit. on p. 116).

[32] H.C. Fu, T.R. Powers, and C.W. Wolgemuth. *Theory of Swimming Filaments in Viscoelastic Media*. In: **Physical Review Letters** 99.25 (Dec. 2007), p. 258101. DOI: 10.1103/PhysRevLett.99.258101 (cit. on p. 116).

[33] T.K. Chaudhury. *On swimming in a visco-elastic liquid*. In: **Journal of Fluid Mechanics** 95.01 (Nov. 1979), pp. 189–197. DOI: 10.1017/S0022112079001415 (cit. on p. 116).

[34] S. Camalet, F. Jülicher, and J. Prost. *Self-Organized Beating and Swimming of Internally Driven Filaments*. In: **Physical Review Letters** 82.7 (Feb. 1999), pp. 1590–1593. DOI: 10.1103/PhysRevLett.82.1590 (cit. on p. 116).

[35] A. Hilfinger, A.K. Chattopadhyay, and F. Jülicher. *Nonlinear dynamics of cilia and flagella*. In: **Physical Review E** 79.5 (May 2009), p. 051918. DOI: 10.1103/PhysRevE.79.051918 (cit. on p. 116).

[36] E.M Purcell. *The efficiency of propulsion by a rotating flagellum*. In: **Proceedings of the National Academy of Sciences** 94.21 (Oct. 1997), pp. 11307–11311 (cit. on p. 116).

[37] S.E. Spagnolie, B. Liu, and T.R. Powers. *Locomotion of Helical Bodies in Viscoelastic Fluids: Enhanced Swimming at Large Helical Amplitudes*. In: **Physical Review Letters** 111.6 (Aug. 2013), p. 068101. DOI: 10.1103/PhysRevLett.111.068101 (cit. on p. 116).

[38] J.T. Pham et al. *Deformation and shape of flexible, microscale helices in viscous flow*. In: **Physical Review E** 92.1 (July 2015), p. 011004. DOI: 10.1103/PhysRevE.92.011004 (cit. on p. 116).

[39] B. Liu, T.R. Powers, and K.S. Breuer. *Force-free swimming of a model helical flagellum in viscoelastic fluids*. In: **Proceedings of the National Academy of Sciences** 108.49 (Dec. 2011), pp. 19516–19520. DOI: 10.1073/pnas.1113082108 (cit. on p. 116).

[40] S. Chattopadhyay et al. *Swimming efficiency of bacterium Escherichiacoli*. In: **Proceedings of the National Academy of Sciences** 103.37 (Sept. 2006), pp. 13712–13717. DOI: 10.1073/pnas.0602043103 (cit. on p. 116).

[41] J. Xing et al. *Torque–speed relationship of the bacterial flagellar motor*. In: **Proceedings of the National Academy of Sciences** 103.5 (Jan. 2006), pp. 1260–1265. DOI: 10.1073/pnas.0507959103 (cit. on p. 116).

[42] J.E. Avron, O. Gat, and O. Kenneth. *Optimal Swimming at Low Reynolds Numbers*. In: **Physical Review Letters** 93.18 (Oct. 2004), p. 186001. DOI: 10.1103/PhysRevLett.93.186001 (cit. on p. 116).

[43] M. Reichert and H. Stark. *Synchronization of rotating helices by hydrodynamic interactions*. In: **The European Physical Journal E** 17.4 (Aug. 2005), pp. 493–500. DOI: 10.1140/epje/i2004-10152-7 (cit. on p. 116).

[44] M. Kim and T.R. Powers. *Hydrodynamic interactions between rotating helices*. In: **Physical Review E** 69.6 (June 2004), p. 061910. DOI: 10.1103/PhysRevE.69.061910 (cit. on p. 116).

[45] S.Y. Reigh, R.G. Winkler, and G. Gompper. *Synchronization, Slippage, and Unbundling of Driven Helical Flagella*. In: **PLoS ONE** 8.8 (Aug. 2013), e70868. DOI: 10.1371/journal.pone.0070868 (cit. on p. 116).

[46] S.Y. Reigh, R.G. Winkler, and G. Gompper. *Synchronization and bundling of anchored bacterial flagella*. In: **Soft Matter** 8.16 (Mar. 2012), pp. 4363–4372. DOI: 10.1039/C2SM07378A (cit. on p. 116).

[47] T.R. Powers. *Role of body rotation in bacterial flagellar bundling*. In: **Physical Review E** 65.4 (Apr. 2002), p. 040903. DOI: 10.1103/PhysRevE.65.040903 (cit. on p. 116).

[48] M. Manghi, X. Schlagberger, and R.R. Netz. *Propulsion with a Rotating Elastic Nanorod*. In: **Physical Review Letters** 96.6 (Feb. 2006), p. 068101. DOI: 10.1103/PhysRevLett.96.068101 (cit. on p. 116).

[49] B. Qian, T.R. Powers, and K.S. Breuer. *Shape Transition and Propulsive Force of an Elastic Rod Rotating in a Viscous Fluid*. In: **Physical Review Letters** 100.7 (Feb. 2008), p. 078101. DOI: 10.1103/PhysRevLett.100.078101 (cit. on p. 116).

[50] N. Coq et al. *Rotational dynamics of a soft filament: Wrapping transition and propulsive forces*. In: **Physics of Fluids (1994-present)** 20.5 (May 2008), p. 051703. DOI: 10.1063/1.2909603 (cit. on p. 116).

[51] N. Coq et al. *Helical beating of an actuated elastic filament*. In: **Journal of Physics: Condensed Matter** 21.20 (May 2009), p. 204109. DOI: 10.1088/0953-8984/21/20/204109 (cit. on p. 116).

[52] E. Lauga. *Floppy swimming: Viscous locomotion of actuated elastica*. In: **Physical Review E** 75 (4 Apr. 2007), p. 041916. DOI: 10.1103/PhysRevE.75.041916 (cit. on pp. 116, 117, 119, 120, 145).

[53] C.H. Wiggins et al. *Trapping and Wiggling: Elastohydrodynamics of Driven Microfilaments*. In: **Biophysical Journal** 74.2 (Jan. 1998), pp. 1043–1060. DOI: 10.1016/S0006-3495(98)74029-9 (cit. on pp. 116, 122).

[54] C.H. Wiggins and R.E. Goldstein. *Flexive and Propulsive Dynamics of Elastica at Low Reynolds Number*. In: **Physical Review Letters** 80.17 (Apr. 1998), pp. 3879–3882. DOI: 10.1103/PhysRevLett.80.3879 (cit. on p. 116).

[55] K. Machin. *Wave propagation along flagella*. In: **J. exp. Biol** 35.4 (1958), pp. 796–806 (cit. on p. 116).

[56] R. Dreyfus et al. *Microscopic artificial swimmers*. In: **Nature** 437.7060 (Oct. 2005), pp. 862–865. DOI: 10.1038/nature04090 (cit. on p. 116).

[57] M. Roper et al. *On the dynamics of magnetically driven elastic filaments*. In: **Journal of Fluid Mechanics** 554 (May 2006), pp. 167–190. DOI: 10.1017/S0022112006009049 (cit. on p. 116).

[58] E. Gauger and H. Stark. *Numerical study of a microscopic artificial swimmer*. In: **Physical Review E** 74.2 (Aug. 2006), p. 021907. DOI: 10.1103/PhysRevE.74.021907 (cit. on p. 116).

[59] S. Namdeo, S.N. Khaderi, and P.R. Onck. *Swimming dynamics of bidirectional artificial flagella*. In: **Physical Review E** 88.4 (Oct. 2013), p. 043013. DOI: 10.1103/PhysRevE.88.043013 (cit. on p. 116).

[60] A. Ghosh and P. Fischer. *Controlled Propulsion of Artificial Magnetic Nanostructured Propellers*. In: **Nano Letters** 9.6 (June 2009), pp. 2243–2245. DOI: 10.1021/nl900186w (cit. on p. 116).

[61] D. Schamel et al. *Nanopropellers and Their Actuation in Complex Viscoelastic Media*. In: **ACS Nano** 8.9 (Sept. 2014), pp. 8794–8801. DOI: 10.1021/nn502360t (cit. on p. 116).

[62] B.J. Williams et al. *A self-propelled biohybrid swimmer at low Reynolds number*. In: **Nature Communications** 5 (Jan. 2014). DOI: 10.1038/ncomms4081 (cit. on p. 116).

[63] A.M Maier et al. *Microswimmers driven by a bundle of self-assembled DNA-based artificial flagella*. In: **ACS Nano** (2015). Submitted (cit. on pp. 116, 119, 141, 145).

[64] J.P K. Tillett. *Axial and transverse Stokes flow past slender axisymmetric bodies*. In: **Journal of Fluid Mechanics** 44.03 (Nov. 1970), pp. 401–417. DOI: 10.1017/S0022112070001908 (cit. on p. 120).

[65] G.K. Batchelor. *Slender-body theory for particles of arbitrary cross-section in Stokes flow*. In: **Journal of Fluid Mechanics** 44.03 (Nov. 1970), pp. 419–440. DOI: 10.1017/S002211207000191X (cit. on p. 120).

[66] T.S. Yu, E. Lauga, and A.E. Hosoi. *Experimental investigations of elastic tail propulsion at low Reynolds number*. In: **Physics of Fluids** 18.9, 091701 (2006). DOI: http://dx.doi.org/10.1063/1.2349585 (cit. on pp. 121, 146).

[67] D. Riveline et al. *Elastohydrodynamic study of actin filaments using fluorescence microscopy*. In: **Physical Review E** 56 (2 Aug. 1997), R1330–R1333. DOI: 10.1103/PhysRevE.56.R1330 (cit. on p. 122).

[68] C. Meijer. *Über Whittakersche bzw. Besselsche Funktionen und deren Produkte*. German. In: **Nieuw Arch. Wiskd** 18 (1936), pp. 10–39 (cit. on p. 125).

[69] R. Beals and J. Szmigielski. *Meijer G-functions: a gentle introduction*. In: **Notices of the AMS** 60.7 (2013) (cit. on p. 126).

[70] A. Shapere and F. Wilczek. *Self-Propulsion at Low Reynolds Number*. In: **Physical Review Letters** 58.20 (May 1987), pp. 2051–2054. DOI: 10.1103/PhysRevLett.58.2051 (cit. on pp. 129, 130).

[71] R.G. Cox. *The motion of long slender bodies in a viscous fluid. Part 1. General theory*. In: **Journal of Fluid Mechanics** 44 (1970), pp. 791–810. DOI: 10.1017/S002211207000215X (cit. on p. 131).

[72] B.S. Massey and J. Ward-Smith. **Mechanics of fluids**. Vol. 1. CRC Press, 1998 (cit. on pp. 131, 142).

[73] G.K. Batchelor. **An Introduction to Fluid Dynamics**. Feb. 2000 (cit. on p. 131).

[74] W.H. Press et al. **Numerical recipes in C++ : the art of scientific computing**. 2002 (cit. on p. 138).

[75] R. Storn and K. Price. *Differential Evolution - A simple and efficient adaptive scheme for global optimization over continuous spaces*. 1995 (cit. on p. 139).

[76] M.M.A.E. Claessens et al. *Actin-binding proteins sensitively mediate F-actin bundle stiffness*. In: **Nature Materials** 5.9 (Sept. 2006), pp. 748–753. DOI: 10.1038/nmat1718 (cit. on pp. 139, 143).

[77] C. Heussinger, M. Bathe, and E. Frey. *Statistical Mechanics of Semiflexible Bundles of Wormlike Polymer Chains*. In: **Physical Review Letters** 99.4 (July 2007), p. 048101. DOI: 10.1103/PhysRevLett.99.048101 (cit. on pp. 139, 143).

[78] M. Bathe et al. *Cytoskeletal Bundle Mechanics*. In: **Biophysical Journal** 94.8 (Apr. 2008), pp. 2955–2964. DOI: 10.1529/biophysj.107.119743 (cit. on pp. 139, 143).

[79] P.W.K. Rothemund. *Folding DNA to create nanoscale shapes and patterns*. In: **Nature** 440.7082 (Mar. 2006), pp. 297–302. DOI: 10.1038/nature04586 (cit. on p. 141).

[80] N.C. Seeman. *Nanomaterials Based on DNA*. In: **Annual review of biochemistry** 79 (2010), pp. 65–87. DOI: 10.1146/annurev-biochem-060308-102244 (cit. on p. 141).

[81] H. Dietz, S.M Douglas, and W.M Shih. *Folding DNA into Twisted and Curved Nanoscale Shapes*. In: **Science** 325.5941 (Aug. 2009), pp. 725–730. DOI: 10.1126/science.1174251 (cit. on p. 141).

[82] S.M Douglas et al. *Self-assembly of DNA into nanoscale three-dimensional shapes*. In: **Nature** 459.7245 (May 2009), pp. 414–418. DOI: 10.1038/nature08016 (cit. on p. 141).

[83] P. Yin et al. *Programming DNA Tube Circumferences*. In: **Science** 321.5890 (Aug. 2008), pp. 824–826. DOI: 10.1126/science.1157312 (cit. on pp. 141, 143).

[84] Y. Yang et al. In: **Nano Letters** 13.4 (Apr. 2013), pp. 1862–1866. DOI: 10.1021/nl400859d (cit. on p. 141).

[85] D. Schiffels, T. Liedl, and D.K. Fygenson. *Nanoscale structure and microscale stiffness of DNA nanotubes*. In: **ACS Nano** 7.8 (2013), pp. 6700–6710. DOI: 10.1021/nn401362p (cit. on pp. 141, 142).

[86] N.M Green. *Avidin and streptavidin*. In: **Methods in enzymology** 184 (1990), p. 51 (cit. on p. 142).

[87] C. Yuan et al. *Energy Landscape of Streptavidin−Biotin Complexes Measured by Atomic Force Microscopy†*. In: **Biochemistry** 39.33 (Aug. 2000), pp. 10219–10223. DOI: 10.1021/bi992715o (cit. on p. 142).

[88] P. J. Flory. *Molecular Size Distribution in Linear Condensation Polymers*. In: **Journal of the American Chemical Society** 58.10 (Oct. 1936), pp. 1877–1885. DOI: 10.1021/ja01301a016 (cit. on p. 143).

[89] C. Heussinger, F. Schüller, and E. Frey. *Statics and dynamics of the wormlike bundle model*. In: **Physical Review E** 81 (2 Feb. 2010), p. 021904. DOI: 10.1103/PhysRevE.81.021904 (cit. on p. 143).

[90] D. B. Dusenbery. *Minimum size limit for useful locomotion by free-swimming microbes*. In: **Proceedings of the National Academy of Sciences** 94.20 (Sept. 1997), pp. 10949–10954. DOI: 10.1073/pnas.94.20.10949 (cit. on p. 145).

[91] E. Lauga. *Enhanced Diffusion by Reciprocal Swimming*. In: **Physical Review Letters** 106.17 (Apr. 2011), p. 178101. DOI: 10.1103/PhysRevLett.106.178101 (cit. on p. 146).

[92] P. Mandal and A. Ghosh. *Observation of Enhanced Diffusivity in Magnetically Powered Reciprocal Swimmers*. In: **Physical Review Letters** 111.24 (Dec. 2013), p. 248101. DOI: 10.1103/PhysRevLett.111.248101 (cit. on p. 146).

[93] H. Gadêlha. *On the optimal shape of magnetic swimmers*. In: **Regular and Chaotic Dynamics** 18.1-2 (Apr. 2013), pp. 75–84. DOI: 10.1134/S156035471301005X (cit. on p. 146).

[94] M. C. Lagomarsino, F. Capuani, and C. P Lowe. *A simulation study of the dynamics of a driven filament in an Aristotelian fluid*. In: **Journal of Theoretical Biology** 224.2 (Sept. 2003), pp. 215–224. DOI: 10.1016/S0022-5193(03)00159-0 (cit. on p. 146).

[95] E. Lauga et al. *Swimming in Circles: Motion of Bacteria near Solid Boundaries*. In: **Biophysical Journal** 90.2 (Jan. 2006), pp. 400–412. DOI: 10.1529/biophysj.105.069401 (cit. on p. 146).

[96] A. A. Evans and E. Lauga. *Propulsion by passive filaments and active flagella near boundaries*. In: **Physical Review E** 82.4 (Oct. 2010), p. 041915. DOI: 10.1103/PhysRevE.82.041915 (cit. on p. 146).

[97] W. R. DiLuzio et al. *Escherichia coli swim on the right-hand side*. In: **Nature** 435.7046 (June 2005), pp. 1271–1274. DOI: 10.1038/nature03660 (cit. on p. 146).

[98] A. P Berke et al. *Hydrodynamic Attraction of Swimming Microorganisms by Surfaces*. In: **Physical Review Letters** 101.3 (July 2008), p. 038102. DOI: 10.1103/PhysRevLett.101.038102 (cit. on p. 146).

[99] E. E. Riley and E. Lauga. *Enhanced active swimming in viscoelastic fluids*. In: **EPL (Europhysics Letters)** 108.3 (Nov. 2014), p. 34003. DOI: 10.1209/0295-5075/108/34003 (cit. on p. 146).

[100] Y. W. Kim and R. R. Netz. *Pumping Fluids with Periodically Beating Grafted Elastic Filaments*. In: **Physical Review Letters** 96.15 (Apr. 2006), p. 158101. DOI: 10.1103/PhysRevLett.96.158101 (cit. on p. 146).

[101] A. Sokolov and I.S. Aranson. *Reduction of Viscosity in Suspension of Swimming Bacteria*. In: **Physical Review Letters** 103.14 (Sept. 2009), p. 148101. DOI: 10.1103/PhysRevLett.103.148101 (cit. on p. 146).

[102] J. Gachelin et al. *Non-Newtonian Viscosity of Escherichia coli Suspensions*. In: **Physical Review Letters** 110.26 (June 2013), p. 268103. DOI: 10.1103/PhysRevLett.110.268103 (cit. on p. 146).

[103] J. Wang. *Can Man-Made Nanomachines Compete with Nature Biomotors?* In: **ACS Nano** 3.1 (Jan. 2009), pp. 4–9. DOI: 10.1021/nn800829k (cit. on p. 146).

[104] B.J. Nelson, I.K. Kaliakatsos, and J.J. Abbott. *Microrobots for Minimally Invasive Medicine*. In: **Annual Review of Biomedical Engineering** 12.1 (2010), pp. 55–85. DOI: 10.1146/annurev-bioeng-010510-103409 (cit. on p. 146).

A Appendix Part I

A.1 Force calculation in wormlike chain

We define the connecting vectors of two different beads $\boldsymbol{u}_i = \boldsymbol{r}_{i+1} - \boldsymbol{r}_i$ and use the shorthand notation $u_i = |\boldsymbol{u}_i|$. Then, it holds that

$$\partial_{r_j} \boldsymbol{u}_i = \delta_{j,i+1} - \delta_{ij} \qquad \text{and} \qquad \partial_{r_j} u_i = \partial_{r_j} \sqrt{\boldsymbol{u}_i^2} = \frac{\boldsymbol{u}_i}{u_i}(\delta_{j,i+1} - \delta_{ij}) \ . \tag{A.1}$$

We use a bending potential of the form (2.2),

$$U_{bend} = -\sum_i \alpha_i \frac{\boldsymbol{u}_i \cdot \boldsymbol{u}_{i+1}}{u_i \, u_{i+1}} \ . \tag{A.2}$$

Therefore, the force acting on bead j is given by

$$\begin{aligned}
\boldsymbol{F}_j &= \nabla_j U_{\triangleleft} \\
&= \sum_i \alpha_i \Bigg(\frac{1}{u_i \, u_{i+1}} \Big(\boldsymbol{u}_{i+1}(\delta_{j,i+1} - \delta_{ji}) + \boldsymbol{u}_i(\delta_{j,i+2} - \delta_{j,i+1}) \Big) - \\
&\qquad \frac{(\boldsymbol{u}_i \cdot \boldsymbol{u}_{i+1})}{(u_i \, u_{i+1})^2} \Big(u_{i+1} \frac{\boldsymbol{u}_i}{u_i}(\delta_{j,i+1} - \delta_{ji}) + u_i \frac{\boldsymbol{u}_{i+1}}{u_{i+1}}(\delta_{j,i+2} - \delta_{j,i+1}) \Big) \Bigg) \\
&= \sum_i \alpha_i \Bigg(\Big(\frac{\boldsymbol{u}_{i+1}}{u_i \, u_{i+1}} - \frac{(\boldsymbol{u}_i \cdot \boldsymbol{u}_{i+1})}{u_i^3 \, u_{i+1}} \boldsymbol{u}_i \Big)(\delta_{j,i+1} - \delta_{ji}) + \\
&\qquad \Big(\frac{\boldsymbol{u}_i}{u_i \, u_{i+1}} - \frac{(\boldsymbol{u}_i \cdot \boldsymbol{u}_{i+1})}{u_i \, u_{i+1}^3} \boldsymbol{u}_{i+1} \Big)(\delta_{j,i+2} - \delta_{j,i+1}) \Bigg)
\end{aligned}$$

Using the definition $I_{i,i+1} = \frac{1}{u_i \, u_{i+1}} \boldsymbol{u}_i - \frac{(\boldsymbol{u}_i \cdot \boldsymbol{u}_{i+1})}{u_i \, u_{i+1}^3} \boldsymbol{u}_{i+1}$, this becomes

$$\boldsymbol{F}_j = -\alpha_j I_{j+1,j} + \alpha_{j-1}(I_{j,j-1} - I_{j-1,j}) + \alpha_{j-2} I_{j-2,j-1} \ , \tag{A.3}$$

where it is implied that for a linear polymer with N beads, $I_{ij} = 0$ if $i < 0 \vee i > N-1 \vee j < 0 \vee j > N-1$. Further, we can identify repeating terms in subsequent force calculations, $J_i = \alpha_i I_{i+1,i} + \alpha_{i-1} I_{i-1,i}$. Using these definitions, the forces along the chain become:

j	$\boldsymbol{F}_j$
1	$-\alpha_1 I_{2,1}$
2	$\alpha_1 I_{2,1} - J_2$
$\vdots$	
j	$J_{j-1} - J_j$
$\vdots$	
$N-1$	$J_{N-2} - \alpha_{N-2} I_{N-2,N-1}$
N	$\alpha_{N-2} I_{N-2,N-1}$

Therefore, the numerical implementation can make use of this "actio equals reactio" principle when calculating the forces along the chain. This allows to re-use a partial result for the force on bead $j-1$ when calculating the force on bead j, speeding up the force calculation by about a factor of two.

This structure of the force calculation is also preserved for related bending potentials. As long as the bending potential has the form

$$U_{\sphericalangle} = -\sum_i \alpha_i \, f_i\Big(\frac{\boldsymbol{u}_i \cdot \boldsymbol{u}_{i+1}}{u_i \, u_{i+1}}\Big) \tag{A.4}$$

the transfer of forces can be employed via

$$\boldsymbol{F}_j = -\beta_j I_{j+1,j} + \beta_{j-1}(I_{j,j-1} - I_{j-1,j}) + \beta_{j-2} I_{j-2,j-1} \ ,$$

where $\beta_i = \alpha_i \, f_i'$.

A.2 Detailed captions for the tSNE-plots

A.2.1 Detailed caption for the tSNE-plots in the dry case

The center shows a tSNE-plot of the complete time evolution of the system of filaments, as described in 4.1.1. In essence, this visualization groups similar density configurations together, whereas dissimilar configurations are usually spaced apart. Every simulation snapshot is represented by a dot in the tSNE-plot whose color indicates its simulation time from dark blue (early) to bright yellow (late).

The eight panels surrounding the central tSNE-plot show visualizations of the filament configuration in a regular interval of 1/8 of the total simulation time. The series of snapshots is arranged in a row-wise fashion, starting with the first in the upper left corner. The arrows locate the particular snapshot on the tSNE-plot. The size of the simulation domain is $80\,L \times 80\,L$ with up to 30000 filaments. Note that a single filament is so small that in a printout it appears as a single black dot.

A.2.2 Detailed caption for the tSNE-plots in the wet case

The general remarks from A.2.1 here apply as well. In addition, the surrounding snapshots also show a few streamlines of the fluid (red), i.e. the traces of virtual particles that are advected by the fluid.

A.2.3 Detailed caption for the tSNE-plots in the 3D wet case

The general remarks from A.2.1 here apply as well. In addition, the snapshots also show a few streamlines of the fluid, i.e. the traces of virtual particles that are advected by the fluid. For that, we cut the 3D fluid into several layers and generate the streamlines from the projected 2D flow field in one layer. This yields an approximation of the streamlines in the bottom fluid layer where the filaments are (thick red), and the topmost fluid layer close to the slip boundary (thin blue).

Due to the increased computational demand of a full 3D fluid layer, these runs were done with a simulation box of $40\,L \times 40\,L \times 3.3\,L$ with up to 7500 filaments. The filaments were effectively confined to a 2D layer with a distance of $0.17\,L$ to the lower boundary.

A.3 Local vorticity in wet systems

We discussed in section 5.2.2 that the integrated curl is no apt measure for the global vorticity in a toroidal topology. However, it helps the intuition to see where vorticity is generated. This section therefore shows examples of the vorticity field for a few selected examples.

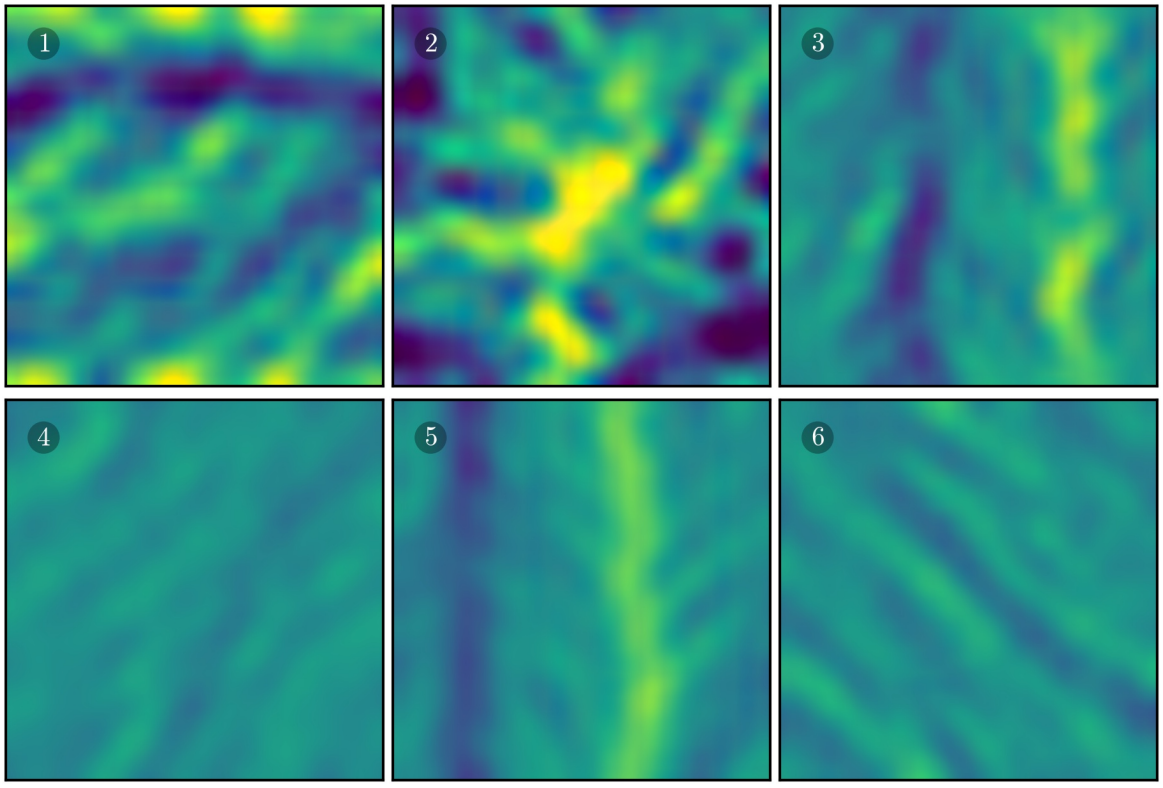

Figure A.1 | Local curl $\nabla_z \times \boldsymbol{v} = \partial_x v_y - \partial_y v_x$ in arbitrary units of the final states in Figs. 5.1–5.3 on pp. 78-81 (in sequence). **Active content:** In a flash enabled viewer, clicking the images plays a movie of the time evolution of the curl.

Section 5.2.2 used the curl of the velocity field $\nabla_z \times \boldsymbol{v} = \partial_x v_y - \partial_y v_x$ to define a measure for total vorticity, $\mathcal{V}[\boldsymbol{v}] = \int_A \big|\nabla_z \times \boldsymbol{v}\big| \mathrm{d}A$. For a better intuition of the local curl, Fig. A.1 shows the local curl of the examples in Figs. 5.1–5.3. Panel 1 belongs to Fig. 5.1 (top) where thermal noise distorts the flow field of the fluid, leading to strong curl. Panel 2 of Fig. A.1 shows an example with a vortex in the center, showing as a compact region very strong curl. Panels 3 and 5 both have a zig-zag band structure, whose transition regions show as narrow vertical stripes in Fig. A.1. Finally, panels 4 and 6 correspond to very well polarly ordered systems whose vorticity is flat.

A.4 Comparison to angular momentum conserving MPC

The MPC collision operator that was used throughout this work violates the conservation of angular momentum. To make sure that the results in this work remain valid when angular momentum *is* conserved, this appendix shows analogous simulations with an **L**-conserving variant of MPC.

The MPC collision operator as defined in 2.10 violates the conservation of angular momentum:

$$\boldsymbol{p}_i' = \frac{m_i}{M_c}\boldsymbol{P}_c + \boldsymbol{p}_i^{\mathrm{ran}} - \frac{m_i}{M_c}\sum_{j\in\mathrm{cell}} \boldsymbol{p}_j^{\mathrm{ran}} = \boldsymbol{p}_i^{\mathrm{ran}} + \frac{m_i}{M_c}\sum_{j\in\mathrm{cell}} \Big(\boldsymbol{p}_j - \boldsymbol{p}_j^{\mathrm{ran}}\Big)$$

where $M_c = \sum_{j\in\mathrm{cell}} m_j$ is the total mass in the cell. Here, the conservation of momentum was achieved through the term in parentheses, where the new total momentum is subtracted while the total old momentum is added. A similar approach works for the angular momentum, although it requires a little more work. Consider the angular momentum with respect to the center-of-mass before and after the collision in each cell,

$$\mathbf{L}_c = \sum_{i\in\mathrm{cell}} \boldsymbol{r}_i^{\mathrm{cm}} \times \boldsymbol{p}_i \qquad\qquad \mathbf{L}_c' = \sum_{i\in\mathrm{cell}} \boldsymbol{r}_i^{\mathrm{cm}} \times \boldsymbol{p}_i^{\mathrm{ran}} \ , \tag{A.5}$$

where $\boldsymbol{r}_i^{\mathrm{cm}} = \boldsymbol{r}_i - \frac{1}{M_c}\sum_{j\in\mathrm{cell}} m_j \boldsymbol{r}_j$ is the distance of the particle to the center-of-mass in the cell. To bring the angular momentum into balance, one needs to counter-rotate the particles with respect to the center-of-mass by the angular velocity $\boldsymbol{\omega} = \boldsymbol{\Pi}^{-1} \cdot (\mathbf{L}_c - \mathbf{L}_c')$, where $\boldsymbol{\Pi} = \sum_{i\in\mathrm{cell}} m_i \big((r_i^{\mathrm{cm}})^2 \mathbb{E}_d - \boldsymbol{r}_i^{\mathrm{cm}} \otimes \boldsymbol{r}_i^{\mathrm{cm}}\big)$ is the moment-of-inertia tensor of the mass distribution in the cell. Consequently, the modified collision operator

$$\boldsymbol{p}_i' = \boldsymbol{p}_i^{\mathrm{ran}} + \frac{m_i}{M_c}\Bigg(\sum_{j\in\mathrm{cell}} \big(\boldsymbol{p}_j - \boldsymbol{p}_j^{\mathrm{ran}}\big)\Bigg) + m_i \sum_{j\in\mathrm{cell}} \Big(\boldsymbol{\Pi}^{-1}\big(\boldsymbol{r}_j^{\mathrm{cm}} \times (\boldsymbol{p}_j - \boldsymbol{p}_j^{\mathrm{ran}})\big)\Big) \times \boldsymbol{r}_j^{\mathrm{cm}} \ , \tag{A.6}$$

conserves both momentum $\boldsymbol{P}_c$ as well as angular momentum $\mathbf{L}_c$ [72]. Because of the increased complexity of the collision operator, **L**-conserving MPC simulations are also considerably slower. For that reason, the **L**-conserving variant should only be used if necessary.

Figures A.2–A.8 show comparisons of all the observables that were introduced in section 4.2 for **L**-conserving and non-conserving simulations. None of these observables shows a significant difference. Therefore, the MPC variant that violates the conservation of angular momentum is sufficient to model the interactions among filaments.

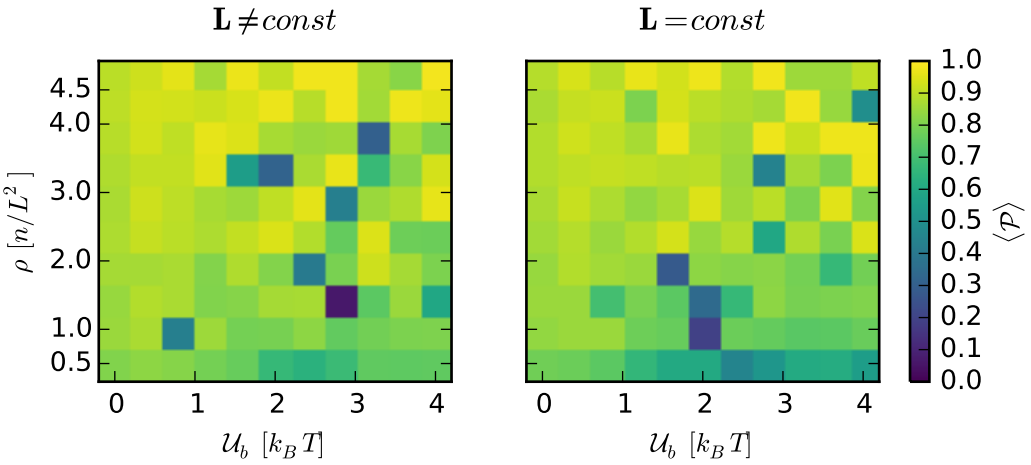

Figure A.2 | Comparison of the order parameter as defined by (4.6) scanned over the interaction strength $\mathcal{U}_b$ and filament density ρ without (**left**) and with (**right**) angular momentum conservation. The left panel shows the identical data as Fig. 5.4 (left). Because every data point is based on a single realisation, the error range is unknown.

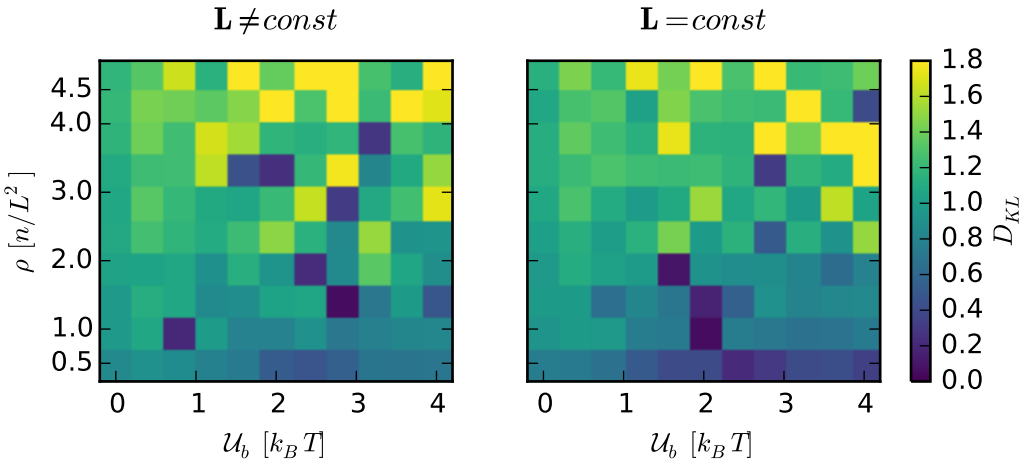

Figure A.3 | Comparison of the observed Kullback-Leibler divergence of the measured angular distribution from a flat distribution as defined in (4.8) scanned over the interaction strength $\mathcal{U}_b$ and filament density ρ without (**left**) and with (**right**) angular momentum conservation. The left panel shows the identical data as Fig. 5.5 (left). Because every data point is based on a single realisation, the error range is unknown.

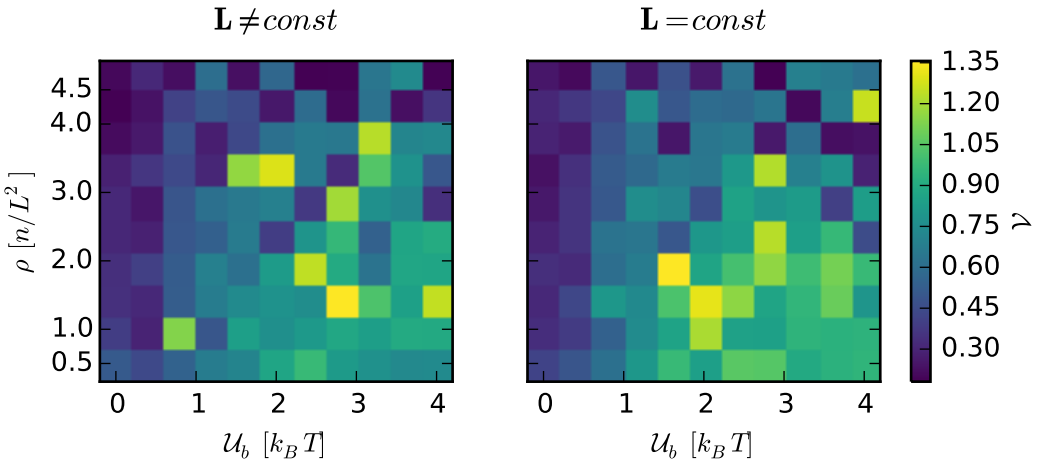

Figure A.4 | Comparison of the vorticity measure $\mathcal{V}$ as defined by (5.1) scanned over the interaction strength $\mathcal{U}_b$ and filament density ρ without (**left**) and with (**right**) angular momentum conservation. The left panel shows the identical data as Fig. 5.6 (left). Because every data point is based on a single realisation, the error range is unknown.

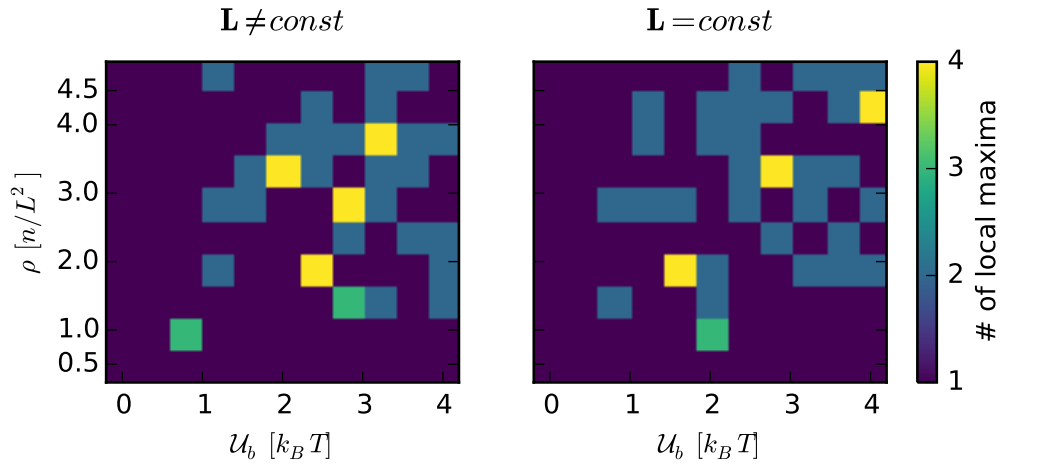

Figure A.5 | Comparison of the number of peaks of the angular distribution $P(\varphi)$ scanned over the interaction strength $\mathcal{U}_b$ and filament density ρ without (**left**) and with (**right**) angular momentum conservation. The left panel shows the identical data as Fig. 5.7. Because every data point is based on a single realisation, the error range is unknown.

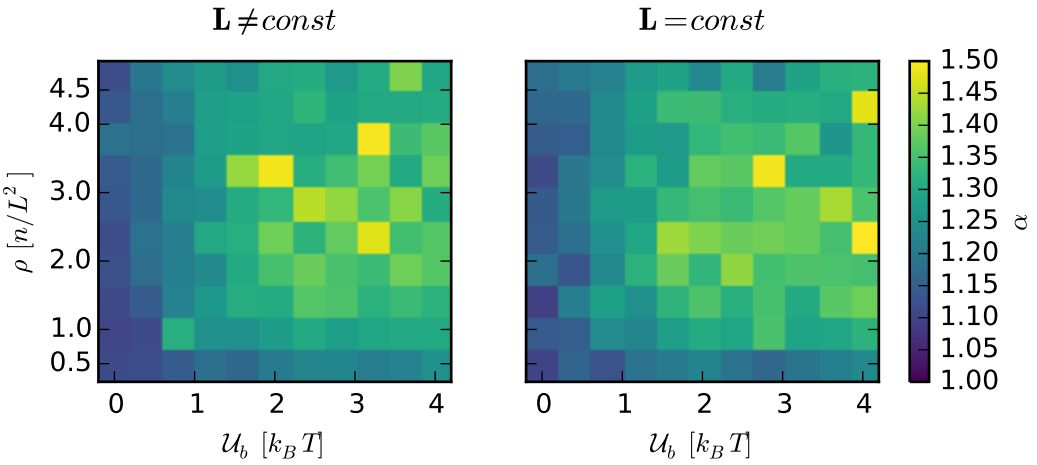

Figure A.6 | Comparison of the observed scaling exponents of the number fluctuations scanned over the interaction strength $\mathcal{U}_b$ and filament density ρ without (**left**) and with (**right**) angular momentum conservation. The left panel shows the identical data as Fig. 5.8 (left). Because every data point is based on a single realisation, the error range is unknown.

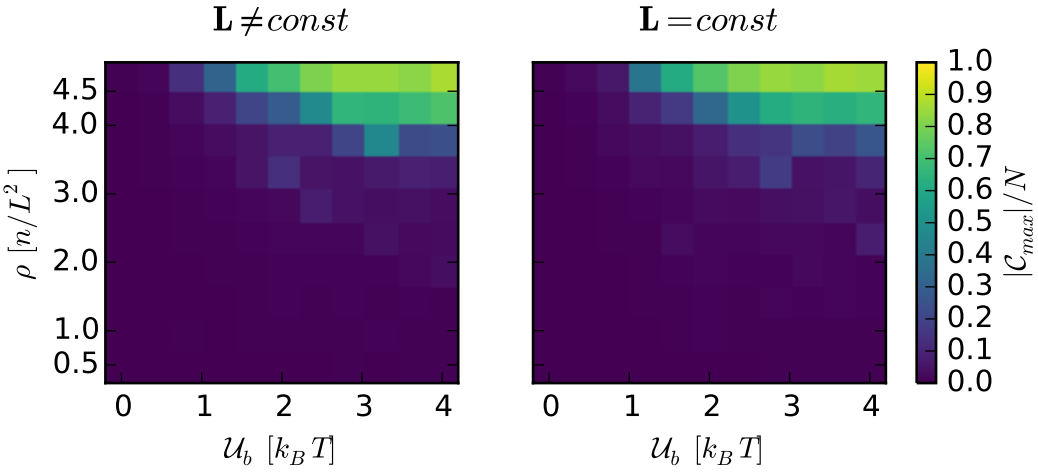

Figure A.7 | Comparison of the relative cluster size of the largest cluster in the system, $|C_{max}|/N$, as defined in 4.2.4 scanned over the interaction strength $\mathcal{U}_b$ and filament density ρ without (**left**) and with (**right**) angular momentum conservation. The left panel shows the identical data as Fig. 5.9 (left). Because every data point is based on a single realisation, the error range is unknown.

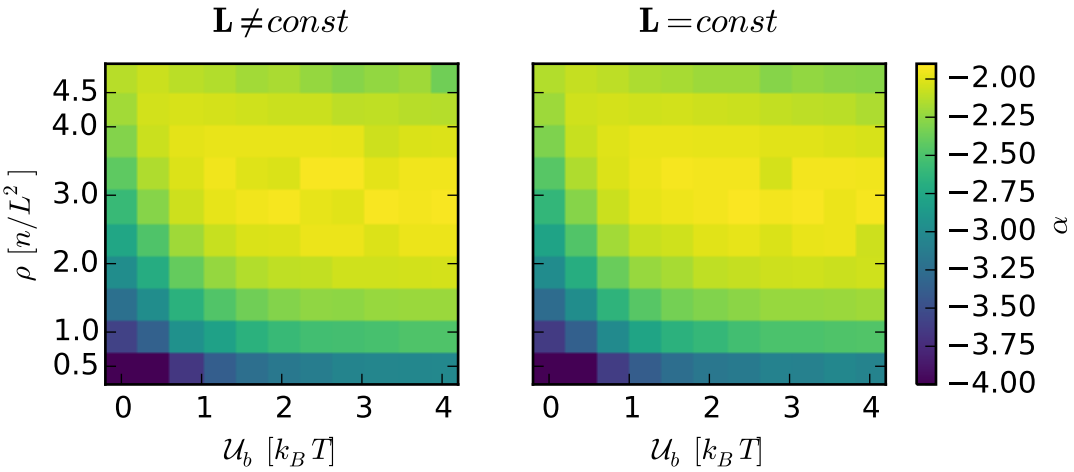

Figure A.8 | Comparison of the measured scaling exponents α of the cluster size distribution as defined by (4.16) scanned over the interaction strength $\mathcal{U}_b$ and filament density ρ without (**left**) and with (**right**) angular momentum conservation. The left panel shows the identical data as Fig. 5.10 (left). Because every data point is based on a single realisation, the error range is unknown.

We want to stress that vortices or circular flows are inherently unstable in **L**-violating MPC simulations [73]. Because the intermediate states and also some final states of the wet systems *do* have vortices, the **L**-conservation could have made a difference. We can speculate why this is not the case. A vortex is stable, because the fluid revolves around a center at a constant angular speed, so that there is no friction between circular layers around this center. The constant angular speed requires, that regions close to the center move slower than distant regions. However, the filaments in our model always move at the same speed so that the inner domains are too fast while the outer domains are too slow. Hence, when the fluid interacts with the filaments, its angular momentum cannot be conserved. Thus, the interaction with filaments is the major reason for changes in the angular momentum, so that the non-conservation of **L** during the MPC collision simply does not matter.

To sum up, this appendix has shown that **L**-conserving and violating MPC variants are completely equivalent as far as the observables of the systems of driven filaments are concerned.

A.5 Flow fields for finite hydrodynamic range

Section 5.3.1 introduces an effective friction for two-dimensional MPC simulations, leading to an effective hydrodynamic range l_h. In addition to the example for $l_h = 3\,a$ (Fig. 5.12), we now give three more examples for larger l_h.

In comparison to Fig. 5.12, Fig. A.9 shows how for larger l_h the backflow of fluid becomes weaker (left), and the flow field extends farther. For that, consider in particular the size of the black arrows, which indicates the magnitude of the local flow speed. At some point, no backflow is observed at all and only a distortion of the flow field is observed (middle). For

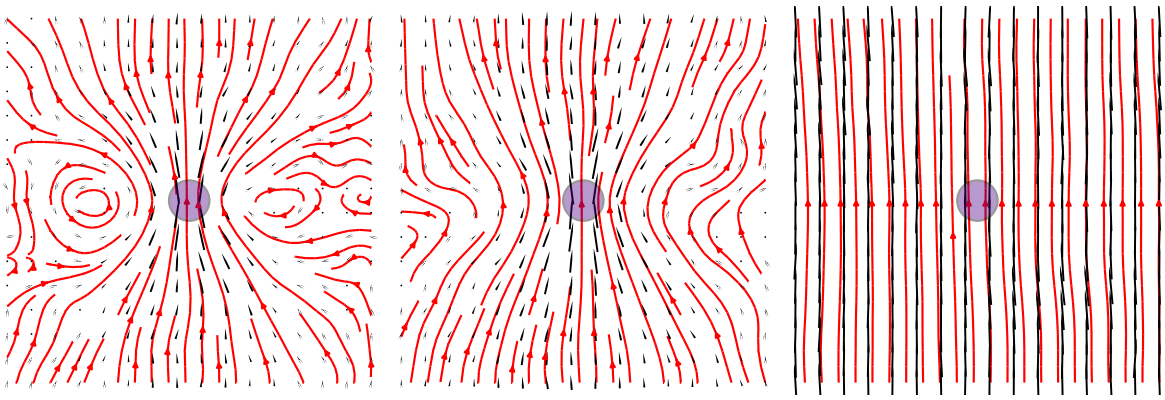

Figure A.9 | The flow field (black arrows) and streamlines (red) for two-dimensional hydrodynamics of a sedimenting sphere of diameter $5\,a$ in a box of side-length $48\,a$ with hydrodynamic range $l_h = 24\,a$ (left), $l_h = 48\,a$, and $l_h = \infty$.

completeness and as a consistency check, the right panel also shows the flow for $l_h = \infty$ which simply is a laminar flow because no momentum is dissipated here.

B Appendix Part II

B.1 Code listing for the parametric solution of the tail shape

For the solution of the swimmer shape and speed in 8.3, we used the following Mathematica code:

swimmingSpeedParametricNDSolveNoHom[ratio_, length_, a_,
ϵ1_, ϵ2_, ferromagneticFixation_:False]:=
Module $\left[\left\{\chi = N\left[\frac{\text{length}}{\text{Log[ratio]}}\right], \zeta\text{par}, \zeta\text{ih}, \text{upperlimit} = 10., \text{error}, L = \text{length}, A, \text{speed}, \text{offset}\right\},\right.$
A[x_]:=ratioExp $\left[\frac{-x}{\chi}\right]$;
offset $= \sqrt{a^2 - \epsilon 1 \text{Conjugate@}\epsilon 1}$;
Block $\left[\left\{\text{RpFU} = \frac{6\pi\eta a}{\gamma\text{perp}}, \text{RoFU} = \frac{6\pi\eta a}{\gamma\text{perp}}, \text{RpL}\Omega = \frac{8\pi\eta a^3}{\gamma\text{perp}}, \text{RoL}\Omega = \frac{8\pi\eta a^3}{\gamma\text{perp}},\right.\right.$
$\left.\left.\beta = \frac{1}{\text{RoFU}} + \frac{\text{offset}^2}{\text{RoL}\Omega}, \sigma = \frac{\text{offset}}{\text{RoL}\Omega}, \lambda = \frac{-\text{offset}}{\text{RoL}\Omega}, \mu = \frac{-1}{\text{RoL}\Omega}\right\},\right.$
If[ferromagneticFixation,
RpLΩ = 500RpLΩ;
RoLΩ = 500RoLΩ;
];
ζpar = ParametricNDSolveValue[
$\{-i\zeta[x] + A\text{''}[x]\zeta\text{''}[x] + 2A'[x]\zeta\text{'''}[x] + A[x]\zeta\text{''''}[x] == (\beta + x\sigma)(\kappa 3\ A[0] + \kappa 2\ A'[0]) + (\lambda + x\mu)A[0]\kappa 2,$
$\zeta[0] == \epsilon 1, \zeta'[0] == \epsilon 2, \zeta\text{''}[L] == 0, \zeta\text{'''}[L] == 0\}, \zeta, \{x, 0, L\}, \{\kappa 2, \kappa 3\}, \text{InterpolationOrder} \to 4];$
With[{Ps = FindRoot[{ζpar[κ2, κ3]''[0] == κ2, ζpar[κ2, κ3]'''[0] == κ3},

```
{{κ2, 0., upperlimit}, {κ3, 0., upperlimit}}]},
ζih = ζpar[κ2, κ3]/.Ps;
];
error =
NIntegrate[Abs[−iζih[x] + A"[x]ζih"[x] + 2A'[x]ζih"'[x] + A[x]ζih""[x] −
((β + xσ)(ζih"'[0]A[0] + ζih"[0] A'[0]) + (λ + xμ)A[0]ζih"[0])], {x, 0, L}];
speed = With[{ζ1 = ζih'[0],
ζ2 = ζih"[0],
ζ3 = ζih"'[0],
ζ4 = ζih""[0],
F0 = ζih"'[0]A[0] + ζih"[0] A'[0],
T0 = A[0]ζih"[0]
},
1/(γRpFU+L) (((RoFU−γRpFU)/(RoFURoLΩ)) A[0]^2Im[ζ2Conjugate@ζ3]+
(1 − γ)Re[ζ2Conjugate[T0] − ζ1Conjugate[F0] + NIntegrate[A[x]ζih"[x]Conjugate[ζih"'[x]], {x, 0, L}]])
];];
Return[{(*final swimming speed*){speed, ζih}, L, a, ratio, error}
];]
```

The input parameters are

ratio The estimated number of attached filaments

length The length of the swimmer tail in μm

a The bead diameter, in our case this was $0.5\,\mu m$

ε_1 The radius of the attachment point in the local coordinates

ε_2 The angle of the tail with the x-axis in the local coordinates

ferromagneticFixation Whether the external magnetic field impedes rotations of the swimmer about its y- and z-axes.

The function return a list with the projected swimmer speed, the calculated swimmer shape, the input tail length (in μm), the input bead radius (in μm), the input ratio, and the residual error of the obtained solution as defined in (8.29). Note that the returned list contains the unaltered input parameters for bookkeeping of the results.

Danksagung

Zuallererst gilt mein Dank Prof. Erwin Frey. Ohne seine Offenheit für meine Ideen, wäre diese Arbeit wesentlich weniger spannend gewesen. Insbesondere für sein großes Vertrauen in mich und meine Projekte bin ich sehr dankbar. Gerne erinnere ich mich an so manches Treffen, das mich unheimlich motiviert hat und mir einen Weg gezeigt hat, wie es weitergehen könnte. Doch nicht nur fachlich warst Du, Erwin, mir ein Vorbild, sondern vor allem auch durch Deine umsichtige und herzliche Art. Ich hoffe, viel von Dir gelernt zu haben.

Danke auch an Prof. Holger Stark, der wertvolle Stunden der Vorweihnachtszeit geopfert hat, um diese Arbeit zu lesen und zu meiner Verteidigung extra aus Berlin angereist kam.

Besonderer Dank geht an Prof. Tim Liedl und Alexander Mario Maier, die bereit waren, die vage Idee eines DNA-Schwimmers mutig umzusetzen. An dieser Stelle sorry Alex, dass sich diese Mammutaufgabe als so viel schwieriger herausgestellt hat, als es zunächst den Anschein hatte. Ich werden den Diavola-Tag im Lo Studente mit dir vermissen.

Das *Internationale Doktorandenkolleg NanoBio Technology* hat mich ein Jahr lang finanziert und außerdem mein Doktorandenleben mit vielen wertvollen Workshops bereichert. Dies war vor allem der Verdienst von Marilena Pinto. Weiterhin durfte ich ein Jahr lang mit Hsin-Yi Chiu und Svenja Lippok die Interessen der Studenten des `CeNS` vertreten. Danke Euch und Susanne Hennig für die abwechslungsreiche Zusammenarbeit.

Doch was wäre diese Zeit ohne die vielen Mitstreiter am Lehrstuhl gewesen? In loser Generationen-Abfolge versuche ich, niemanden zu vergessen: da sind Jonas Cremer und Anna Melbinger als Vorbilder am Anfang meiner Promotion. Jan-Timm Kuhr, der ein wenig Kunstakademie-Flair verbreitet hat. Cristina Pop, das originale Cookie-Monster. Louis Reese, der gute Geist des Lehrstuhls mit seinem offenen Ohr am absoluten Tiefpunkt. Markus Weber, der einfach jedes Paper kennt. Matthias Rank mit seiner gute Laune. Mattias Lechner, der offizielle Mensa-Rufer. Johannes Knebel, der streitbare Kreative. Lorenz Huber, mit dem ich unsere Bezzera BZ07 pflegen durfte. Marianne Bauer, die so schön herzlich lachen kann. Felix Kempf, der es sich durch viele Korrekturen hart erkämpft hat, nicht mit den anderen Neulingen genannt zu werden. Isabella Krämer und Timo Krüger, die ich gerne länger als Kollegen gehabt hätte. Aus der Reihe geht mein besonderer Dank an Philipp Lang, der mit mir von Anfang bis Ende Raum A337 bewohnt hat. Seine große Erfahrung mit Polymeren brachte in so mancher Diskussion Erleuchtung. — Ihr alle macht mir den Abschied schwer.

Auch bedanken möchte ich mich bei meinen Masterstudenten Anatolij Gelimson und Marc von Reutern.

Noch einmal hervorheben möchte ich all jene, die geholfen haben meine Arbeit von ein oder zwei kleinen Rechtschreibfehlern zu befreien, namentlich Felix Kempf, Johannes Knebel, und Philipp Lang. Durch Eure Mühen hat diese Arbeit enorm an Lesbarkeit und logischer Stringenz gewonnen. Außerdem hat die Rechnerbetriebsgruppe durch die Betreuung einer

hervorragenden Infrastruktur die sehr rechenintensiven Abschnitte dieser Arbeit erst möglich gemacht.

Mein besonderer Dank geht an meine Eltern Eva und Josef Weig. Nur dank ihrer immerwährenden Unterstützung und der vorbehaltlosen Freiheit mir meinen eigenen Weg zu suchen, bin heute hier. Vollkommen selbstverständlich haben sie mich während meines gesamten Studiums großzügig unterstützt — und ich habe gründlich studiert. Damit gebührt Euch ein wesentlicher Anteil am Gelingen dieser Arbeit. Danke Euch für alles!

Zu guter Letzt geht mein Dank an all jene nicht namentlich genannten Freunde, die mich in so manch angespannter Situation ertragen haben. Direkt betroffen waren vor allem meine ehemaligen Mitbewohner Janek Landsberg, Quirin Kronseder und mein guter alter Johannes *Maria* Rieger.

Schlussendlich meine liebe Carolin, der Ehrenplatz ist für Dich.